Studies on protein corona formation and cellular uptake mechanism for nanoparticles covered with polyglycerol and its derivatives

ZOU Yajuan

論　文　要　旨

論文題目　Studies on protein corona formation and cellular uptake mechanism for nanoparticles covered with polyglycerol and its derivatives
（ポリグリセロールおよびその誘導体で被覆されたナノ粒子のタンパク質コロナ生成と細胞取り込み機構に関する研究）

申 請 者　ZOU Yajuan

論文要旨

表面化学修飾を経たナノ粒子は、癌の治療や診断などの生物医療応用において有用なプラットフォームとなり得る。一般にナノ粒子は、生体液中でタンパク質を吸着して、タンパク質コロナと呼ばれる表層を形成し、これがナノ粒子の生物学的性質を決め、生体系との相互作用を変化させる。コロナタンパク質とナノ粒子との複合体は、疎水相互作用や静電相互作用により熱力学的に安定化されため、生理学的環境下におけるナノ粒子表面の性質とナノ粒子のタンパク質への吸着や細胞表面との相互作用を関連づけることは、意義深いことと考えられる。本論文では、特にポリグリセロール（PG）によるナノ粒子の表面化学修飾に焦点を当て、PG 修飾の度合いと PG 表面上の荷電官能基および標的指向性部位がタンパク質コロナ形成とその後の細胞取り込みにどのように影響するかを定量的に研究した。

本論文は六章で構成されている。第一章は序論であり、タンパク質コロナとナノ粒子の表面化学修飾、およびそれらの相関について述べる。

第二章では、ポリエチレングリコール（PEG）との定量的比較により、PG の可能性を検討した。その結果、PG は PEG に比べ、タンパク質の吸着やマクロファージの取り込みをはるかに効率的に抑制することが明らかになった。特に、30 wt%の高密度で PG 修飾されたナノ粒子の表面には、ほとんどタンパク質は吸着されず、その結果、マクロファージ（貪食細胞）への取り込みもほとんどなかった。

第三章では、PG のタンパク質を吸着しない性質を利用し、荷電官能基と特定のタンパク質との相互作用を定量的に評価した。その結果、官能基の電荷と反対の電荷を有するタンパク質が排他的に相互作用することを明らかにした。また、アルブミンとアンモニウムとの会合定数は、ナノ粒子表面におけるアミノ基の密度に比例することも見出された。

第四章では、荷電官能基と血清タンパク質との正味の相互作用および細胞取り込みに対するそれらの影響を検討した。その結果、荷電ナノ粒子の細胞取り込み効率がナノ粒子のタンパク質への親和性と相関し、また、それらの取り込みメカニズムはタンパク質コロナの組成によって決まることが明らかになった。

第五章では、トリフェニルホスホニウム（TPP）のミトコンドリアへの標的指向性に対するタンパク質コロナの影響を検討した。TPP が結合した PG 修飾ナノ粒子の表面にある薄いタンパク質コロナ層は、その標的指向性に影響を与えなかった。一方で、より厚いタンパク質コロナ層により TPP の標的指向性が著しく減少することが明らかになった。さらに、いずれの場合においても、タンパク質コロナ層は TPP の細胞毒性を顕著に減少させることが見出された。

第六章は結論であり、この論文の内容がタンパク質コロナ形成の理解をより一層深めるとともに、次のよう

な新しい方法論、 1）ナノ粒子の非特異的な取り込みを回避するためのタンパク質コロナ形成の抑止、2）様々なナノ粒子表面のタンパク質に対する親和性の定量的な比較、3）タンパク質コロナの組成を制御することによるナノ粒子の細胞への取り込みの制御、4）細胞内レベルでより正確で安全な薬物送達のための標的指向性部位の設計、を提供すると述べている。

Table of contents

Chapter 1: Introduction

1-1 Nanoparticles and their biomedical applications

Nanoparticles (NPs) are defined as 'the small particles having at least one dimension on the nanoscale (1-100 nm)' [1]. Over the last decades, a broad range of NPs with diverse compositions, shapes and surface chemistries have been developed as shown in Figure 1-1. NPs can be made from various materials including inorganic materials such as nanocarbons and metal oxides, and organic polymers and biopolymers such as dendrimers and liposomes [2]. Although most of the NPs have a spherical shape, non-spherical NPs such as nanorods, nanotubes and nanosheets with suitable aspect ratios are emerging in recent years [3]. More importantly, the colloidal stability of NPs can be improved by tailoring their surface chemistries such as charge and hydrophilicity [4].

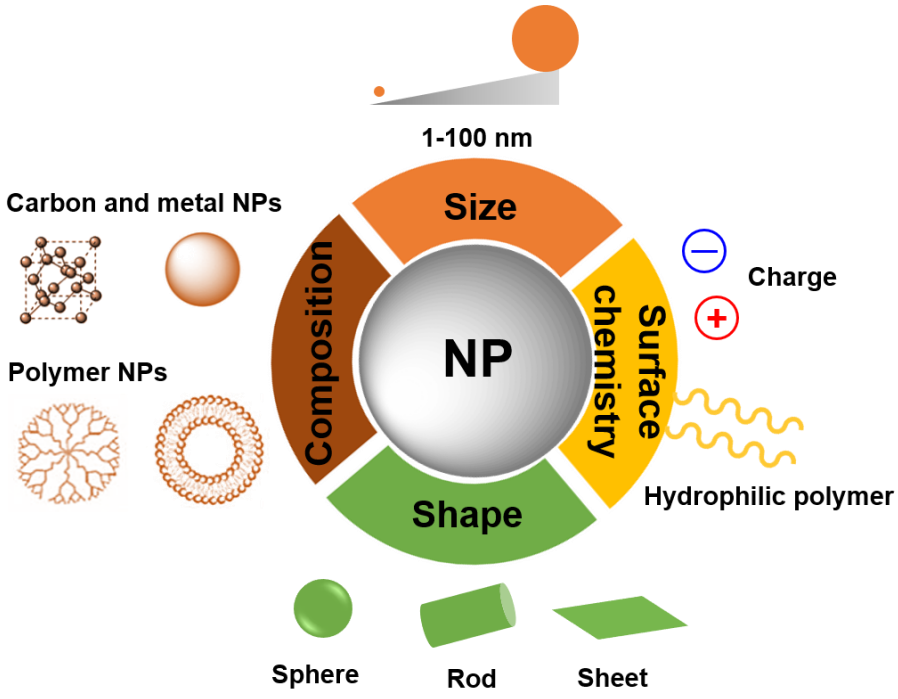

Figure 1-1. General description of NP in terms of its characteristics; size, composition, shape and surface chemistry.

Surface-functionalized NPs are promising platforms for biomedical applications especially in

cancer theranostics, as they offer many advantages over small molecules and bulk materials [5]. NPs within the size range of 10-100 nm are most likely to be accumulated in neoplastic regions through the mechanism known as the enhanced permeability and retention (EPR) effect [6]. It results from the hyperpermeable vasculature and dynamic openings on the vessel walls of tumor cells as well as the impaired lymphatic drainage from tumor tissues [7] (Figure 1-2a). In addition to the proper size for EPR effect, the amenability for further surface functionalization is another important merit of NPs. For example, a couple of targeting ligands such as RGD peptide, folic acid, biotins, and antibodies can be conjugated to NP [8] (Figure 1-2b), which allow NPs to preferentially interact with specific receptors overexpressed on the cancer cells. This leads to accurate delivery of NPs to desired sites. Moreover, a myriad of additional functions such as imaging [9] and hyperthermia treatment [10] can be incorporated into NPs (Figure 1-2c) to improve their biological performances.

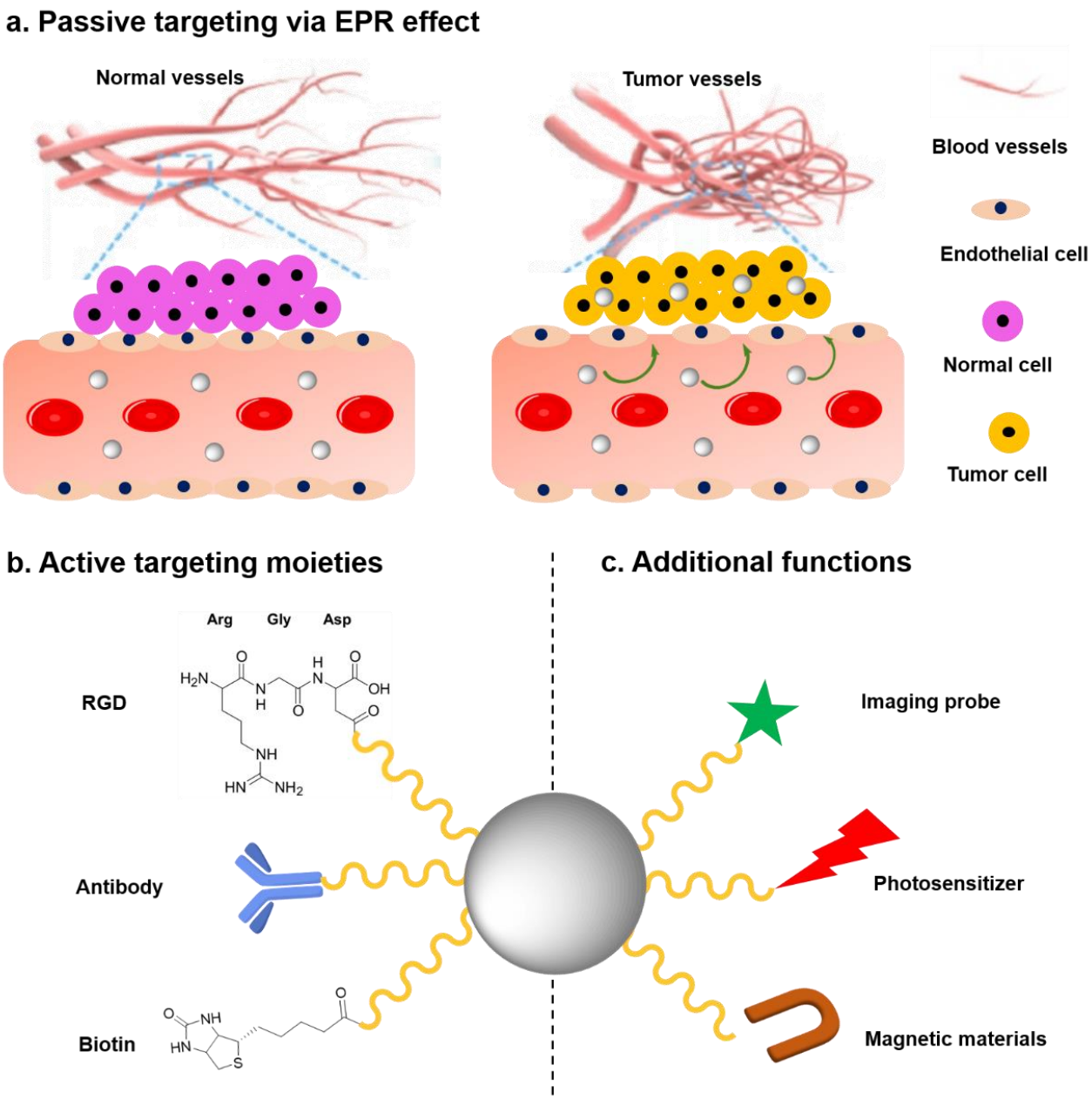

Figure 1-2. Advantages of NPs for biomedical applications. (a) Accumulation of NPs in tumor regions through EPR effect, (b) targeting moieties on NP surface for site specific delivery, and (c) functional groups which can be incorporated into NPs.

1-2 Protein corona formation alters the biological fate of NPs

Although NPs have demonstrated great potential in cancer therapy, few of them have reached clinical practice. The wide gap between discoveries at benches and applications at beds is mainly due to insufficient knowledge of the interactions between NPs and the biological systems [11]. In biofluids,

NPs absorb proteins to form a coating layer known as protein corona due to their high surface energy [12]. After NPs are covered with protein corona, their pristine identities are buried. On the other hand, the proteins in the corona layer give NP the biological identity which is 'seen' by cells [13] (Figure 1-3). Therefore, the biological fate of NPs such as cellular uptake, biodistribution, biotransformation and clearance are affected by the corona proteins [14].

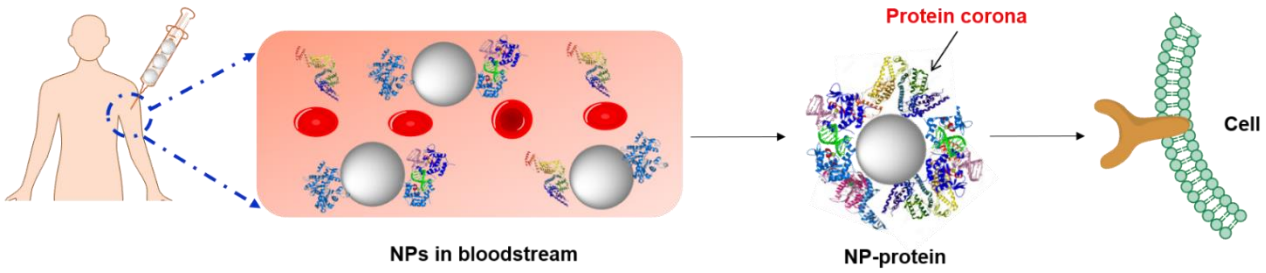

Figure 1-3. Protein corona reflects the biological identity of NPs and alters their interaction with cells.

To date, a couple of undesired effects resulting from protein corona formation have been reported as shown in Figure 1-4a. For instance, the opsonizing proteins such as IgG and complement proteins facilitate the uptake of NPs by macrophage of the mononuclear phagocyte system (MPS), thereby initiating the rapid removal of NPs from bloodstream and diminishing the amounts of NPs to reach their destination in the body [15]. Besides the accelerated clearance of NPs by the MPS, protein corona is also proved to be detrimental to active-targeting strategies, since the targeting moieties engineered on NP surface are masked by protein corona and become inaccessible to their receptors. Salvati et al. found that the targeting ability of transferrin-conjugated NPs to A549 cells was decreased when the NPs were coated by serum proteins [16]. On the other hand, the 'sweet side' of protein corona has been revealed as shown in Figure 1-4b; Lesniak et al. reported that the protein corona lowered toxicity of NPs by reducing the uptake efficiency of NPs, probably because the adhesion affinity of NPs to cell membranes as well as the non-specific interaction between NPs and cell membranes were reduced [17]. More interestingly, some research groups have attempted to use the protein corona to target specific

cells and/or disease lesion. Kreuter et al. demonstrated that apolipoprotein coating enhanced delivery efficacy of NPs, rendering NPs to cross over the blood-brain barrier [18].

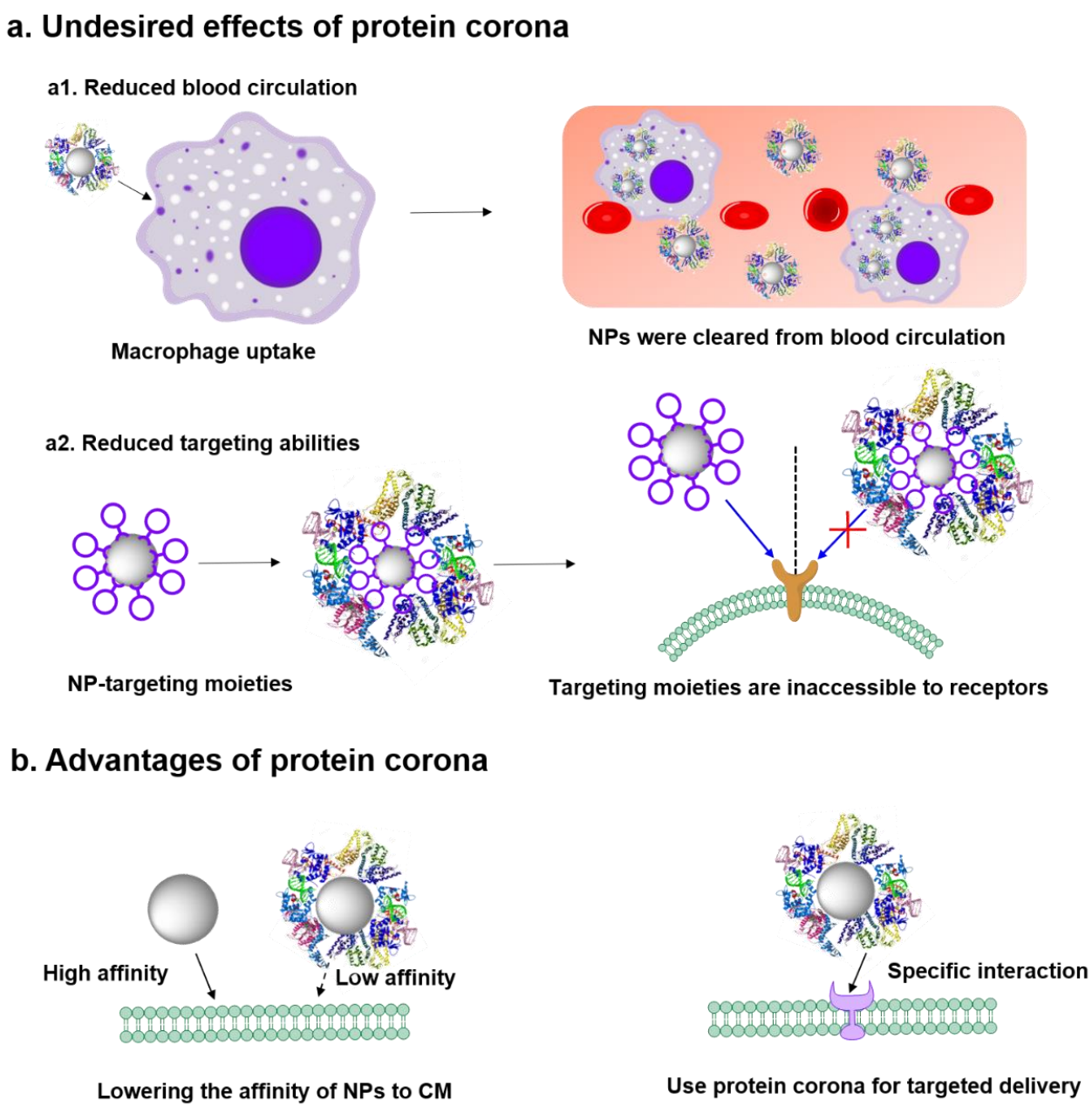

Figure 1-4. The formation of protein corona can be either (a) harmful or (b) beneficial for medical application of NPs.

1-3 NP surface functionality and protein corona formation

In order to control the behavior of NPs in physiological environment, it is necessary to gain deep insights into the formation processes of protein corona, because the biological fate of NPs is more related to the protein coronas. Although many interactions such as hydrophobic, electrostatic and van der Waals ones, and hydrogen bonding are contributing to protein attachment, hydrophobic and electrostatic interactions are demonstrated to be the driving forces for protein corona formation [19] (Figure 1-5). Consequently, the protein corona formation is found to be closely related to the surface properties.

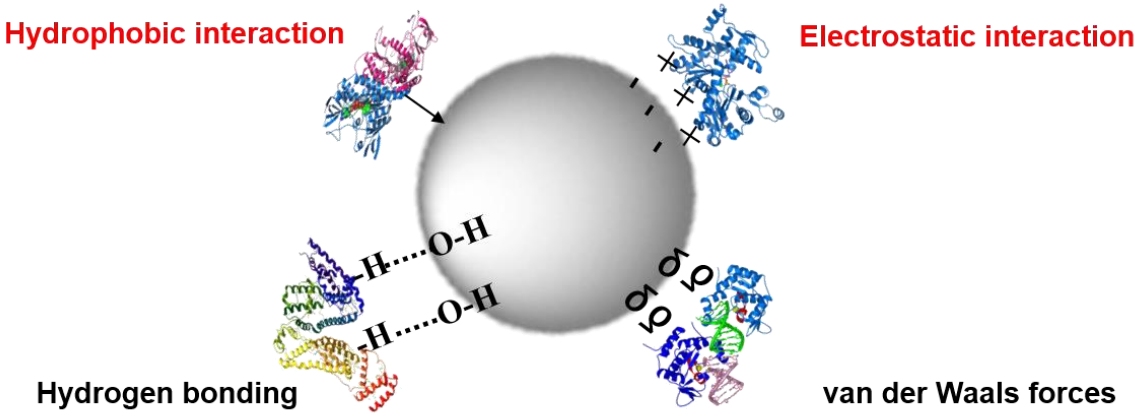

Figure 1-5. Interactions between NP surface and proteins.

In order to minimize the negative effects of protein corona, NPs are typically functionalized with hydrophilic and neutral polymers to repel proteins from adsorbing onto NP surface (Figure 1-6a). Polyethylene glycol (PEG) is the current gold standard to suppress protein corona formation (Figure 1-6b), and has been used to increase the circulation time of a variety of NPs including gold NPs, polymeric NPs and liposomes [20]. Despite the widespread application of PEG, it was reported that PEG cannot fully prevent protein corona formation [21]. Moreover, the development of PEG antibodies as well as the accelerated blood clearance (ABC) after repeated injection of PEGylated

nano-formulations were also reported [22]. To circumvent the PEG dilemma, zwitterionic molecules (Figure 1-6b) such as polybetaines (PB) or polysaccharides have been discussed as PEG alternatives [23]. However, a comparison study made clear the lower ability of PB compared to that of PEG to resist protein adsorption, cellular uptake, and *in vivo* excretion [24, 25]. On the other hand, we have established the facile methodology to functionalize NP surfaces densely with polyglycerol (PG) [26, 27] (Figure 1-6b) and demonstrated very low nonspecific cellular uptake [28] as well as the extremely long blood half-life [9] of NP-PG, implying that PG grafting might be a promising alternative to PEG.

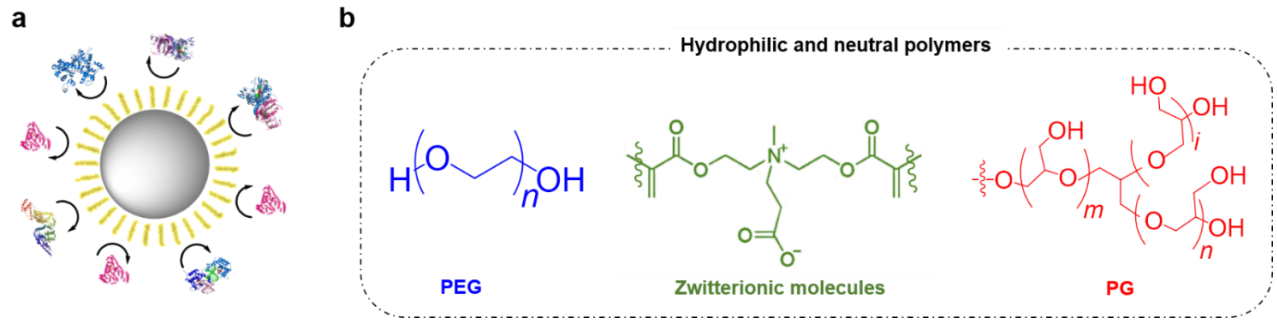

Figure 1-6. Surface functionalization of hydrophilic neutral polymers is the typical approach to prevent protein corona formation. (a) Schematic representation, and (b) structures of PEG, zwitterionic molecules and PG.

In addition to prevention of protein adsorption, there is a growing interest to study how the NP surface functionality affects protein corona formation and the subsequent cellular uptake of NPs [29]. The surface charge has been one of the main focuses in this regard. Charge has long been the most important parameter in NP design to regulate their uptake, and it is generally accepted that the positively charged NPs exhibit a higher affinity to cell membrane than the negative ones to give a higher uptake possibility (Figure 1-7a) [30]. In fact, after protein corona formation, the NP-protein complexes are all negatively charged, regardless of the zeta potentials of the pristine NPs [31]. Hence, the cellular uptake of charged NPs relates more to the adsorbed proteins rather than their original

charges. However, the cascade effects of NP surface charge on protein corona formation and cell uptake have not been well documented (Figure 1-7b). For instance, some studies reported that both negatively and positively charged NPs interact similarly with serum proteins which leads to no difference in their uptake behavior [32, 33]. On the other hand, the preferential association of specific proteins with charged functional groups to result an enhanced cellular uptake of NPs was also reported by other groups [34]. These inconsistent conclusions imply that the non-charged interactions exist at nano-bio interfaces to make the charge effect unclear and that a corona-free interface is required to reach reliable conclusion.

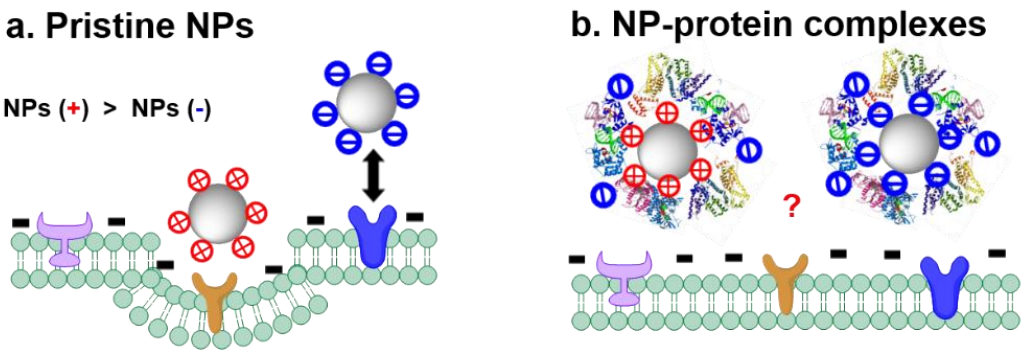

Figure 1-7. Schematic representation of the interaction of charged NPs with cells. (a) Pristine NPs and (b) the NP-protein complexes.

1-4 Aim of this thesis

The aim of this PhD thesis is to advance protein corona study. In the first project, the potential of PG was fully explored as an alternative to PEG in terms of resistivity to protein adsorption and macrophage uptake. Through a series of quantitative comparisons, the author revealed clearly that PG resisted the protein adsorption and the macrophage uptake much more efficiently than did PEG. In particular, only a little protein was adsorbed on the NP surface coated with densely PG, leading to almost no macrophage uptake. Based on this "corona-free" PG interface, in the second project, the net interaction between proteins and charged functional groups were investigated in a quantitative manner.

In the third project, the net interactions among charged functional groups, serum proteins and cells were clarified; that is, the cellular uptake efficacy and mechanism of charged NPs were found to be dictated by their affinity to proteins and the distinct protein corona compositions formed on their surface, respectively. In the fourth project, the effect of protein corona on the targeting ability was studied at a subcellular level. The author revealed that a thinner proteins corona layer on the surface of NP did not affect its targeting ability, whereas a thicker protein corona layer diminished its targeting specificity.

Chapter 2: Polyglycerol grafting shields nanoparticle from protein corona formation to avoid macrophage uptake

2-1 Introduction

To reduce NP clearance by MPS, various hydrophilic and electrically neutral polymer coatings including polyether, PB and polyol [20] have been investigated for anti-biofouling. Although PEG is the most widely used non-fouling material, it has been revealed that PEG cannot completely shield protein adsorption, and accordingly induces immune response such as ABC and pseudo-anaphylaxis [22, 35-37]. Due to these limitations of hydrophilic polymer coating, the research direction has changed to protein pre-adsorption [38, 39]; NPs precoated with clusterin or plasma proteins showed macrophage evading abilities [40]. However, proteins with higher affinity to NP surface can replace the precoated proteins through Vroman effect [41], implying that the fundamental solution should be complete shielding of protein corona formation.

PG, which consists of a large number of hydroxyl groups on the PEG backbone (Scheme 2-1), is expected to have a higher potential to prevent protein adsorption due to its non-ionic and more hydrophilic nature [9, 28, 42]. Actually, PG on a gold substrate was reported to exhibit similar or even higher protein resistance than PEG to the proteins such as fibrinogen, lysozyme, albumin and pepsin [43-45]. On the other hand, we established the methodology to functionalize NP surfaces more facilely and densely with PG [26, 46, 47] and demonstrated their very low non-specific cellular uptake [27, 28].

In this work, in order to fully explore the potential of PG as alternative to PEG, the author here quantitatively compared the PG- and PEG-functionalized NPs in protein corona formation and macrophage uptake. It is clearly revealed that PG resists to the protein adsorption and the macrophage

uptake much more efficiently than PEG, in particular, only a little protein is adsorbed on the NP surface coated with PG at 30 wt%, leading to almost no macrophage uptake.

2-2 Results and discussion

2-2-1 Synthesis and characterization of NP-PG and NP-PEG

Nanodiamod (ND) with 30, 50 and 100 nm (ND_{30}, ND_{50} and ND_{100}, respectively) and super paramagnetic iron oxide nanoparticle (SPION) with 22 nm (Table 2-1) were functionalized with PG at *l* (low), *m* (medium) and *h* (high) contents, and PEG at *l* and/or *m* contents as shown in Scheme 2-1 (see details in Methods). NP-PG-*l*, -*m* and -*h* were prepared by "grafting from" method *via* ring opening polymerization of glycidol (Route A in Scheme 2-1) according to the procedure we reported previously [26]. In the PG functionalization, we tried to control the degree of polymerization either by reaction temperature or reaction time, and realized precise control of the PG contents at *l*, *m* and *h* corresponding to 10, 20 and 30 wt%, respectively, by tuning the reaction temperature rather than reaction time. Since we also found that the PG content did not change so much after 4 h, the reaction time was fixed to be 4 h in all the PG functionalization. The reaction temperatures optimized for *l*, *m* and *h* PG contents are summarized in Table 2-1. The higher reaction temperatures are required for higher PG contents in each NP to facilitate the polymerization. Actual weight increase from NP-PG-*l* to NP-PG-*h* in one particle is shown in Table 2-3. At the same PG content (*l*, *m* or *h*), the higher reaction temperature is needed for larger diameter, because specific surface area becomes smaller and actual weight in PG layer becomes larger, as the size becomes larger (Table 2-3). However, the reaction temperatures of SPION with 22 nm in diameter are higher than those of ND_{30} with 30 nm in diameter (Table 2-1), although the specific surface area of SPION is slightly less than that of ND_{30} (Table 2-3). This is probably due to difference in the density of the functional groups such as carboxyl and hydroxyl groups, which can initiate the ring opening polymerization. The above oxygen-containing functional groups are considered to be denser on the surface of ND_{30} than SPION.

Scheme 2-1. Surface functionalization of NPs with PG and PEG at low (*l*), medium (*m*) and high (*h*) contents.

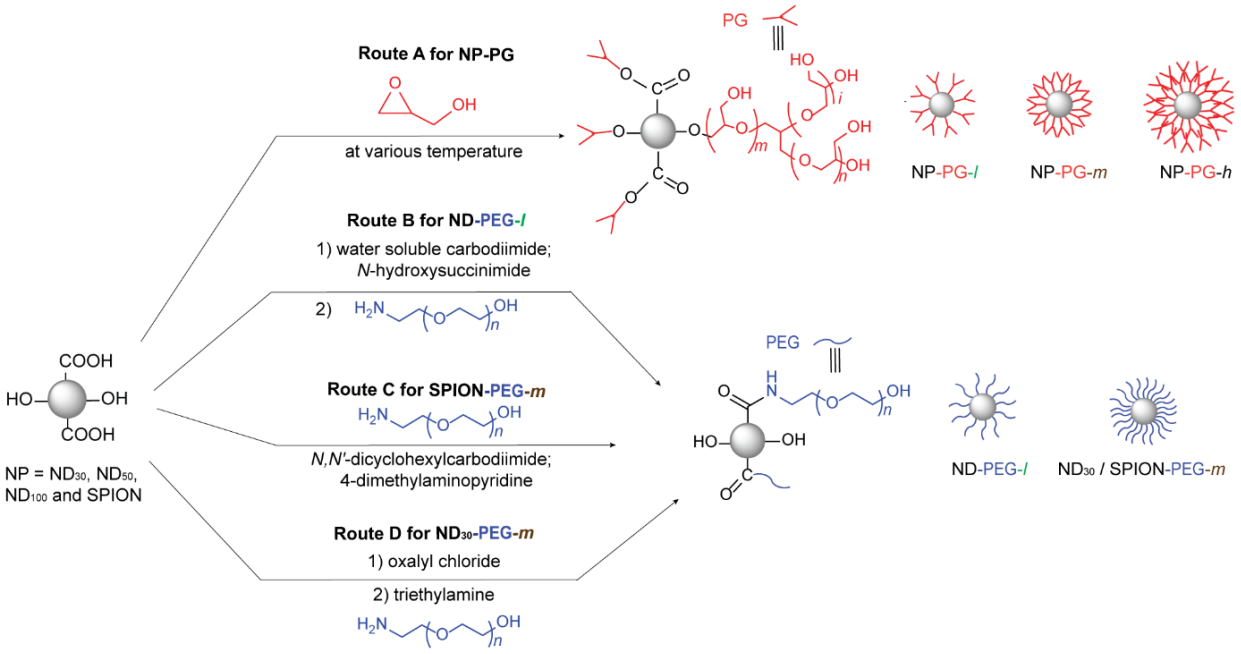

Table 2-1. Core size of NP-PG-*h* and reaction temperatures in the PG functionalization of NPs to control the PG contents at *l*, *m* and *h*.

	core size of	reaction temperature (°C)		
NP	NP-PG-*h* (nm)[a]	NP-PG-*l*	NP-PG-*m*	NP-PG-*h*
ND_{30}	29 ± 13	rt[b]	45	60
ND_{50}	52 ± 20	70	105	140
ND_{100}	102 ± 32	80	120	140
SPION	22 ± 5	50	100	140

[a]Mean diameter ± standard deviation determined by more than 50 particles in STEM images shown in Figure 2-1. [b]Room temperature.

NP-PEG-*l* and -*m* were synthesized by "grafting to" method *via* amidation of NP by PEG with 5 kDa (PEG_{5k}) as shown in Scheme 2-1 (see details in Methods). PEG_{5k} was selected in comparison with the shorter PEG including $PEG_{1.5k}$, PEG_{2k} and PEG_{3k} in terms of the specific surface area in one ND_{100}

particle (Table 2-2). Although the number of the PEG chain is larger in the shorter PEG, the specific surface area is larger in the longer PEG. Therefore, we chose PEG_{5k} among the PEG with various lengths. The ND-PEG-*l* was prepared in an aqueous solution (*N,N*-dimethylformamide (DMF)/H_2O) in the presence of water soluble carbodiimide hydrochloride (WSCD·HCl) and *N*-hydroxysuccinimide (Route B in Scheme 2-1). A similar method using *N,N′*-dicyclohexylcarbodiimide (DCC) and 4-dimethylaminopyridine (DMAP) was applied to PEGylation of SPION in an organic solvent, giving SPION-PEG-*m* (Route C in Scheme 2-1). To increase PEG content from *l* to *m* in ND-PEG, the amide linkage between PEG and ND_{30} was constructed *via* acyl chloride on the ND surface prepared by oxalyl chloride (Route D in Scheme 2-1) [48]. Although we tried many times, NP-PEG-*h* was not able to be obtained. This implies that the linear PEG cannot cover the NP surface as densely as the branched PG, which will be quantitatively discussed below.

Table 2-2. Comparison among ND_{100}-PEG with 1.5 - 5 kDa in one ND_{100} particle.

PEG molecular weight (MW_{PEG}) (kDa)	PEG						
	Content[a] (wt%)	Weight (ag)	Number of PEG chain	r_{PEG}[b] (nm)	S_{PEG}[c] (nm^2)	Total Surface area (nm^2)	Specific surface area (m^2/g)
1.5	8.4	174.2	7.0×10^4	1.2	17.3	3.0×10^5	1.7×10
2	11.1	237.2	7.1×10^4	1.4	23.8	4.2×10^5	1.8×10^3
3	12.2	264.0	5.3×10^4	1.7	37.3	4.9×10^5	1.9×10^3
5	9.0	186.8	2.2×10^4	2.3	65.9	3.7×10^5	2.0×10^3

[a]Based on TGA. [b]Defined in eq. 2-1. [c]Defined in eq. 2-2.

The hydrodynamic radius of PEG ($\boldsymbol{r_{PEG}}$) is calculated by eq. 2-1 based on the linear relationship between $\boldsymbol{r_{PEG}}$ and PEG molecular weight ($\boldsymbol{MW_{PEG}}$) [49].

$$\boldsymbol{r_{PEG} = 0.0201 \times MW_{PEG}^{0.556}} \qquad \textbf{(eq. 2-1)}$$

The surface area of PEG ($\boldsymbol{S_{PEG}}$) is calculated by eq. 2-2 on the assumption of spherical shape of PEG.

$$\boldsymbol{S_{PEG} = 4\pi r_{PEG}^2} \qquad \textbf{(eq. 2-2)}$$

Table 2-3. Quantitative data of NP, NP-PG and NP-PEG at *l*, *m* and *h* contents in one particle.

NP, NP-PG or NP-PEG	NP		PG or PEG[a]					
	Weight[b] (ag)	Surface area[b,c] (nm^2)	Weight[d] (wt%)	Weight (ag)	Degree of PG polymerization	Number of PEG chains	Density of PG monomer[e] (nm^{-2})	Density of PEG chain[e] (nm^{-2})
ND_{30}	45	2.7×10^3 (60)	–	–	–	–	–	–
ND_{30}-PG-*l*			10.2	5.1	4.2×10^4	–	15 (1.1)	–
ND_{30}-PG-*m*			19.3	11	8.8×10^4	–	32 (2.4)	–
ND_{30}-PG-*h*			33.0	22	1.8×10^5	–	67 (4.9)	–
ND_{30}-PEG-*l*			11.9	6.1	–	7.3×10^2	–	0.27 (1.4)
ND_{30}-PEG-*m*			19.5	11	–	1.3×10^3	–	0.49 (2.4)
ND_{50}	2.6×10^2	8.4×10^3 (32)	–	–	–	–	–	–
ND_{50}-PG-*l*			10.5	31	2.5×10^5	–	30 (2.2)	–
ND_{50}-PG-*m*			22.4	75	6.1×10^5	–	73 (5.4)	–
ND_{50}-PG-*h*			37.1	1.5×10^2	1.2×10^6	–	150 (11)	–
ND_{50}-PEG-*l*			12.3	36	–	4.4×10^3	–	0.52 (2.6)
ND_{100}	1.9×10^3	3.3×10^4 (17)	–	–	–	–	–	–
ND_{100}-PG-*l*			8.6	1.8×10^2	1.5×10^6	–	44 (3.3)	–
ND_{100}-PG-*m*			20.6	4.9×10^2	4.0×10^6	–	120 (9.0)	–
ND_{100}-PG-*h*			34.1	9.8×10^2	8.0×10^6	–	240 (18)	–
ND_{100}-PEG-*l*			9.0	1.9×10^2	–	2.3×10^4	–	0.69 (3.4)
SPION	28	1.5×10^3 (54)	–	–	–	–	–	–
SPION-PG-*l*			11.2	4.1	3.3×10^4	–	22 (1.6)	–
SPION-PG-*m*			22.2	9.5	7.7×10^4	–	51 (3.8)	–
SPION-PG-*h*			32.8	17	1.4×10^5	–	91 (6.7)	–
SPION-PEG-*m*			25.6	12	–	1.4×10^3	–	0.93 (4.6)

[a]Molecular weights of one unit of PG and one chain of PEG are 74 and 5000 Da, respectively. [b]Calculated on the assumption of spherical shape with the diameters shown in Figure 2-1 and density of 3.5 and 5.1 g cm^{-3} for ND and SPION, respectively. [c]Specific surface area (m^2 g^{-1}) is indicated in parentheses. [d]Based on TGA (Figure 2-4). [e]Density of PG or PEG MW (kD nm^{-2}) is indicated in parentheses.

All the NP-PG-*h* synthesized in the Route A (Scheme 2-1) were analyzed by scanning transmission electron microscopy (STEM) as shown in Figure 2-1. In these images, the core sizes are almost the same as those before functionalization and the cores seem to be individualized without aggregation.

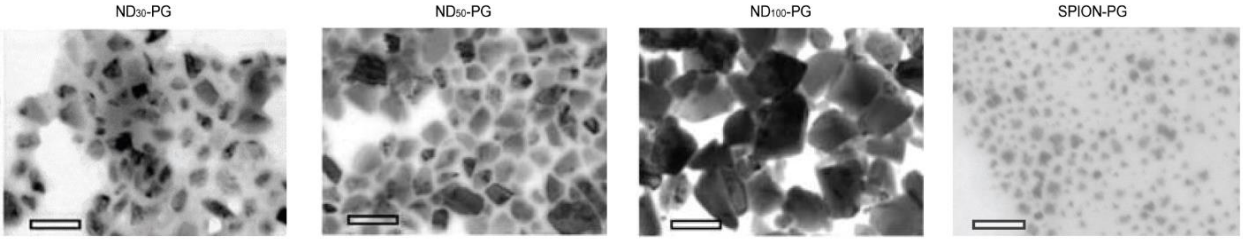

Figure 2-1. STEM images (scale bar: 100 nm) of NP-PG-*h* (NP = ND_{30}, ND_{50}, ND_{100} and SPION).

The dynamic light scattering (DLS) median size of ND_{100}-PG-*h* was confirmed to be stable around 130 nm in water and PBS at least over 72 h (Figure 2-2).

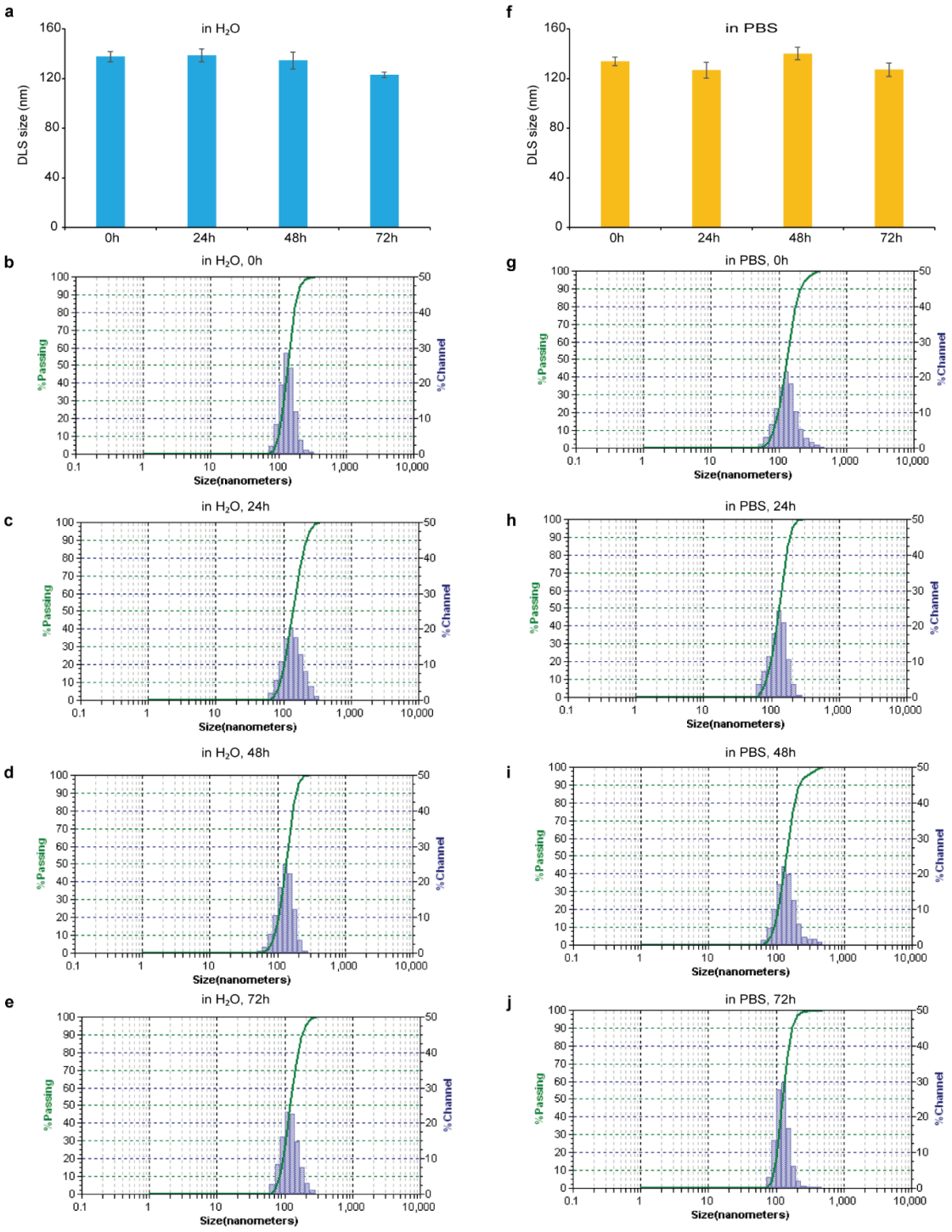

Figure 2-2. DLS median sizes (a and f) and profiles (b-e and g-j) of ND_{100}-PG-*h* in H_2O (a-e) and PBS (f-j) over 72 h.

In addition, the surface polymers in NP-PG and NP-PEG were characterized by the C-H and C-O-C stretching at 2900 and 1100 cm^{-1}, respectively, in the infrared (IR) spectroscopy (Figure 2-3).

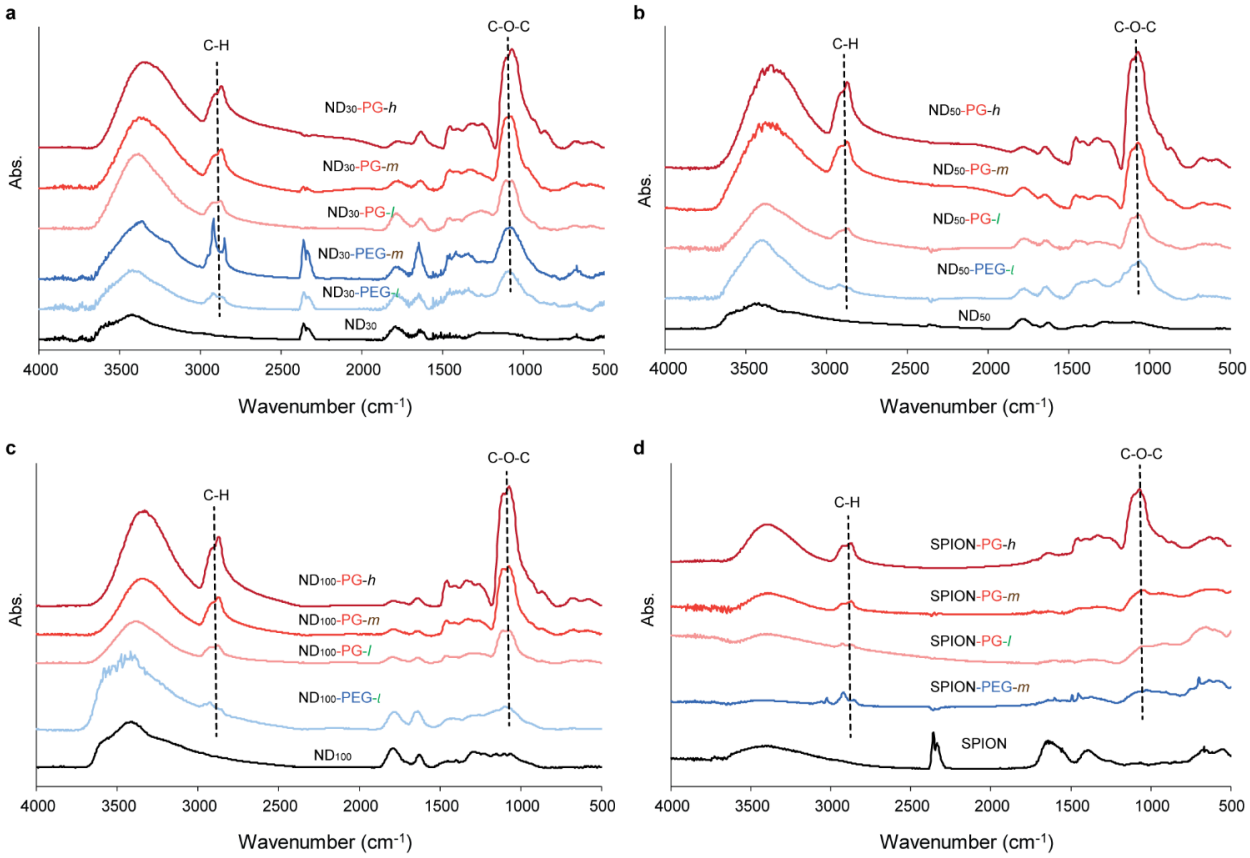

Figure 2-3. IR spectra of NP (black traces), NP-PEG (blue traces) and NP-PG (red traces). (a - d) are the spectra of ND_{30} (a), ND_{50} (b), ND_{100} (c) and SPION (d) before and after polymer coating, respectively.

NP-PG and NP-PEG were also characterized quantitatively by thermogravimetric analysis (TGA) as shown in Figure 2-4.

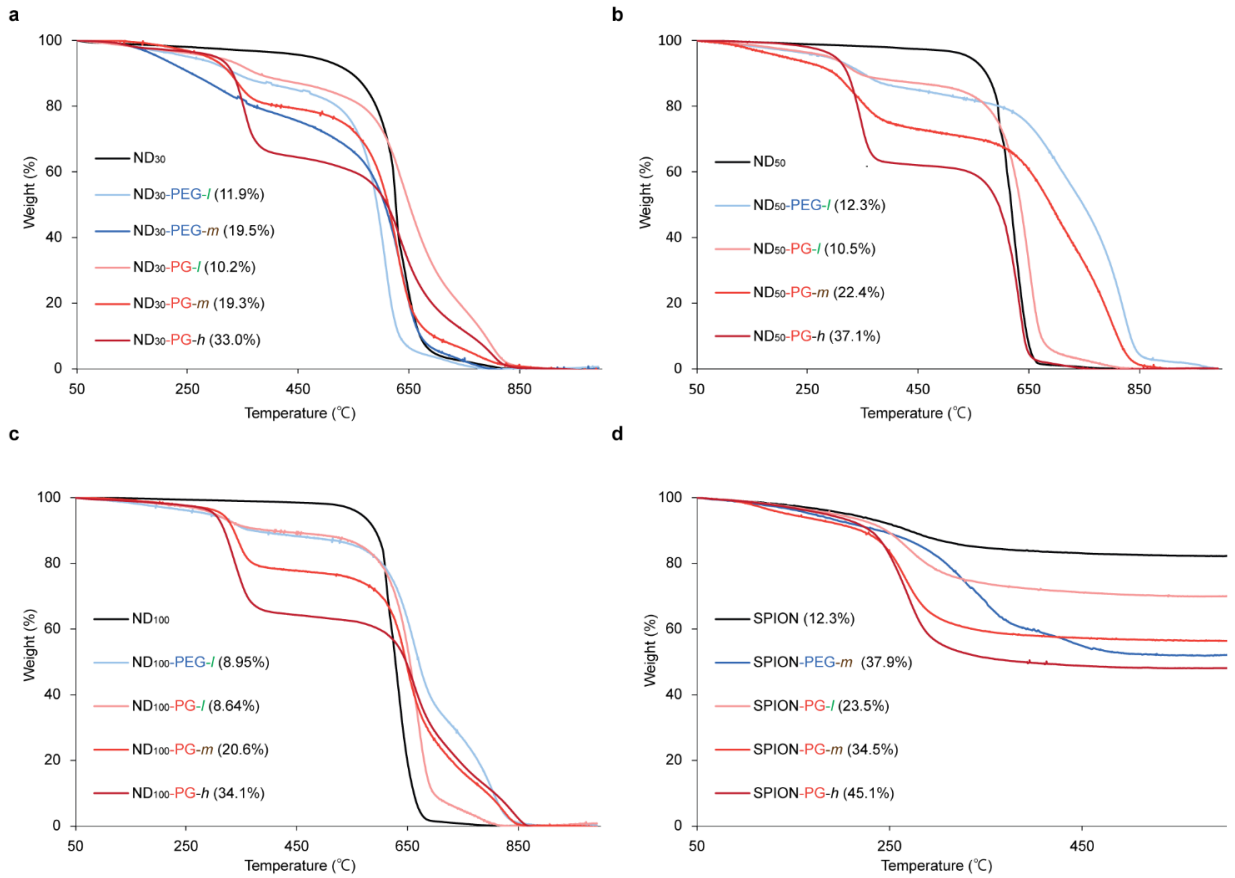

Figure 2-4. TGA profiles of ND_{30} (a), ND_{50} (b), ND_{100} (c) and SPION (d) before and after polymer functionalization. TGA profiles of NP, NP-PEG and NP-PG are indicated in black, blue and red traces. The weight loss (%) in the range from 200 to 450 ℃ is indicated in parentheses and 10, 20 and 30% weight loss is corresponding to *l*, *m*, and *h*, respectively.

The summary of the TGA results shown in Table 2-3 indicates that *l*, *m* and *h* polymer contents are corresponding to ~10, 20 and 30 wt%. The weights of the surface polymer in one particle are derived from the weights of one core NP and wt% of polymer in TGA. This leads to degree of PG polymerization and number of PEG chains in one particle, which are converted to the densities of PG

monomer and PEG chain by dividing them with the surface area (nm^{-2}) and further to the densities of PG and PEG MW on NP surface (kD nm^{-2}) by use of the MWs of PG monomer unit and PEG chain (74 and 5000 Da, respectively). At the same kind of core NP (ND_{30}, ND_{50}, ND_{100} or SPION), the weights of PG and PEG, the degree of PG polymerization, number of PEG chains, and the densities of PG monomer and PEG chains and their MW densities are proportional to the wt% of PG and PEG in TGA, respectively. At the same content (*l*, *m* or *h*), the weights of PG and PEG, the degree of PG polymerization and number of PEG chains are almost proportional to the weights of NPs. In the densities of PG monomer and PEG chain, and their MW densities, the order is ND_{30} < SPION < ND_{50} < ND_{100} in all three kinds of densities at *l*, *m* and *h*, respectively. When the PG and PEG MW densities are compared, they are similar at the same content on the same core NP. For example, almost the same PG and PEG MW densities are given at ND_{30}-*m* and ND_{100}-*l*. However, the MW densities in NP-PG-*h* are higher than those in NP-PG- and -PEG-*l* and -*m* with the same core NP, indicating that PG-*h* covers the NP surface more densely than the other NP-PG and NP-PEG. Since NP-PEG-*h* cannot be obtained as mentioned above, the dense coating on NP with PG-*h* is attributable to the branched structure of PG. In the previous papers, on the other hand, the density of PEG_{5k} chain was determined to be 0.08 and 0.20 nm^{-2} by fluorescence and proton nuclear magnetic resonance (^{1}H-NMR) spectroscopies, respectively [50, 51]. Although their methods are different from our TGA-based method, the PEG chain density in the range of 0.27 - 0.93 nm^{-2} shown in Table 2-3 is much higher than those in these previous papers.

2-2-2 Comparison of NP-PG, NP-PEG and bare NP in protein corona formation

For the protein corona formation, the NP-PG and NP-PEG as well as bare NP were incubated in 10% fetal bovine serum (FBS) or 55% human plasma. The amounts of these NPs are determined to be 0.12 - 0.52 mg (Table 2-4, Experimental section), so that the total surface area of NP cores is normalized to be 66 cm^2. After the corona proteins were detached with 10% sodium dodecyl sulfate

(SDS), the resulting SDS solution was subjected to polyacrylamide gel electrophoresis (PAGE), bicinchoninic acid (BCA) assay and liquid chromatography-tandem mass spectrometry (LC-MS/MS) (see details in Methods).

In SDS-PAGE (Figure 2-5a – 2-5d for ND, and Figure 2-5e – 2-5f for SPION), the amount of corona proteins is estimated from the number and intensity of the bands. The amounts of both FBS and plasma corona proteins are determined to be in the following order; bare NP > NP-PEG > NP-PG, regardless of the core size and core material as shown in the SDS-PAGE images. Although the amount of corona protein is significantly reduced by PEG coating for SPION (Figure 2-5e – 2-5f), the resistivity of ND-PEG to protein corona formation is similar to that of bare ND (Figure 2-5a – 2-5d). This phenomena observed in ND-PEG is consistent with those of mesoporous silica nanoparticles [52]. In contrast to PEG modification, the protein bands become faint, as the content of the PG increases, and disappear mostly in NP-PG-*h*.

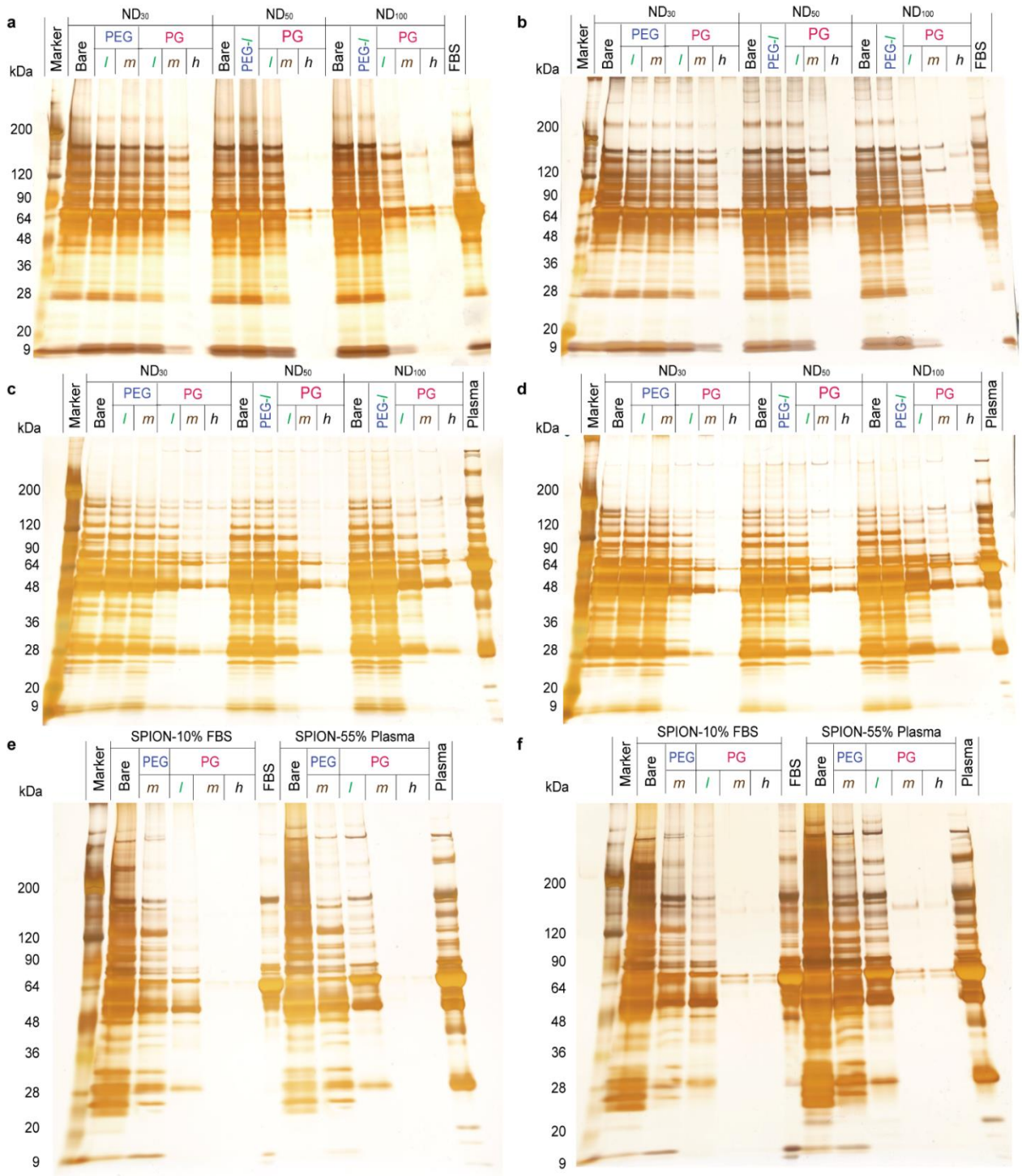

Figure 2-5. SDS-PAGE images of proteins detached from bare NP, NP-PEG and NP-PG after their incubation with 10 % FBS or 55 % plasma proteins; NP = ND in 10% FBS (a, b) and 55% plasma (c, d), and NP = SPION (e, f). The protein amounts in the lane of FBS and plasma were adjusted to those attached on bare NDs quantified by BCA.

These results of SDS-PAGE are in line with those of BCA for the corona proteins detached from

the NP surfaces (Figure 2-6a – 2-6d) and those of DLS size and zeta potential for the NDs with the corona proteins (Figure 2-6e – 2-6f). Little or no proteins are detected at ND-PG-*m* and -*h* in BCA (Figure 2-6a – 2-6d) as in the case of SDS-PAGE (Figure 2-5), which is consistent with the fact that almost no change is observed in DLS sizes and zeta potentials at ND-PG-*m* and -*h* before and after the protein corona formation (Figure 2-6e – 2-6f). In contrast, bare ND and ND-PEG-*l* adsorbed larger amounts of proteins as shown in BCA (Figure 2-6a – 2-6d), which may cause significant differences in DLS sizes and zeta potentials. Small amounts of corona proteins on ND-PG-*l* detected in BCA give almost no difference in DLS sizes, but significant difference in zeta potentials. In these analyses, we conclude that 1) NP-PG-*m* and -*h* are highly resistive to protein corona formation, 2) bare NP, NP-PEG and ND-PG-*l* adsorbed proteins to form corona layer, and 3) NP-PG-*l* are less adsorptive than bare NP and NP-PEG. Although the PG and PEG MW densities of ND_{30}-PG- and -PEG-*m*, and ND_{100}-PG- and PEG-*l* are almost the same as discussed above (Table 2-3), ND_{30}-PG-*m* and ND_{100}-PG-*l* are much more resistive to the protein corona formation than ND_{30}-PEG-*m* and ND_{100}-PEG-*l*, respectively, as shown in Figure 2-5a – 2-5d. Since more hydrophilic PG including many hydroxyl and ether groups can bind water molecules more stably through hydrogen bonding than PEG including many ether groups (Scheme 2-1), protein adsorption on PG should be thermodynamically less favored than that on PEG. In addition, the high PG content with its branched structure can coat the surface more densely as discussed above (Table 2-3) to sterically hinder the protein corona formation more efficiently.

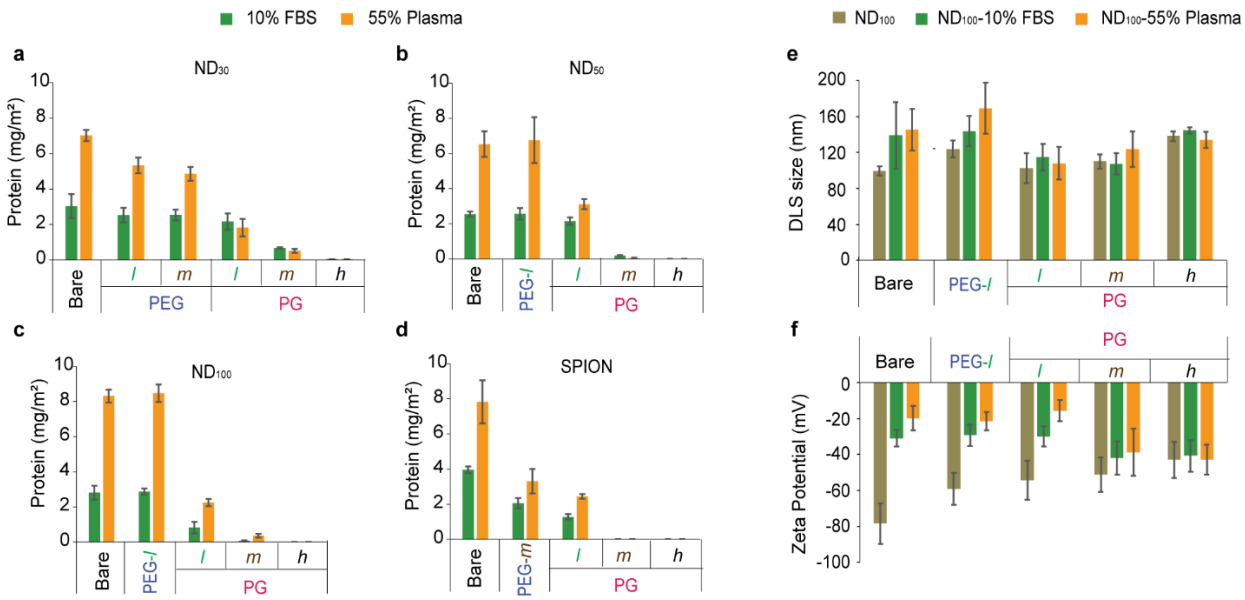

Figure 2-6. BCA quantification of proteins detached from each NP surface (mg/m^2); NP = ND_{30} (a), ND_{50} (b), ND_{100} (c) and SPION (d). The data are presented as mean value ± standard deviation of three independent replicates. DLS size (e) and zeta potential (f) of ND_{100} before and after 10% FBS or 55% plasma incubation. The data of DLS size and zeta potential are presented as mean value ± standard deviation of five and twenty measurements, respectively.

Since the difference between ND-PG-*l* and ND-PEG in the above conclusion 3) is most significant in ND_{100}, the plasma protein corona formed on bare ND_{100}, ND_{100}-PEG-*l*, ND_{100}-PG-*l* and ND_{100}-PG-*h* as well as the plasma proteins were further analyzed by LC-MS/MS coupled with label-free quantification. Relative abundances of the 124 proteins identified with high confidence were determined in each sample based on MS1 signal intensities (see details in Methods). As compared to the protein abundance on bare ND_{100}, those on ND_{100}-PEG-*l*, ND_{100}-PG-*l* and ND_{100}-PG-*h* decreased to 70, 21 and 3%, respectively (Figure 2-7a), supporting the above conclusions more quantitatively. These phenomena can be interpreted by more hydrophilic nature and branched structure of PG as discussed above.

The MW distribution of the identified proteins in Figure 2-7b illustrates that the proteins with <

30, 30 - 60 and 90 - 120 kDa were enriched in their contents on bare ND_{100} and ND_{100}-PEG-*l*, whereas these with 60 - 90 kDa as a major component in plasma constituted smaller fraction on the NDs. These are consistent with SDS-PAGE shown in Figure 2-5c and 2-5d where bare ND_{100} had higher intensity and/or more numbers of the bands in the regions of 9 - 48 and 90 - 120 kDa, underlying the reliability of our analysis. As for isolated point (p*I*) (Figure 2-7c), the content of the basic proteins (p*I* = 8.0 - 10.3) increased on bare ND_{100}, ND_{100}-PEG-*l* and ND_{100}-PG-*l* due to the negative zeta potentials of ND_{100} (Figure 2-6f), though their relative abundance decreased significantly as shown in Figure 2-7a.

The biological function of proteins is found to govern their behavior on the protein corona formation. Serum albumin as a major component in plasma decreased its content from more than 50% in plasma to less than 10% on the ND_{100} surfaces (Figure 2-7d). Its relative abundance (log10 of the signal intensity) also decreased from 6.2 in plasma to 3.9 - 5.5 on the ND_{100} surfaces in the heat map (Figure 2-7e). Since serum albumin works as a carrier of the water-insoluble molecules such as fatty acid and steroid, it should have hydrophobic pockets as well as hydrophilic periphery like surfactant to well solubilize them [53]. Therefore, serum albumin is considered to be stabilized more in water than on the ND surface, giving much less content of serum albumin on bare ND_{100} than in plasma. The minor components, lipoproteins and acute phase proteins, behaved similarly to serum albumin as shown in Figure 2-7e. In contrast, coagulation proteins increased their contents from 6% in plasma to 43% and 47% on bare ND_{100} and ND_{100}-PEG-*l*, respectively (Figure 2-7d), and their relative abundances from 3.6 - 4.7 in plasma to 4.2 - 5.5 on bare ND_{100} and ND_{100}-PEG-*l* (Figure 2-7e). Since coagulation including fibrinogen as major components is prone to aggregate in its biological role, it may be enriched on the surface of bare ND_{100} and ND_{100}-PEG-*l*. However, more hydrophilic PG coating significantly reduced the content of coagulation to 17% on ND_{100}-PG-*l* (Figure 2-7d) and the relative abundances to 2.4 - 3.4 on ND_{100}-PG-*h* (Figure 2-7e). Similar behavior was also observed in the minor components, tissue leakage and complement proteins; their small contents of 1 - 2% in plasma increased to 6 - 7% on bare ND_{100} and 7 - 8% on ND_{100}-PEG-*l*, and decreased to 3 - 6% on

ND_{100}-PG-*l* (Figure 2-7d). On the other hand, immunoglobulin proteins exhibited good affinity not only to the surface of bare ND_{100} and ND_{100}-PEG-*l*, but also ND_{100}-PG-*l* (Figure 2-7d), which is supported by the results of the relative abundances (Figure 2-7e). However, the relative abundances of immunoglobulin diminished significantly on ND_{100}-PG-*h* (Figure 2-7e). Since immunoglobulin on the PEG-coated liposome is known to induce various adverse immune response such as opsonization, ABC and even pseudo-anaphylaxis as mentioned above [35, 36], these results show promise of ND-PG-*h* for *in vivo* applications in terms of both safety and efficacy [9]. Actually, it was reported that ABC phenomenon was not observed in the PG coated liposomes [54].

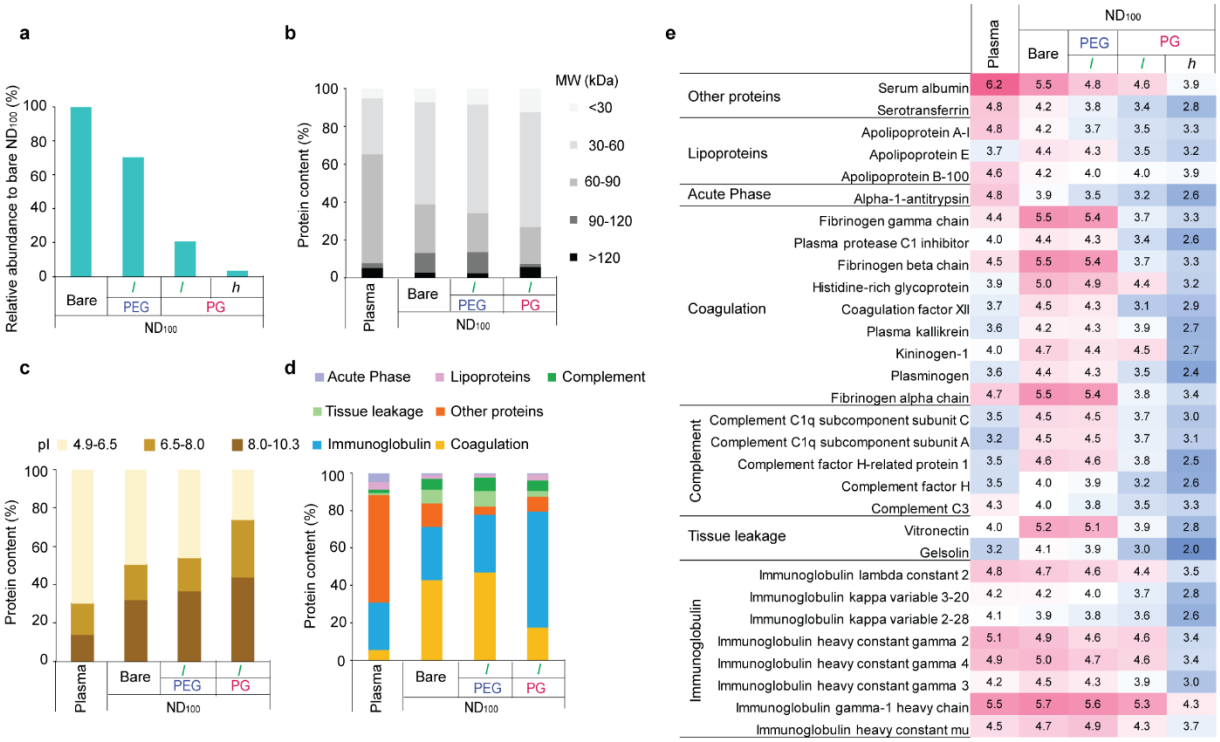

		Plasma	ND100			
			Bare	PEG	PG	
				l	*l*	*h*
Other proteins	Serum albumin	6.2	5.5	4.8	4.6	3.9
	Serotransferrin	4.8	4.2	3.8	3.4	2.8
Lipoproteins	Apolipoprotein A-I	4.8	4.2	3.7	3.5	3.3
	Apolipoprotein E	3.7	4.4	4.3	3.5	3.2
	Apolipoprotein B-100	4.6	4.2	4.0	4.0	3.9
Acute Phase	Alpha-1-antitrypsin	4.8	3.9	3.5	3.2	2.6
Coagulation	Fibrinogen gamma chain	4.4	5.5	5.4	3.7	3.3
	Plasma protease C1 inhibitor	4.0	4.4	4.3	3.4	2.6
	Fibrinogen beta chain	4.5	5.5	5.4	3.7	3.3
	Histidine-rich glycoprotein	3.9	5.0	4.9	4.4	3.2
	Coagulation factor XII	3.7	4.5	4.3	3.1	2.9
	Plasma kallikrein	3.6	4.2	4.3	3.9	2.7
	Kininogen-1	4.0	4.7	4.4	4.5	2.7
	Plasminogen	3.6	4.4	4.3	3.5	2.4
	Fibrinogen alpha chain	4.7	5.5	5.4	3.8	3.4
Complement	Complement C1q subcomponent subunit C	3.5	4.5	4.5	3.7	3.0
	Complement C1q subcomponent subunit A	3.2	4.5	4.5	3.7	3.1
	Complement factor H-related protein 1	3.5	4.6	4.6	3.8	2.5
	Complement factor H	3.5	4.0	3.9	3.2	2.6
	Complement C3	4.3	4.0	3.8	3.5	3.3
Tissue leakage	Vitronectin	4.0	5.2	5.1	3.9	2.8
	Gelsolin	3.2	4.1	3.9	3.0	2.0
Immunoglobulin	Immunoglobulin lambda constant 2	4.8	4.7	4.6	4.4	3.5
	Immunoglobulin kappa variable 3-20	4.2	4.2	4.0	3.7	2.8
	Immunoglobulin kappa variable 2-28	4.1	3.9	3.8	3.6	2.6
	Immunoglobulin heavy constant gamma 2	5.1	4.9	4.6	4.6	3.4
	Immunoglobulin heavy constant gamma 4	4.9	5.0	4.7	4.6	3.4
	Immunoglobulin heavy constant gamma 3	4.2	4.5	4.3	3.9	3.0
	Immunoglobulin gamma-1 heavy chain	5.5	5.7	5.6	5.3	4.3
	Immunoglobulin heavy constant mu	4.5	4.7	4.9	4.3	3.7

Figure 2-7. Identification and quantification of plasma proteins detached from bare ND_{100}, ND_{100}-PEG-*l*, ND_{100}-PG-*l* and ND_{100}-PG-*h* by LC-MS/MS. (a) Comparison of total relative abundances of proteins detached from each ND_{100} to those on bare ND_{100}. b - d) Proteins in plasma itself and on the surface of each ND_{100} are classified according to MW (b), p*I* (c) and biological functions (d). The protein content (%) is corresponding to the protein relative abundance of the total proteins based on the signal intensity. Protein content of ND_{100}-PG-*h* is omitted because of the low relative abundance shown in (a). (e) Heat map representation of 30 most abundant plasma proteins identified from bare ND_{100} surface. Proteins were classified according to their biological functions, and compared in their relative abundances which are shown in colors (blue - red) and numerical values (2.0 - 6.2) corresponding to the log10 of these signal intensities. The full list of the 124 proteins identified by LC-MS/MS can be found at https://pubs.acs.org/doi/10.1021/ acsnano.0c02289.

2-2-3 Comparison of NP-PG, NP-PEG and bare NP in macrophage uptake

In view of targeted theranostics in nanomedicine [7], the macrophage-evading ability was evaluated by applying NP-PG and NP-PEG to U937 macrophage cells (see details in Methods). Human U937 cells were selected as MPS macrophage model cells in our study, because it is a well-documented macrophage cell line to phagocytize foreign materials efficiently [55]. The NP uptake was assayed by transmission electron microscopy (TEM) and extinction spectroscopy for ND and by inductively coupled plasma-mass spectrometry (ICP-MS) for SPION. Fluorescence detection could be used to confirm cellular uptake, if a fluorescence tag is conjugated onto the NP-PG and NP-PEG. However, we did not take such a convenient way to avoid any influence by the surface moiety other than PG and PEG.

In the TEM images shown in Figure 2-8a – 2-8c, many ND aggregates, which appeared as black dots, were observed in the macrophage in the presence of ND_{100} (Figure 2-8a-i and 2-8b-i), while they were not seen in the control (Figure 2-8c). These results indicate that bare ND_{100} without polymer coating was extensively taken up by macrophage cells. The number of the aggregates decreased in ND_{100}-PEG-*l* (Figure 2-8a-ii and 2-8b-ii), but was still in high quantities. This is in agreement with the previous studies [40, 56], where PEG coating is not sufficient to inhibit macrophage uptake of NPs. In contrast to PEG modification, PG-*l* grafting induced a distinct reduction in U937 uptake (Figure 2-8a-iii and 2-8b-iii), and only a few and no aggregates were found in ND_{100}-PG-*l* (Figure 2-8a-iii and 2-

8b-iii) and ND_{100}-PG-*h* (Figure 2-8a- iv and 2-8b-iv), respectively. More TEM images with magnification ranging from cell population to sub-organelle scale are given in Appendix Figure 1-1 – 1-3.

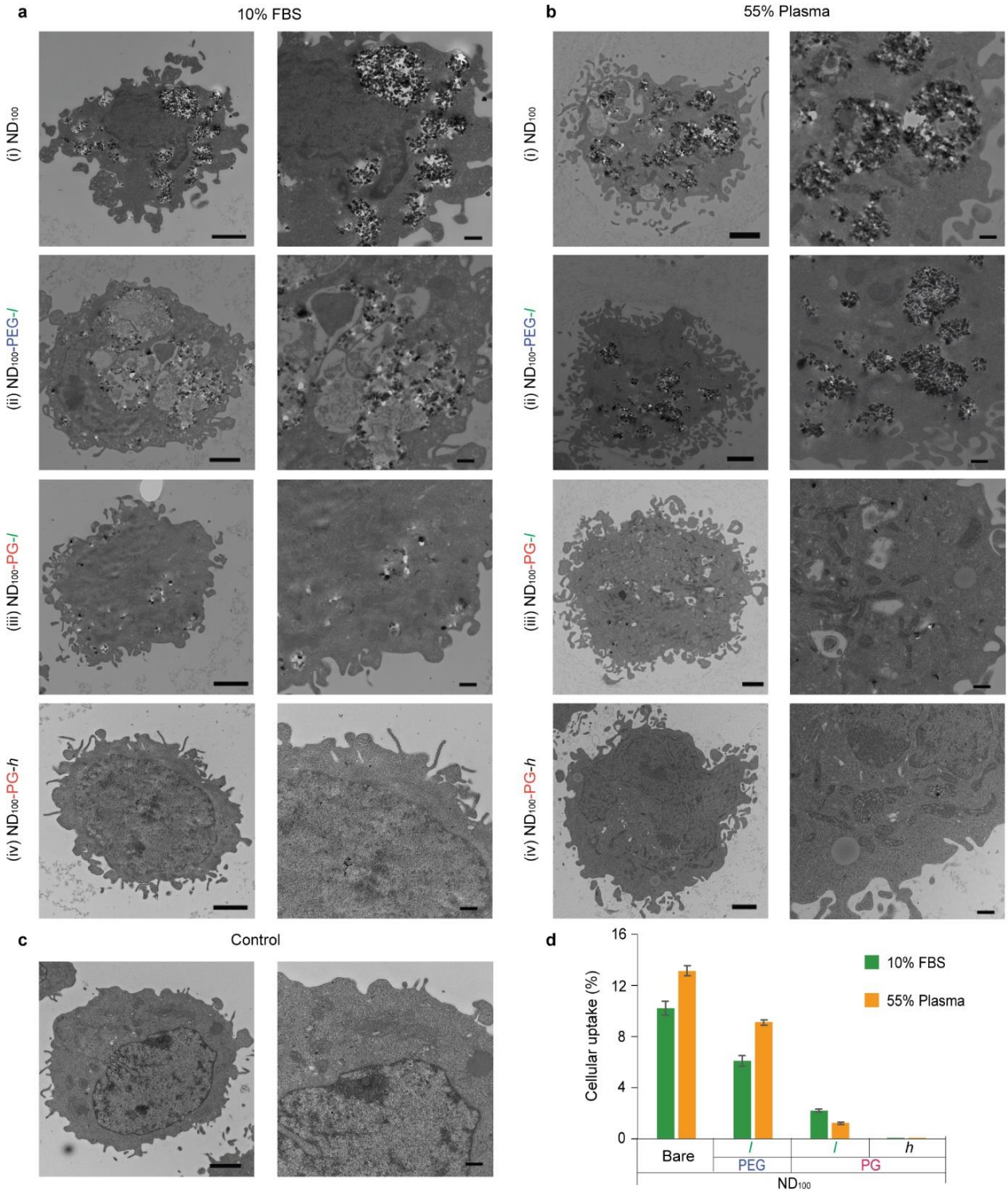

Figure 2-8. U937 macrophage uptake of bare ND_{100}, ND_{100}-PEG-*l*, ND_{100}-PG-*l* and ND_{100}-PG-*h*. a - c) TEM images of macrophages after incubation in 10% FBS in the presence of ND_{100} (i), ND_{100}-PEG-

l (ii), ND_{100}-PG-*l* (iii) and ND_{100}-PG-*h* (iv) without (a) and with (b) 55% plasma pretreatment, and in the absence of NDs (c). Pairs of the images are corresponding to low magnification (left, scale bar: 2 μm) and high magnification (right, scale bar: 500 nm) of the same macrophage. More images are shown in Appendix Figure 1-1 – 1-3. (d) Quantification of NDs extracted from the above samples in (a) and (b) by extinction spectroscopy. The data are presented as mean value ± standard deviation of three independent replicates.

To evaluate the NDs in the macrophage more quantitatively, the NDs extracted from the macrophage were subjected to extinction spectroscopy (Figure 2-9 and 2-10 for cell samples and standard curves, respectively). The results shown in Figure 2-8d are in accordance with TEM observations mentioned above; the abundance of ND decreased in the order of ND_{100} > ND_{100}-PEG-*l* > ND_{100}-PG-*l* > ND_{100}-PG-*h* both with and without plasma precoating, and PG-*h* grafting completely inhibited the ND_{100} uptake.

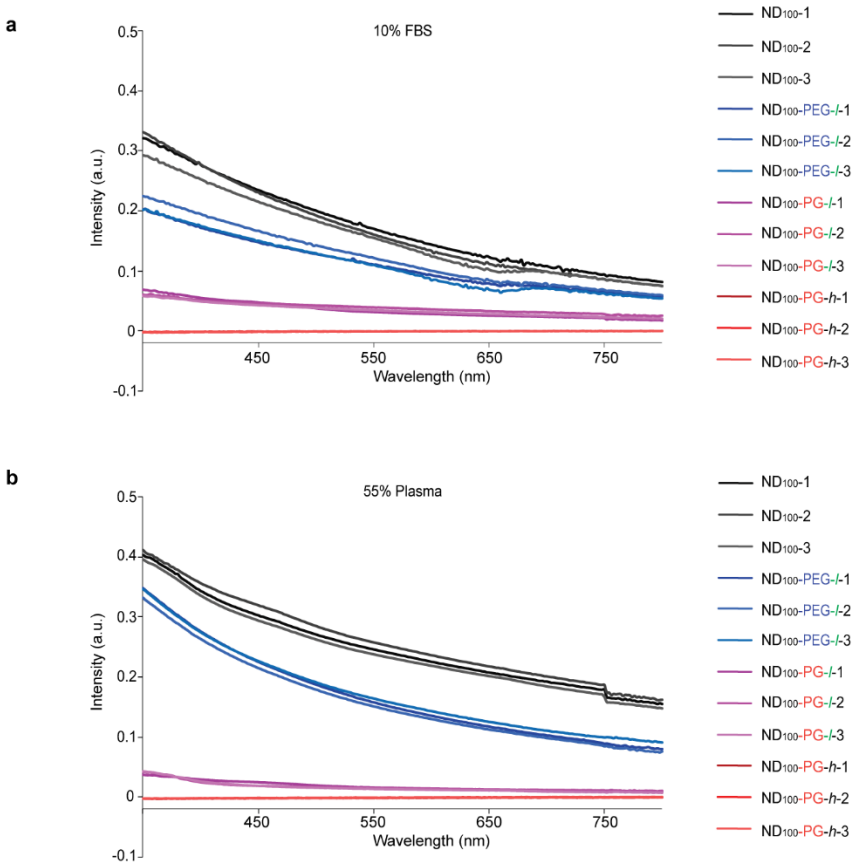

Figure 2-9. Extinction spectra of ND_{100}, ND_{100}-PEG-*l*, ND_{100}-PG-*l* and ND_{100}-PG-*h* after macrophage uptake. NDs without (a) or with (b) 55% plasma protein pretreatment were incubated with macrophages in culture medium containing 10% FBS, results are obtained from three independent experiments.

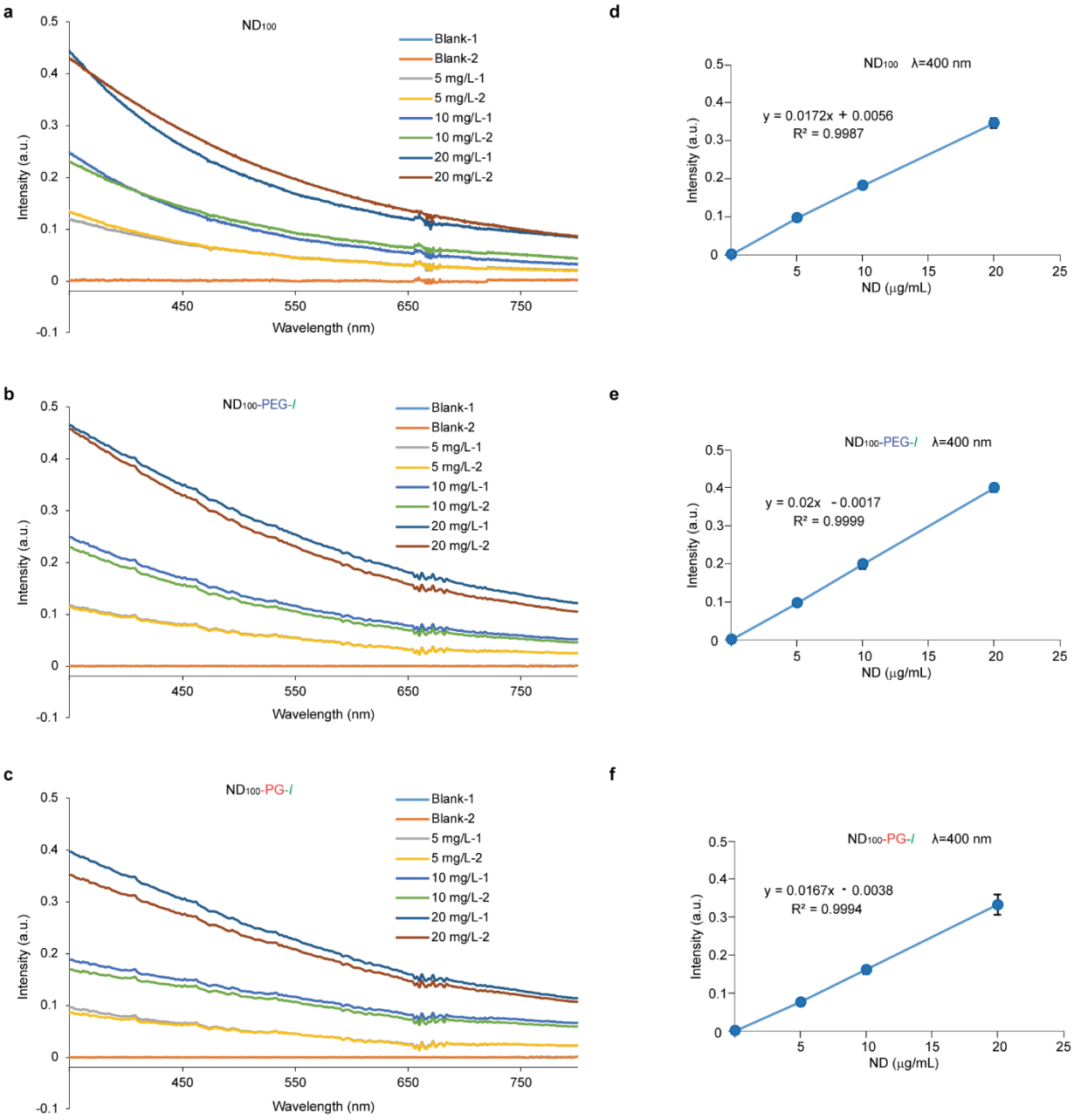

Figure 2-10. Calibration curves of standard ND samples. Extinction spectra of ND_{100} (a), ND_{100}-PEG-*l* (b) and ND_{100}-PG-*l* (c) after their co-digest with cell pellets. For each sample, concentrations of 5, 10 and 20 mg L^{-1} were analyzed in two independent experiments. Calibration curves of ND_{100} (d), ND_{100}-PEG-*l* (e) and ND_{100}-PG-*l* (f) based on the intensity of the standard samples at 400 nm.

On the other hand, the amounts of SPION taken up by macrophage were determined by ICP-MS (Figure 2-11). The uptake tendency of SPION is similar to that of ND. While 13, 11 and 1 wt% of iron were detected in the extracts from the macrophages incubated with SPION, SPION-PEG-*m* and SPION-PG-*l*, respectively, the iron concentration in SPION-PG-*h* was below the detection limit of ICP-MS.

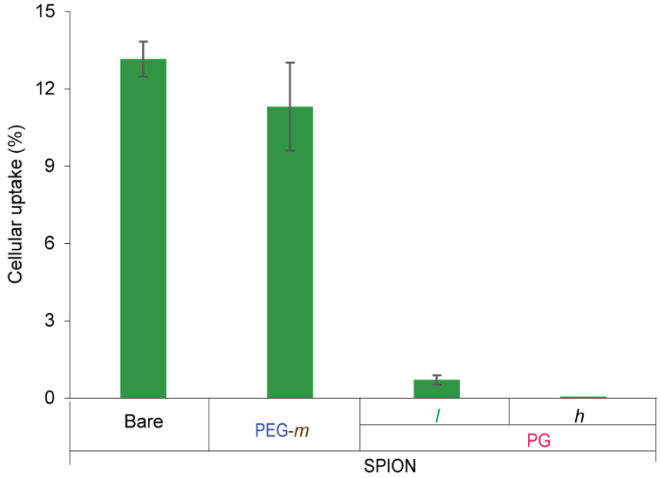

Figure 2-11. ICP-MS measurement of SPION, SPION-PEG-*m*, SPION-PG-*l* and SPION-PG-*h* uptake by U937 macrophage. The data are presented as mean value ± standard deviation of three independent replicates.

The order of macrophage uptake is the same as that of the protein corona formation mentioned above, indicating that efficient shielding of the protein corona formation realized effective reduction in macrophage uptake and that almost complete shielding resulted in no macrophage uptake in NP-PG-*h*. Since the macrophage uptake or clearance by MPS stands a significant barrier for NP

theranostics [57], the effectiveness of PG grafting in passivating macrophage uptake has demonstrated its promise for developing stealth nano-formulations in view of *in vivo* applications. In fact, we have realized tumor-targeted fluorescence imaging by use of ND-PG functionalized with near infrared fluorescence dye (ND-PG-Cy7), which has been reported quite recently [9]. ND-PG-Cy7 exhibited long blood circulation in mice, resulting in its preferential accumulation in tumor without being trapped in liver and spleen owing to the high stealth efficiency of PG.

2-3 Conclusions

Our results demonstrate that PG outperforms PEG in terms of the resistivity to protein corona formation and the resulting evasion of macrophage uptake. In addition to more hydrophilic nature of PG, the hyperbranched structure of PG through the “grafting from” process is another advantage over PEG due to dense surface coverage of NP [58], which should improve the protein resistivity. Furthermore, biocompatibility [59], facility [26], applicability and extensibility make PG more attractive; that is, PG functionalization is a simple one-pot process which can be applied to various nanomaterials not only NP, but also porous NP, one-dimensional nanotube and two-dimensional nanosheet [46, 47, 60, 61]. A number of hydroxyl groups on PG can be derivatized to add more functions such as targeted cancer imaging and drug delivery by conjugating with fluorescence dye (Cy7), active targeting moiety (RGD motif) and anticancer drugs (cisplatin and doxorubicin) [9, 28, 62] . The outstanding anti-biofouling property of PG presented here may bring about a paradigm shift in nanomedicine to change the design of the NPs for *in vivo* theranostic applications and even the coating of the film for *ex vivo* biosensor applications.

2-4 Materials and methods

2-4-1 Chemicals and materials

Powders of ND_{30}, ND_{50} and ND_{100} were kindly provided by Tomei Diamond Co., Ltd. Japan. The following reagents were purchased from Wako Pure Chemicals, Japan; iron (II) sulfate heptahydrate, iron (III) citrate *n*-hydrate, *N*-hydroxysuccinimide, oxalyl chloride, 4-dimethylaminopyridine (DMAP), *N*,*N*-dimethylformamide (DMF), anhydrous tetrahydrofuran (THF), triethylamine, sodium dodecyl sulfate (SDS), phorbol 12-myristate 13-acetate (PMA), 20% glutaraldehyde, paraformaldehyde, sulfuric acid, nitric acid, LC-MS grade water, acetonitrile, and formic acid. The following reagents were purchased from Nacalai Chemicals, Japan; *N*,*N'*-Dicyclohexylcarbodiimide (DCC), sodium hydroxide, pre-stained protein markers (02525-35), running buffer (30329-61), hydrochloric acid, and iron standard solution. PEG ($HO\text{-}PEG_{5k}\text{-}NH_2$, HE002005-5k) was supplied by Funakoshi, Co, Ltd., Japan. Protein loading buffer (AE-1430) and 5-20% precast polyacrylamide gel (E-R520L) were purchased from ATTO, Japan. BCA protein assay kit (T9300A) and Fetal bovine serum (FBS) were supplied by Takara, Bio., Inc., Japan and Biosera, Inc., France, respectively. Roswell park memorial institute 1640 medium (RPMI-1640), 0.25% trypsin-EDTA solution, antibiotics penicillin/streptomycin (100 U/mL), pierce silver stain kit (24600) and in-gel tryptic digestion kit were supplied by Thermo Fisher Scientific. Sodium L-ascorbate, water soluble carbodiimide hydrochloride (WSCD·HCl) and glycidol were purchased from Tokyo Chemical Industry, Japan, Peptide Institute

Inc., Japan and Kanto Chemical Co. Inc., respectively. Human leukemic monocyte lymphoma cells (U937 (JCRB9021) prepared from CRL1593) was purchased from Japanese Collection of Research Bioresources Cell Bank.

2-4-2 Synthesis of NP-PG and NP-PEG

SPION was synthesized according to the reported method with slight modification [63] and characterized by X-ray diffraction (XRD) (Figure 2-12). The preparation of SPION was described as follows. The mixture of iron (II) sulfate heptahydrate (0.41 g, 1.5 mmol) and iron (III) citrate (0.74 g, 3.0 mmol) in water (40 mL) was sonicated for 10 min (Branson-2800 sonication bath). After L-ascorbate (0.10 g, 0.50 mmol) was added, the pH of the suspension was made to be 10 by using 1 M NaOH solution, was transferred into a Teflon-lined autoclave with a 50 mL capacity, and heated at 160 °C overnight. The product was purified by dialysis against Milli-Q water and washed with ultracentrifugation, and kept at room temperature until. XRD patterns of SPION were recorded on a RINT 2200U X-ray diffractometer (Rigaku) using Cu-Kα radiation (λ = 1.5418 nm) at an operating voltage of 40 kV and a current of 40 mA, with a speed of 2° per min in the range from 20° to 80°. The diffraction pattern of the SPION we synthesized is consistent with the reported one [64].

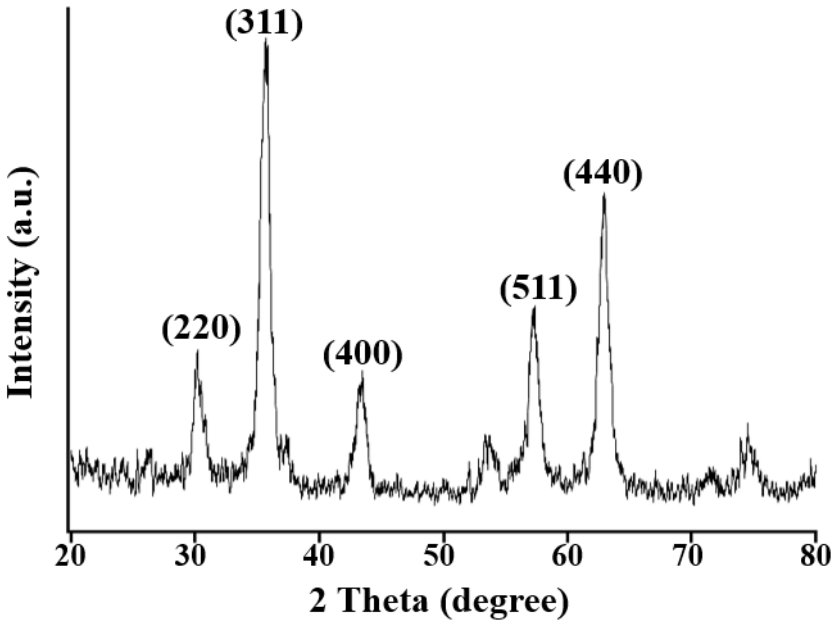

Figure 2-12. XRD patterns of as-synthesized SPION.

ND_{30} was oxidized by a mixture of nitric and sulfuric acids prior to use, and ND_{50} and ND_{100} were used as received. NP-PG-*l*, -*m* and -*h* were obtained by "grafting from" method we reported previously. NP-PEG was synthesized by "grafting to" method to conjugate PEG with 5 kDa (PEG_{5k}) onto NP surface *via* amide linkage as follows.

For ND-PG, after being bath-sonicated for 30 min, ND (10 mg) in glycidol was stirred at the temperature shown in Table 2-1 for 4 h. The resulting mixture was post-treated in the same procedure as that in our previous report.

For ND-PEG-*l*, the suspension of NP (10 mg), water soluble carbodiimide hydrochloride (WSCD·HCl, 10 mg) and *N*-hydroxysuccinimide (3 mg) in DMF/H_2O (1/2 v/v, 3 mL) was stirred at

30 °C for 30 min to activate the carboxylic groups on NP. After an aqueous solution of PEG_{5k} (30 mg) in water (1 mL) was added, the suspension was stirred at 30 °C overnight. The PEG-functionalized NP was collected by centrifugation at 50,400*g* for 1 h and washed with Milli-Q water by repeated redispersion/centrifugation cycles. For ND_{30}-PEG-*m*, ND_{30} was refluxed with oxalyl chloride (1 mL) in anhydrous THF (1.2 mL) for 2 h to convert the carboxylic groups on ND_{30} surface to acyl chloride. After complete removal of oxalyl chloride on a rotary evaporator, PEG_{5k} (30 mg) in THF (1.5 mL) and trimethylamine (0.2 mL) were added to the THF suspension (2 mL) of the residual brownish solid, and the suspension was stirred at 70 °C under N_2 for 24 h. The functionalized NP was collected by centrifugation and washed with methanol and Milli-Q water in a manner similar to those of ND-PEG-*l* mentioned above. For SPION-PEG-*m*, the DMF solution (2 mL) of PEG_{5k} (30 mg), *N,N'*-dicyclohexylcarbodiimide (DCC, 10 mg) and 4-dimethylaminopyridine (DMAP, 3 mg) was stirred at 30 °C for 10 min. After the suspension of SPION (10 mg) in DMF (1 mL) was added, the suspension was stirred at 30 °C overnight. The PEG-functionalized SPION was collected by centrifugation at 50,400*g* for 1 h and washed with methanol and Milli-Q water by repeated redispersion/centrifugation cycles.

The NP-PG and NP-PEG concentration in the aqueous dispersion was determined by the weight of the residue after drying up the aqueous dispersion (100 μL) in an oven at 80 °C overnight.

2-4-3 Characterization of NP-PG and NP-PEG

All the NP-PG-*h* samples were observed by STEM (Figure 2-1), where the core size of each NP was measured by ImageJ software. STEM was performed at 25 kV accelerating voltage on a JSM-7500F field emission scanning electron microscope (JEOL). IR measurements were conducted on an IR Prestige-21 (Shimadzu Co. Ltd.), and 16 scans of the spectra were collected with a resolution of 4 cm^{-1} in the wavenumber range of 4000 to 500 cm^{-1} for each sample (Figure 2-3). All the TGA analysis was run from room temperature to 1000 °C at a heating rate of 20 °C/min under air on a Q-50 analyzer (TA instruments), and all the TGA profiles were shown in Figure 2-4.

2-4-4 Adsorption of proteins from plasma and serum, and desorption of the corona proteins

Human blood was taken from three healthy authors (YZ, FY and NK) in accordance with the Declaration of Helsinki. The plasma samples were prepared according to the method reported previously [65]. The human blood sample was collected into the tubes containing EDTA 2K to prevent blood clotting, followed by two rounds of centrifugation to pellet the red and white blood cells (1,500*g* for 15 min and 2,000*g* for 15 min, respectively). The yellowish supernatant was divided into several tubes and stored at -80 °C. Just before the protein corona preparation, an equal aliquot of plasma sample from each donor was well mixed and centrifuged at 134,000*g* for 20 min to remove protein aggregates. The protein concentration of the plasma mixture was determined to be around 74 mg/mL, which is in

good agreement with that in the literature [11].

The SDS solution of the corona proteins detached from NP surface, designated as protein corona solution, was prepared in the following procedure (Figure 2-13). First, all the NP-PG, NP-PEG and bare NP were incubated with 10% fetal bovine serum (FBS) or 55% plasma proteins at 37 °C for 1 h. These concentrations were determined in view of the *in vitro* cellular incubation and *in vivo* biological conditions, respectively. The weight of NP used in each experiment was adjusted to have the same total core surface area of 66 cm^2 (Table 2-4). After incubation, the free proteins unattached to the NP surface were completely washed out by centrifugation at 434,000*g* for 20 min three times. The proteins in the corona layer were detached from NP surface by adding 10% SDS (100 μL). After centrifugation at 108,000*g* for 20 min, the protein corona solution was obtained as a supernatant and used for further protein identification and quantification.

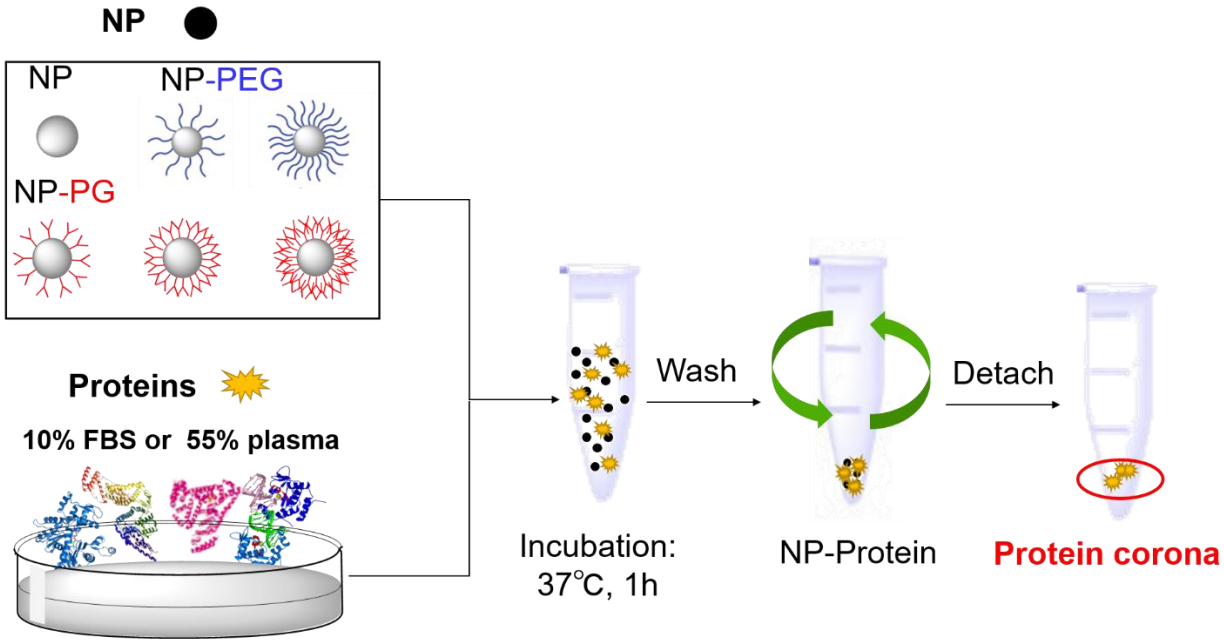

Figure 2-13. Schematic representation of the preparation of protein corona.

Table 2-4. Weights of NP, NP-PEG and NP-PG used for the protein corona formation.

NP	Weight (μg)					
	Bare	PEG		PG		
		l	*m*	*l*	*m*	*h*
ND_{30}	116	130	139	128	138	154
ND_{50}	194	218	–	214	237	266
ND_{100}	387	422	–	420	467	519
SPION	126	–	158	140	154	167

2-4-5 SDS-PAGE

An aliquot (15 μL) of the protein corona solution was mixed with an equal volume of protein loading buffer (2×), and the solution was boiled at 100 °C for 5 min to denature the proteins. After collecting the droplets on the wall by centrifugation at 5,000*g* for 3 min, the mixture was loaded into a precast polyacrylamide gel. The electrophoresis was run at a constant voltage of 100 V until the blue indicator was approached to the bottom. Then, the gels were stained with pierce silver stain kit and scanned on a fluorescence scanner (GT-X900, EPSON, Japan) with a resolution of 600 dpi. The experiment results are shown in Figure 2-5.

2-4-6 Bicinchoninic acid (BCA)

An aliquot (20 μL) of the protein corona solution was mixed with PBS (80 μL) in a clean 96-well plate. After freshly prepared BCA working reagent (100 μL) was added to each well, the plate was incubated at 37 °C for 1 h. The absorbance was recorded at 570 nm on a microtiter plate reader (MTD-310, Corona Electric Co., Japan). The protein concentrations were determined based on the calibration curve drawn by use of the BCA solutions of known concentrations. The experiment was repeated three times (Figure 2-6 a-d).

2-4-7 DLS and zeta potential measurements

The hydrodynamic diameters and the surface charges of bare ND, ND-PEG and ND-PG without and with treatment of 10% FBS and 55% plasma were analyzed by DLS and zeta potential

measurements (Figure 2-6 e and f). DLS analysis was performed five times for each sample on a Nanotrac UPA-UT151 system (Microtrac, Inc.). The zeta potential was recorded twenty times for each sample on a zeta Sizer Nano Series (Malvern Instruments, UK) at 25 °C.

2-4-8 LC-MS/MS analysis

Prior to LC-MS/MS analysis, in-gel digestion was performed for the plasma protein corona solutions from ND_{100}, ND_{100}-PEG-*l*, ND_{100}-PG-*l* and ND_{100}-PG-*h*, and the plasma protein solution. The procedure of the in-gel digestion (protein band preparation) was similar to that of SDS-PAGE mentioned above. After the gels at the protein-containing areas were excised out, proteins were recovered using in-gel tryptic digestion kit according to the manufacturer's instruction. The recovered protein digests were resuspended in 0.1% formic acid and separated using Nano-LC-Ultra 2D-plus equipped with cHiPLC Nanoflex (Eksigent, Dublin, CA, USA) in trap-and-elute mode, with trap column (200 μm × 0.5 mm ChromXP C18-CL 3 μm 120 Å (Eksigent)) and analytical column (75 μm × 15 cm ChromXP C18-CL 3 μm 120 Å (Eksigent)). The separation was carried out using a binary gradient in which 0.1% formic acid/water and 0.1% formic acid/acetonitrile were used as solvent A and B, respectively. The gradient program was as follows; 2 to 33.2% B for 125 min, 33.2 to 98% B in 2 min, 98% B for 5 min, 98 to 2% B in 0.1 min, and 2% B for 17.9 min. The flow rate was 300 nL/min, and the analytical column temperature was set to 40 ºC. The eluates were infused on-line to a mass spectrometer (TripleTOF 5600 + System with NanoSpray III source and heated interface (SCIEX,

Framingham, MA, USA)) and ionized in an electrospray ionization-positive mode. Data acquisition was carried out with an information-dependent acquisition method. The acquired datasets were analyzed using ProteinPilot software version 5.0.1 (SCIEX) with the UniProtKB/Swiss-Prot database for human (May 2018) appended with known common contaminants (SCIEX). The quality of the database search was confirmed by the false discovery rate analysis in which the reversed amino acid sequences were used as decoy. The reliabilities of protein identifications were evaluated by the numbers of identified peptides with confidence at least 95%, and Unused ProtScores that were calculated by the Pro Group algorithm (SCIEX). Relative abundances of the identified proteins were estimated on the platform of Progenesis QI for Proteomics software version 4.1 (Nonlinear Dynamics, Newcastle upon Tyne, UK). All raw data files with wiff format (SCIEX) were imported to generate aggregate, and the peptide identification results by ProteinPilot, with confidence at least 95%, were used for assignment. Label-free quantification of proteins was performed using relative quantitation using Hi-N (3) method (Nonlinear Dynamics), proteins with at least two unique peptides matched were used for data interpretation (Figure 2-7).

2-4-9 Macrophage uptake

U937 cells were maintained in RPMI-1640 culture medium supplemented with 10% FBS and 1% antibiotics penicillin/streptomycin, and the cells were grown in a humidified incubator (MCO-5ACUV-PJ, Panasonic) supplied with 5% CO_2 at 37 °C. Phorbol 12-myristate 13-acetate (PMA) was

used to differentiate U937 cells into macrophages according to our previous method with slight modification [28]. U937 cells were harvested from ~80% confluent culture dishes and adjusted to a concentration of 5×10^5 cells/mL with culture media containing PMA at a concentration of 100 ng/mL. After the cell suspension (3 mL) was transferred to each well of a 6-well plate and incubated overnight, PMA-treated U937 cells were washed with PBS twice to remove non-adherent cells, and the adherent cell monolayers, which are referred to as the U937 macrophages, were used for uptake analysis. NDs (ND_{100}, ND_{100}-PEG-*l*, ND_{100}-PG-*l* and ND_{100}-PG-*h*) with and without 55% plasma pretreatment and SPIONs (SPION, SPION-PEG-*m*, SPION-PG-*l* and SPION-PG-*h*) without plasma pretreatment were applied to the U937 macrophages in culture medium containing 10% FBS. The amounts of ND and SPION in each well were 200 μg and 100 μg, respectively. After 12 h incubation, the uptake of ND was confirmed by TEM observation (Figure 2-8a – 2-8c and Appendix I) and quantified by extinction spectroscopy (Figure 2-8d, Figure 2-9 and 2-10), and SPION uptake was assayed by ICP-MS (Figure 2-11).

2-4-10 Preparation of TEM samples

Each cell pellet was pre-fixed with 2% glutaraldehyde and 4% paraformaldehyde in 100 mM PBS buffer (1 mL) for 1 h, and post-fixed with 1% osmium tetroxide for 2 h. The cells were dehydrated in ethanol (50%, 60%, 70%, 80%, 90%, 99% and 100%) and in propylene oxide, passed through propylene oxide/epoxy resin (1/1 and 1/3) mixtures, and embedded in epoxy resin. After baking at

60 °C for 72 h, the frontal ultrathin sections (60 - 80 nm) were cut by an ultra-microtome (EM UC6, Leica, Germany), and stained with uranyl acetate and lead citrate. The slices were observed by a H-7650 TEM (Hitachi, Japan).

2-4-11 Preparation of the ND samples for extinction spectroscopy

The NDs taken up by macrophage were quantified with extinction spectroscopy (UV-3600, Shimadzu Co. Ltd.) according to the reported procedure [66]. In brief, the cell pellets from each 6-well plate were collected after 12 h incubation and digested by nitric acid (100 μL). After the cell components were removed by washing with 2% SDS, the NDs were resuspended in Milli-Q H_2O (8 mL). The concentration of NDs was determined by the extinction at 400 nm based on the calibration curves drawn by use of ND_{100}, ND_{100}-PEG-*l* and ND_{100}-PG-*l* co-digested with control cell pellets (Figure 2-9 and 2-10, respectively).

2-4-12 Preparation of the SPION samples for ICP-MS

The samples for ICP-MS to determine the iron concentration were prepared in a similar procedure to those for extinction spectroscopy to determine the ND concentration mentioned above. The nitric acid solutions after digestion were submitted to ICP-MS measurement (Agilent, 7700a, USA).

Chapter 3: Quantitative investigation of the interaction between proteins and charged functional groups on the polyglycerol-grafted nanodiamond surface

3-1 Introduction

Since the behavior of NPs in biological milieu is critically affected by the protein corona, it is important to control its formation and constitution, and hence to understand the interaction between the NP surface and the proteins [7, 67, 68]. Among the interactions, electrostatic one plays the most important role [69, 70], when charged groups exist both in the NP surface and the proteins [71-73]. However, we have not yet fully understood the charge-charge interaction at the interface between protein and NP surface. In fact, some reports demonstrated adsorption of proteins on the NP surface regardless of their charges [74-78], while NP has been reported to attract proteins with the opposite charges preferentially [79-82]. These discrepancies may be caused by the insufficient exclusion of the protein interaction with non-charged functional groups on the NP surface. Although some neutral polymers such as PEG have been believed to evade protein corona formation, it is revealed that they are not enough to give a protein-free surface to NPs [36, 83]. This means that it is difficult to evaluate the net charge effect quantitatively without “transparent” background behind the charged functional groups on the NP surface.

Quite recently, PG has been proved to resist protein corona formation completely [84]. In order to clarify the charge effect, we selectively introduced carboxyl and amino groups, exhibiting negative

and positive charges, respectively, in phosphate buffer saline (PBS, pH: 7.4), in a quantitative manner on the surface of PG-coated nanodiamond (ND-PG). These negatively and positively charged ND-PG showed the exclusive attraction to the protein of opposite charges. Thanks to the "transparent" background of PG, we successfully determined the association constants (*K*) between bovine serum albumin (BSA) and the ammonium group on ND-PG at the densities of low (*l*), medium (*m*), high (*h*) and extra-high (*xh*), found linear relationship between *K* and the ammonium group density, and proposed the slope (*K* divided by the density) as an index to demonstrate the affinity between a specific functional group and a protein.

3-2 Results

3-2-1 Synthesis and characterization of ND-PG-COOH and ND-PG-NH_2

ND with 50 nm size was analyzed before and after PG functionalization by STEM as shown in Figure 3-1.

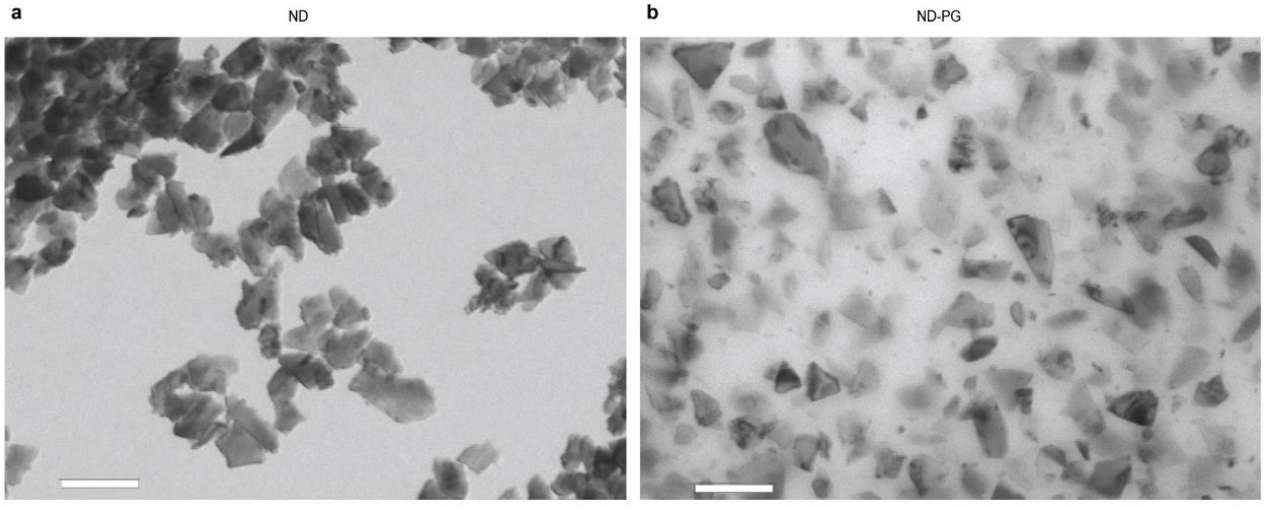

Figure 3-1. STEM images (scale bar: 100 nm) of ND (a) and ND-PG (b).

ND-PG-COOH and ND-PG-NH_2 were prepared through organic transformations of ND-PG as shown in Scheme 3-1. The carboxyl groups were introduced through ring-opening of succinic anhydride by nucleophilic attack of the hydroxyl groups on ND-PG, and the hydroxyl groups on ND-PG were converted to the amino groups via tosylates and azides [27].

Scheme 3-1. Surface functionalization of ND-PG for substituting hydroxyl groups with carboxyl (ND-PG-COOH) and amino (ND-PG-NH_2) groups, respectively.

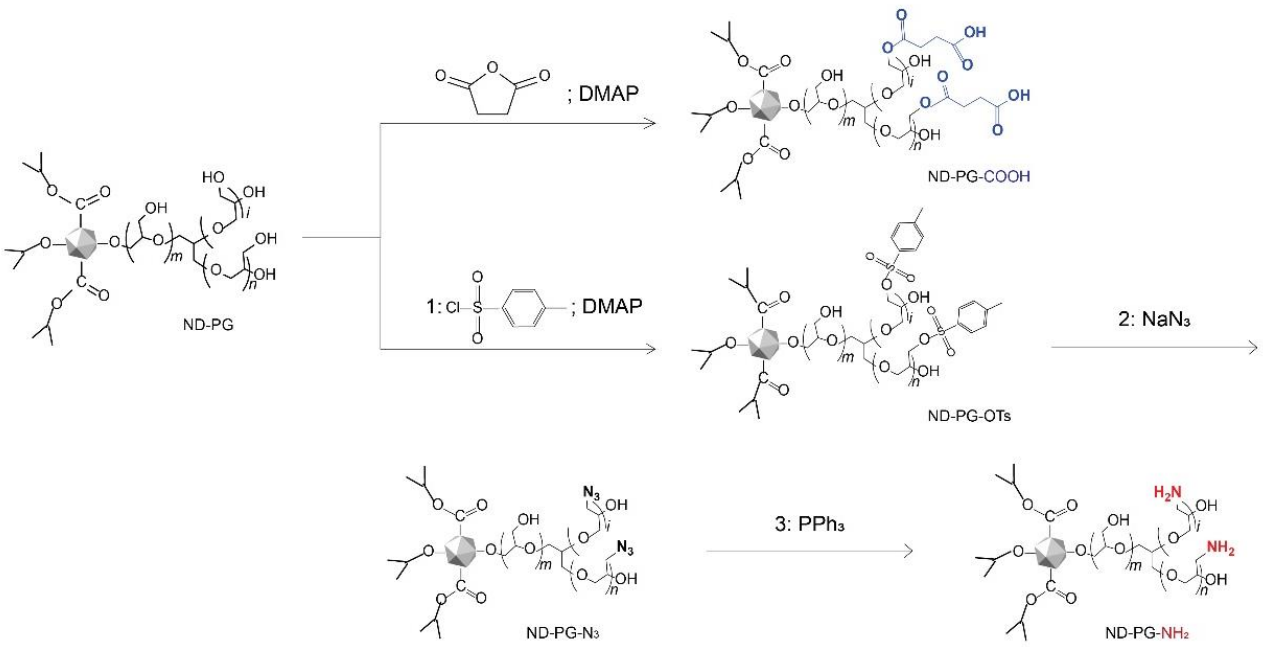

The numbers of the carboxyl and amino groups were controlled at *l*, *m*, *h* and *xh* by changing the duration of the ring-opening and tosylation reactions, respectively. The chemical structures of these materials with various densities of the functional groups are depicted in Figure 3-2.

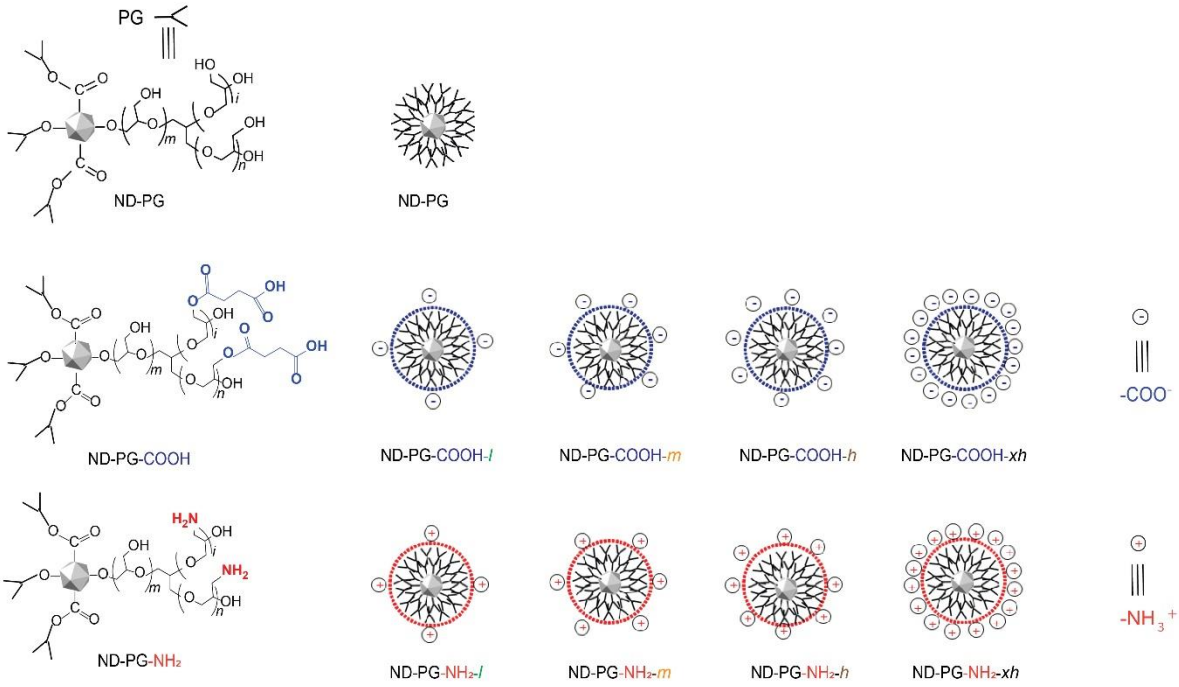

Figure 3-2. Chemical structures of ND-PG, ND-PG-COOH and ND-PG-NH_2 at various densities (ND-PG-COOH-*l*, -*m*, -*h*, -*xh* and ND-PG-NH_2-*l*, -*m*, -*h*, -*xh*).

All the ND-PG-COOH, ND-PG-OTs, ND-PG-N_3 and ND-PG-NH_2 with various densities of the functional groups (*l*, *m*, *h* and *xh*) were characterized by IR spectroscopy (Figure 3-3). In order to compare the relative abundance of the function groups, all the IR spectra were normalized at the band around 1110 cm^{-1} due to the C-O-C stretching in the PG, which constitutes a constant component throughout the organic transformation processes. As shown in Figure 3-3a, the absorption bands at

around 1730 cm^{-1} are assigned to C=O stretching of the carboxyl groups in ND-PG-COOH, and the intensity of these bands should be proportional to the number of COOH groups (1.0 : 3.0 : 4.8 : 6.6 for *l* : *m* : *h* : *xh*). The absorptions corresponding to S→O bonds in ND-PG-OTs at 1350 and 1176 cm^{-1} and azido group in ND-PG-N_3 at 2100 cm^{-1} are also correlated with the numbers of these functional groups (Figure 3-3b and Figure 3-3c, respectively). However, such correlation is not clear in the amino groups in ND-PG-NH_2, although azido groups are disappeared in the spectra (Figure 3-3d).

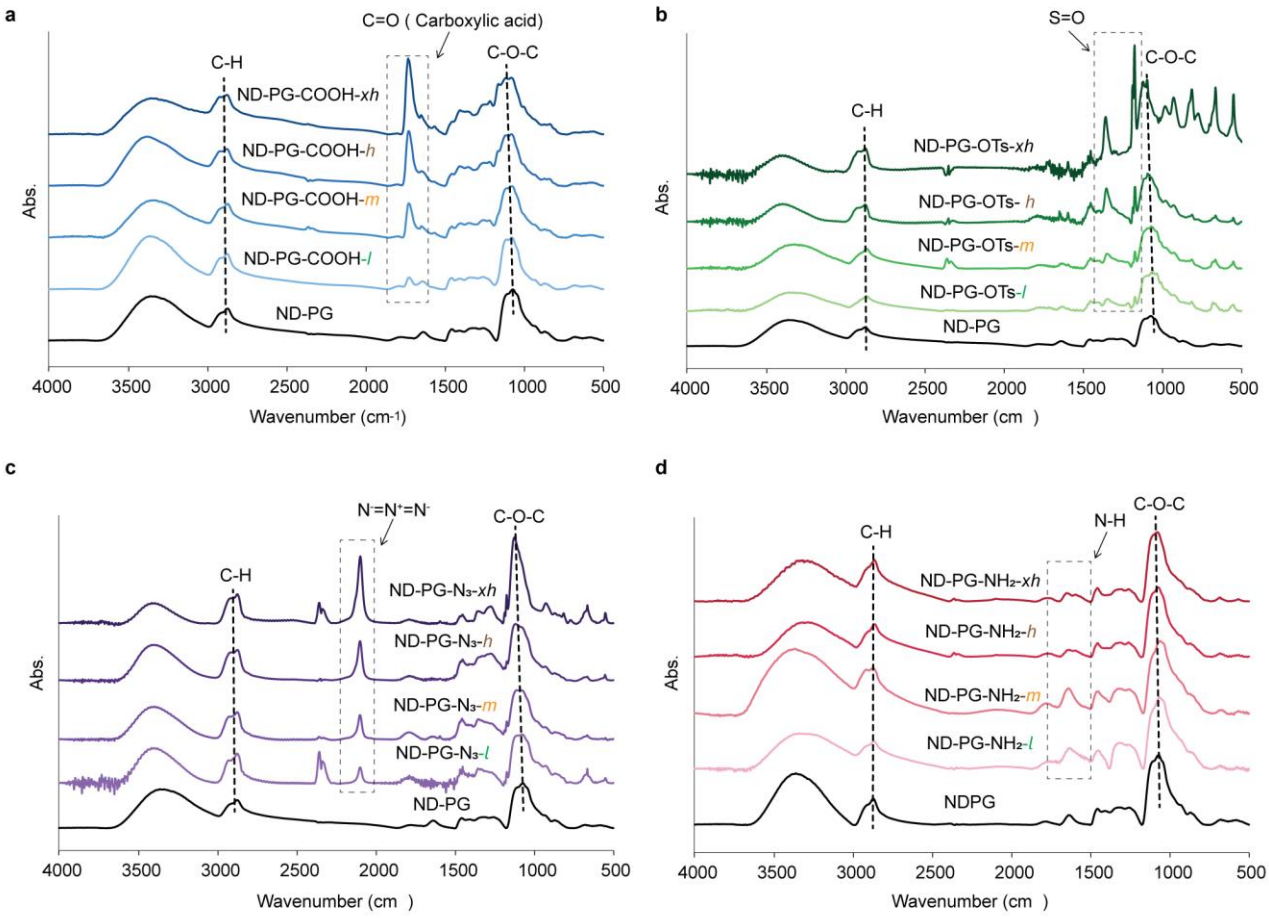

Figure 3-3. IR spectra of ND-PG-COOH with *l*, *m*, *h* and *xh* densities of carboxyl groups.

In order to know the number of amino groups on ND-PG-NH_2, elemental analysis (EA) was performed by combustion method for ND-PG-NH_2. Since the average number of carbon atoms in one ND-PG particle was determined to be 1.5×10^7 (eq. 3-2) [62], the nitrogen contents were converted to the average number of amino groups on one particle and density of amino groups (Table 3-1), which will be correlated with the protein amount below.

Table 3-1. Content of C and N, the average number of amino groups on one particle and the density of amino groups in ND-PG-NH_2.

Entry	Particle[a]	Content (wt%)		Average number of amino groups on one particle	Density of amino groups (/ nm^2)
		C	N		
1	ND-PG-NH_2-*l*	80.5	0.19	3.2×10^4	2.0
2	ND-PG-NH_2-*m*	81.37	0.3	4.8×10^4	3.0
3	ND-PG-NH_2-*h*	78.92	0.85	1.4×10^5	9.0
4	ND-PG-NH_2-*xh*	79.58	1.55	2.6×10^5	16

[a] Number of carbon atoms in one particle are calculated to be 1.5×10^7 in all the particles (eq. 3-2).

Calculation of the number of amino groups in one ND-PG-NH_2 particle.

(a) The number of oxygen atoms consisted in one ND particle ($\boldsymbol{N_{O-ND}}$) was calculated from eq. 3-1.

The number of carbon atoms included in one ND particle $\boldsymbol{N_{C-ND}}$ is 1.2×10^7 [62]. $\boldsymbol{W_{O-ND}}$ **(2.93%)** and $\boldsymbol{W_{C-ND}}$ **(95.95%)** are the weight ratio of oxygen and carbon in bare ND, and $\boldsymbol{M_O}$ and $\boldsymbol{M_C}$ are the molar mass of oxygen and carbon.

$$\frac{N_{O-ND}}{N_{C-ND}} = \frac{W_{O-ND}/M_O}{W_{C-ND}/M_C} \quad \textbf{(eq. 3-1)}$$

$$N_{O-ND} = 2.75 \times 10^5$$

(b) The degree of PG polymerization ($C_3H_6O_2$) *n* in ND-PG was calculated from eq. 3-2. $\boldsymbol{N_{O-ND-PG}}$ and $\boldsymbol{N_{C-ND-PG}}$ are the number of oxygen atoms consisting one ND-PG particle, and $\boldsymbol{W_{O-ND-PG}}$ **(17.34%)** and $\boldsymbol{W_{C-ND-PG}}$ **(77.56%)** are the weight ratio of oxygen and carbon in ND-PG.

$$\frac{N_{O-ND-PG}}{N_{C-ND-PG}} = \frac{N_{O-ND}+2n}{N_{C-ND}+3n} = \frac{W_{O-ND-PG}/M_O}{W_{C-ND-PG}/M_C} \quad \textbf{(eq. 3-2)}$$

$$n = 1.2 \times 10^6 \quad N_{C-ND-PG} = 1.5 \times 10^7$$

(c) The number of amino groups in ND-PG-NH_2 ($\boldsymbol{N_{N-ND-PG-NH2}}$) were calculated from eq. 3-3. $\boldsymbol{W_{N-ND-PG-NH2}}$ and $\boldsymbol{W_{C-ND-PG-NH2}}$ are the weight ratio of nitrogen and carbon in ND-PG-NH_2, and $\boldsymbol{M_N}$ is the molar mass of nitrogen.

$$\frac{N_{N-ND-PG-NH2}}{N_{C-ND-PG}} = \frac{W_{N-ND-PG-NH2}/M_N}{W_{C-ND-PG-NH2}/M_C} \quad \textbf{(eq. 3-3)}$$

The zeta potentials of both ND-PG-COOH and ND-PG-NH_2 were measured in PBS. As

shown in Figure 3-4, they are proportional to the density of the functional groups from *l* to *xh*, verifying the validity in the determination of the density of carboxyl and amino groups with IR and EA analysis, respectively. The zeta potentials will also correlate with the amounts of corona proteins in the Discussion.

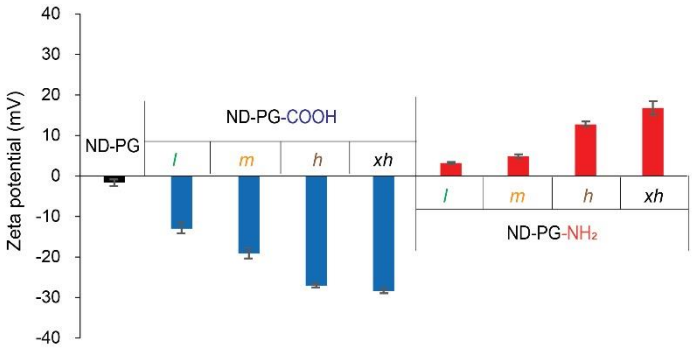

Figure 3-4. Zeta potentials of ND-PG, ND-PG-COOH-*l*, -*m*, -*h* and -*xh*, and ND-PG-NH_2-*l*, -*m*, -*h* and -*xh* in PBS.

3-2-2 Adsorption of single proteins on ND-PG-COOH and ND-PG-NH_2

To probe net charge effect of these functional groups, a positively charged protein (lysozyme (LYS), p*I*: 11) and negatively charged ones (bovine serum albumin (BSA), p*I*: 4.8 and γ-globulin (γ-GLO), p*I*: 6.9) were applied to the dispersions of ND-PG, ND-PG-COOH and ND-PG-NH_2 with various functional group densities in PBS. The protein mixtures such as LYS/BSA and LYS/γ-GLO were also applied to make clear the selectivity toward the protein with opposite charge. The images of these NDs before and after incubation with these proteins and their mixture are shown in Figure 3-5. Although ND-PG dispersion in PBS was quite stable even in the presence of proteins, most of the ND-

PG-COOH and ND-PG-NH_2 dispersions exhibited precipitates in the presence of the proteins with opposite charge.

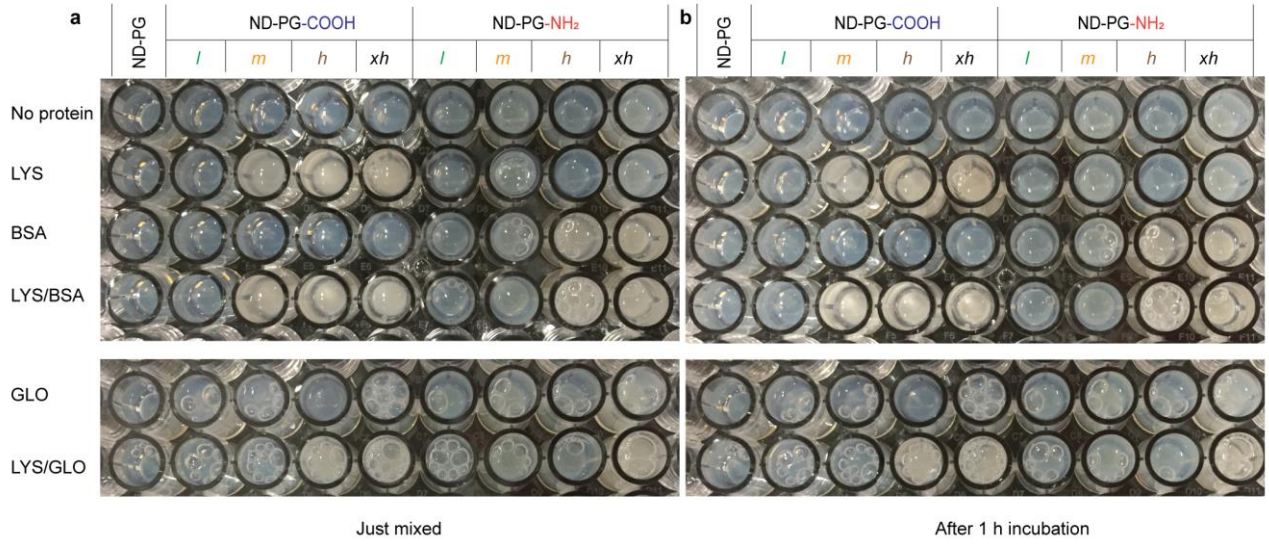

Figure 3-5. Images of ND-PG, ND-PG-COOH and ND-PG-NH_2 in PBS and those with proteins (LYS, BSA, GLO, LYS/BSA or LYS/GLO) just after mixing (a) and after 1 h incubation (b).

After the incubation, the corona proteins were recovered and subjected to SDS-PAGE for identification and semi-quantification, and BCA for quantification. In the SDS-PAGE, LYS and BSA protein bands appear only in the lanes of ND-PG-COOH and ND-PG-NH_2, respectively, as shown in Figure 3-6a and 3-6b at the protein concentration of 2.0 mg/mL, and Figure 3-7a and 3-7b at the protein concentration of 24.0 mg/mL. The thickness of these bands is proportional to the density of the functional groups. No protein bands are observed in the ND-PG-NH_2 lanes in Figure 3-6a and Figure 3-7a and in the ND-PG-COOH lanes in Figure 3-6b and Figure 3-7b regardless of the density of these functional groups, the amount of the corona proteins for SDS-PAGE and concentration of the proteins at the incubation. In addition, ND-PG formed protein corona with neither of the proteins, as we reported previously [84]. When a mixture of LYS and BSA was applied to ND-PG-COOH and ND-PG-NH_2 at the 1:1 weight and molar ratios (Figure 3-6c and 3-7c, respectively), only one of these

proteins were selectively adsorbed on the surface of ND-PG with the opposite charge in the amounts proportional to the density of the functional group. Since almost all the carboxyl and amino groups are carboxylate and ammonium ions in PBS which will be demonstrated in the Discussion, these results clearly indicate that the electrostatic, or charge-charge, interaction between the ND-PG surface and the protein is dominant and the charge density dictates the protein affinity.

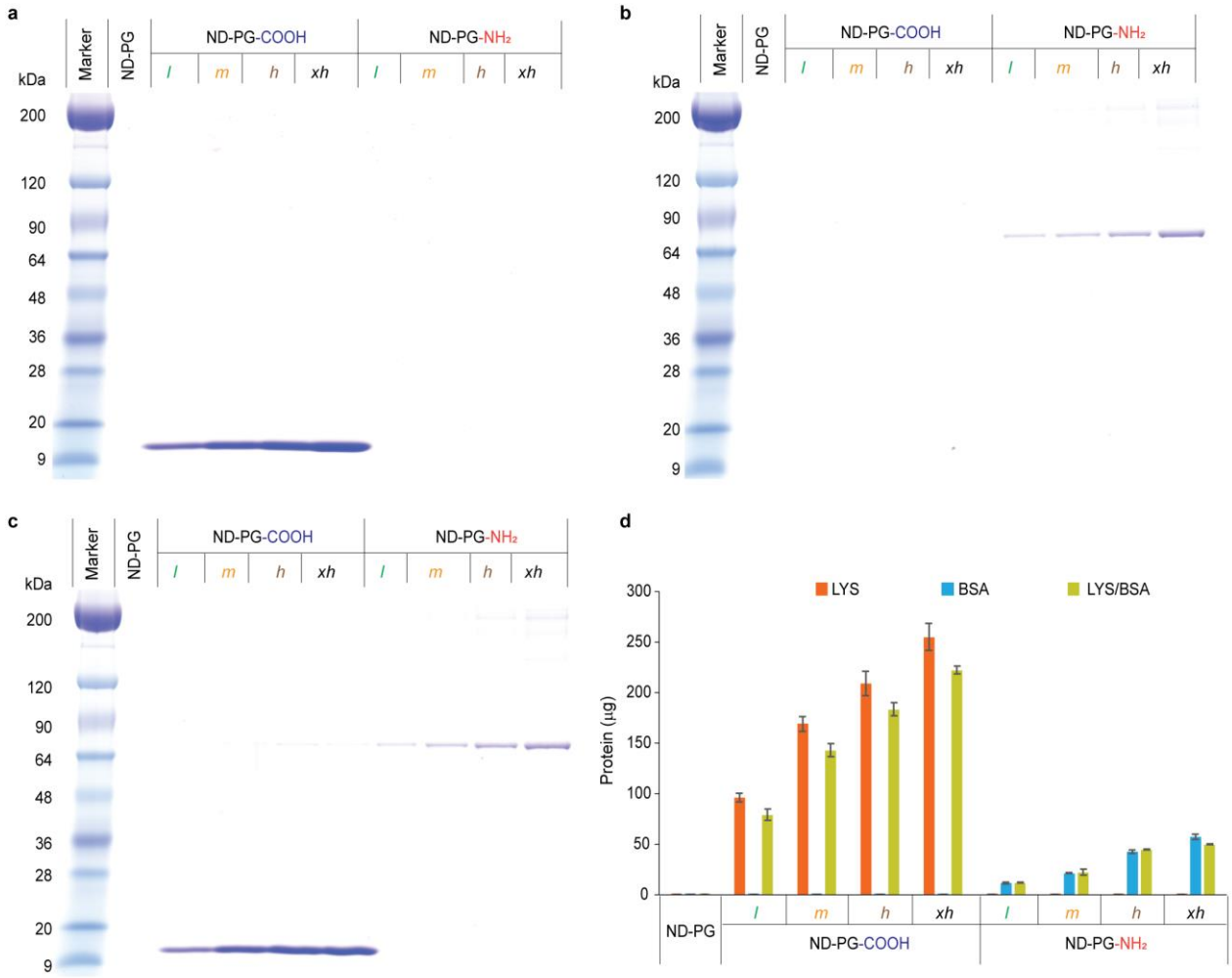

Figure 3-6. Characterization and quantification of LYS and BSA adsorbed on ND-PG, ND-PG-COOH and ND-PG-NH_2 surfaces. (a-c) SDS-PAGE images of proteins detached from ND-PG, ND-PG-COOH and ND-PG-NH_2 after their incubation with (a) LYS (2.0 mg/mL), (b) BSA (2.0 mg/mL) and (c) LYS/BSA mixture (2.0/2.0 mg/mL). (d) BCA quantification of proteins (μg) detached from ND-PG, ND-PG-COOH and ND-PG-NH_2. The results are presented as mean value ± standard deviation of three independent replicates.

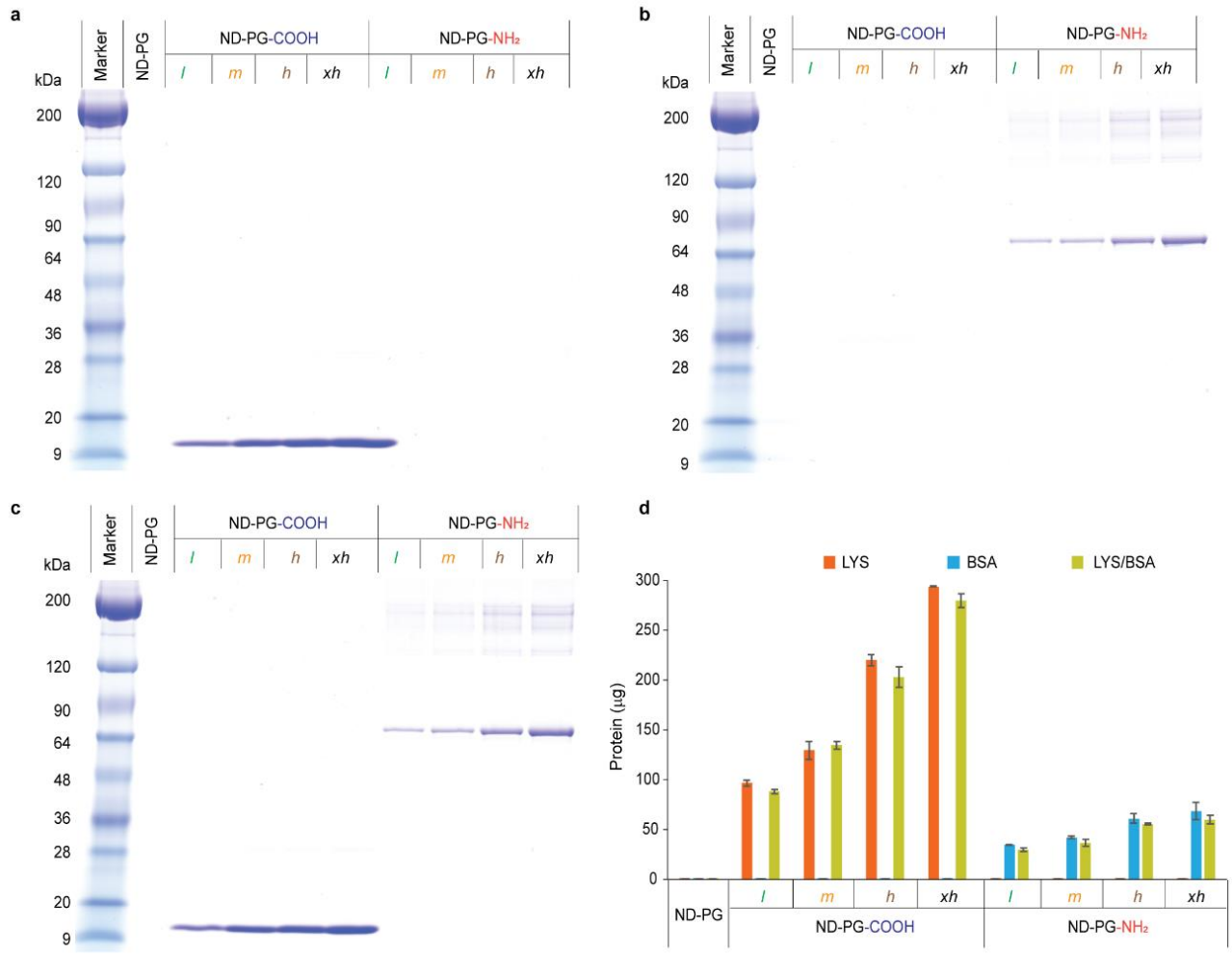

Figure 3-7. Characterization and quantification of LYS and BSA adsorbed on ND-PG, ND-PG-COOH and ND-PG-NH_2 surfaces. (a-c) SDS-PAGE images of proteins detached from ND-PG, ND-PG-COOH and ND-PG-NH_2 after their incubation with (a) LYS (24.0 mg/mL), (b) BSA (24.0 mg/mL) and (c) LYS/BSA mixture (2.0 and 9.2 mg/mL of LYS and BSA, respectively, to adjust the mole ratio of LYS and BSA to 1:1). (d) BCA quantification of proteins (μg) detached from ND-PG, ND-PG-COOH and ND-PG-NH_2. The results are presented as mean value ± standard deviation of three independent replicates.

The result of BCA shown in Figure 3-6d and Figure 3-7d support the conclusion of SDS-PAGE shown in Figure 3-6a – 3-6c and Figure 3-7a – 3-7c more quantitatively. While almost no proteins were attached on the surface of ND-PG, LYS and BSA were exclusively adsorbed on ND-PG-COOH and ND-PG-NH_2, respectively. The amounts of the proteins linearly increase according to the density of the functional groups from *l* to *xh*, although the proportionality is different clearly between LYS – ND-PG-COOH, and BSA – ND-PG-NH_2, which will be quantitatively discussed below. In addition, a similar adsorption behavior was observed both in the SDS-PAGE (Figure 3-8a and Figure 3-8b) and BCA (Figure 3-8c), when the γ-GLO and LYS/γ-GLO were applied in place of BSA and LYS/BSA. This strengthens the above qualitative conclusion of the exclusive affinity of the protein to the oppositely charged functional groups.

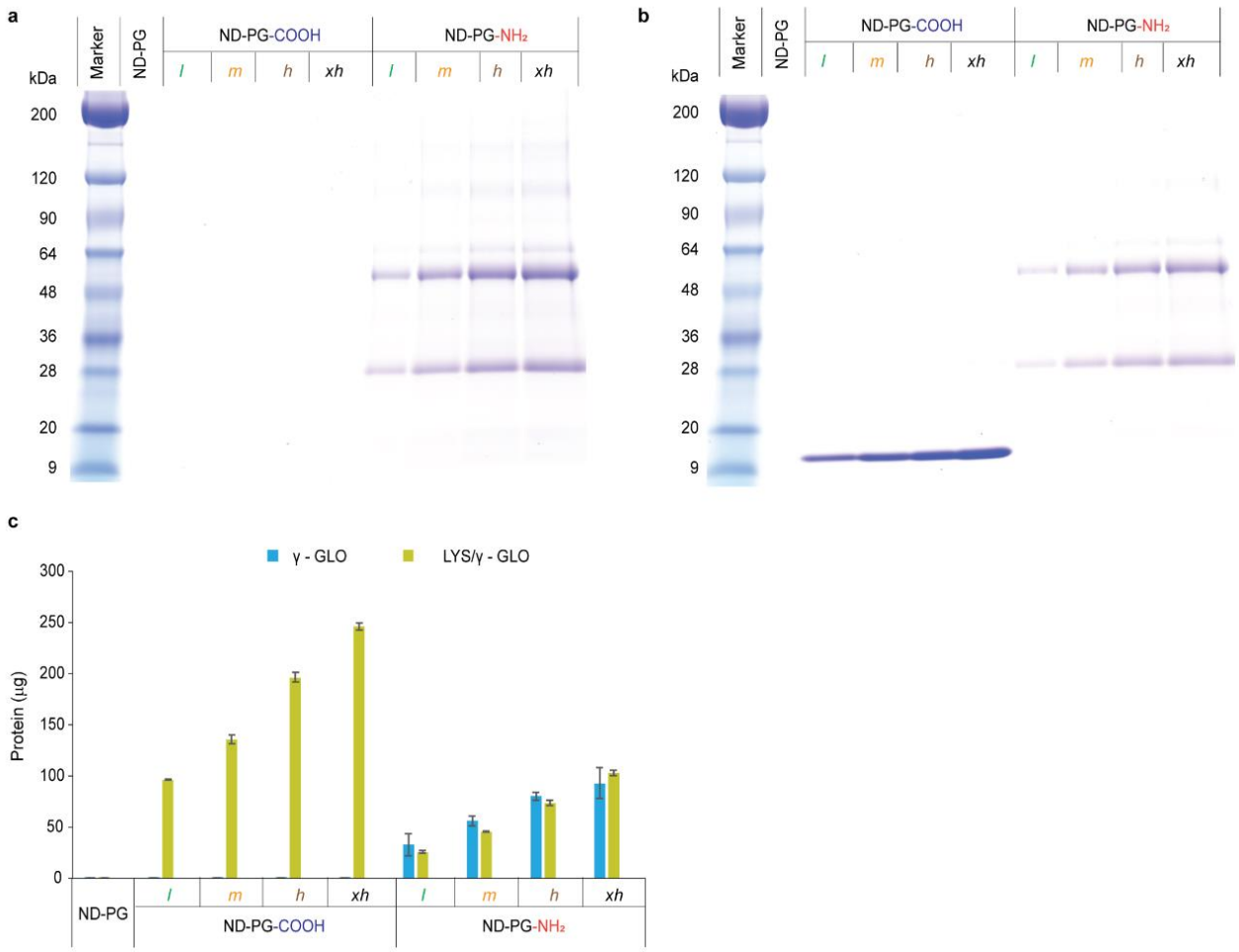

Figure 3-8. Characterization of γ-GLO and LYS / γ-GLO adsorption onto ND-PG, ND-PG-COOH and ND-PG-NH_2 surface. (a-b) SDS-PAGE images of proteins detached from ND-PG, ND-PG-COOH and ND-PG-NH_2 after their incubation with (a) γ-GLO (21.7 mg/mL) and (b) LYS/γ-GLO (2.0 and 21.7 mg/mL for LYS and γ-GLO, respectively, to have 1:1 mole ratio of LYS and GLO). (c) BCA quantification of proteins (μg) detached from ND-PG, ND-PG-COOH and ND-PG-NH_2. The results are presented as mean value ± standard deviation of three independent replicates. Note: γ-GLO is a Y-shaped protein comprising of two heavy chains (55-60 kDa) and two light chains (25-28 kDa).

3-3 Discussion

Before discussing the interaction with proteins, the ionic state of the functional groups on the ND-PG surface in PBS (pH: 7.4) is considered. Since the typical pK_a values of the ammonium and carboxyl compounds are about 10.6 and 4.8, respectively, the ion contents are calculated to be more than 99% by Henderson - Hasselbach equation as follows. Similarly, these proteins, BSA (p*I*: 4.8) and LYS (p*I*: 11), are ionized negatively and positively in PBS (pH: 7.4), respectively.

$$log\frac{[-NH_2]}{[-NH_3^+]} = pH - pK_a = -3.2 \qquad \frac{[-NH_3^+]}{[-NH_2]} = 10^{3.2} \quad \textbf{(eq. 3-4)}$$

$$log\frac{[-COO^-]}{[-COOH]} = pH - pK_a = 2.6 \qquad \frac{[-COO^-]}{[-COOH]} = 10^{2.6} \quad \textbf{(eq. 3-5)}$$

Since the charge of the ND-PG-COOH and ND-PG-NH_2 in PBS is reflected by zeta potential as shown in Figure 3-4, we correlate zeta potential with the amount of the proteins in the corona layer measured by BCA (Fig. 3-6, 3-7 and 3-9).

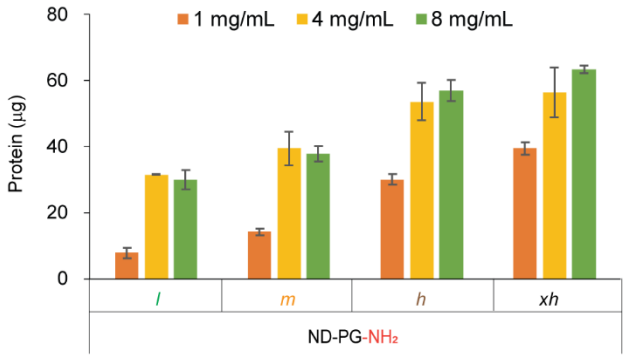

Figure 3-9. BCA quantification of BSA (μg) detached from ND-PG-NH_2 after their incubation with BSA at the concentrations of 1.0, 4.0 and 8.0 mg/mL, respectively. The results are presented as mean value ± standard deviation of three independent replicates.

The amounts of BSA adsorbed on ND-PG-NH_2 is strictly proportional to the zeta potentials of ND-PG-NH_2-*l*, -*m*, -*h* and -*xh* at the correlation coefficients of 0.99 in the BSA concentrations of 1.0 and 2.0 mg/mL (Figure 3-10a). When we add one more result of almost no protein adsorption on ND-PG with the zeta potential of –1.6 mV, the correlation coefficients even increase, improving the reliability of the linear relationship. On the other hand, the y-intercepts increase significantly, when the BSA concentrations increased to 4.0, 8.0 and 24.0 mg/mL (Figure 3-10a). This implies interaction between BSA molecules other than the electrostatic interaction between BSA and the ammonium groups; that is, a BSA molecule in PBS may be attracted not only by the ammonium groups, but also another BSA adsorbed on the ND-PG-NH_2 surface probably due to saturation at the adsorptive cites especially at the lower zeta potential corresponding to the lower amino group density. In this sense,

the conditions at lower concentration of BSA should give more reliable relationship between BSA and the ammonium groups on the ND-PG-NH_2 surface. The amounts of LYS are also proportional to the zeta potentials of ND-PG-COOH (Figure 3-10b), although the correlation coefficient is not so high as that between BSA at lower concentrations (1.0 and 2.0 mg/mL) and the ND-PG-NH_2 surface. A large difference can be found in the slopes of these linear plots; the absolute value of the slope in Figure 3-10b is about three times larger than that in Figure 3-10a, implying the difference in the interactions of BSA – ND-PG-NH_2 and LYS – ND-PG-COOH.

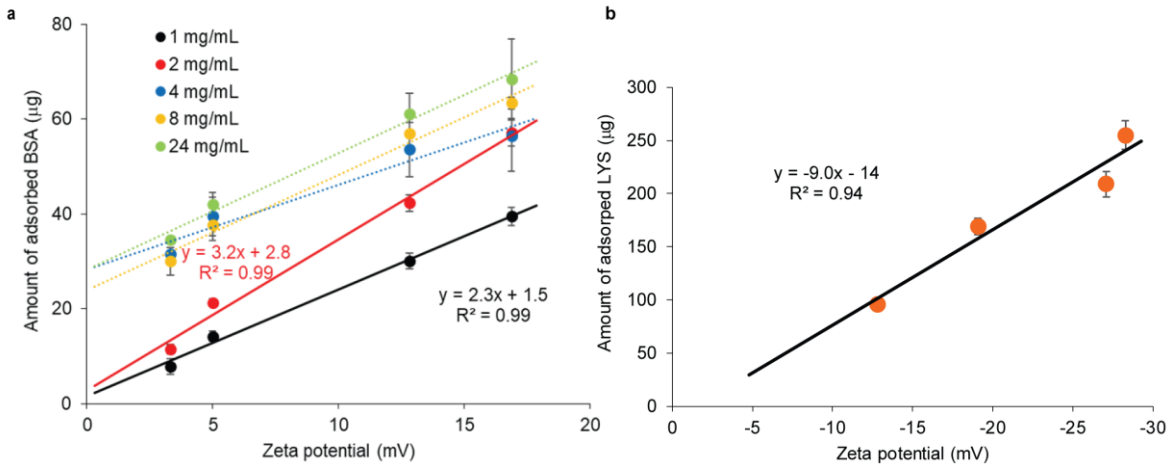

Figure 3-10. Linear relationship of the amounts of BSA and LYS in corona layer with zeta potentials of ND-PG-NH_2 (a) and ND-PG-COOH (b), respectively.

If the affinity of the specific functional group to the certain protein is provided quantitatively by association constant, it should be very helpful in quantitative interpretation of the protein corona

formation on NPs with various surface coatings. As shown in Table 3-2, we determined association constants (K) of the ammonium group ($-NH_3^+$) on the surface of ND-PG at various densities with BSA at the concentrations of 1.0 and 2.0 mg/mL in PBS by Langmiur equation. The K from 1.0 and 2.0 mg/mL BSA concentrations are similar at the same NH_2 density, giving validity to the K determined by the following Langmiur equation. This can be attributed to the exclusive interaction of the ammonium groups on the ND-PG surface with BSA at the concentrations of 1.0 and 2.0 mg/mL as described in the linear relationship between zeta potential and the adsorbed BSA amount (Figure 3-10a). The Gibbs free energy (ΔG) was also drawn from the K. This is realized by virtue of no protein adsorption property of PG coating on ND as shown in Figure 3-6, 3-7 and 3-8 and selective introduction of the specific functional groups on PG in a quantitative manner as mentioned above. In addition, single BSA layer formed on the ND surface was reported, while LYS is adsorbed on the ND surface to form multilayer, to which Langmiur equation cannot be applied [85]. The association constants shown in Table 3-2 were determined by the following equations;

$$K = \frac{\theta}{(1-\theta)C} \quad \textbf{(eq. 3-6)}$$

$$\theta = \frac{S_{\mathrm{Protein}}}{S_{\mathrm{ND-PG}}} \quad \textbf{(eq. 3-7)}$$

where C, S_{Protein} and $S_{\mathrm{ND\text{-}PG}}$ are the concentration (mol / L) of the unbound protein in PBS, total

surface area of proteins adsorbed on one ND-PG-NH_2 particle (eq. 3-8) and the whole surface area of one ND-PG particle (eq. 3-10), respectively. Herein, it is assumed that BSA can be adsorbed on the whole surface of ND-PG-NH_2 at the same saturated adsorption amounts irrespective of the ammonium group density. Since the surface of ND-PG-NH_2 is acidic due to a number of ammonium groups (-NH_3^+), BSA is supposed to change the conformation from an equilateral triangular "*N* form" (size: 8 × 3 nm) under neutral conditions to ellipsoidal "*F* form" (size: 4 × 13 nm) under acidic conditions [86]. In addition, ellipsoidal BSA is reported to attach to the ND surface in the "end-on" form [85]. Based on the electrostatic BSA corona model shown in Fig. 3-11a, we assume that BSA occupies 13 nm^2 per molecule on the ND-PG surface, which is corresponding to the area of the round slice at the center of the ellipsoid.

Table 3-2. Association constant (K) and Gibbs free energy (ΔG) of the corona formation between ND-PG-NH_2 and BSA.

BSA (mg/mL)	ND-PG-NH_2	C ($\times 10^{-5}$ mol/L) in PBS	$S_{protein}/S_{ND\text{-}PG}$ (θ)	K ($\times 10^4$ L/mol)	ΔG (kJ/mol)
1.0	ND-PG-NH_2-*l*	1.5	0.075	0.56	-22
	ND-PG-NH_2-*m*	1.4	0.14	1.1	-24
	ND-PG-NH_2-*h*	1.3	0.29	3.2	-27
	ND-PG-NH_2-*xh*	1.2	0.38	5.0	-28
2.0	ND-PG-NH_2-*l*	2.9	0.11	0.42	-21
	ND-PG-NH_2-*m*	2.9	0.21	0.90	-23
	ND-PG-NH_2-*h*	2.7	0.41	2.5	-26
	ND-PG-NH_2-*xh*	2.6	0.55	4.7	-28

The total surface area of the adsorbed BSA ($\boldsymbol{S_{Protein}}$) on one ND-PG particle is calculated by eq. 3-8.

$$\boldsymbol{S_{Protein}} = \boldsymbol{N_{Protein}} \times 13\ nm^2 \quad \textbf{(eq. 3-8)}$$

The number of adsorbed BSA ($\boldsymbol{N_{Protein}}$) on one ND-PG particle is calculated from eq. 3-9. $\boldsymbol{N_A}$, $\boldsymbol{W_{Protein}}$ and $\boldsymbol{M_{Protein}}$ are the Avogadro's constant (6.02×10^{23} mol^{-1}), the weight of absorbed BSA by BCA quantification and the molecular weight of BSA (66 kDa), respectively. The number of ND-PG particles ($\boldsymbol{N_{ND-PG}}$, 7.77×10^{11}) used for BSA adsorption is determined according to our recent work [84].

$$\boldsymbol{N_{Protein}} = \boldsymbol{N_A} \frac{\boldsymbol{W_{Protein}/N_{ND-PG}}}{\boldsymbol{M_{Protein}}} \quad \textbf{(eq. 3-9)}$$

When the *K* shown in Table 3-2 is correlated with the density of amino group shown in Table 3-1, good linearity at the correlation coefficients of 0.98 and 0.99 is found at the BSA concentrations of 1.0 and 2.0 mg/mL, respectively (Figure 3-11b). Both linear lines direct to the origin (0, 0), which is consistent with the experimental fact of no protein adsorption on ND-PG. These similar slopes (0.12 and 0.10 L mol^{-1} nm^{-2}) obtained at relatively low protein concentrations should be indices to represent the affinity of the protein (BSA) to the functional group ($-NH_3^+$) on NP surface upon corona formation.

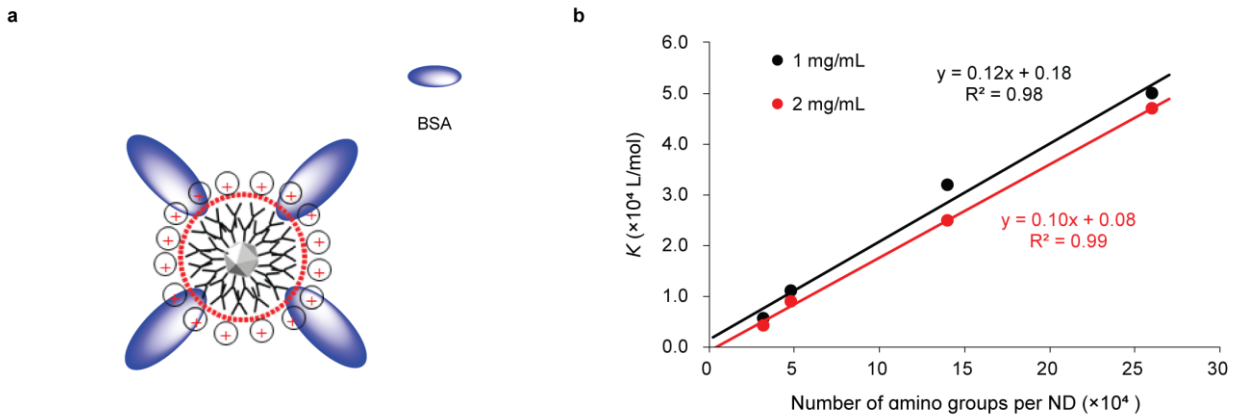

Figure 3-11. Adsorption pattern of BSA on ND-PG-NH_3^+ (a) and the linear relationship between density of amino groups on ND-PG (Table 3-1) and the association constants of ND-PG-NH_3^+ with BSA (Table 3-2) (b).

3-4 Conclusions

The net interaction at the interface between protein and ND-PG surface was quantitatively assessed by introducing carboxyl and amino groups onto the periphery of corona-free ND-PG surface at various densities. Both carboxylate (-COO^-) and ammonium (-NH_3^+) groups exclusively interacted with proteins of opposite charge in a charge-density dependent manner. The association constants (K) between BSA and the ammonium group on ND-PG at various densities were successfully determined and found to be proportional to the amino group density, which is applicable generally to the quantitative comparison of the protein affinity on NPs with various surface coatings.

3-5 Materials and methods

3-5-1 Materials and chemicals

ND of 50 nm size was kindly provided by Tomei Diamond Co., Ltd., Japan. The following reagents or kits were purchased from Wako Pure Chemicals, Japan; *N*,*N*-dimethylformamide (DMF), albumin (from bovine serum, BSA), lysozyme (from egg white, LYS), γ-globulin (from human plasma, γ-GLO), sodium dodecyl sulfate (SDS) and Coomassie blue G-250. The following reagents were purchased from Nacalai Chemicals, Japan; 4-dimethylaminopyridine (DMAP), pyridine, succinic anhydride, *p*-toluenesulfonyl chloride (TsCl), sodium azide, triphenylphosphine, pre-stained protein markers (02525-35), and running buffer (30329-61). Protein loading buffer (AE-1430) and 5-20% precast polyacrylamide gel (E-R520) were purchased from ATTO, Japan. Bicinchoninic acid assay (BCA) protein assay kit (T9300A) was supplied by Takara, Co., Ltd., Japan.

3-5-2 Equipment

Scanning transmission electron microscopy (STEM) observation was performed on a JSM-7500F field emission scanning electron microscope (JEOL) at 25 kV accelerating voltage. IR characterization was performed on an IR Prestige-21 (Shimadzu Co. Ltd.) with 16 scans and a 4 cm^{-1} resolution in the wavenumber range of 4000 to 500 cm^{-1}. EA of C, N and O content was performed at Organic Elemental Microanalysis Center of Kyoto University. The zeta potential and the DLS was recorded on a Zeta Sizer Nano Series (Malvern Instruments, U.K.) and a Nanotrac UPA-UT151 system (Microtrac, Inc.,

USA), respectively. Centrifugation was carried out on a Himac CS 150GXII (Hitachi, Japan) at 434,000*g* - 108,000*g* and a MRX-152 (Tomy, Japan) at 5,000*g*. The PAGE gel was scanned by a GT-X900 (Epson, Japan) scanner, and the fluorescent intensity of BCA quantification was recorded on a MTD-310 (Corona Electric, Japan) microtiter plate reader.

3-5-3 Preparation of ND-PG-COOH-*l, -m, -h, -xh* and ND-PG-NH_2-*l, -m, -h, -xh*

The ND-PG, ND-PG-COOH and ND-PG-NH_2 was prepared according to our previous methods [26, 27], and the *l, m, h* and *xh* densities of charge groups were obtained by controlling the reaction time. ND-PG-COOH-*l*, -*m*, -*h* and -*xh* were obtained by stopping the ring-opening reaction of succinic anhydride at 3, 5, 8 and 24 h, respectively. On the other hand, ND-PG-OTs- *l*, -*m*, -*h* and -*xh* were obtained by stopping tosylation reactions at 3, 5, 8 and 24 h, respectively. Then, each of the resulting tosylates was transformed to ND-PG-NH_2-*l*, -*m*, -*h* and -*xh* through OTs $\rightarrow$ N_3 $\rightarrow$ NH_2 transformations.

3-5-4 Protein corona formation

The protein corona formation was performed according to our previous methods [84]. ND-PG, ND-PG-COOH and ND-PG-NH_2 of *l*, *m*, *h* and *xh* densities were incubated with LYS (2.0 and 24.0 mg/mL), BSA (1.0, 2.0, 4.0, 8.0 and 24.0 mg/mL), γ-GLO (21.7 mg/mL), LYS/BSA (2.0 and 9.2 mg/mL of LYS and BSA, respectively), and LYS/γ-GLO (2.0 and 21.7 mg/mL of LYS and γ-GLO, respectively) in a PBS solution (200 μL) at 37 °C for 1 h. The weights (~300 μg) of ND-PG-COOH

and ND-PG-NH_2 used in each incubation was adjusted to have an equal total surface area of 125 cm^2 for ND-PG (Table 3-3). After the incubation, the free unbound proteins were fully removed by centrifugation at 434,000*g* for 20 min three times. Then, the corona proteins were extracted by 10% SDS solution (150 μL) and separated from ND by centrifugation at 108,000*g* for 20 min. The supernatant containing the corona proteins designated as protein corona solution was used for further analysis.

Table 3-3. DLS measurement of ND-PG.

Measurement	DLS size (nm)
1#	73.32
2#	66.12
3#	68.64
4#	74.28
5#	75.12
AVG	71.50
SD	3.91

The surface area of one ND-PG particle (S_{ND-PG}) is calculated to be 1.61 × 10^4 nm^2 based on eq. 3-10, where r is the radius of ND-PG determined by DLS measurement.

$$S_{ND-PG} = 4\pi r^2 \quad \textbf{(eq. 3-10)}$$

3-5-5 SDS-PAGE

An aliquot of protein corona solution (5 μL) was mixed with an equal volume of protein loading buffer (2 ×) in a new Eppendorf tube and boiled at 100 °C for 5 min. After collecting the droplets on the wall of Eppendorf tube by centrifugation (5,000*g* for 3 min), the mixtures were loaded into a precast polyacrylamide gel along with pre-stained protein markers. The electrophoresis was run at a constant voltage of 100 V until the blue indicator reached the bottom. The gels were stained by Coomassie blue G-250 and scanned on a scanner with a resolution of 600 dpi to visualize the protein bands. All the experiments were conducted at least for three times to ensure reproducibility of the results.

3-5-6 BCA

The amount of each protein corona samples was quantified by a BCA protein assay kit according to the manufacturer's instruction. In brief, an aliquot of protein corona solution (20 μL) was mixed with PBS (80 μL) and freshly prepared BCA working reagent (100 μL) in a clean 96-well plate and then incubated at 37 °C for 1 h. Meanwhile, standard BCA solutions in the concentration ranges of 25, 50, 100, 150 and 200 μg/mL were assayed to prepare the calibration curves. After incubation, the

absorbance was recorded on a microtiter plate reader at 570 nm. The absorbance of 10% SDS (20 μL) was also measured as blank control and subtracted during the calculation. All the experiments were performed in triplicates.

Chapter 4: Probing the role of charged functional groups on corona-free polyglycerol-functionalized nanoparticle in protein absorption and cellular uptake

4-1 Introduction

Charged functional groups on NP surface are the key parameters to modulate the affinity of NPs to cellular membranes and hence their uptake [87]. However, in biofluids, the charged functional groups associated with serum proteins and the resulting NP-protein complexes are known to be slightly negative regardless the initial charges of NPs [31]. This eliminates the affinity difference of original charge groups to cell membranes and emphasizes the role of absorbed proteins in NP uptake.

In order to gain insights into NP design for improved theranostic performance, extensive efforts have been made for comprehensive understanding of the relationship among charged functional groups, absorbed proteins and cellular uptake [19]. However, inconsistent results have been reported so far. While the anionic and cationic liposomal NPs were revealed to attract the proteins with specific p*I* range [80], many investigations showed that the protein binding were independent of the charged functional groups and the p*I* of proteins [32, 33]. Noteworthy is that Tenzer et al. reported rapid absorption of anionic plasma proteins onto both carboxylate and ammonium functionalized NP surfaces [76]. The contradictory findings extended from protein absorption to subsequent cellular response. Although some studies reported that positively charged NPs had a higher uptake efficacy than negatively charged ones in the presence of protein corona [34], opposite trends were revealed by

Melby et al. [88] and Kokkinopoulou et al [89]. They reported that the serum proteins on the surface of anionic NPs induced a higher uptake ratio or a stronger affinity to the supported lipid bilayers, as compared to the cationic ones. The discrepant results reported so far can be interpreted by participation of the other surface chemical groups than the charged functional ones to attract proteins [69]. Therefore, the charged functional groups were introduced at the terminals of the protein-resistant polymers such as PEG [90] and amphiphilic ones [75, 91]. However, the net charge effect remains elusive, because these polymers cannot completely suppress the protein adsorption.

Quite recently, we have demonstrated that PG grafting prevented protein corona formation almost completely [84], which renders PG layer is a suitable interface to study the net charge effects. Herein, the carboxyl, sulfate and amino groups were introduced on the NP-PG surface in a quantitative manner. Thanks to this corona-free PG layer, we demonstrated that uptake efficiency of NPs was correlated with the protein affinity of charged functional groups. That is, the carboxylate ($–COO^-$) and sulfate ($–OSO_3^-$ up to 4.1 groups / nm^2) exhibited no affinity to the proteins in FBS induced negligible or no cellular uptake. In contrast, $–OSO_3^-$ (25 groups / nm^2) and ammonium ($–NH_3^+$) provoked substantial cellular uptake through association with the serum proteins. In addition, the distinct protein corona profiles on NP-PG-OSO_3^- and NP-PG-NH_3^+ were revealed to suppress or enhance uptake through the regulation of specific uptake pathways.

4-2 Results and discussion

4-2-1 Functionalization of NP-PG with carboxyl, sulfate and amino groups and their characterization

NDs of 50 nm in diameter and SPIONs with 8 nm in diameter were grafted with PG, a corona-free interface, at 33 and 41 wt%, respectively, which were determined by TGA (Figure 4-1).

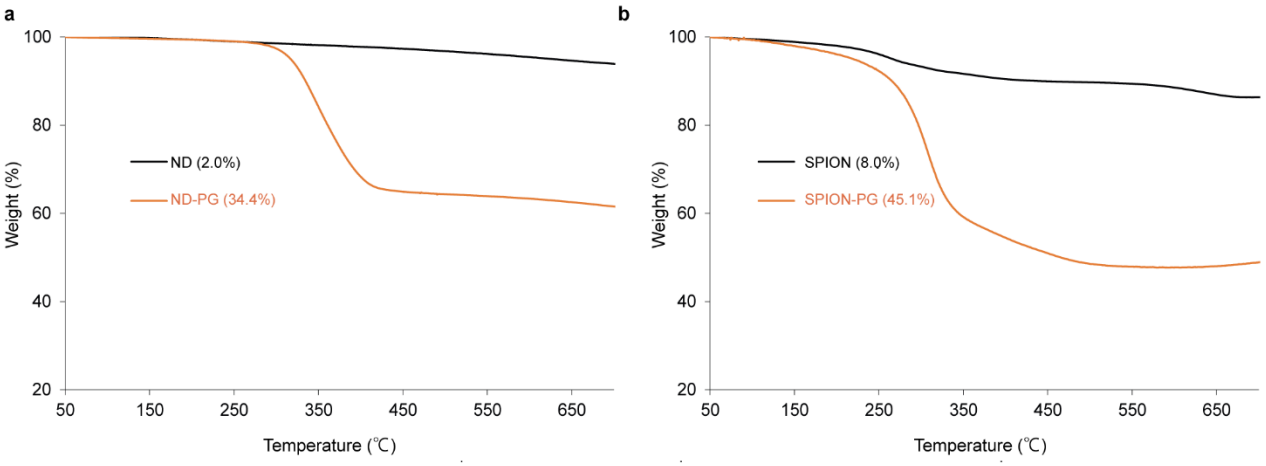

c

NP or NP-PG	NP core (wt%)	Organic component on NP surface (wt%)[a]	Weight loss in 200-450 ℃ (wt%)	PG (wt%)
ND	97.4	2.0		
ND-PG	64.9	1.4	34.4	33.0
SPION	90.0	8.0		
SPION-PG	51.0	4.5	45.1	40.6

[a]The organic component refers to the hydroxyl and carboxyl groups on ND or TREG on SPION surface, respectively.

Figure 4-1. TGA of NP-PG. (a-b) TGA profiles of ND (a) and SPION (b) before and after PG functionalization, the weight loss (wt%) in the range from 200 to 450 ℃ is indicated in parentheses. (c) PG content (wt%) in NP-PG is derived from the difference of its weight loss (wt%) in the range from 200 to 450 ℃ and the weight of organic component on NP surface.

The resulting ND-PG and SPION-PG were analyzed by TEM and DLS to determine their core sizes (Figure 4-2a – 4-2b for ND-PG and Figure S4-2d – 4-2e for SPION-PG) and hydrodynamic diameters (Figure S4-2c for ND-PG and Figure S4-2f for SPION-PG), respectively. The PG coating was evidenced by the gray area at the periphery of NP core in TEM images (Figure S4-2a for ND-PG and Figure S4-2d for SPION-PG). The thickness of the PG layers was estimated to be 6.9 and 8.6 nm for ND-PG and SPION-PG, respectively, from the difference between the hydrodynamic diameters by DLS and core sizes by TEM (Table 4-1).

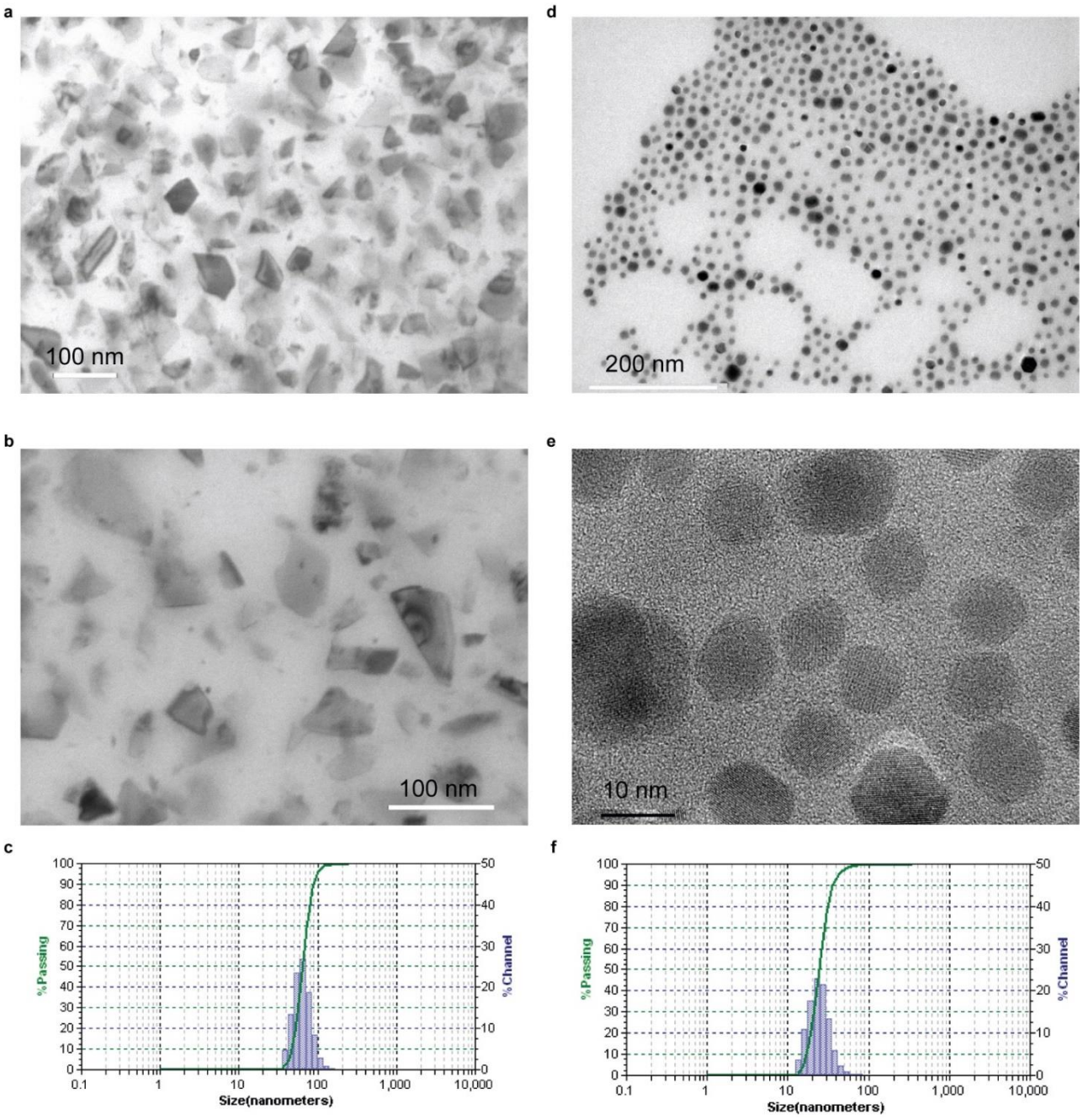

Figure 4-2. TEM and DLS measurements of NP-PG. TEM images of ND-PG (a, b) and SPION-PG (d, e), DLS profiles of ND-PG (c) and SPION-PG (f) in PBS.

Table 4-1. Thickness of PG layer.

NP-PG	NP core size (nm) [a]	Hydrodynamic diameter of NP-PG (nm) [b]	Thickness of PG layer (nm)
ND-PG	50.2±5.1	64.0±1.7	6.9
SPION-PG	7.9±0.9	25.0±1.3	8.6

[a]Mean diameter ± standard deviation determined by particles in TEM images (Figure S2a - 2b for ND-PG and Figure S2d - 2e for SPION-PG).

[b] Hydrodynamic diameter determined from DLS measurement (Figure S2c for ND-PG and Figure S2f for SPION-PG).

In the next step, a number of hydroxyl groups in NP-PG were further converted to carboxyl, sulfate and amino groups through organic transformations (Scheme 4-1, see details in Methods), yielding NP-PG-Y (Y = $COOCH_2CH_2COOH$, OSO_3Na and NH_2, respectively) at low (*l*) and high (*h*) contents of the functional groups. NP-PG-COOH and NP-PG-NH_2 were prepared according to our previous methods [92] with slight modification (routes A and C in Scheme 4-1, respectively). The sulfate groups were introduced in a quantitative manner by choosing appropriate solvent, based on the procedures reported by Türk et al. [93] (route B in Scheme 4-1). The introduction of these functional groups was demonstrated by their zeta-potentials (Figure 4-4d). That is, the carboxylate ($–COO^–$) and

sulfate ($–OSO_3^-$) anions made the potentials more negative (-25 – -30 mV) than those of NP-PG (-5 mV), whereas the potentials turned into positive (5 – 15 mV) in the NP-PG–NH_3^+.

Scheme 4-1. Functionalization of NP-PG with carboxyl, sulfate and amino groups at low (*l*) and high (*h*) contents.

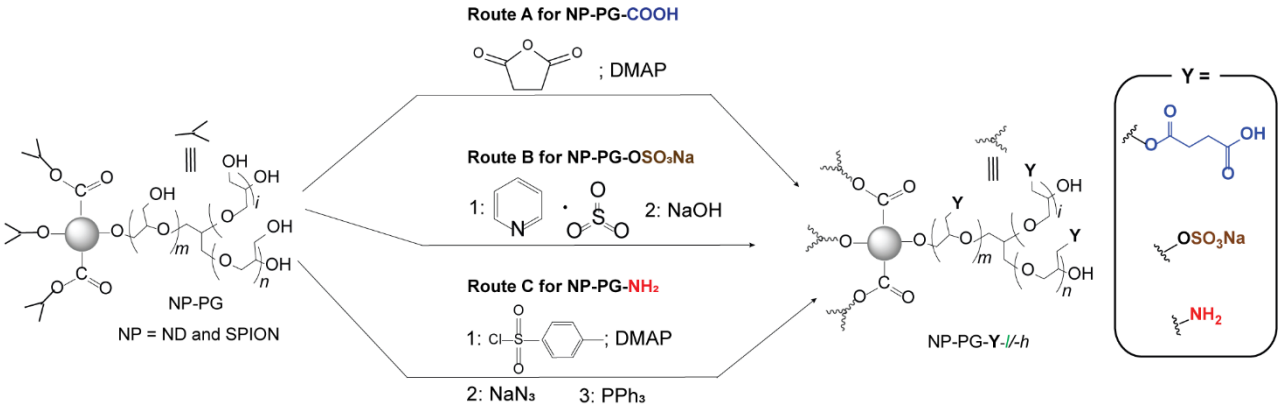

All the NP-PG-Y as well as NP-PG were characterized by IR spectroscopy (Figure 4-3). In order to compare the relative content (*l* and *h*) of the functional groups, the IR spectra were normalized at the absorbance around 1110 cm^{-1} corresponding to C–O–C stretching in PG. As expected, all the absorption bands attributed to C=O stretching at 1730 cm^{-1} in NP-PG-COOH (Figure 4-3a and 4-3b), O–S–O bending at 1200 cm^{-1} in NP-PG-OSO_3Na (Figure 4-3c and 4-3d) and N–H bending in NP-PG-NH_2 at 1670 cm^{-1} (Figure 4-3e and 4-3f) exhibit higher intensities at *h* content than *l* one.

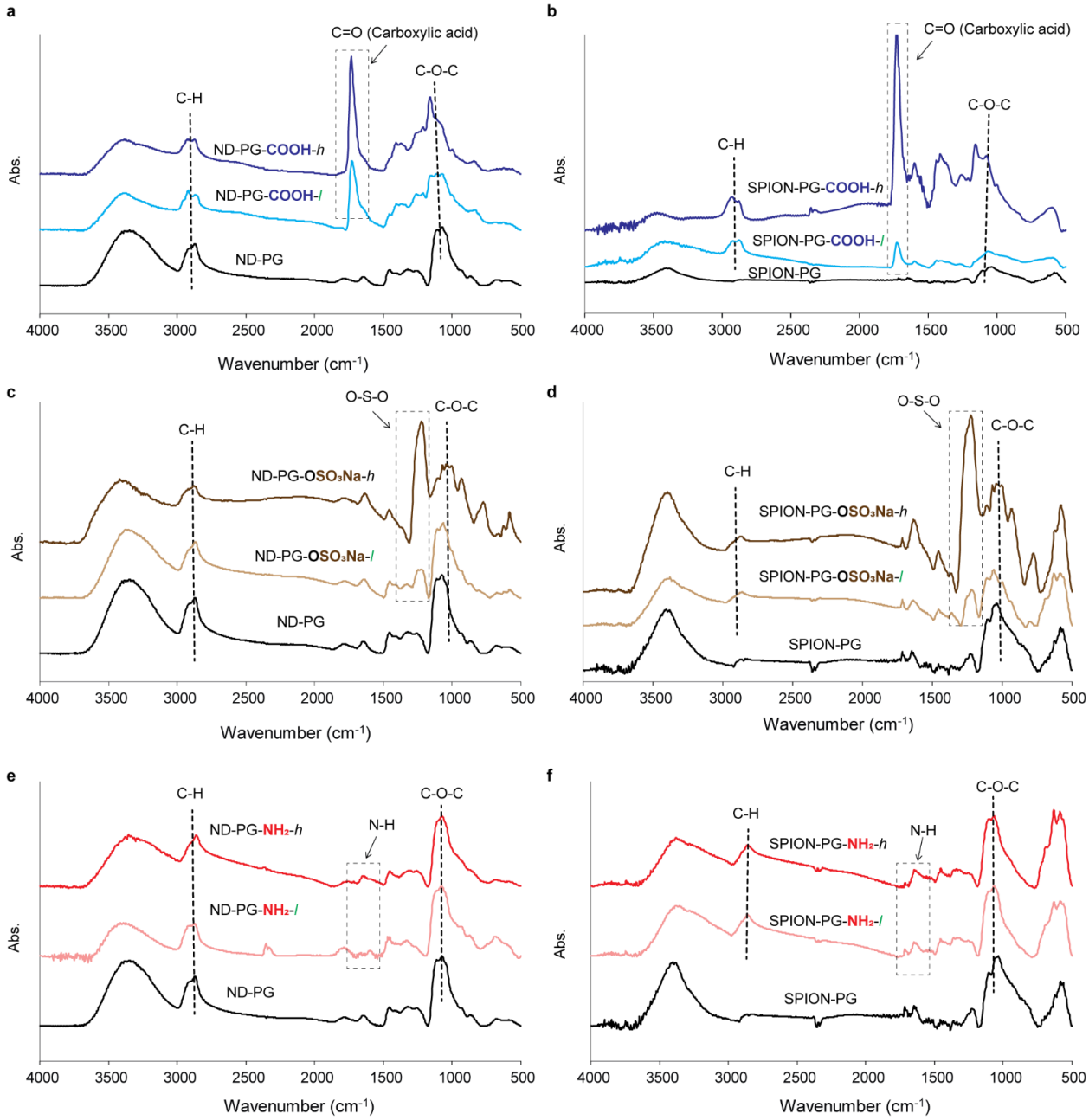

Figure 4-3. IR spectra of NP-PG-COOH (blue traces), NP-PG-OSO_3Na (brown traces) and NP-PG-NH_2 (red traces). (a-b) ND-PG (a) and SPION-PG (b) before and after carboxyl groups functionalization; (c-d) ND-PG (c) and SPION-PG (d) before and after sulfate groups functionalization; (e-f) ND-PG (e) and SPION-PG (f) before and after amino groups functionalization.

The NP-PG-Y were quantitatively analyzed by EA, and/or ICP. The results of EA and ICP are shown in table 4-2 and 4-3, respectively.

Table 4-2. Elemental analysis of NP-PG, NP-PG-COOH, NP-PG-OSO_3Na and NP-PG-NH_2.

NP-PG or	**Element analysis (wt%)**				
NP-PG-Y	**H**	**C**	**O**	**S**	**N**
ND-PG	2.79	77.53	16.99		
ND-PG-COOH-*l*	3.05	73.96	21.71		
ND-PG-COOH-*h*	2.84	71.51	23.34		
ND-PG-OSO_3Na-*l*	2.82	76.50		0.69	
ND-PG-OSO_3Na-*h*	1.76	68.06		4.26	
ND-PG-NH_2-*l*	2.87	79.34			0.35
ND-PG-NH_2-*h*	2.98	79.20			1.32
SPION-PG	2.90	17.41			
SPION-PG-OSO_3Na-*l*				1.54	
SPION-PG-OSO_3Na-*h*				4.55	
SPION-PG-NH_2-*l*	3.19	19.93			0.39
SPION-PG-NH_2-*h*	3.34	16.52			1.57

Table 4-3. ICP analysis of Fe and the calculation of carboxyl group content in SPION-PG-COOH.

SPIONs	Fe (μg) [a]	Content of each component (wt%) [b]			
		SPION	TREG	PG	($C_4H_5O_3$) *n*
SPION-PG-COOH-*l*	21.7 (61.8)	49.7	4.4	39.6	6.3
SPION-PG-COOH-*h*	24.8 (87.5)	40.0	3.6	31.8	24.6

[a] The mass of Fe was calculated based on ICP analysis, and mass of assayed SPION-PG-COOH is indicated in parentheses.

[b] The content of SPION is derived from the mass ratio of Fe_3O_4 in SPION-PG-COOH, and the contents of TREG and PG were calculated based on SPION content and the ratio of SPION and TREG determined from TGA in Figure 4-1b.

For ND-PG-Y, the number of carboxyl, sulfate and amino groups (Table 4-4) was calculated according to eq 4-1, eq 4-2 and our previous paper [92], respectively, based on the results of EA (Table 4-2). The degree of PG polymerization ($C_3H_6O_2$) *n* in ND-PG was calculated to be 1.13×10^6 according to our previous report [62], and the number of C and O in one ND-PG particle was determined to be 1.54×10^7 and 2.53×10^6, respectively. The degree of succinic anhydride polymerization (C4H5O3) *n* or the number of COOH groups in ND-PG-COOH was calculated in a similar way as that of PG polymerization in ND-PG via eq 4-1. $\boldsymbol{W_{O-ND-PG-COOH}}$ and $\boldsymbol{W_{C-ND-PG-COOH}}$ are the weight ratio of oxygen and carbon in ND-PG-COOH, $\boldsymbol{M_O}$ and $\boldsymbol{M_C}$ are the molar mass of oxygen and carbon.

$$\frac{N_{O-ND-PG-COOH}}{N_{C-ND-PG-COOH}} = \frac{N_{O-ND-PG}+3n}{N_{C-ND-PG}+4n} = \frac{W_{O-ND-PG-COOH}/M_O}{W_{C-ND-PG-COOH}/M_C} \qquad \textbf{(eq 4-1)}$$

The number of sulfate groups in ND-PG-OSO_3Na ($\boldsymbol{N_{S-ND-PG-OSO3Na}}$) were calculated from eq 4-2. $\boldsymbol{W_{S-ND-PG-OSO3Na}}$ and $\boldsymbol{W_{C-ND-PG-OSO3Na}}$ are the weight ratio of sulfur and carbon in ND-PG-OSO_3Na, and $\boldsymbol{M_S}$ is the molar mass of sulfur.

$$\frac{N_{S-ND-PG-OSO_3Na}}{N_{C-ND-PG}} = \frac{W_{S-ND-PG-OSO_3Na}/M_S}{W_{C-ND-PG-OSO_3Na}/M_C} \qquad \textbf{(eq 4-2)}$$

For the SPION-PG-Y, the number of carboxyl groups in one SPION-PG-COOH particle (Table 4-4) was calculated based on the results of ICP (Table 4-3) and TGA (Figure 4-1b). The number of sulfate and amino groups was determined by the sulfur and nitrogen contents (wt%) in EA and the weight of SPION core (Table 4-2). The densities of functional groups on NP-PG surface are given by dividing the number of functional groups by the surface area based on their hydrodynamic sizes (Table 4-1). As shown in Table 4-4, the NP-PG-Y-*h* have 4-6 folds larger number of functional groups than their *l* analogues. However, the number and density of functional groups on ND-PG surface were much higher than those on SPION-PG, despite a similar content. This is due to the larger surface area of PG coating and higher degree of PG polymerization on NPs with larger core sizes [84], thus leading to more numbers of functional groups in higher densities.

Table 4-4. The quantitative data of carboxyl, sulfate and amino groups on NP-PG surface at *l* and *h* contents.

NP-PG-Y	Number of functional groups in one NP-PG-Y particle [a]		Density of functional group [b] (nm^{-2})	
	l	***h***	***l***	***h***
ND-PG-COOH	1.2 × 10^5	6.5 × 10^5	8.9	51
SPION-PG-COOH	1.5 × 10^3	5.6 × 10^3	0.75	2.9
ND-PG-OSO$_3$Na	5.1 × 10^4	3.6 × 10^5	4.0	28
SPION-PG-OSO$_3$Na	7.9 × 10^2	2.6 × 10^3	0.40	1.3
ND-PG-NH$_2$	5.7 × 10^4	2.2 × 10^5	4.5	17
SPION-PG-NH$_2$	4.6 × 10^2	1.8 × 10^3	0.23	0.92

[a] Calculation based on the results of EA (Table 4-2), ICP (Table 4-3) and TGA (Figure 4-1).

[b] Calculation based on the assumption of spherical shape of NP-PG with a diameter of 64.0 and 25.0 nm for ND-PG and SPION-PG (Table 4-1), respectively.

4-2-2 Protein corona formation of NP-PG-COOH, NP-PG-OSO_3Na and NP-PG-NH_2

To probe the role of charged functional groups in protein corona formation, the dispersions of NP-PG-COOH, NP-PG-OSO_3Na and NP-PG-NH_2 as well as NP-PG were incubated with 10 and 55% FBS in PBS buffer. The weights of NP-PG-Y were adjusted (Table 4-5, see details in Methods), so that the total number of functional groups were in the same range at *l* and *h* contents. Since the typical p*K*a values of the carboxylic acid, sulfuric acid and ammonium are around 5, -3, and 11, respectively, these functional groups on NP-PG surface are expected to be fully ionized as carboxylate ($–COO^–$), sulfate ($–OSO_3^–$) and ammonium ($–NH_3^+$) in PBS to associate with proteins. After incubation, the NP-protein complexes were pelleted and washed by centrifugation, giving NP-PG-Y with hard corona. The corona proteins were detached by 10% SDS solution and subjected to PAGE, BCA and LC-MS/MS (see details in Methods). The zeta potentials and DLS sizes of NP-PG and NP-PG-Y were also recorded in the presence and absence of FBS proteins.

In the SDS-PAGE of both 10 and 55% FBS coronas (Figure 4-4a and 4-4b, respectively), no noticeable protein band was observed in the lanes of ND-PG and SPION-PG, as we reported previously [84, 92], demonstrating that PG coating effectively prevented protein corona formation onto NP surfaces. Based on this corona-free PG interface, we clearly show that both the species and densities of charged functional groups affect the protein corona formation. For the positively charged ammonium groups, many protein bands are observed in all the lanes of NP-PG-NH_3^+. In contrast,

protein bands appear only in the lane of ND-PG-OSO_3^--*h* among NP-PG-OSO_3^- and NP-PG-COO^-. As marked with red stars, the protein band profile of ND-PG-OSO_3^--*h* is different from those of NP-PG-NH_3^+ (Figure 4-4a and 4-4b), indicating that the protein corona composition on ND-PG-OSO_3^--*h* and NP-PG-NH_3^+ is different. In addition, their difference signifies, as the density of amino group and concentration of FBS increase. The different composition of the corona proteins will be discussed in detail based on LC-MS/MS results.

The BCA results (Figure 4-4c) quantitatively support those of SDS-PAGE. While corona proteins are detected on NP-PG-NH_3^+ and ND-PG-OSO_3^--*h* surfaces in the following order of abundance for both 10 and 55% FBS: NP-PG-NH_3^+-*h* > NP-PG-NH_3^+-*l* > ND-PG-OSO_3^--*h;* there was almost no detectable protein on the surfaces of NP-PG-COO^-. The high affinity of positively charged NP-PG-NH_3^+ to serum proteins is consistent with previous studies, because most of the FBS proteins are negatively charged under physiological conditions which could facilitate their complexation through electrostatic force [19, 69]. On the other hand, relatively low protein affinity of NP-PG-COO^- was revealed in our study. The high affinity of carboxyl groups to serum proteins has been observed so far on bare and functionalized NP surfaces [88, 90]. In some extreme cases, for example, the carboxyl groups even acquired a denser corona layer than ammonium groups on the surface of polystyrene NPs [89, 94]. In this study, we show unambiguously that the carboxylate has no affinity to FBS at the density up to 18 groups / nm^2. This is probably due to the “transparent

background" of PG layer in contrast to the protein attracting backbone in the previous papers. Similarly, the NP-PG-OSO_3^- also exhibited almost no affinity to FBS proteins except ND-PG-OSO_3^--*h* (Figure 4-4a – 4-4c). Actually, a similar phenomenon was reported by Dernedde et al. [95]. They claimed that a certain density of sulfate groups in the dendritic PG was required for high affinity binding to proteins. In our results, the corona proteins were below the detection limit in the case of SPION-PG-OSO_3^--*h* as opposed to ND-PG-OSO_3^--*h* (Figure 4-4a – 4-4c), although SPION-PG-OSO_3^--*h* was controlled to have almost the same total number of sulfate groups as that of ND-PG-OSO_3^--*h* (Table 4-5). Therefore, the higher affinity of ND-PG-OSO_3Na-*h* to FBS proteins is attributable to the higher density of sulfate groups (Table 4-4).

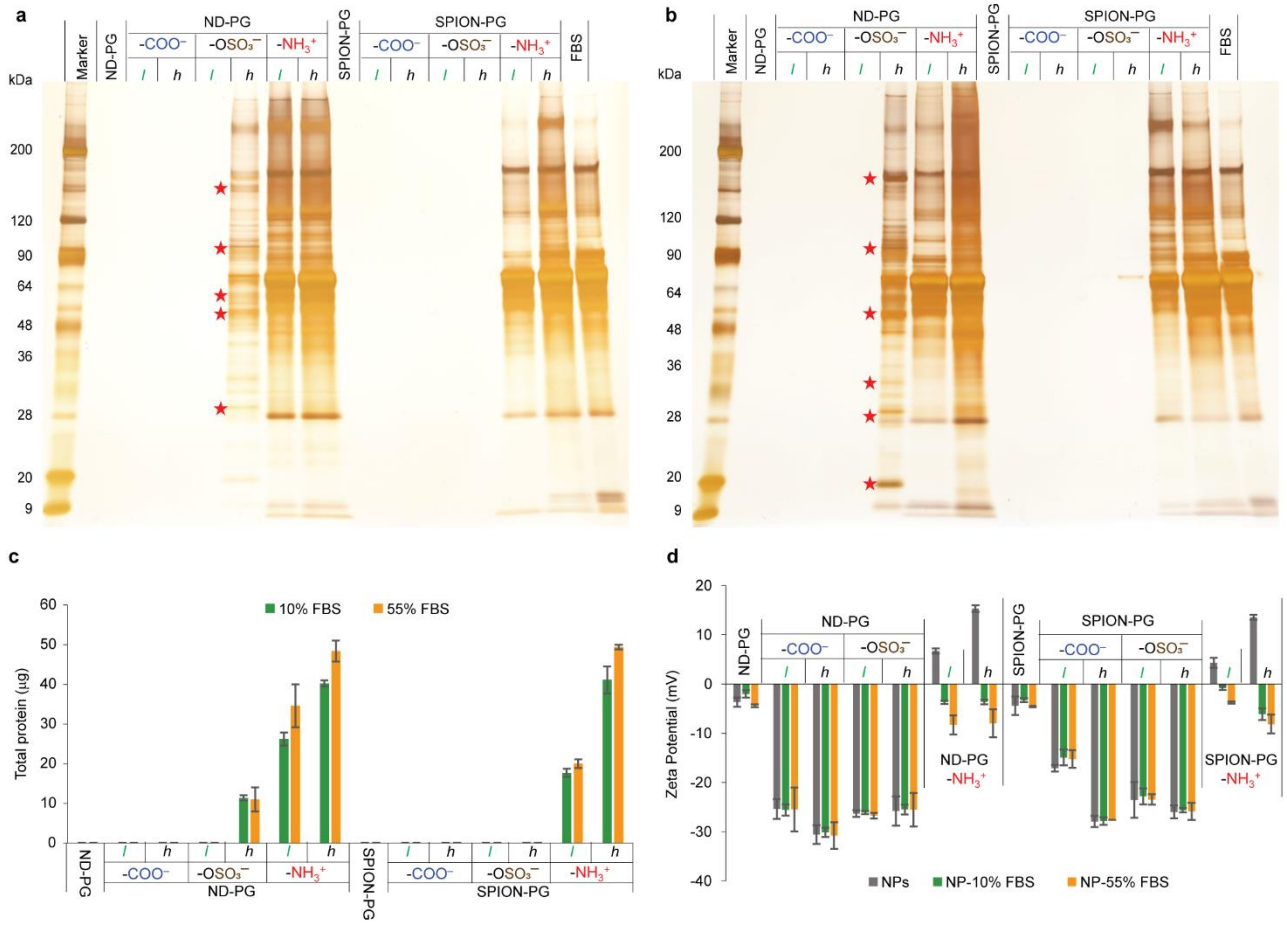

Figure 4-4. Characterization of FBS corona formed on NP-PG, NP-PG-COOH, NP-PG-OSO_3Na and NP-PG-NH_2 surfaces. (a-b) SDS-PAGE images of protein coronas detached from NP-PG, NP-PG-COOH, NP-PG-OSO_3Na and NP-PG-NH_2 after their incubation with 10% (a) or 55% (b) FBS in 2 mL PBS (10 mM). (c) BCA quantification of proteins detached from NPs after their incubation with 10 or 55% FBS, the data are presented as mean value ± standard deviation of three measurements. (d) Zeta potentials of NP-PG, NP-PG-COOH, NP-PG-OSO_3Na and NP-PG-NH_2 after their incubation with 10 or 55 % FBS, the data are presented as mean value ± standard deviation of 20 measurements. In all cases, NP=ND or SPION.

It is well recognized that protein corona alters not only biological identity, but also physical properties of NPs [12]. In our study, the protein corona on the surface of NP-PG-NH_3^+ changed the zeta potentials from positive to negative (Figure 4-4d), and increased the DLS median sizes (Figure 4-5a and 4-5b) and the size distribution (Figure 4-5c – 4-5f). As for ND-PG-OSO_3^--*h*, however, no change was observed in zeta potentials and DLS sizes before and after the protein corona formation (Figure 4-4d and Figure 4-5a). These difference in their physical properties might be due to the difference in the amount and composition of corona proteins as shown in the SDS-PAGE and BCA (Figure 4-4a – 4-4c).

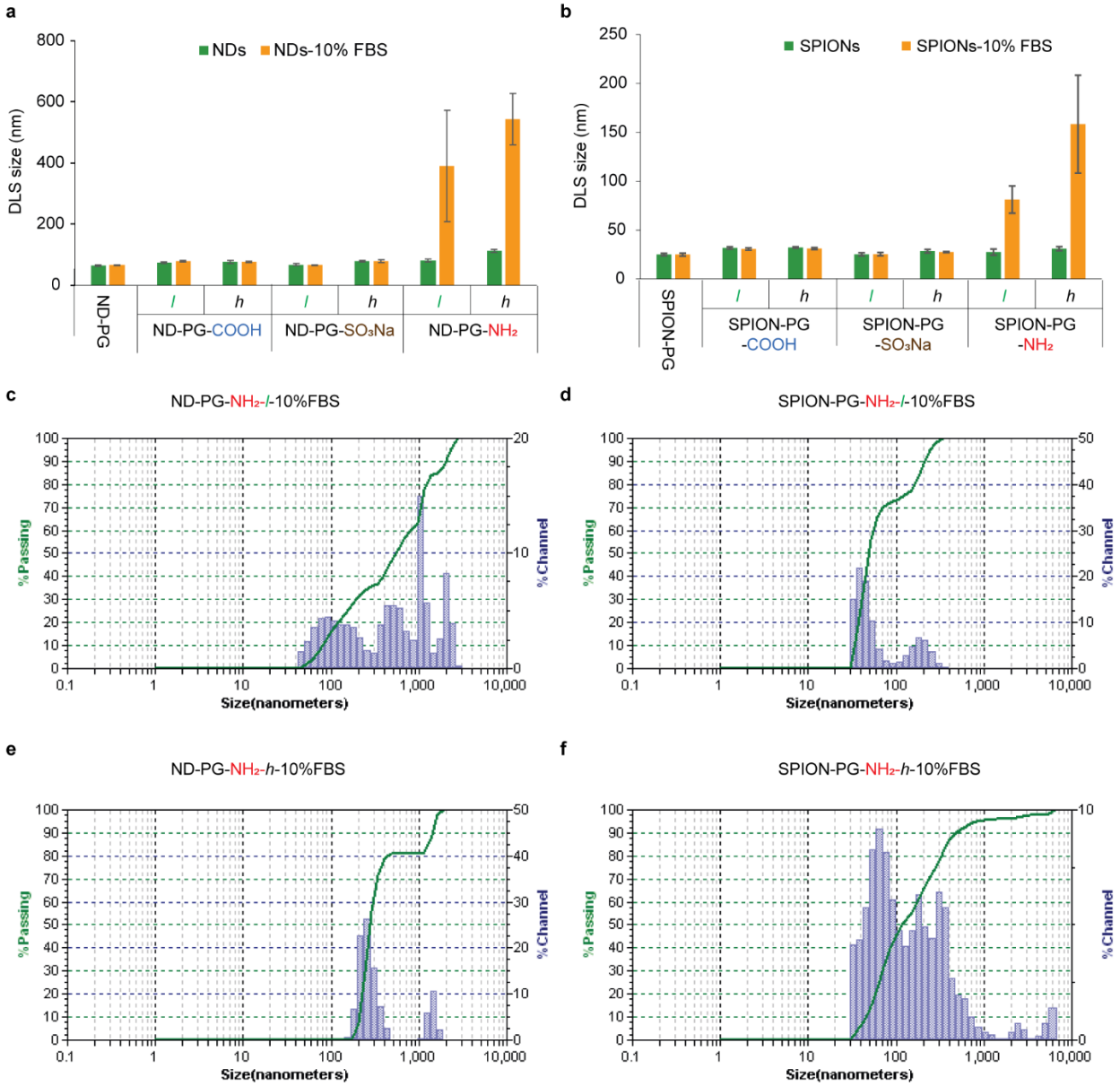

Figure 4-5. DLS measurements of NPs before and after FBS incubation. (a-b) DLS median sizes of NDs (a) and SPIONs (b) before and after FBS incubation. (c-f) DLS profiles of ND-PG-NH_2-*l* (c), SPION-PG-NH_2-*l* (d), ND-PG-NH_2-*h* (e) and SPION-PG-NH_2-*h* (f) after their incubation with FBS.

To investigate the protein corona composition in detail, corona proteins from10% FBS on the surface of ND-PG-OSO_3^--*h*, ND-PG-NH_3^+-*l* and ND-PG-NH_3^+-*h* together with FBS proteins were analyzed by LC-MS/MS. A full list of the identified proteins with high confidence (unique peptides ≥ 2) and their relative raw abundance are shown in AppendixⅣ. The total relative raw abundance of the corona proteins detected by LC-MS/MS increased in the order of ND-PG-OSO_3^--*h*, ND-PG-NH_3^+-*l* and ND-PG-NH_3^+-*h* (Figure 4-6) in a similar manner to the protein amounts quantified by BCA (Figure 4-4c).

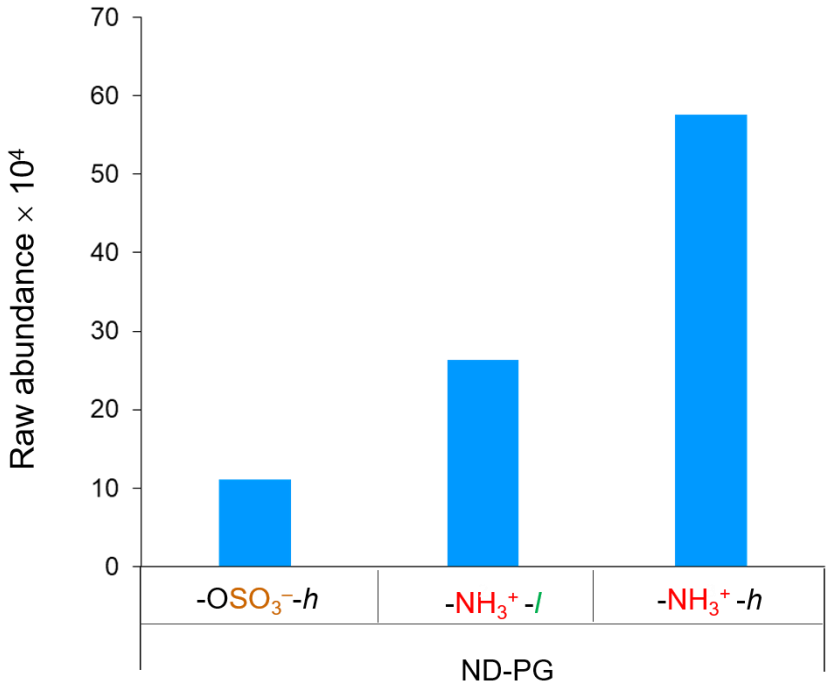

Figure 4-6. Raw abundances of proteins detected on the surface of ND-PG-OSO_3^--*h*, ND-PG-NH_3^+-*l* and ND-PG-NH_3^+-*h*.

As illustrated in Figure 4-7a, the MW distribution of FBS proteins was altered after their absorption onto the surfaces of ND-PG-OSO_3^--*h* and ND-PG-NH_3^+. Moreover, the MW distribution of corona proteins on ND-PG-OSO_3^--*h* is different from those on ND-PG-NH_3^+. For example, proteins of 50-60, 80-90, 120-150, and >200 kDa were enriched 4-30 folds in their contents on the surface of ND-PG-OSO_3^--*h* as compared to those of FBS. In addition, their contents are much higher than those of ND-PG-NH_3^+. On the other hand, proteins with 30-40 and 90-120 kDa are more abundant on ND-PG-NH_3^+ than ND-PG-OSO_3^--*h*.

The different composition of the corona proteins is also verified by the p*I* distribution (Figure 4-7b) and their relative abundance on ND-PG-OSO_3^--*h* and ND-PG-NH_3^+ as compared to the ones in FBS (Figure 4-7c). As shown in Figure 4-7b, the FBS proteins in the p*I* range of 4-8 and 8-10, which exhibit negative and positive charge under physiological conditions, respectively, are determined to be 99.45% and 0.55% in their abundance. The proteins with p*I* = 8-10 were enriched from 0.55% in FBS to 9.78% on the surface of ND-PG-OSO_3^--*h*, but remained to be minor components on ND-PG-NH_3^+ (0.76% and 0.71% for ND-PG -NH_3^+-*l* and ND-PG-NH_3^+-*h*, respectively). Similarly, the proteins with p*I* = 4-5 increased their content from 0.12% in FBS to 2.42% on ND-PG-OSO_3^--*h*, but exhibited almost no change on ND-PG-NH_3^+. In contrast, the major proteins with p*I* = 5-8 decreased their contents from 99.4% to 87.8% on ND-PG-OSO_3^--*h*, but remained to be 98.9% for both ND-PG-NH_3^+-*l* and ND-PG-NH_3^+-*h*.

These variations are further demonstrated by the raw abundance of top 5 FBS proteins (log 10 of the signal intensity) from each p*I* range as shown in Figure 4-7c. The basic proteins (p*I* = 8-10) including plasma serine protease inhibitor, beta-2-glycoprotein 1 and cationic trypsin enriched their contents on ND-PG-OSO_3^--*h* (1.9-3.6) as compared to the ones in FBS (1.3-2.6). Moreover, the abundance of these basic proteins is much higher on ND-PG-OSO_3^--*h* than those on ND-PG-NH_3^+ (1.0-3.1). In contrast, the abundance of acidic proteins (p*I*=4-8) such as albumin, alpha-2-HS-glycoprotein and inter-alpha-trypsin inhibitor heavy chain proteins on ND-PG-NH_3^+ (1.8-5.1) are higher than those on ND-PG-OSO_3^--*h* (1.0-4.4). The enrichment of basic proteins (p*I*=8-10) and acidic proteins (p*I*=4-8) on the surface of negatively charged ND-PG-OSO_3^--*h* and positively charged ND-PG-NH_3^+, respectively, is in agreement with our previous study [92], implying that charged functional groups prefer to interact with proteins of opposite charge. However, the higher abundance of Thrombospondin-1 (TSP-1, p*I*=4.7) on ND-PG-OSO_3^--*h* (3.4) as compared to those on ND-PG-NH_3^+ (2.6-2.8) is unexpected, which indicated that other than the bulk isoelectric point of proteins, the surface charge of amino acid residues at specific regions may account for protein corona formation [96]. TSP-1 is a calcium-binding protein that participates in cellular responses to extracellular proteases and growth factors [97]. The N-terminal domain of human TSP-1 was identified to be rich in basic residues including Arg29, Arg42, and Arg77, which can specifically associate with the sulfate groups in heparin [98]. This may also be the case of high affinity of bovine

TSP-1 to the sulfate groups in ND-PG-OSO_3^--*h*, since dendritic polyglycerol sulfate has already been demonstrated as an excellent heparin analogue [99].

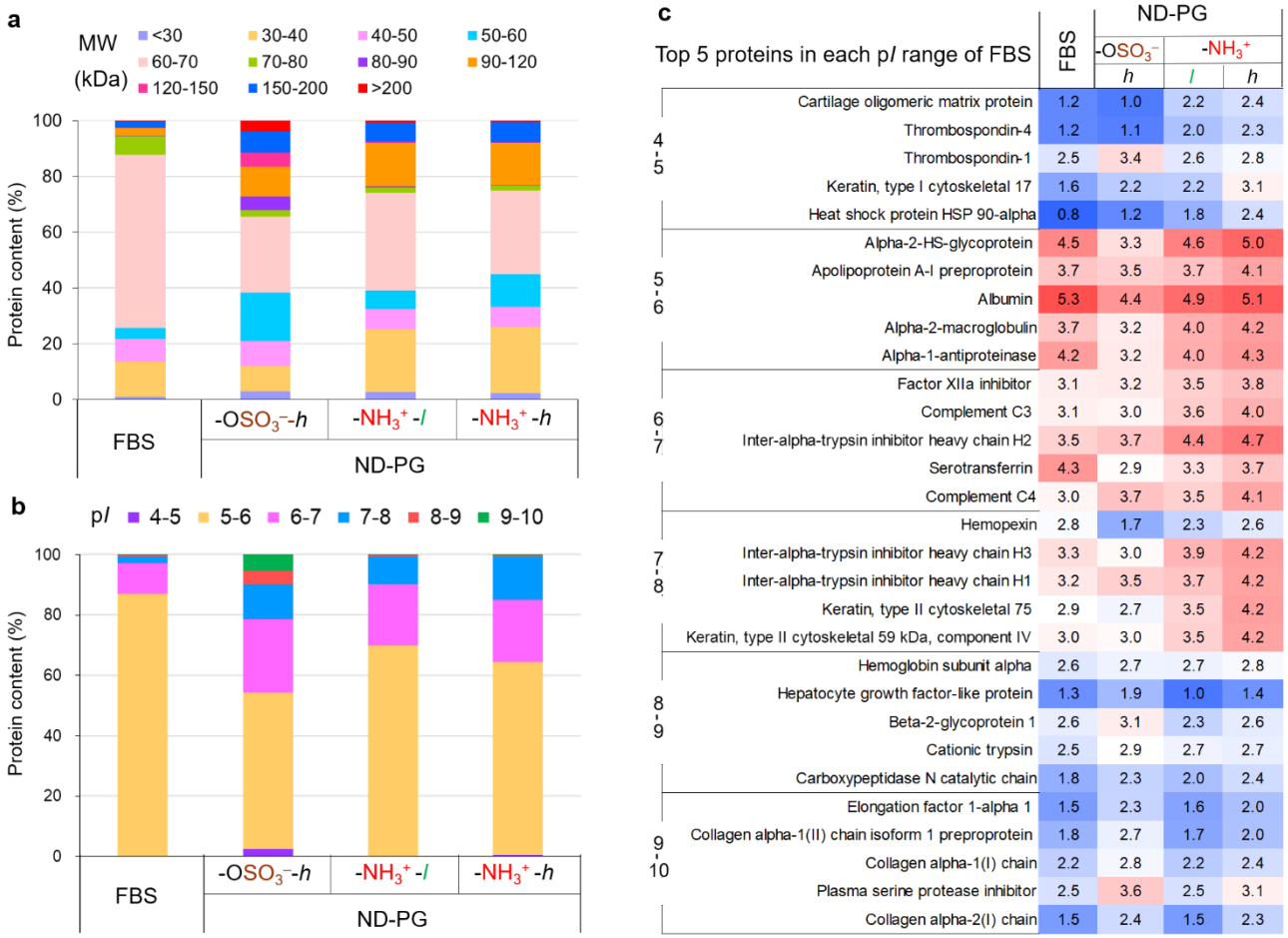

Figure 4-7. Identification and semi-quantification of 10% FBS protein corona detached from ND-PG-OSO_3^--*h*, ND-PG-NH_3^+-*l* and ND-PG-NH_3^+-*h*, as well as FBS proteins by LC-MS/MS. (a-b) Identified proteins are classified according to their MW (a) and p*I* (b). The content of identified proteins (%) is calculated from their relative abundance shown in AppendixⅣ. (c) Heat map representation of the raw abundance of top 5 proteins in FBS from the p*I* ranges of 4-5, 5-6, 6-7, 7-8, 8-9, and 9-10, respectively. The log10 values of the protein abundance are shown in colors (blue - red) and numerical values (0.8 - 5.3).

4-2-3 Cellular uptake of NP-PG-COOH, NP-PG-OSO_3Na and NP-PG-NH_2 in the presence of FBS proteins

After clarifying the protein corona profiles, we investigated the cellular uptake of NP-PG-Y in the presence of FBS proteins. The dispersions of NP-PG-COOH, NP-PG-OSO_3Na, NP-PG-NH_2 and NP-PG were applied to human cervix epithelium HeLa cells and human lung epithelial carcinoma A549 cells in the culture medium containing 10% FBS. After 12 h incubation, the cellular uptake of NDs and SPIONs were measured by TEM and ICP, respectively.

As shown in TEM images (Figure 4-8, Appendix Figure 2-1 and Appendix Figure 2-2), no ND particles were found in the ND-PG treated HeLa (Figure 4-8b, Appendix Figure 2-1b) and A549 (Appendix Figure 2-2b) cells, which exhibited similar morphologies to those of control cells (Figure 4-8a, Appendix Figure 2-1a and Appendix Figure 2-2a). This gives the conclusions consistent with our previous studies that corona-free PG grafting shields NPs from non-specific uptake almost completely [28, 62, 84]. Based on this transparent NP-PG background, we found that the cellular uptake of ND-PG-Y is correlated with their affinity to serum proteins. That is, the ND-PG-OSO_3^--*h* and ND-PG-NH_3^+ with higher protein affinities (Figure 4-4 and 4-7) showed a substantial number of internalized NDs (Figure 4-8f-h, Appendix Figure 2-1f-h and Appendix Figure 2-2f-h). In contrast, ND-PG-COO^- and ND-PG-OSO_3^--*l* (Figure 4-4) with almost no protein affinities induced negligible or no uptake (Figure 4-8c-e, Appendix Figure 2-1c-e and Appendix Figure 2-2c-e). A similar uptake trend was

observed in the case of SPION-PG-Y (Figure 4-9).

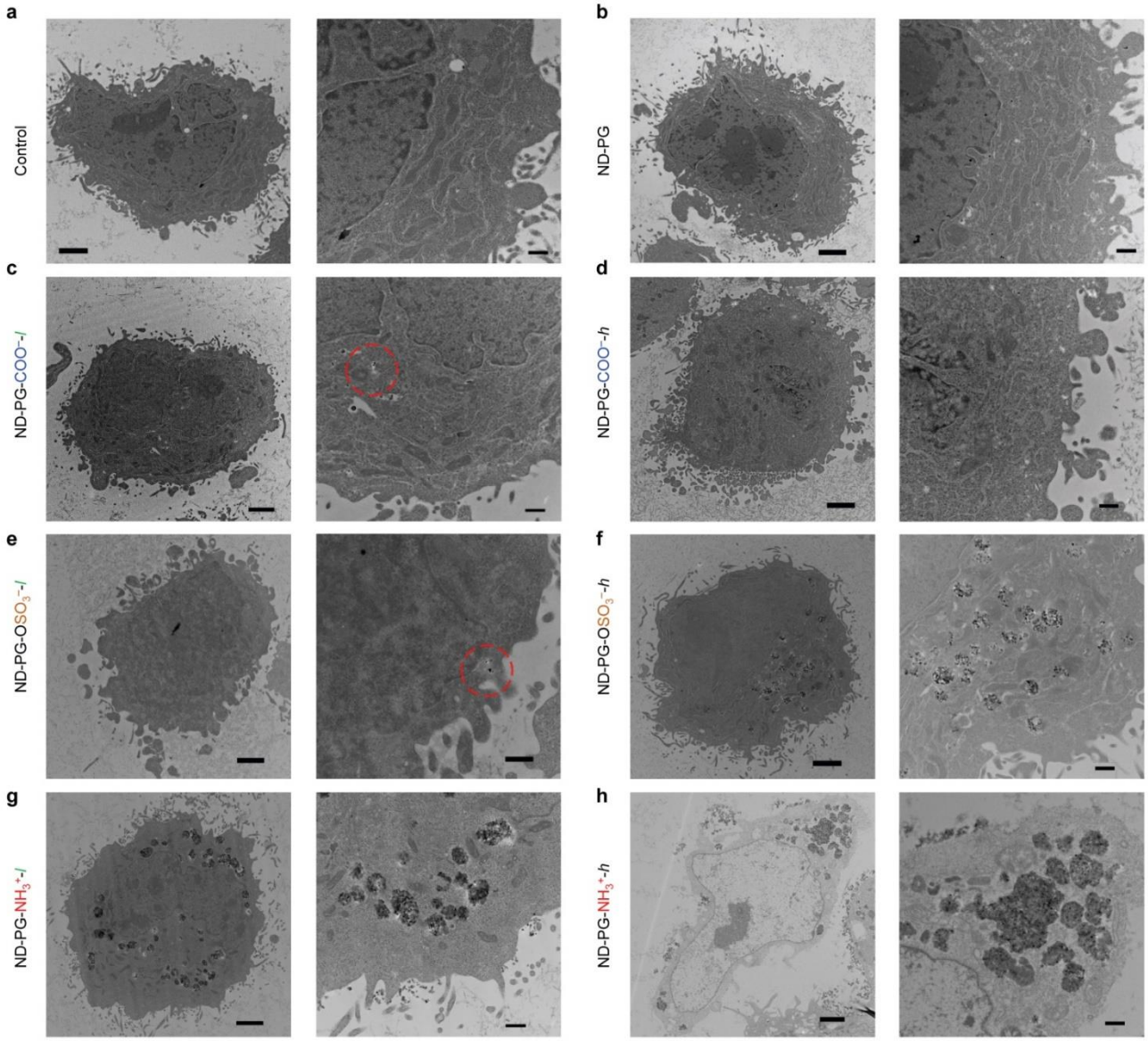

Figure 4-8. TEM images of HeLa cells (a) and after their incubation with ND-PG (b), ND-PG-COOH (c-d), ND-PG-OSO_3Na (e-f) and ND-PG-NH_2 (g-h) in 10% FBS. Pairs of the images are corresponding to low magnification (left, scale bar: 2 μm) and high magnification (right, scale bar: 500 nm) of the same cell. More images of NDs uptake by HeLa and A549 cells are shown in Appendix Figure 2-1 and 2-2, respectively.

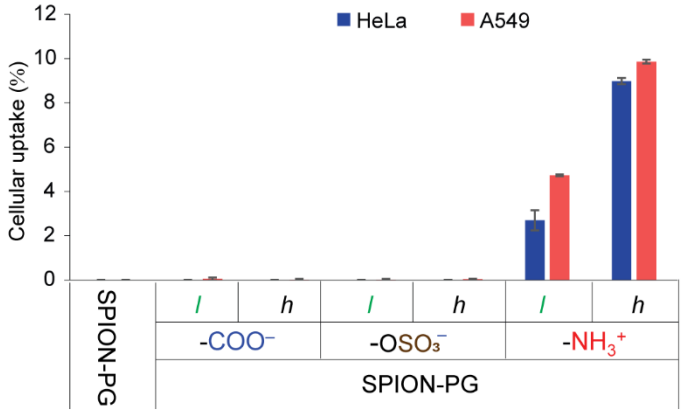

Figure 4-9. The uptake of SPION-PG-Y by HeLa and A549 cells in the presence of FBS.

In the TEM images of cells treated by ND-PG-COO^--*l* (Figure 4-8c, Appendix Figure 2-1c and Appendix Figure 2-2c) and ND-PG-OSO_3^--*l* (Figure 4-8e, Appendix Figure 2-1e and Appendix Figure 2-2e) in the presence of FBS, a relatively small amount of NDs was detected as indicated by red dash circles in these images. In serum-free culture medium, however, there were no and fewer dots in the cells treated by ND-PG-COO^--*l* (Appendix Figure 2-3a) and ND-PG-OSO_3^--*l* (Appendix Figure 2-3c), respectively. Therefore, the small amount of ND-PG-COO^--*l* and ND-PG-OSO_3^--*l* uptake in the presence of FBS might be facilitated by the soft protein coronas [100], which are hard to access via current analytical approaches [101]. As for the cells treated by ND-PG-COO^--*h*, no NDs were observed in the TEM images with (Figure 4-8d, Appendix Figure 2-1d and Appendix Figure 2-2d) and without FBS (Appendix Figure 2-3b). This indicates that the effect of soft corona might be suppressed by high density of carboxyl groups. Although the substantial cellular uptake of carboxylate functionalized NPs

has been reported in the literatures [88, 90], we clearly demonstrated that dense coverage with carboxylate groups did not induce cell uptake. The carboxylate groups on NP surface are not only serving as a charge modulation group, but also acting as a key reactive group for further conjugating with target moieties, drug molecules and other functional groups in nanomedicine. The non-specific uptake of NP-PG-COO^--*h* (Figure 4-8d, Appendix Figure 2-1d and Appendix Figure 2-2d) coupled with its protein-resistance property (Figure 4-4) suggests the potential of NPs with carboxylate anions in biomedical applications in terms of safety and efficiency.

The effect of protein corona on the uptake of charged NPs becomes more distinct, as the amount of adsorbed protein increased. While the treatment of ND-PG-OSO_3^--*h* leads to an extensive uptake (Figure 4-8f, Appendix Figure 2-1f and Appendix Figure 2-2f), more amount of NDs were found in the cells exposed to ND-PG-NH_3^+ (Figure 4-8g-h, Appendix Figure 2-1g-h and Appendix Figure 2-2g-h). The significant uptake of ND-PG-NH_3^+, despite their negative zeta potentials after the protein corona formation (Figure 4-4d), firmly indicated that the surface of the corona layer rather than that of the pristine nanoparticle was the decisive factor for NP uptake. The higher magnification TEM images showed that a large number of NDs are clustered in cellular vesicles in ND-PG-NH_3^+ treated cells (Figure 4-8g-h, Appendix Figure 2-1g-h and Appendix Figure 2-2g-h), while the NDs in cells exposed to ND-PG-OSO_3^--*h* is less aggregated and a small portion of NDs seem to be free in the cytosol (Figure 4-8f, Appendix Figure 2-1f and Appendix Figure 2-2f). This implies a different uptake mechanism of

ND-PG-OSO_3^--*h* and ND-PG-NH_3^+, which may arise from distinct protein corona profiles formed on their surfaces [102].

4-2-4 Effect of FBS corona on the uptake mechanism of sulfate and amino group functionalization

In order to investigate the uptake mechanism, fluorescent nanodiamonds (fNDs, Figure 4-10a) with 54.5 nm in diameter (Figure 4-10b) were used as a starting material to prepare fND-PG-OSO_3Na and fND-PG-NH_2 in procedures similar to those of NP-PG-OSO_3Na-*h* and NP-PG-NH_2-*l*, respectively (Scheme 4-1). The fND was grafted with 38.3 wt% of PG as shown in the TGA of fND-PG in Figure 4-10c. In IR spectra of fND-PG-Y (Figure 4-10d), the absorbance of O−S−O in fND-PG-OSO_3Na and N−H in fND-PG-NH_2 are comparable to those of ND-PG-OSO_3Na-*h* (Figure 4-3c) and ND-PG-NH_2 (Figure 4-3e), respectively.

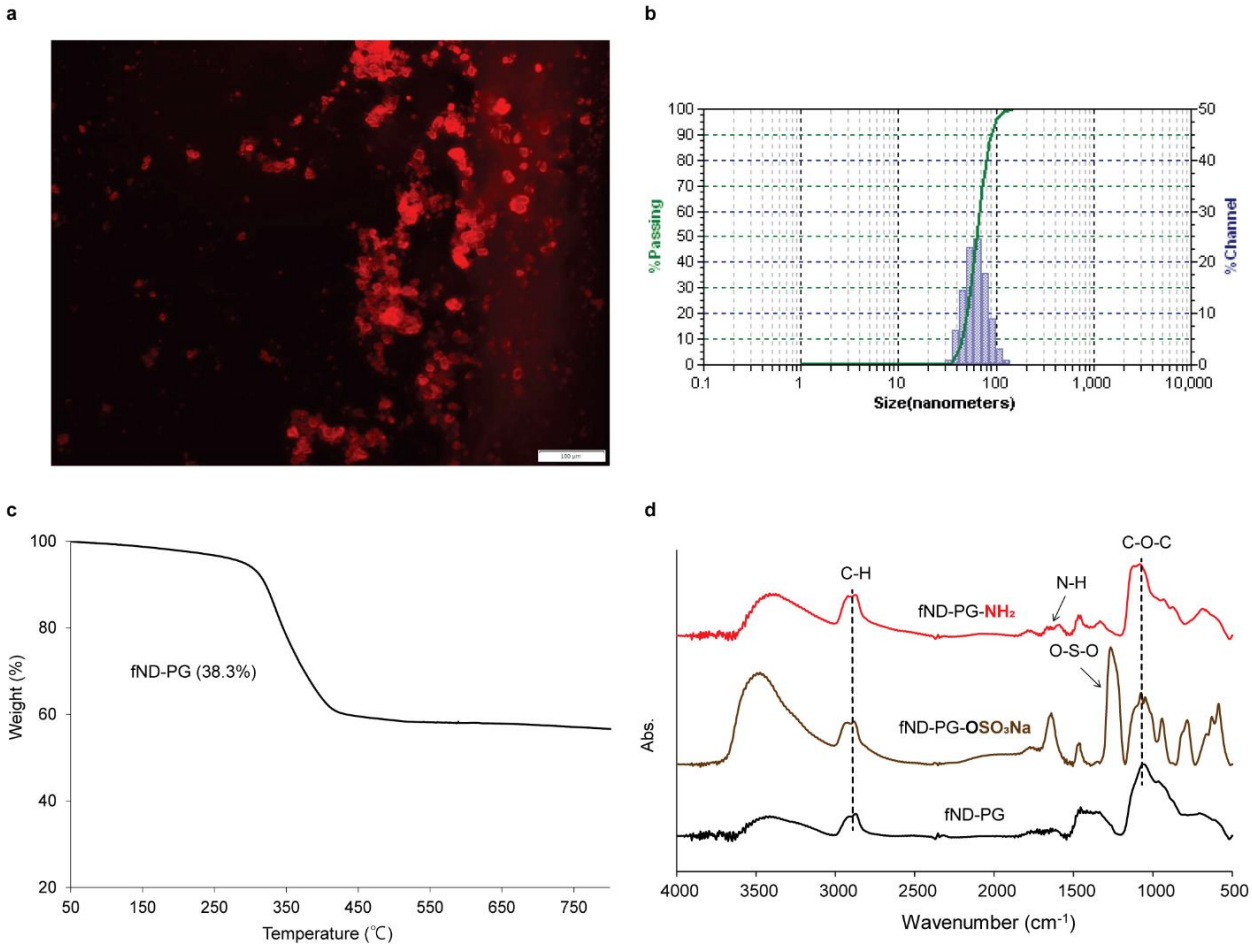

Figure 4-10. Characterization of fNDs. (a-b) microscopy image (a) and DLS size distribution (b) of fND, the scale bar in (a) is 100 μm. (c) TGA weight loss curve of fND-PG. (d) IR spectra of fND-PG, fND-PG-OSO_3Na, and fND-PG-NH_2.

The corona protein compositions of fND-PG-OSO_3^- and fND-PG-NH_3^+ in 10% FBS (Figure 4-11a for SDS-PAGE, Figure 4-11c for MW and 4-11d for p*I*) were similar to those of ND-PG-OSO_3^--*h* and ND-PG-NH_3^+-*l* (Figure 4-4a and Figure 4-7). The raw abundance of top 10 proteins associated with fND-PG-OSO_3^- and fND-PG-NH_3^+ are shown in Figure 4-11b.

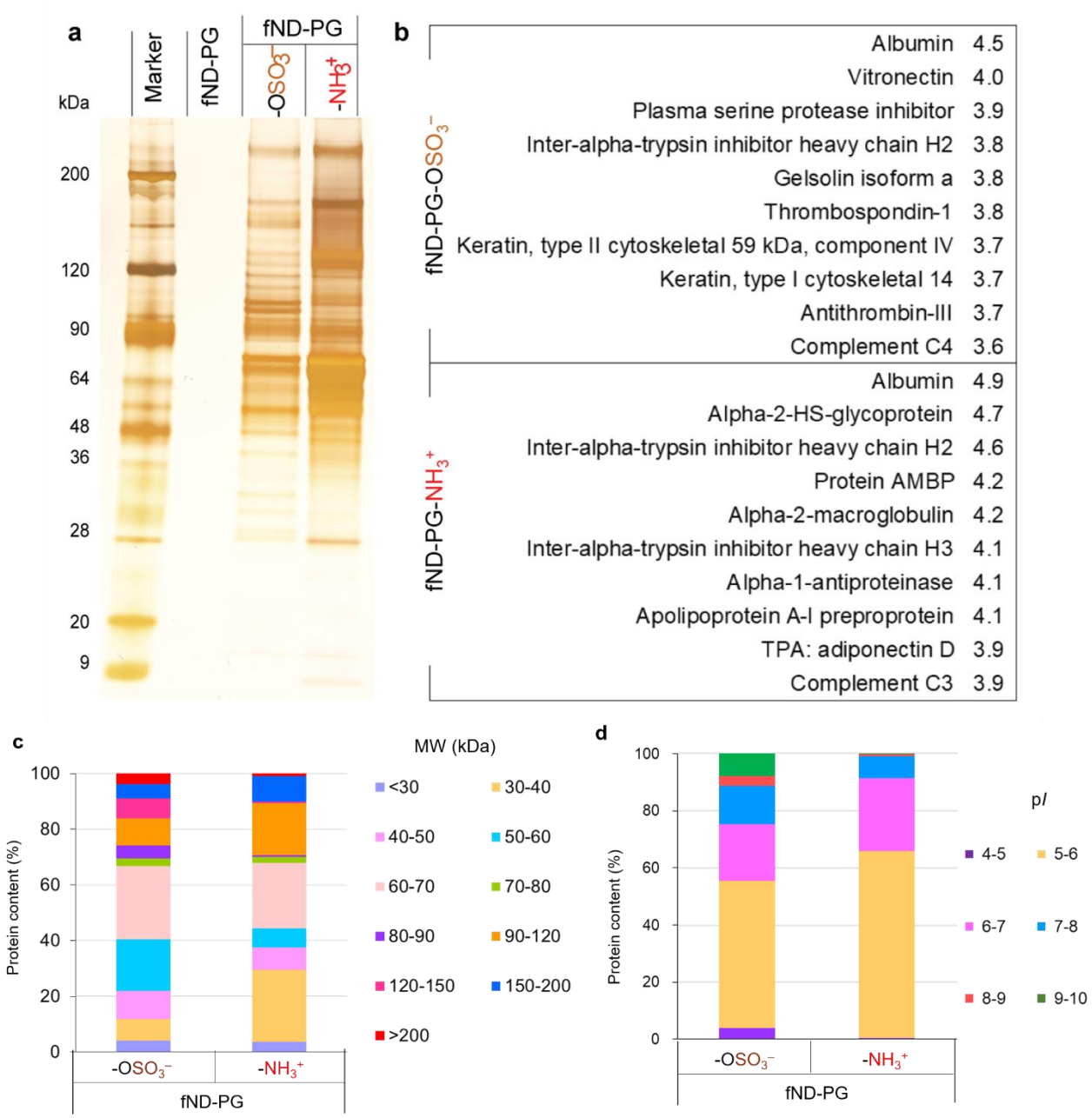

Figure 4-11. FBS coronas of fND-PG-OSO_3^- and fND-PG-NH_3^+. (a) SDS-PAGE image and (b) top10 proteins identified on the surfaces of fND-PG-OSO_3^- and fND-PG-NH_3^+, respectively. (c) MW and (d) p*I* distribution of proteins identified on the surfaces of fND-PG-OSO_3^- and fND-PG-NH_3^+, respectively.

Firstly, we examined the cellular uptake of fND-PG-OSO_3^- and fND-PG-NH_3^+ in the presence and absence of FBS corona (FBS corona (+) and FBS corona (–), respectively). As for the FBS corona (+), two kinds of protein corona formation conditions were investigated. Cells were exposed to 1) fND-PG-Y in the culture medium including 10% FBS (*in situ*), and 2) fND-PG-Y coated with 10% FBS corona in a serum-free culture medium (precoat). In the case of 2), 10% FBS coating of fND-PG-Y was prepared in a manner similar to that of the protein corona formation mentioned above. On the other hand, for FBS corona (–), cells were incubated with fND-PG-Y in a serum-free culture medium. The fluorescence intensity (FI) of fND-PG-Y treated cells was determined by fluorescence-activated cell sorting (FACS) analysis. The results for HeLa and A549 cells were shown in Figure 4-12, after subtracting the background FI from control cells treated by PBS only. As for fND-PG-OSO_3^- treated HeLa cells (Figure 4-12a), the presence of FBS proteins in the cell culture medium (*in situ*) and on the surface of the nanomaterial (precoat) reduced the relative abundance of fNDs in HeLa cells to 40% and 59%, respectively, as compared to that of FBS corona (–). A similar trend was observed in A549 cells (Figure 4-12b). These results are in agreement with previous studies reporting that the protein corona lowered the uptake efficiency by weakening the interaction of NPs with the cell membrane [17, 103]. On the other hand, the relative abundance of fNDs in HeLa cells was enhanced at fND-PG-NH_3^+ FBS corona (+) *in situ* and precoat by 3.2 and 1.6 folds (Figure 4-12a), respectively, as compared to that of FBS (–). Similar trend was observed in the case of SPION-PG-NH_3^+ treated HeLa cells (Figure

4-12c). In A549 cells, FBS corona (+) *in situ* enhanced the uptake of fND-PG-NH_3^+ by 2.5 folds as compared to that of FBS (–), while the FBS corona (+) precoat showed no influence on uptake (Figure 4-12b). These results supporting that the FBS corona on NP-PG-NH_3^+ surface especially the *in situ* one accelerates their uptake. The protein corona is known to retard the cellular uptake of NPs; particularly, the FBS protein corona has been demonstrated to reduce the uptake of ammonium functionalized polymeric NPs [104]. In this study, we make clear that the cellular uptake efficiency of NP-PG-NH_3^+ can be enhanced by the absorbed proteins. As the major proteins on fND-PG-NH_3^+ surface including the inter-alpha trypsin inhibitor heavy chains H2 and H3, and alpha-2-macroglobulin are belonging to hyaluronan binding protein family, they may act as 'bridges' between fND-PG-NH_3^+ and the hyaluronan on cell surface to facilitate uptake [34].

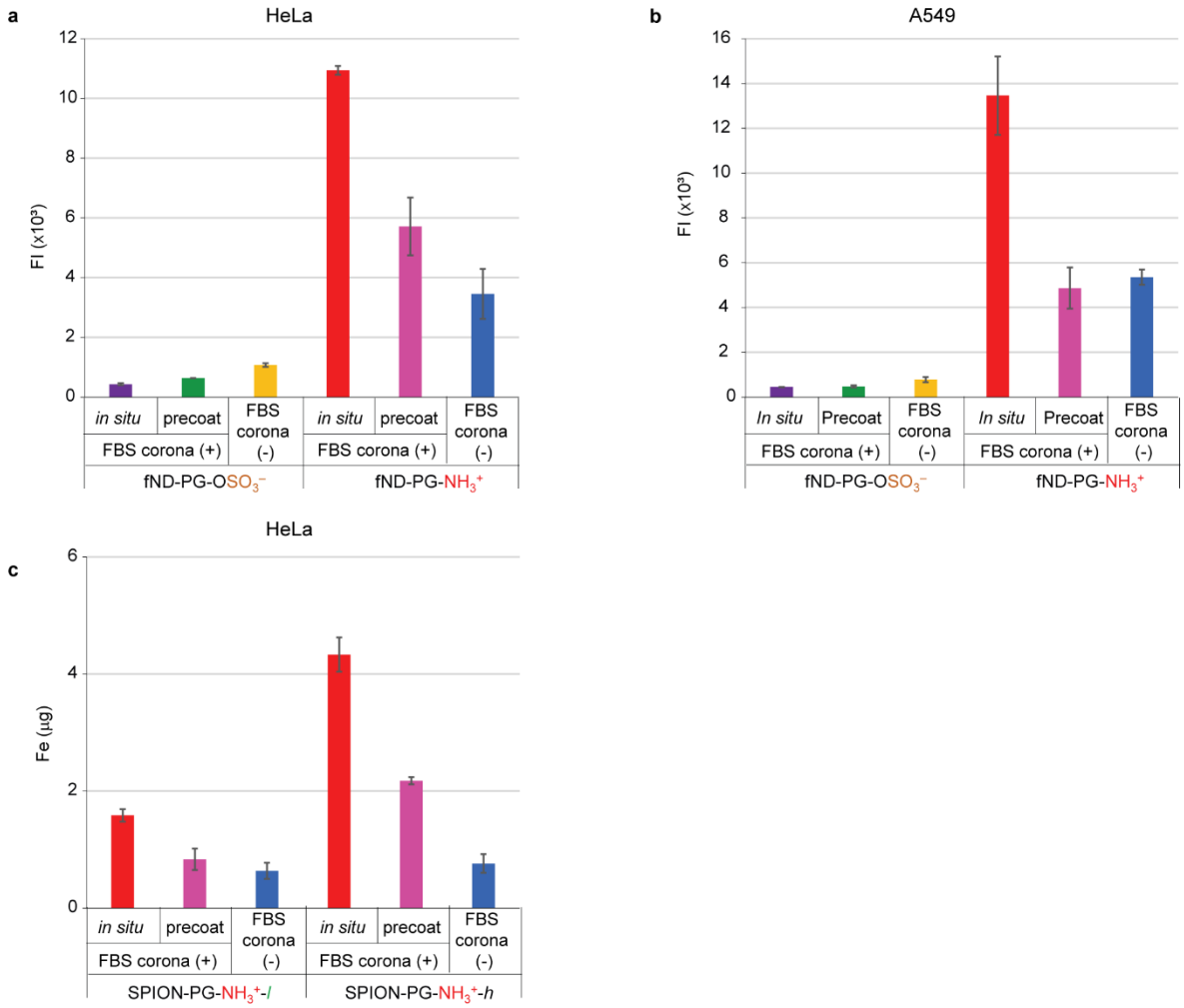

Figure 4-12. Effects of FBS coronas on cell uptake. (a) HeLa and (b) A549 cell uptake of fND-PG-OSO_3^- and fND-PG-NH_3^+ in the presence and absence of FBS corona. (c) HeLa cell uptake of SPION-PG-NH_3^+ in the presence and absence of FBS corona.

Secondly, we investigated how the protein corona alters the uptake mechanisms of fND-PG-OSO_3^- and fND-PG-NH_3^+. Here, we adopted the *in situ* condition, because the *in situ* induced more decrement and increment for fND-PG-OSO_3^- and fND-PG-NH_3^+, respectively, than precoat as shown

in Figure 4-12. The cells were subjected to low temperature incubation (4 °C) to evaluate the effect of receptor-mediated internalization [104], and treated by pharmacological inhibitors such as cytochalasin D (CytoD), chlorpromazine hydrochloride (CPZ) and genistein (GEN) for macropinocytosis, clathrin- and caveolae-mediated endocytosis [105], respectively. The FI (%) in Figure 4-13a – 4-13d is defined to be the FI under inhibition conditions divided by the FI observed without inhibition. As mentioned above, FI from the background was subtracted in both of these FI before calculating FI (%).

As for the HeLa cell uptake of fND-PG-OSO_3^- (Figure 4-13a), the actual FI of fND-PG-OSO_3^- *in situ* and FBS (–) at 4°C were almost similar to the background, making these FI (%) around 0%. Since the low temperature is known to suppress the activity of cell membrane receptors to hinder the endocytic pathway, the significant decrease in the uptake of fND-PG-OSO_3^- at 4°C indicates that fND-PG-OSO_3^- with and without protein corona were internalized into cells mainly via receptor-mediated pathway. This is consistent with previous study about sulfate group functionalized graphene nanosheets [106]. Upon the treatments of CytoD and CPZ, more amount of fND-PG-OSO_3^- were taken up under FBS corona (+) *in situ* than FBS corona (–), meaning that macropinocytosis and clathrin-mediated pathways are less inhibited in the presence of FBS corona. These results coupled with the lower uptake of fND-PG-OSO_3^- in the presence of FBS (Figure 4-12a) imply that FBS corona suppressed the uptake of fND-PG-OSO_3^- mainly by blocking the macropinocytosis and clathrin-

mediated entry routes. On the other hand, the slightly lower uptake of fND-PG-OSO_3^- FBS corona (+) *in situ* as compared to fND-PG-OSO_3^- FBS (–) after the treatment of GEN, suggesting that the FBS corona on the surface of fND-PG-OSO_3^- may facilitate their internalization through caveolae-mediated endocytosis.

As opposed to the results in fND-PG-OSO_3^-, the fND-PG-NH_3^+ FBS (–) had higher FI (%) at 4°C (62%, Figure 4-13b), indicating that most of fND-PG-NH_3^+ enter HeLa cells through receptor-independent pathway or passive defusing mechanism. However, the FI (%) of fND-PG-NH_3^+ at 4°C was decreased to 23% in the presence of protein corona, implying that higher ratio of fND-PG-NH_3^+ FBS corona (+) *in situ* was internalized through receptor-mediated pathway. These results together with the enhanced uptake of fND-PG-NH_3^+ in the presence of FBS (Figure 4-12a) indicate that FBS corona promoted the uptake of fND-PG-NH_3^+ via energy-dependent pathway. In detail, the lower FI (%) of fND-PG-NH_3^+ FBS corona (+) *in situ* after the treatments of CytoD and GEN, as compared to those of fND-PG-NH_3^+ FBS (–), suggests that the FBS corona increased the uptake of fND-PG-NH_3^+ mainly through the macropinocytosis and caveolae-mediated internalization. The enhanced uptake of fND-PG-NH_3^+ FBS corona (+) *in situ* by macropinocytosis pathway might be due to the aggregation of fND-PG-NH_3^+ after FBS corona formation (Figure 4-14), since this pathway favors the larger size NPs [30]. The enhanced uptake of caveolin-mediated pathways might be mediated by albumin which has a high abundance on the surface of fND-PG-NH_3^+ (Figure 4-11b), since it is reported that the

albumin can bind to the glycoprotein 60 in caveolae of endothelial cells to facilitate the NP uptake [107]. A similar trend was observed in HeLa cells treated by SPION-PG-NH_3^+ FBS corona (+) *in situ* and SPION-PG-NH_3^+ FBS (–) (Figure 4-13e), supporting the role of FBS corona on NP-PG-NH_3^+ in their uptake mechanism.

The effects of FBS corona on uptake mechanisms of fND-PG-OSO_3^- and fND-PG-NH_3^+ by A549 cells were shown in Figure 4-13c and 4-13d, respectively. The uptake trends of fND-PG-Y FBS corona (+) *in situ* and FBS (–) by A549 cells were similar to those of HeLa cells under 4°C, CytoD and CPZ treatment conditions, expected for GEN treatment. The difference in caveolae-mediated internalization may arise from the cell line difference. However, the consistent results observed from both HeLa and A549 cells give conclusions that FBS corona suppressed the uptake of fND-PG-OSO_3^- through blocking the macropinocytosis and clathrin-mediated entry routes, and increased the uptake of fND-PG-NH_3^+ mainly through the macropinocytosis internalization.

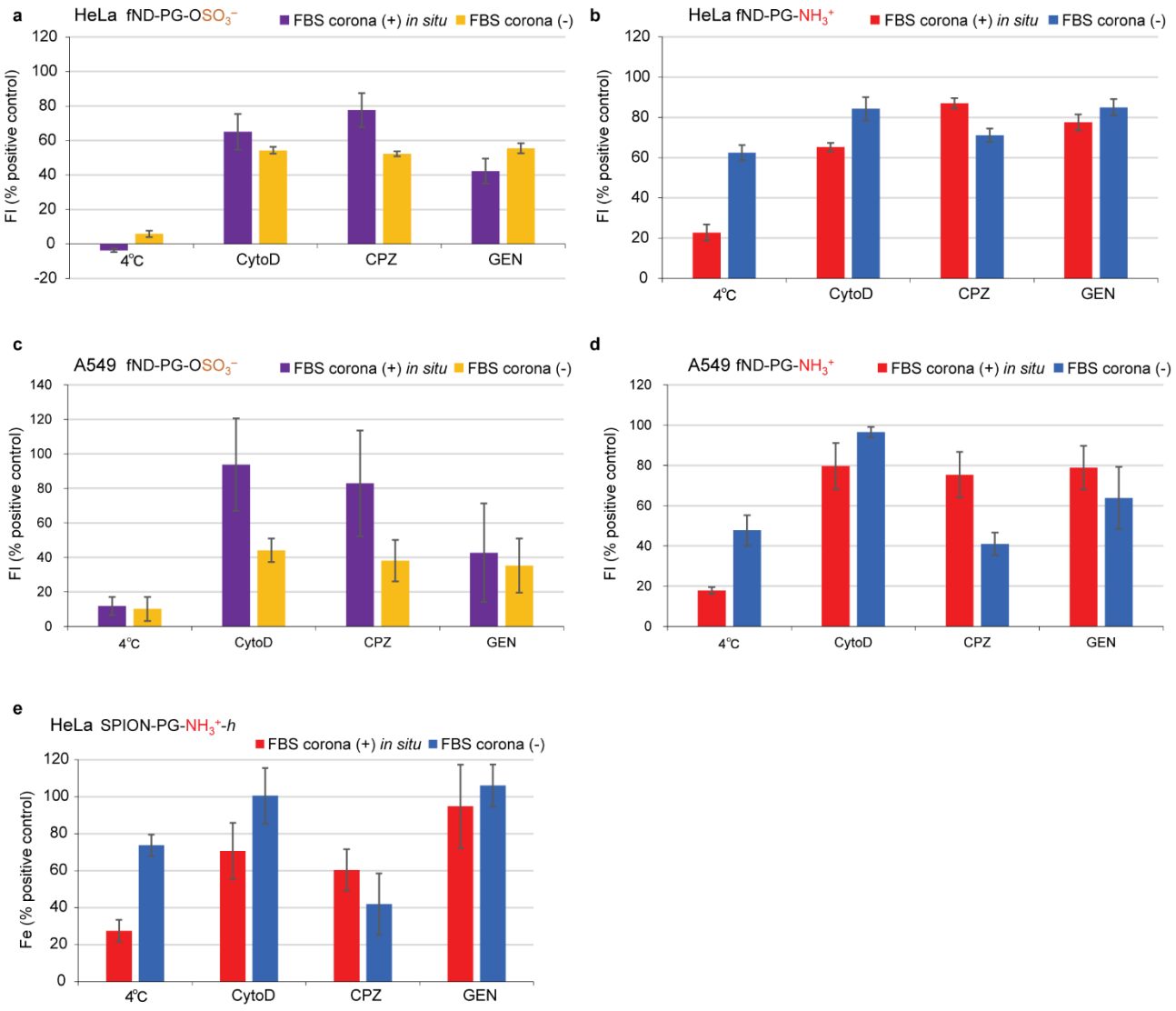

Figure 4-13. Effects of FBS coronas on cell uptake mechanism. (a-b) HeLa cell uptake mechanism of (a) fND-PG-OSO_3^- and (b) fND-PG-NH_3^+ in the presence and absence of FBS corona. (c-d) A549 cell uptake mechanism of (c) fND-PG-OSO_3^- and (d) fND-PG-NH_3^+ in the presence and absence of FBS corona. (e) HeLa cell uptake mechanism of SPION-PG-NH_3^+-*h* in the presence and absence of FBS corona.

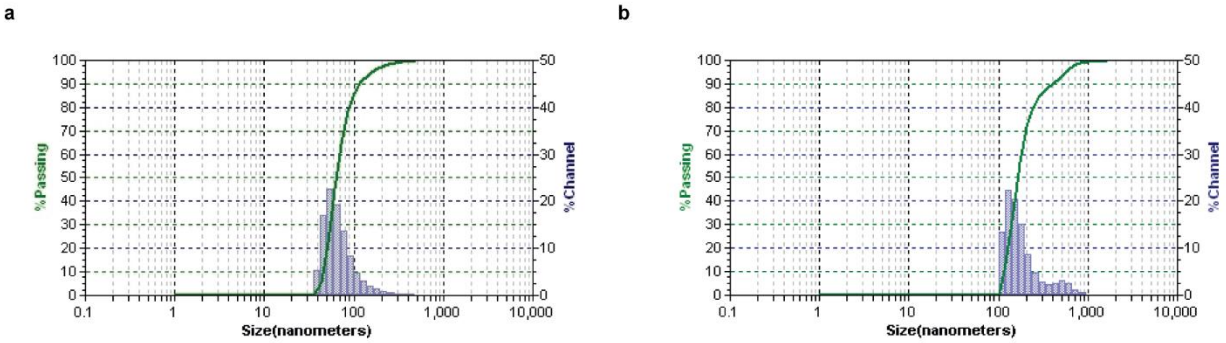

Figure 4-14. DLS size distribution of fND-PG-NH_3^+ (a) and fND-PG-NH_3^+-10%FBS (b).

4-3 Conclusions

The cascade effects of charged functional groups on protein corona formation and subsequent cellular uptake were clarified thanks to the corona-free PG interface. We demonstrated that uptake efficiency of NPs was correlated with the protein affinity of charged functional groups. The NP-PG-$COO^-$and NP-PG-OSO_3^--*l* (<4.1 groups / nm^2) exhibited no affinity to FBS proteins induced negligible or no cellular uptake. In contrast, NP-PG-OSO_3^--*h* (25 groups / nm^2) and NP-PG-NH_3^+ provoked substantial cellular uptake through association with proteins. In addition, we revealed that the uptake of NP-PG–OSO_3^- and NP-PG–NH_3^+ were suppressed or enhanced by their distinct protein corona profiles. Taking the cellular uptake pathways into consideration, the corona proteins on the fND-PG-OSO_3^- are considered to down-regulate the macropinocytosis and clathrin-mediated endocytosis, whereas the ones on NP-PG-NH_3^+ surface up-regulated the macropinocytosis. Our results present here

not only clarified the role of charged functional groups in protein absorption and cellular uptake, but also shed light on NP design for programmed uptake.

4-4 Materials and methods

4-4-1 Chemicals and materials

The powder of ND was kindly provided by Tomei Diamond Co., Ltd., Japan. The suspension of fND (1.0 mg/mL) was purchased from FND Biotech, INC. The following reagents were supplied by Wako Pure Chemicals, Japan; pyridine sulfur trioxide complex (SO_3-Py), pyridine, *N*,*N*-dimethylformamide (DMF), nitric acid, sodium dodecyl sulfate (SDS), LC-MS grade water, acetonitrile, formic acid, Dulbecco's modified eagle medium (DMEM), 0.25% trypsin-EDTA solution, antibiotics penicillin/streptomycin (100 U/mL), 20% glutaraldehyde, paraformaldehyde, cytochalasin D and genistein. The following reagents were purchased from Nacalai Chemicals, Japan; iron (III) acetylacetonate, thioglycerol, succinic anhydride, 4-dimethylaminopyridine (DMAP), *p*-toluenesulfonyl chloride (TsCl), sodium azide (NaN_3), triphenylphosphine (PPh_3), sodium hydroxide (NaOH), SDS-PAGE running buffer (30329-61), prestained protein markers (02525-35) and iron standard solution. FBS (556-33865) and BCA protein assay kit (T9300A) were supplied by Biosera, Inc., France and Takara, Bio., Inc., Japan, respectively. 5-20% precast polyacrylamide gel (E-R520L) and protein loading buffer (AE-1430) were purchased from ATTO, Japan. Pierce silver stain kit (24612) and in-gel tryptic digestion kit were supplied by Thermo Fisher Scientific. Chlorpromazine hydrochloride and glycidol were purchased from Tokyo Chemical Industry, Japan and Kanto Chemical Co. Inc., Japan, respectively. Dimethyl sulfoxide (D8418) and Kaighn’s modification of Ham’s F12

medium (F-12K medium) were supplied by Sigma-Aldrich and American Type Culture C, respectively. Human cervix epithelium HeLa cells were received as a gift from Prof. Amano from Shiga University of Medical Science, and human lung epithelial carcinoma A549 cells (IFO50153) were purchased from Japanese Collection of Research Bioresources Cell Bank.

4-4-2 Equipment

TGA was run from room temperature to 1000 °C at a heating rate of 20 °C/min under N_2 on a Q-50 analyzer (TA Instruments). TEM observation of NPs and cell samples was performed on a field emission transmission electron microscope (JEOL, JEM-2200FS) and a H-7650 TEM (Hitachi, Japan), respectively. The DLS sizes and zeta potentials were measured on a Nanotrac UPA-UT151 system (Microtrac, Inc., USA) and a zeta Sizer Nano Series (Malvern Instruments, UK), respectively. The IR spectra was recorded on an IR Prestige-21 (Shimadzu Co. Ltd.) in the wavenumber range of 4000 to 500 cm^{-1} with a resolution of 4 cm^{-1} for 16 scans. The EA was performed via a combustion method at Organic Elemental Microanalysis Center of Kyoto University. The SDS-PAGE gels were scanned on a fluorescence scanner (GT-X900, EPSON, Japan) at a resolution of 600 dpi. FACS and ICP analysis were carried out on FACSArea II Cell Sorter (BD, USA) and ICPS-8100 (Shimadzu, Japan), respectively.

4-4-3 Preparation of NP-PG-COOH, NP-PG-OSO_3Na and NP-PG-NH_2

The SPION, NP-PG, as well as NP-PG-COOH and NP-PG-NH_2 containing *l* and *h* densities of charge groups were synthesized according to our previous methods [92]. NP-PG-COOH-*l* and -*h* were obtained by stopping the ring-opening reaction of succinic anhydride at 1 and 24 h, respectively. On the other hand, NP-PG-OTs- *l* and -*h* were obtained by stopping tosylation reactions at 1 and 24 h, respectively. Then, the resulting tosylates was transformed to NP-PG-NH_2-*l* and *h* through OTs → N_3 → NH_2 transformations.

NP-PG-OSO_3Na was prepared according to the reported procedure [93] with slight modification. For NP-PG-OSO_3Na-*l*, a DMF solution (2.5 mL) of SO_3-Py (40 mg) was added dropwise to the DMF suspension (2.5 mL) of NP-PG (15 mg), then the mixture was stirred at 60 °C for 5h and room temperature overnight. After that, the pH of the reaction suspension was brought to 11 by adding NaOH solution (1M), giving the desired product. The NP-PG-OSO_3Na-*l* was collected by centrifugation at 50,400g for 1 h and washed with Milli-Q water by repeated redispersion/centrifugation cycles. The NP-PG-OSO_3Na-*h* was prepared from a procedure similar to that of NP-PG-OSO_3Na-*l* by using pyridine/DMF (1/2 v/v) suspended NP-PG as starting material.

4-4-4 Protein corona formation

The suspensions of NP-PG-COOH, NP-PG-OSO_3Na and NP-PG-NH_2 as well as NP-PG were incubated with 10 or 55 % FBS in 10 mM PBS (2 mL) at 37 °C for 1 h. The weights of NPs used in

each experiment were adjusted (Table 4-5), so that the total number of functional groups in each density and each NP was almost the same. To remove protein aggregates in FBS, the freshly thawed FBS solution was centrifuged at 134,000*g* for 20 min just before use. After incubation, the NP-protein complexes were pelleted by centrifugation at 108,000*g* for 20 min and the pellets were subjected to three redispersion/centrifugation washing cycles in Milli-Q water (1.0 mL) to fully remove the free unbound proteins. Subsequently, the proteins adsorbed onto NP surface were detached by 10% SDS (100 μL) and separated from NPs by centrifugation at 108,000*g* for 20 min. The SDS solution containing the corona proteins isolated from the NP surface, designated as protein corona solution, was used for further analyses.

Table 4-5. The weights of NP-PG, NP-PG-COOH, NP-PG-OSO_3Na and NP-PG-NH_2 used in protein corona formation experiment.

NPs	**Weight (μg)**		**Total number of functional groups ($\times 10^{16}$)**	
	NDs	**SPIONs**	**NDs**	**SPIONs**
NP-PG	308	196	/	/
NP-PG-COOH-*l*	328	145	8.9	7.4
NP-PG-COOH-*h*	423	330	50	52
NP-PG-OSO_3Na-*l*	317	145	4.0	3.7
NP-PG-OSO_3Na-*h*	369	340	27	32
NP-PG-NH_2-*l*	308	264	4.4	4.4
NP-PG-NH_2-*h*	308	252	17	17

4-4-5 Protein corona analysis

The protein corona was analyzed according to our previous procedure. For SDS-PAGE, an aliquot (5 μL) of the protein corona solution was mixed with an equal volume of protein loading buffer (2×) for sample loading. The protein mixtures were separated by a 5-20% precast polyacrylamide gel and stained with Pierce silver stain kit for visualization. The total protein amount was determined via BCA by using an aliquot (20 μL) of the protein corona solution, according to the manufacture's instruction. For the LC-MS/MS identification, an in-gel digestion protocol was performed for the protein corona solution detached from ND-PG-OSO_3^--*h*, ND-PG-NH_3^+-*l* and ND-PG-NH_3^+-*h*, and fND-PG-OSO_3^- and fND-PG-NH_3^+, as well as the FBS protein solution prior to the analysis. The analysis procedure was performed in a manner similar to our previous study [84]. NCBI protein library for Bostaurus (September 2020) appended with known contaminants database (SCIEX) were used for the peptide and protein identification by ProteinPilot software (SCIEX). The relative abundances of the identified proteins were estimated on the platform of Progenesis QI for Proteomics software version 4.2 (Nonlinear Dynamics, Newcastle upon Tyne, UK). All raw data files with wiff format (SCIEX) were imported to generate aggregate, and the peptide identification results by ProteinPilot, with confidence at least 95%, were used for assignment. Label-free quantification of proteins was performed using relative quantitation using Hi-N (3) method (Nonlinear Dynamics), proteins with at least two unique peptides matched were used for data interpretation.

4-4-6 Cell culture

HeLa and A549 cells were maintained in DMEM and F-12K culture medium, respectively, supplemented with 10% FBS and 1% antibiotics penicillin/streptomycin. All the cells were grown in a humidified incubator (MCO-5ACUV-PJ, Panasonic) supplied with 5% CO_2 at 37 °C, and passaged until 70 -80% confluent reached.

4-4-7 TEM observation of ND-PG, ND-PG-COOH, ND-PG-OSO_3Na and ND-PG-NH_2 uptake

HeLa and A549 cells were seeded into a ϕ 60mm cell culture dish at a density of 5×10^5 cells per dish and incubated overnight to allow cell adhesion. On the following day, the culture medium was aspirated and replaced with fresh medium (4 mL) containing ND-PG, ND-PG-COOH, ND-PG-OSO_3Na or ND-PG-NH_2. The concentration of NDs in each dish was adjusted to be 100 μg/ mL. After 2 or 24 h incubation, cells were washed with 10 mM PBS (4 mL) three times and collected into a microcentrifuge tube. The cell pellet was prefixed with 2% glutaraldehyde/4% paraformaldehyde in 100 mM PBS buffer (1 mL) overnight, and post-fixed with 1% osmium tetroxide for 2 h. The pellet was dehydrated in ethanol series and propylene oxide, passed through propylene oxide/epoxy resin (1/1 and 1/3) mixtures, and embedded in epoxy resin. After being baked at 60 °C to reach polymerization, the frontal sections (60 - 80 nm) were cut by an ultramicrotome (EM UC6, Leica, Germany). The slices were stained with uranyl acetate and lead citrate, and observed by a H-7650

TEM (Hitachi, Japan).

4-4-8 Cellular uptake mechanisms of fND-PG-OSO_3Na and fND-PG-NH_2

HeLa cells were seeded into a 6-well plate at a density of 2.0×10^5 cells per well and incubated overnight prior to experiment. After confirming cell confluency and morphology, the cells were preincubated at 4 ℃ for 30 min or pretreated by inhibitors including CytoD (2 μg/mL), CPZ (75 μg/mL) and GEN (7.5 μg/mL) for 10 min. Then, the culture medium was discarded and replaced with fresh medium (2 mL) without or with the aforementioned inhibitors. Subsequently, fND-PG-OSO_3Na and fND-PG-NH_2 were directly applied to culture medium containing 10% FBS or serum-free medium, and those with 10% FBS pretreatment were also added to serum-free medium. These fNDs were further incubated with cells at 4 or 37 ℃, respectively, for 2 h. In all case, the fNDs were adjusted to have a core weight of 200 μg. The concentrations of the inhibitors and treatment time was optimized based on cell viability and cell uptake efficiency, respectively. After incubation, the treatment solution was discarded, and the cells were washed by 10 mM PBS and collected in a procedure similar to that of TEM observation. The cellular uptake was assayed by FACS for fNDs at excitation of 532 nm and emission of 645-695 nm, and the results are presented as the averaged mean of the cell fluorescence intensity. The cells treated with fNDs only or without any treatment were served as positive and negative controls, respectively. Error bars are obtained by measuring the standard deviation among the replicates (n = 3).

4-4-9 Cellular uptake efficacy and mechanisms of SPIONs

The cellular uptake efficacy and mechanisms of SPIONs were performed in a manner similar to that of fNDs. The different points are described as follows. (1) The concentration of SPION was adjusted to 50 μg/mL per dish/well, and (2) the uptake was estimated based on Fe content determined from ICP measurements.

Chapter 5: Effect of protein corona on mitochondrial targeting ability and cytotoxicity of triphenylphosphonium conjugated with polyglycerol-functionalized nanodiamond

5-1 Introduction

The efficiency of targeting moieties on NP surface is known to be altered by the as formed protein corona [12, 108, 109]. For example, NPs with covalently attached bio-functional proteins such as transferrin [16] and anti-CD63 antibody [32], and aptamer such as RGD peptide [110] are reported to decrease or even lose their specificity to the corresponding receptors in a protein rich medium. These studies demonstrated that protein corona compromised the targeting ability of NPs at cellular level. However, little is known about the influence of protein corona on the subcellular targeting ability of NPs. Such knowledge is imperative for development of precision nanomedicine, because treatment at subcellular organelles maximizes the therapeutic efficacy of various cancer therapies [111].

In this chapter, triphenylphosphonium (TPP), a most widely used mitochondrial targeting ligand [112, 113], was adopted as a typical example to demonstrate the effect of protein corona on subcellular targeting ability. In addition, the effect of protein corona on the cytotoxicity of TPP was investigated, because the toxicity of TPP is another concern in its practical use [114]. In order to make them clear, TPP was introduced on the surface of ND grafted with PG, a corona-free interface we demonstrated recently [84, 92], in low (*l*) and high (*h*) densities in a quantitative manner. The resulting ND-PG-TPP is found to adsorb proteins to form a corona layer, the amount of which is strictly proportional to the

TPP density. The effects of protein corona on the mitochondrial targeting and cytotoxicity of ND-PG-TPP were examined on HeLa and A549 cells. It was revealed that 1) the protein corona mitigated the cytotoxicity of both ND-PG-TPP-*l* and -*h*, 2) ND-PG-TPP-*l* with a thinner protein corona layer maintained its targeting ability to mitochondria, though the ND-PG-TPP-*h* with a thicker protein corona layer lost its specificity to mitochondria.

5-2 Results and discussion

5-2-1 Synthesis and characterization of ND-PG-TPP

As a core of the platform, ND is chosen because we have mainly used it so far in view of its high biocompatibility and rich chemistry for further functionalization as well as its potentials in translational nanomedicine [115, 116]. According to our previous method [26], ND with 50 nm size (Figure 5-1a and 5-1b) was grafted with PG to give ND-PG (Figure 5-1c and 5-1d) at the PG content of 34 wt% determined by TGA (Figure 5-2). The ND-PG was further functionalized with TPP through esterification between the hydroxy groups in the PG layer and the carboxy groups in TPP-COOH, as shown in Scheme 5-1. The ND-PG-TPP-*l* and -*h* were obtained by adjusting the amounts of TPP-COOH in these reactions (see details in Methods). While the shape and size of ND-PG-TPP (Figure 5-1e – 5-1i) were confirmed to be similar to those of ND and ND-PG by TEM analysis (Figure 5-1a – 5-1d), the introduction of TPP groups was confirmed by their zeta-potentials; the negative zeta potential of ND-PG (–4.6 mV) was brought to the positive ones (0.8 and 22.6 mV) in ND-PG-TPP-*l* and -*h*,

respectively (Figure 5-3e). The zeta potential differences before and after TPP functionalization (5.4 and 27.2 mV) are considered to reflect the differences in the TPP densities (*l* and *h*) on the ND-PG surfaces, which will be discussed below more quantitatively.

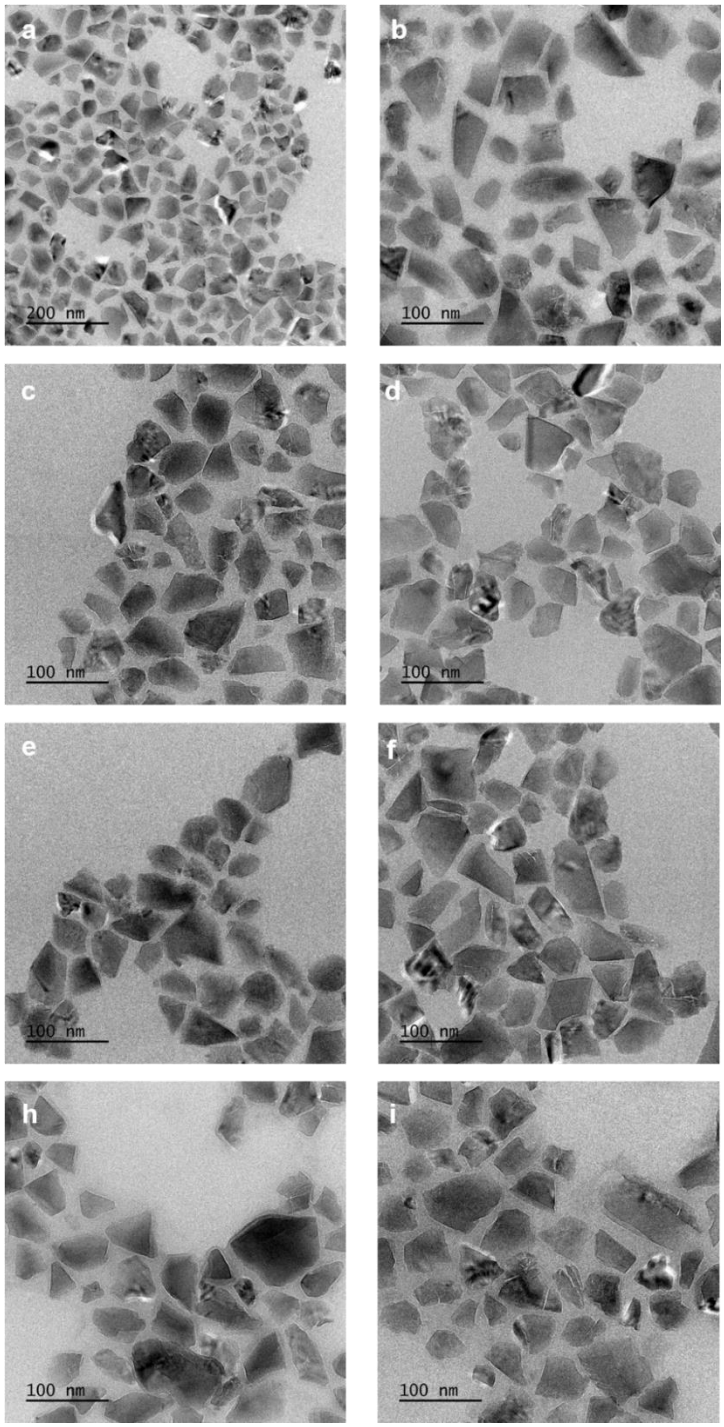

Figure 5-1. TEM images of ND, ND-PG and ND-PG-TPP; (a)-(b), (c)-(d), (e)-(f) and (h)-(i) are images of ND, ND-PG, ND-PG-TPP-*l* and ND-PG-TPP-*h*, respectively. The scale bar is indicated in each image.

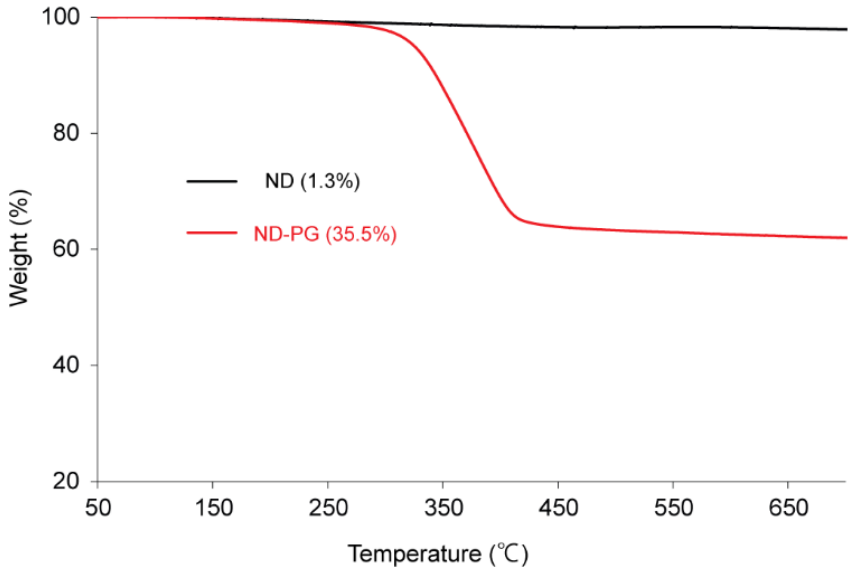

Figure 5-2. TGA profiles of ND (black trace) and ND-PG (red trace). The weight losses (wt%) of ND and ND-PG in the range from 200 to 450℃ are indicated in parentheses.

Scheme 5-1. Functionalization of ND-PG with TPP at low (*l*) and high (*h*) densities.

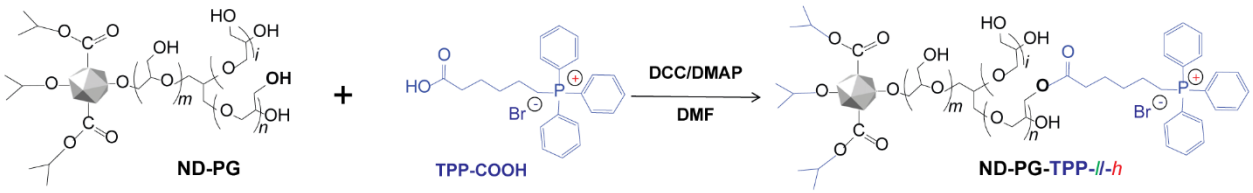

The ND-PG-TPP, along with TPP-COOH and ND-PG, was further characterized by IR and ^{1}H NMR spectroscopies as shown in Figure 5-3 and 5-4, respectively. In the IR spectra of ND-PG-TPP (Figure 5-3), the peaks around 1716, 1435 and 740-690 cm^{-1} are attributed to the stretching vibrations of C=O, aromatic C=C and aromatic C−H in TPP, respectively [117, 118], indicating the conjugation of TPP onto ND-PG. The peak of the C=O is shifted from 1705 cm^{-1} in TPP-COOH to 1716 cm^{-1} in ND-PG-TPP, supporting that TPP and ND-PG are connected by ester linkage (Scheme 5-1). Since the IR spectra of ND-PG and ND-PG-TPP are normalized at the absorption of C−O−C stretching in the PG around 1110 cm^{-1}, the higher intensities at the peaks corresponding to TPP in ND-PG-TPP-*h* indicates a higher density of TPP in ND-PG-TPP-*h* than ND-PG-TPP-*l*.

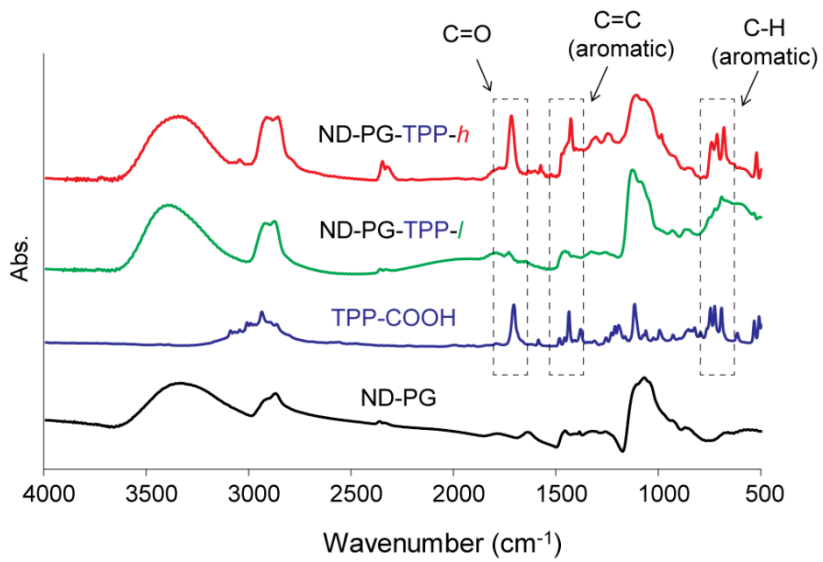

Figure 5-3. IR spectra of ND-PG, TPP-COOH and ND-PG-TPP with *l* and *h* densities.

The ^{1}H NMR characterization is consistent with and more quantitative than that of IR spectra. As shown in Figure 5-4, the PG layer in ND-PG is characterized by the broad signal around 3.7 ppm corresponding to OCH_2 and OCH. The rest of the characteristic peaks in ND-PG-TPP are attributed to the TPP at δ 7.9–7.6 (m, 15H, Ph), 3.31 (t, 2H, PCH_2), 2.14 (t, 2H, $COCH_2$), 1.74 (m, 2H, CH_2) and 1.55 (m, 4H, CH_2) [119, 120]. The ester linkage in the ND-PG-TPP is verified by the upper field shift of $COCH_2$ from 2.29 ppm to 2.14 ppm. The number of TPP moieties at ND-PG-TPP-*h* is determined to be nine times larger than that at ND-PG-TPP-*l* through the calculation based on the integrals of the signals at 7.7–7.9 and 3.0–4.5 ppm (Table 5-1).

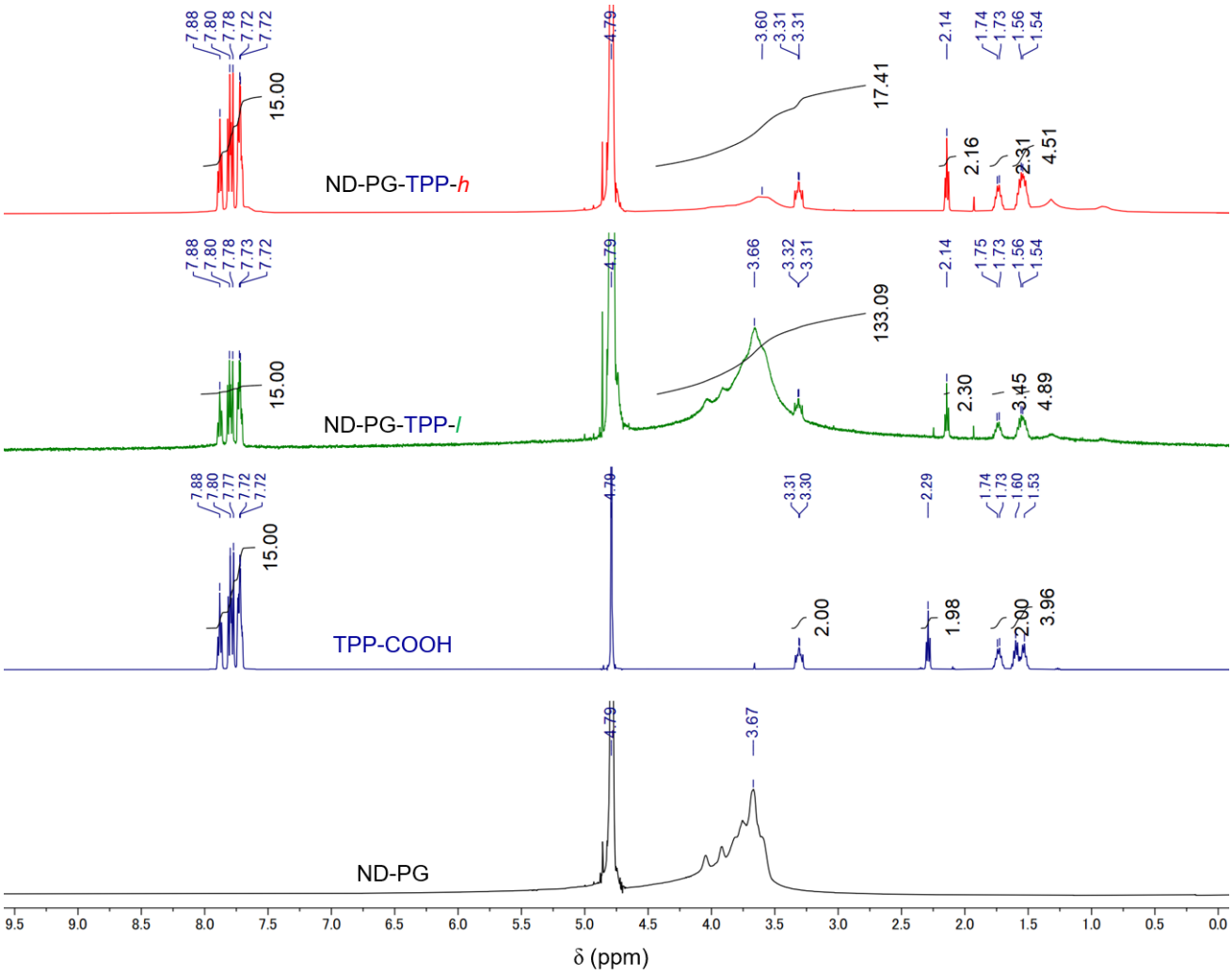

Figure 5-4. ^{1}H NMR spectra of ND-PG, TPP-COOH and ND-PG-TPP with *l* and *h* densities in D_2O.

Table 5-1. Ratio in the number of TPP groups at ND-PG-TPP-*h* and -*l* based on the NMR integrals.

	Ph group hydrogens at 7.7 - 7.9 ppm	PCH_2 at 3.3 ppm	PG hydrogens and PCH_2 at 3.0 - 4.5 ppm	PG hydrogens (calcd.)	Ph group hydrogens / PG hydrogens
TPP-COOH	15.0	2.0	2.0	–	–
ND-PG-TPP-*l*	15.0	2.0[a]	133.1	131.1	0.11
ND-PG-TPP-*h*	15.0	2.0[a]	17.4	15.4	0.97

[a] The same integral values are assumed as that of TPP-COOH.

The absolute number of TPP groups in one ND-PG-TPP particle is calculated based on the content of phosphorus and the weight ratio between ND core and PG layer determined by the elemental analysis (Table 5-2) and the TGA (Figure 5-2), respectively. As a result, TPP groups are found to be included at 1.2×10^5 and 9.3×10^3 on one ND-PG-TPP-*h* and ND-PG-TPP-*l* particle, respectively. Validity of these calculated TPP numbers is confirmed by the fact that the ratio in these absolute numbers (Table 5-2) is roughly comparable to that in integrals of ^{1}H NMR mentioned above (Table 5-1).

Table 5-2. Elemental analysis of phosphorus contents in ND-PG-TPP and the calculated number of TPP groups in one ND-PG-TPP particle.

ND-PG-TPP	Content of each component (wt%)				TPP in one ND-PG-TPP	
	phosphorus [a]	TPP [b]	PG [c]	ND [c]	Weight [d] (ag)	Number [e]
l	0.12	1.4	33.5	65.1	5.6	9.3×10^3
h	1.32	15.3	28.8	55.9	71.3	1.2×10^5

[a] The contents of phosphorus was determined from elemental analysis.

[b] The calculation of TPP content is based on the content of phosphorus and the mass ratio of phosphorus in TPP moiety (31:360).

[c] The contents of PG and ND in ND-PG-TPP were calculated based on the ND-PG content in ND-PG-TPP and the ratio of ND and PG in ND-PG determined from TGA in Figure 5-2.

[d] The weights of TPP in one ND-PG-TPP particle were calculated based on the weight ratio of TPP and ND as well as the weight of one ND core with 50 nm size (260 ag) reported previously [84].

[e] The number of TPP in one ND-PG-TPP particle was derived from its weight and molecule weight (360 Da).

5-2-2 Protein corona formation on ND-PG-TPP

To examine the effect of TPP moiety on protein corona formation, the dispersions of ND-PG-TPP-*l*, ND-PG-TPP-*h* and ND-PG were incubated in 10% FBS and 55% human plasma (HP) solutions at 37℃ for 1 h (see details in Methods). After washing out the free unbound proteins, the corona proteins were detached by 10% SDS solution and the resulting protein corona solutions were subjected to SDS-PAGE and BCA assays. Since the amounts of corona proteins in 10% FBS are found to be saturated in both ND-PG-TPP-*l* and -*h* at 1 h (Figure 5-5a and 5-5b for SDS-PAGE and BCA assays, respectively), we determined the incubation time to be 1 h, which is consistent with that reported in the previous study [65]. The zeta potentials and DLS sizes of NDs with and without protein corona were also measured.

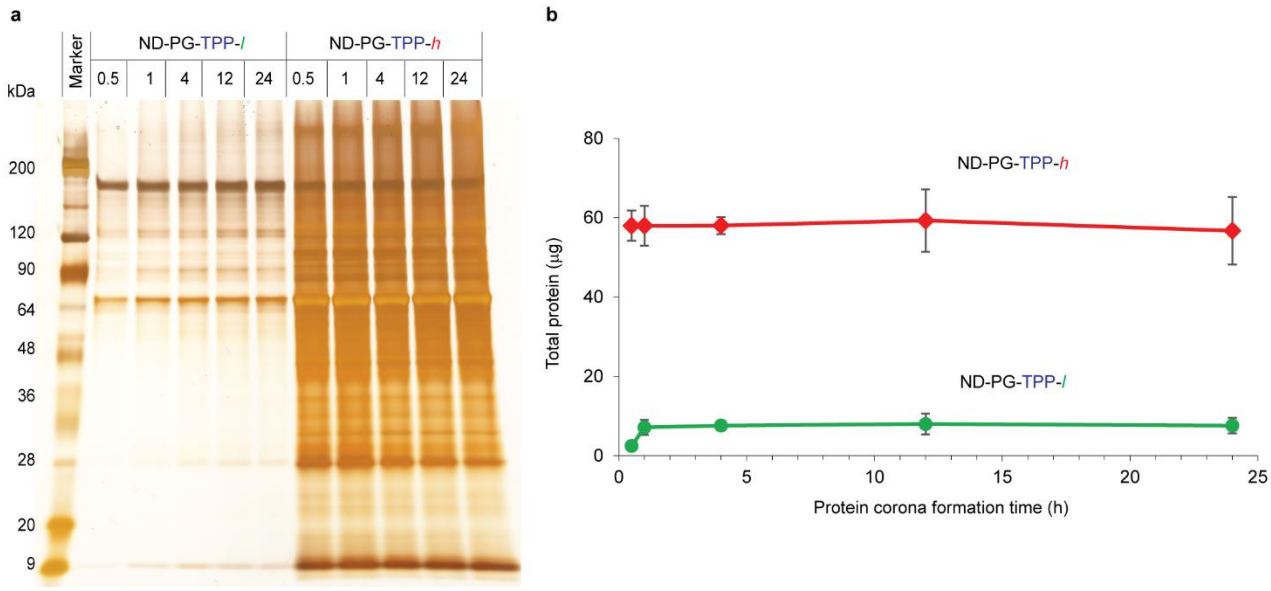

Figure 5-5. Analysis of proteins adsorbed on ND-PG-TPP in 10% FBS at different incubation time. (a) SDS-PAGE identification and (b) BCA quantification of 10% FBS corona formed on ND-PG-TPP-*l* and -*h* at 0.5, 1, 4, 12 and 24 h.

In the SDS-PAGE of the corona proteins from 10% FBS and 55% HP shown in Figure 5-6a and 5-6b, respectively, no observable protein band appears in the lanes of ND-PG. This is in line with our previous studies demonstrating that PG grafting resists protein corona formation onto NP surfaces [84, 92]. Based on this corona-free PG layer, we found that TPP moiety induced protein corona formation in a density-dependent manner in both 10% FBS and 55% HP solutions. That is, the number and intensity of protein bands in the lanes of ND-PG-TPP increased significantly as the density of TPP increased from *l* to *h* (Figure 5-6a and 5-6b). The SDS-PAGE results are quantitatively supported by those of BCA (Figure 5-6c). While almost no proteins (< 0.05 μg) were detected on the surface of ND-

PG without TPP moieties, 7.1 and 58.0 μg of FBS proteins, and 7.2 and 74.4 μg of HP proteins were adsorbed on the surfaces of ND-PG-TPP-*l* and ND-PG-TPP-*h*, respectively. As shown in the three-point plots of these protein amounts against the TPP densities (Table 5-2) in Figure 5-6d, strict linearity is observed at the correlation coefficients of 0.998 and 1.000 for 10% FBS and 55% HP, respectively.

The protein attraction of ND-PG-TPP is attributable to its positive zeta potential (Figure 5-6e) and hydrophobicity, which arise from the phosphonium cation and the phenyl rings at TPP, respectively. Since most of proteins are negatively charged under physiological conditions, they are prone to be adsorbed onto the positively charged ND-PG-TPP through electrostatic interaction [19]. In addition, the complex of ND-PG-TPP and proteins can be stabilized through hydrophobic interaction between the phenyl rings at TPP and the hydrophobic parts in proteins [31].

In the zeta potential and DLS measurements, ND-PG exhibits similar zeta potentials (Figure 5-6e) and DLS sizes (Figure 5-6f) before and after the treatment with FBS and HP proteins, supporting almost no corona proteins on the surface as mentioned above (Figure 5-6a – 5-6c). However, significant decrement in zeta potential (Figure 5-6e) and increment in DLS size (Figure 5-6f) are considered to be caused by the large amounts of proteins on ND-PG-TPP-*h* surface. Although smaller amount of corona proteins on ND-PG-TPP-*l* may decrease its zeta potential to a much lesser extent (Figure 5-6e), DLS sizes did not change after the protein treatment (Figure 5-6f). The zeta potentials of ND-PG-TPP complexes with proteins are in the range of −5 to −10 mV, which are

comparable to those of gold, silica and polystyrene NPs after their incubation with serum proteins [34, 76].

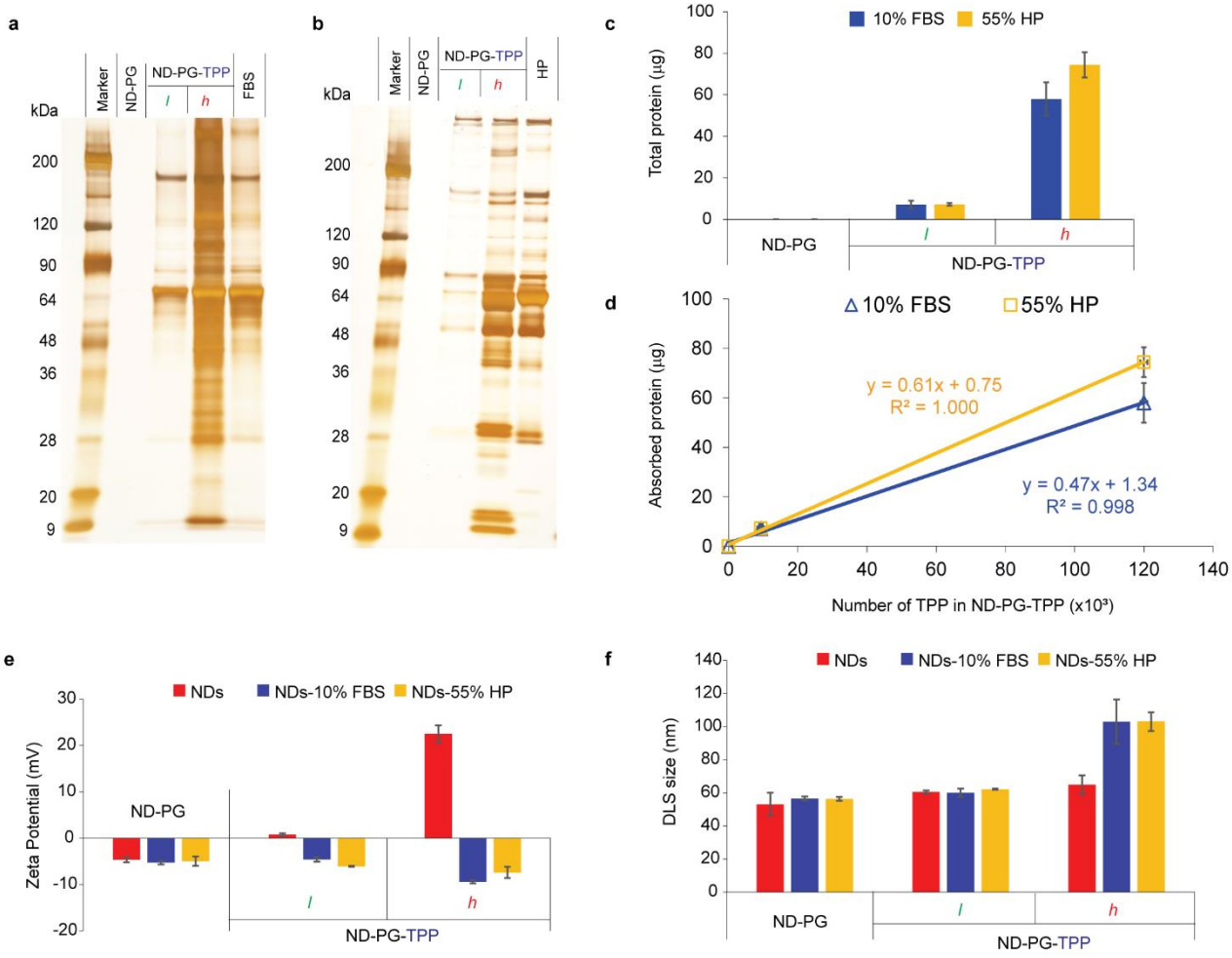

Figure 5-6. Analysis of protein corona formed on ND-PG and ND-PG-TPP surfaces in 10% FBS and 55% HP solutions. (a, b) SDS-PAGE identification of 10% FBS (a) and 55% HP (b) as well as BCA quantification (c) of proteins detached from ND-PG and ND-PG-TPP. The BCA results in (c) are presented as mean value ± standard deviation of three repeats. (d) Linear relationship between the amounts of corona proteins (c) and numbers of TPP on one ND-PG-TPP particle (Table 5-2). (e, f)

Zeta potentials (e) and DLS mean sizes (f) of ND-PG and ND-PG-TPP before and after their incubation with 10% FBS and 55% HP. The data for zeta potentials and DLS sizes are presented as mean value ± standard deviation of 20 and five measurements, respectively.

5-2-3 Effect of protein corona on cytotoxicity of ND-PG-TPP

The clinical applications of TPP functionalized NPs are limited by its toxicity [121, 122]. If the toxicity of TPP moiety is attributed to its positive charge, the toxicity of ND-PG-TPP should be mitigated due to their negative zeta potentials after protein corona formation (Figure 5-6e). Based on this hypothesis, we examined the viability of the cells incubated with ND-PG-TPP in the presence and absence of FBS proteins. Briefly, HeLa cells were exposed to various concentrations of ND-PG-TPP-*l* and -*h* in a culture medium supplemented with and without 10% FBS (FBS (+) and FBS (－), respectively), and their viability was assayed at 4, 12 and 24 h (Table 5-3).

Table 5-3. Experimental conditions for cytotoxicity assay shown in Figure 5-8 and 5-9. [a]

Abbreviation	Precoat with protein mixture	Incubation with protein mixture	Cell line	Concentration of ND-PG-TPP (μg/mL)	Figure
FBS (−)	×	×	HeLa	25, 50, 100	5-8
Protein (−) [b]	×	×	HeLa	50	5-9a, b
			A549	50	5-9c, d
FBS (+)	×	○ (10% FBS)	HeLa	25, 50, 100	5-8
FBS (p+)	○ (10% FBS)	×	HeLa	50	5-9a, b
			A549	50	5-9c, d
HP (p+)	○ (55% HP)	×	HeLa	50	5-9a, b
			A549	50	5-9c, d

[a] Incubation time is 4, 12 and 24 h.

[b] The conditions of Protein (−) for HeLa cells are exactly the same as those of FBS (−) at concentration of 50 μg/mL.

In addition, we confirmed that HeLa cells grew similarly in the presence and absence of FBS in culture medium without NPs (Figure 5-7a) and with ND-PG (Figure 5-7b) for 24 h. Therefore, the results in Figure 5-8 should reflect the net effect of FBS corona on the toxicity caused by the TPP moiety.

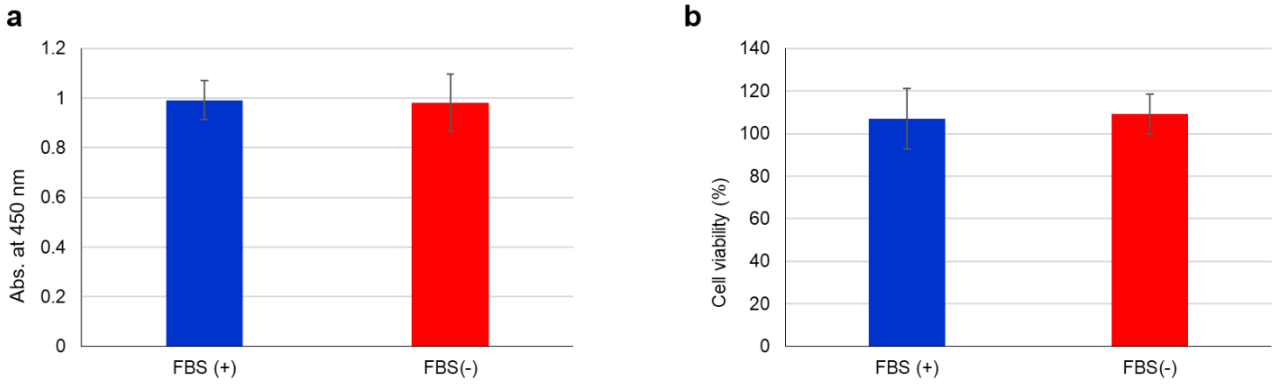

Figure 5-7. Comparison of HeLa cell growth in the presence and absence of FBS (FBS (+) and FBS (–), respectively) without NP (a) and with ND-PG (b) at 24 h.

Under FBS (−) conditions as shown in Figure 5-8, the treatment of ND-PG-TPP-*l* (Figure 5-8a) and ND-PG-TPP-*h* (Figure 5-8b) decreased the cell viability depending on the TPP density, ND concentration and incubation time. The lowest cell viability with the ND-PG-TPP-*l* and ND-PG-TPP-*h* treatment was around 59% and 9%, respectively. In sharp contrast, both ND-PG-TPP-*l* and ND-PG-TPP-*h* showed almost no cytotoxicity at 25 and 50 μg/mL concentrations for all the time points (4, 12 and 24 h) under FBS (+) conditions. Even at the highest concentration (100 μg/mL) for the longest incubation time (24 h), the cell viability was around 89% and 30% for ND-PG-TPP-*l* and ND-PG-TPP-*h*, respectively. In general, the cell viabilities in the presence of FBS are higher than those in the absence of FBS at all the ND concentrations and all the incubation times for both ND-PG-TPP-*l* and ND-PG-TPP-*h*. Particularly, statistical differences between the cell viabilities of FBS (+) and FBS (−) were seen at ND of 100 μg/mL at 12 h and all the ND concentrations at 24 h for ND-PG-TPP-*l* as well

as all the concentrations and incubation times for ND-PG-TPP-*h*.

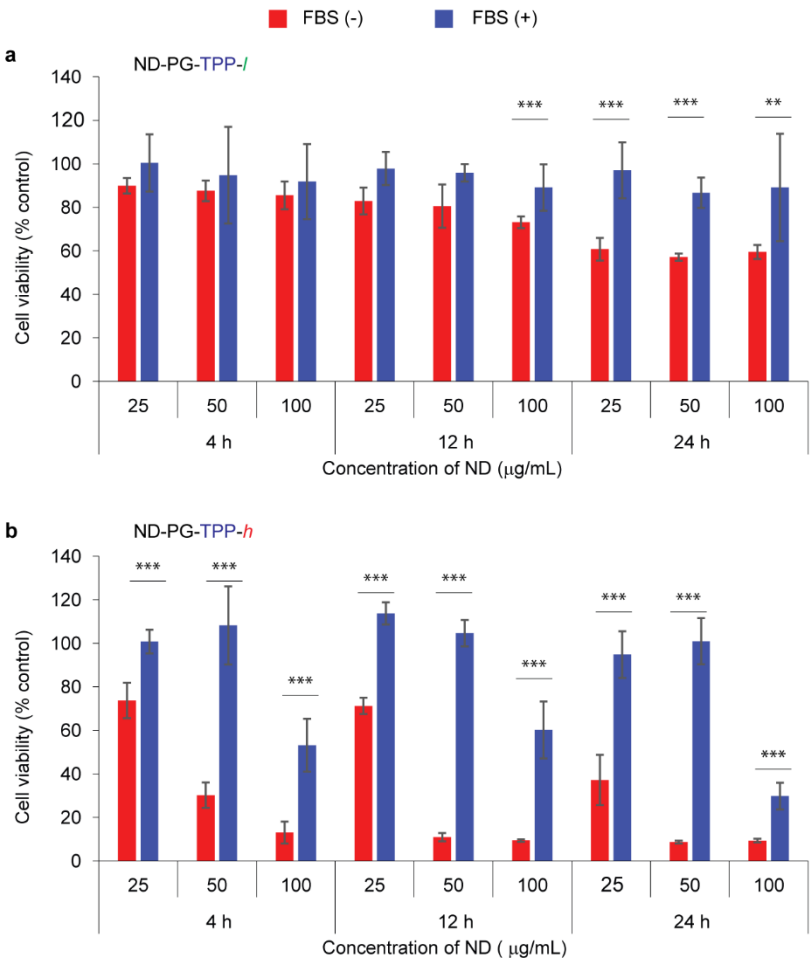

Figure 5-8. Cytotoxicity of ND-PG-TPP to HeLa cells in the presence and absence of FBS corona. Cells were exposed to 25, 50 and 100 μg/mL of ND-PG-TPP-*l* (a) and ND-PG-TPP-*h* (b) in the culture medium supplemented with and without 10% FBS (FBS (+) and FBS (−), respectively) for 4, 12 and 24 h (Table 5-3). Statistical analysis was performed by two-tailed Student's t-test. $^{**}p < 0.01$, $^{***}p < 0.001$ ($n = 5$).

For further confirmation, we investigated the cytotoxicity of ND-PG-TPP-*l* and ND-PG-TPP-*h* to HeLa and A549 cells at the ND concentrations of 50 μg/mL, after these ND-PG-TPP were precoated with 10% FBS and 55% HP designated as FBS (p+) and HP (p+), respectively (Table 5-3). In comparison of FBS (p+) for HeLa cells (Figure 5-9a and 5-9b) with FBS (+) (Figure 5-8), the precoated corona is also revealed to alleviate the cytotoxicity of TPP as efficiently as the corona formed *in situ*, though some toxicity was observed under the hardest conditions (ND-PG-TPP-*h* for 24 h). However, the protein corona from 55% HP is found to remove the TPP cytotoxicity much more efficiently than that from 10% FBS for not only HeLa (Figure 5-9a and 5-9b), but also A549 cells (Figure 5-9c and 5-9d). Taken together, we conclude that the protein corona significantly alleviates the cytotoxicity of ND-PG-TPP irrespective of its concentration (25 - 100 μg/mL), TPP density (*l* and *h*), cell line and gender (HeLa and A549), kind of protein mixture and its source (FBS and HP), and way of corona formation (precoat and *in situ*).

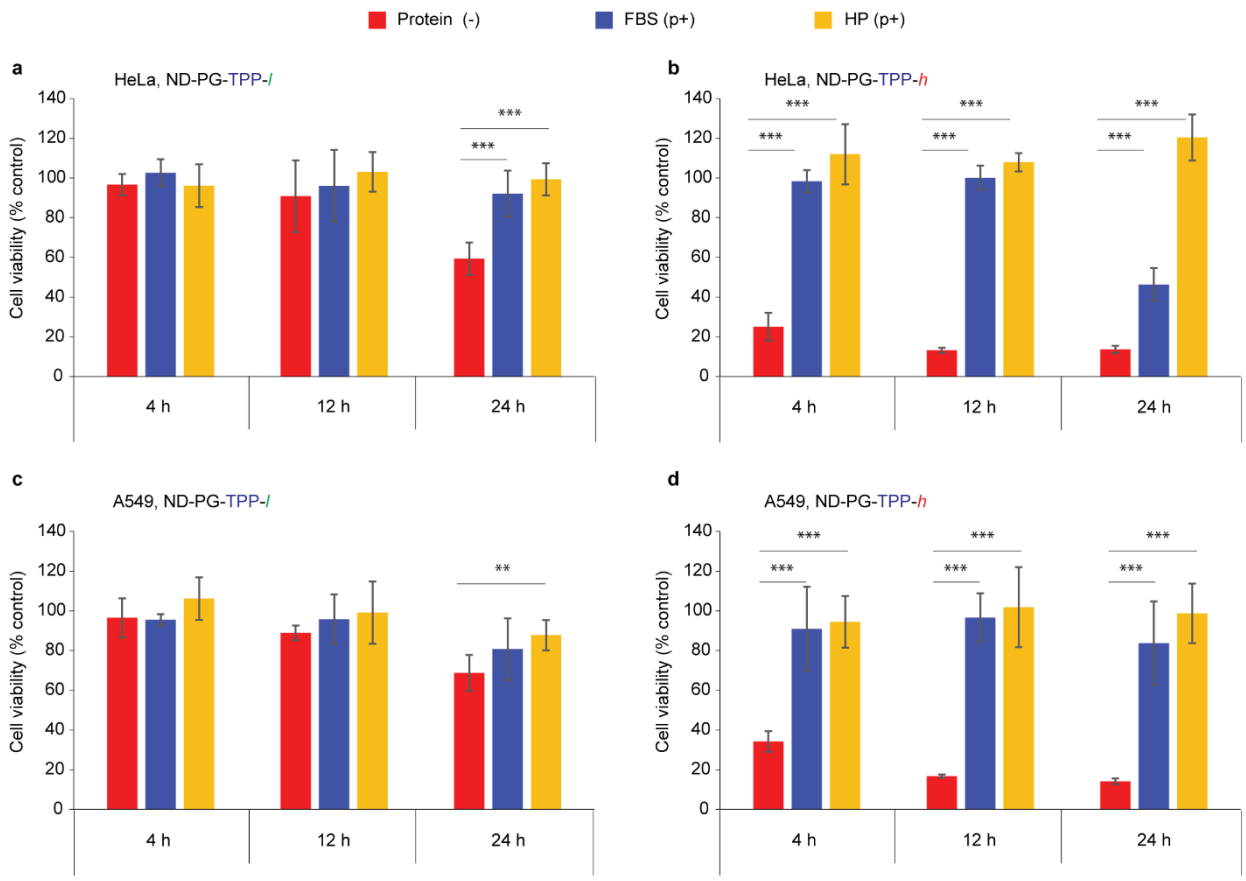

Figure 5-9. Cytotoxicity of HeLa cells (a, b) and A549 cells (c, d) in the presence of ND-PG-TPP (50 μg/mL) precoated with FBS (FBS (p+)) and HP (HP (p+)), and without protein treatment (Protein (–)) in a serum-free culture medium for 4, 12 and 24 h (Table 5-3). The conditions of Protein (–) for HeLa cells are exactly the same as those of FBS (–) at concentration of 50 μg/mL in Figure 5-8. Statistical analysis was performed by two-tailed Student's t-test. $^{**}p < 0.01$, $^{***}p < 0.001$ ($n = 5$).

The mitigation of the cytotoxicity can be interpreted as effects of the protein corona formed on the ND-PG-TPP surface 1) to suppress cell membrane disruption and 2) to lower the cellular uptake efficiency. As for 1), the cationic TPP moieties are known to elicit adverse cytotoxic effects by

depolarizing the cell membrane [112]. Since the surface charge of ND-PG-TPP was turned to be negative after the protein corona formation (Figure 5-6e), the disruptive nature of cationic TPP to cell membrane may be mitigated by this negative protein corona layer. As for 2), the cytotoxicity of TPP functionalized NPs is also correlated with their uptake efficiency, because excessive accumulation of the TPP cations within cells induces non-specific toxicity [114]. However, the negatively charged protein corona layer on the surface of ND-PG-TPP can reduce their association with the cells and thus cause a concomitant decrease in their uptake efficiency. Actually, a similar trend was reported by Lesniak, A. et al.; they concluded that the protein corona reduced the acute cytotoxicity of silica NPs by decreasing their cellular uptake [103].

5-2-4 Effect of protein corona on mitochondrial targeting ability of ND-PG-TPP

To investigate the effect of protein corona on the mitochondrial targeting ability of ND-PG-TPP, HeLa cells were exposed to 50 μg/mL of ND-PG-TPP-*l* and ND-PG-TPP-*h* for 12 h under FBS (+) and FBS (−) conditions in a similar manner to that of the cytotoxicity assay. The ND dose and exposure time were determined based on the cytotoxicity results (Figure 5-8). The ND-PG-TPP-*h* FBS (−) was omitted due to its high cytotoxicity. After the treatment, the intracellular localization of ND-PG-TPP was observed by TEM.

The TEM image of control cell in Figure 5-10a represents the typical structural characteristics of

a HeLa cell [123]; a round shape nucleus surrounded by numerous oval or round mitochondria in the cytoplasm. In the ND-PG treated cell (Figure 5-10b), no ND is observed in the mitochondria and the other organelles, which is the same as the control cell (Figure 5-10a). This is due to the protein-resistance property of PG coating (Figure 5-6), leading to the complete shielding of ND uptake [84].

In ND-PG-TPP-*l* treated cells, only single ND dot is found in a mitochondrion for both FBS (+) and FBS (−) conditions as shown in Figure 5-10c and 5-10d, respectively, demonstrating the targeting ability of TPP. The number of targeted mitochondria in ND-PG-TPP-*l* FBS (+) is comparable to that of ND-PG-TPP-*l* FBS (−), indicating that small amounts of proteins on the surface of ND-PG-TPP-*l* did not compromise the targeting ability of TPP. Moreover, in the cells treated by both ND-PG-TPP-*l* FBS (+) and FBS (−), the ND dots are specifically localized in mitochondria without being trapped in other organelles. This implies that both ND-PG-TPP-*l* with and without protein corona may pass through cellular membrane and accumulate in the mitochondrial matrix owing to the positive charge and the lipophilicity of TPP moiety [112, 113]. Although the protein corona imparts a slightly negative zeta potential to ND-PG-TPP-*l* (Figure 5-6e), it did not affect the targeting efficiency and uptake behavior of ND-PG-TPP-*l*. This is probably because the TPP moieties on the surface of ND-PG-TPP-*l* cannot be fully covered by small amounts of adsorbed proteins and the uncovered ones exert the targeting ability comparable to that of ND-PG-TPP-*l* FBS (−).

As for ND-PG-TPP-*h* FBS (+) treated cells (Figure 5-10e), more ND dots are observed in the

mitochondria (Figure 5-10e1), indicating a higher targeting efficiency of ND-PG-TPP-*h* as compared to that of ND-PG-TPP-*l*. However, relatively large number of NDs are trapped in the vesicles or accumulated in lysosome as shown in Figure 5-10e2. This implies that ND-PG-TPP-*h* with thicker protein corona coating may enter the cells via endocytosis to be trapped in endosomes [102], though caveolae mediated endocytosis is known to preserve the mitochondrial targeting ability of TPP functionalized NPs [124]. For more efficient mitochondrial targeting by NPs, quick escape from endosome may be required [125], but the dense protein corona layer on ND-PG-TPP-*h* surface (Figure 5-6) is considered to decrease the membrane disruption ability of the TPP moiety. Therefore, the protein corona on ND-PG-TPP-*h* may diminish its targeting specificity by restricting the ND inside the endosome and lysosome compartments. However, taking into consideration the high mortality rate with ND-PG-TPP-*h* in the absence of FBS corona as shown in Figure 5-8b, we can conclude that the protein corona is required when the high density of TPP is used as a targeting moiety.

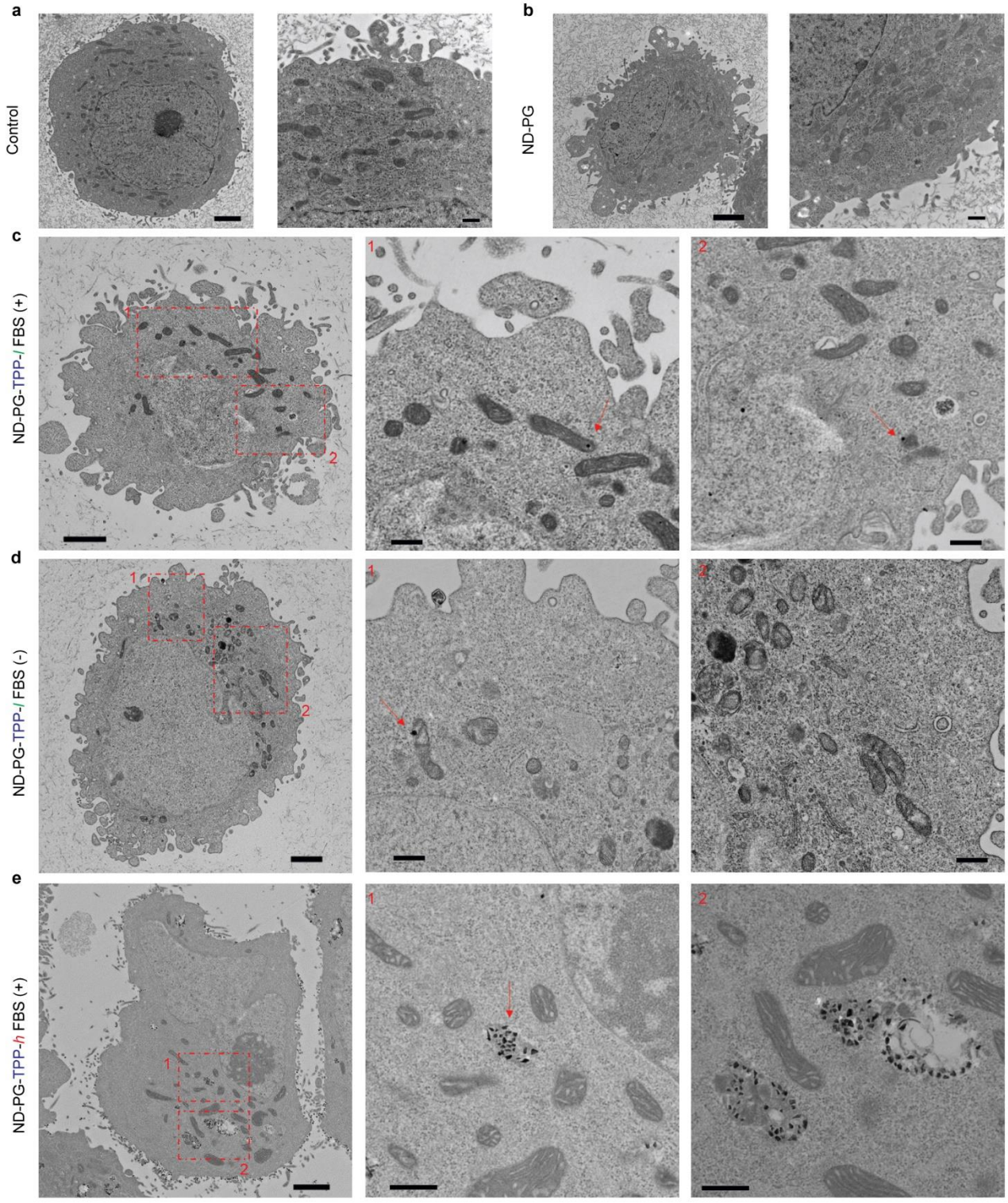

Figure 5-10. TEM images of HeLa cells (a) and after their incubation with ND-PG (b), ND-PG-TPP-*l* FBS (+) (c), ND-PG-TPP-*l* FBS (−) (d) and ND-PG-TPP-*h* FBS (+) (e). The scale bars in low and

high magnification images are 2 μm and 500 nm, respectively. Red arrows indicate the NDs targeted to mitochondria.

In order to generalize the phenomena, we further investigated the mitochondrial targeting ability of ND-PG-TPP-*l* and -*h* precoated with 55% HP (HP (p+)) in HeLa cells (Figure 5-11) and A549 cells (Figure 5-12e and 5-12g) as well as ND-PG-TPP-*l* and -*h* under FBS (+) conditions in A549 cells (Figure 5-12d and 5-12f). In accordance with the results obtained from FBS (+) in HeLa cells (Figure 5-10), the ND-PG-TPP-*l* with a thinner HP corona (Figure 5-6) specifically targeted to mitochondria in small quantities (Figure 5-11a and 5-11b), whereas ND-PG-TPP-*h* with a thicker HP corona (Figure 5-6) lost its specificity to mitochondria despite larger numbers of ND dots accumulated in mitochondria (Figure 5-11c and 5-11d). A similar trend in the mitochondrial targeting ability of ND-PG-TPP-*l* and -*h* was observed in A549 cells under FBS (+) and HP (p+) conditions (Figure 5-12). Taken together, we conclude that a small amount of corona proteins on ND-PG-TPP-*l* did not affect its mitochondrial targeting ability and specificity, while the mitochondrial specificity of TPP was lost by formation of a thick protein corona layer on ND-PG-TPP-*h*.

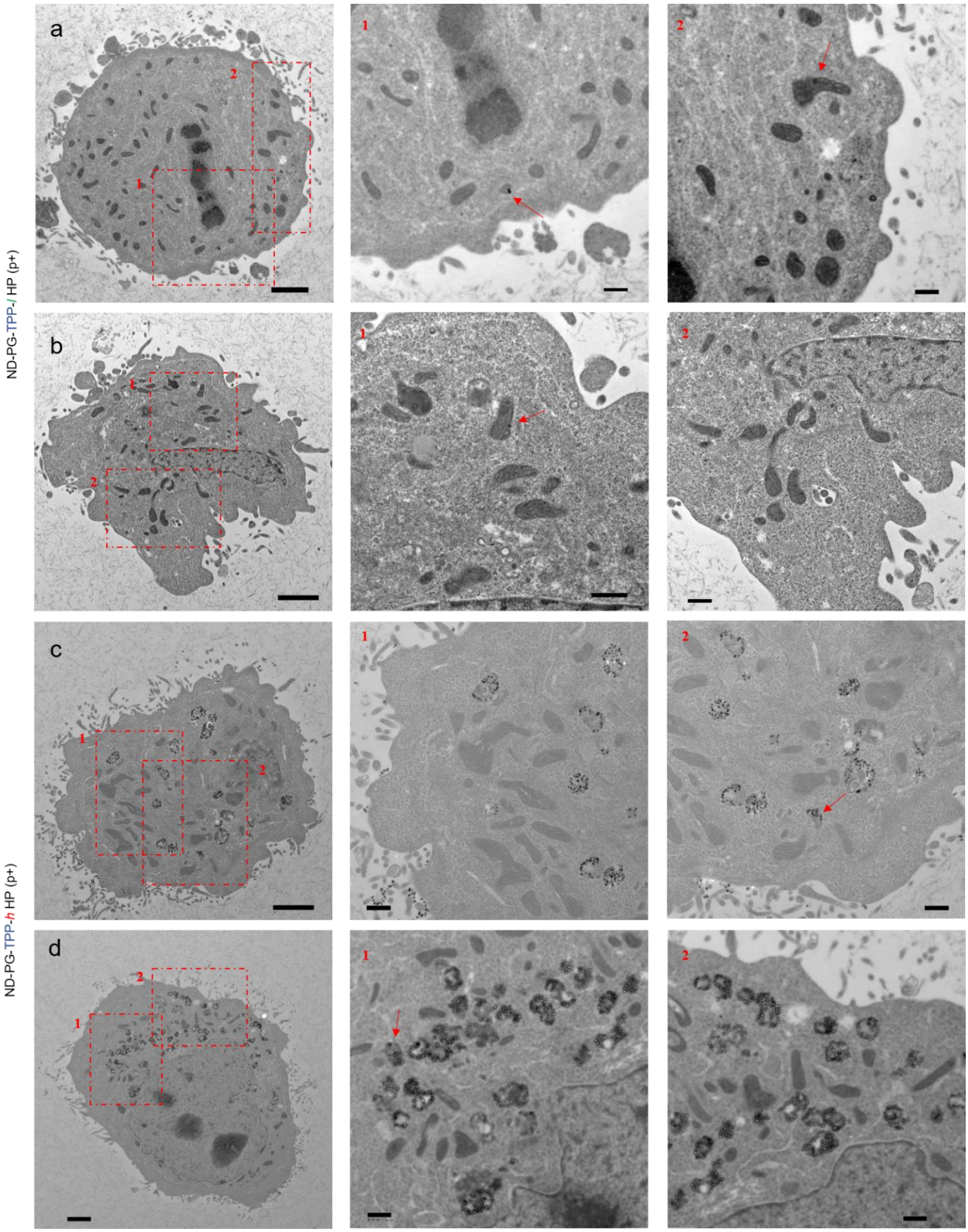

Figure 5-11. TEM images of HeLa cells treated by ND-PG-TPP-*l* HP (p+) (a-b) and ND-PG-TPP-*h* HP (p+) (c-d). The scale bars of low and high magnification ones are 2 μm and 500 nm, respectively. Red arrows indicate the NDs targeted to mitochondria.

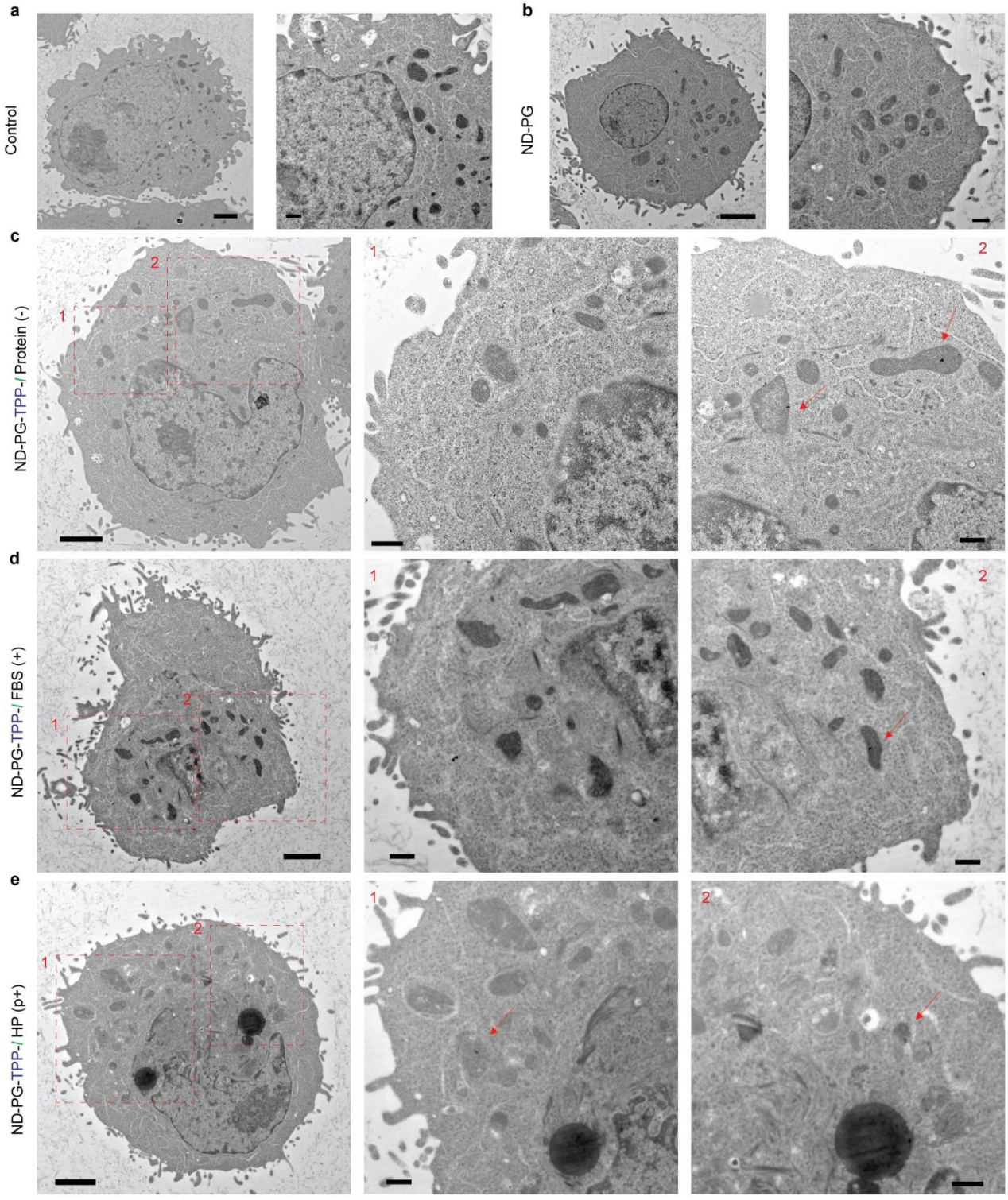
a
Control
b
ND-PG
c
ND-PG-TPP-/ Protein (-)
d
ND-PG-TPP-/ FBS (+)
e
ND-PG-TPP-/ HP (p+)
1
2

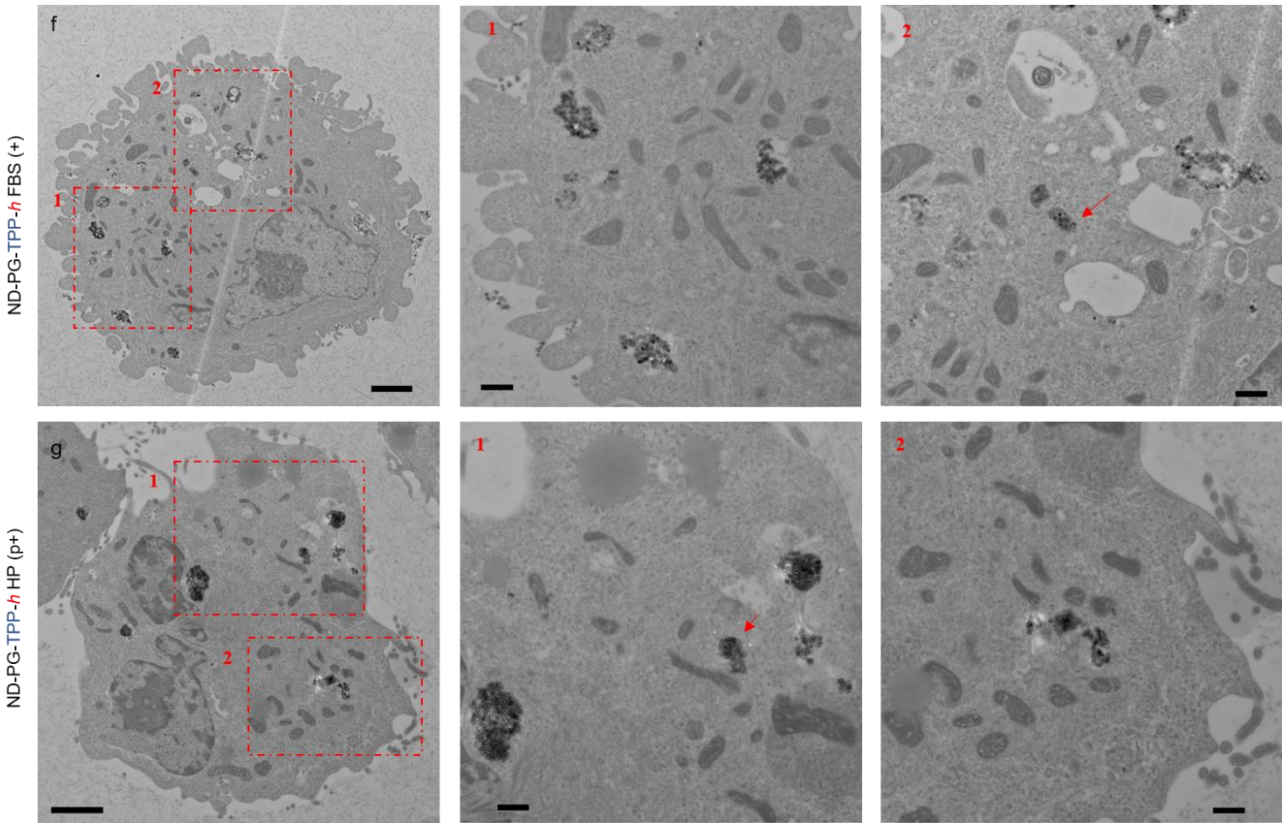

Figure 5-12. TEM images of A549 cells (a) and after their incubation with ND-PG (b), ND-PG-TPP-*l* Protein (−) (c), ND-PG-TPP-*l* FBS (+) (d), ND-PG-TPP-*l* HP (p+) (e), ND-PG-TPP-*h* FBS (+) (f), and ND-PG-TPP-*h* HP (p+) (g). The scale bars of low and high magnification ones are 2 μm and 500 nm, respectively. Red arrows indicate the NDs targeted to mitochondria.

In view of target therapy in nanomedicine, NPs are needed to enter the subcellular organelle of their target cells *in vivo* to elicit a therapeutic effect [111]. Although ND-PG-TPP-*h* was accumulated in mitochondria in larger amount than ND-PG-TPP-*l* in the presence of protein coronas *in vitro* (Figure 5-10 – 5-12), its targeting efficiency *in vivo* may be hampered by the larger amounts of absorbed

proteins, which is known to diminish the NPs from blood circulation by activating the macrophage in MPS to uptake NPs [15]. Therefore, the ND-PG-TPP-*h* with a high protein affinity may be rapidly removed from blood circulation during their *in vivo* transport and cannot reach their target site to fulfill their task. In contrast, the ND-PG-TPP-*l* with a low protein affinity may have a longer retention time in blood, rendering them to reach the mitochondria of their target cells.

5-3 Conclusions

The effect of protein corona on the cytotoxicity and mitochondrial targeting ability of TPP was clarified by functionalizing ND-PG with TPP at *l* and *h* densities. Thanks to the "transparent background" of PG, we demonstrated that the protein adsorption by ND-PG-TPP is proportional to the TPP density. The resulting protein coronas were found to alleviate the cytotoxicity of both ND-PG-TPP-*l* and -*h*. The thinner protein corona layer on ND-PG-TPP-*l* did not affect its mitochondrial targeting ability and selectivity. On the other hand, the thicker protein corona layer on ND-PG-TPP-*h* diminished its selectivity to mitochondria by restricting the NDs inside the endosome and lysosome compartments, though lager amount of ND-PG-TPP-*h* was accumulated in mitochondria. Taken into consideration the role of protein corona facilitating the clearance of NPs by MPS, ND-PG-TPP-*l* with low non-specific uptake should be more promising for *in vivo* mitochondrial targeting.

5-4 Material and methods

5-4-1 Chemicals and materials

ND (50 nm in diameter) was kindly provided by Tomei Diamond Co., Ltd. Japan. The following reagents were purchased from FUJIFILM Wako Pure Chemical Co., Japan: (5-Carboxypentyl)triphenylphosphonium bromide (TPP-COOH), 4-dimethylaminopyridine (DMAP), *N*,*N*-dimethylformamide (DMF), human heparin sodium plasma (pool of donors), sodium dodecyl sulfate (SDS), Dulbecco's modified Eagle medium (DMEM), Ham's F-12K medium (F-12K), 0.25% trypsin-EDTA solution, antibiotics penicillin/streptomycin (100 U/mL), cell counting kit-8 (CCK-8), and 20% glutaraldehyde and paraformaldehyde. The following reagents were purchased from Nacalai Tesque, Inc., Japan: *N*,*N'*-Dicyclohexylcarbodiimide (DCC), pre-stained protein markers (02525-35) and running buffer (30329-61). Protein loading buffer (AE-1430) and 5-20% precast polyacrylamide gel (PAGE, E-R520L) were purchased from ATTO Co., Japan. Glycidol was purchased from Kanto Chemical Co., Inc. Pierce silver stain kit (24600) and bicinchoninic acid (BCA) protein assay kit (T9300A) was supplied by Thermo Fisher Scientific and Takara Bio Inc., Japan, respectively. HeLa cells were kindly provided by Prof. Minoru Suzuki (Kyoto University). Human lung epithelial carcinoma A549 cells (IFO50153) were supplied by Japanese Collection of Research Bioresources Cell Bank. Fetal bovine serum (FBS) was supplied by Biosera, France.

5-4-2 Equipment

Transmission electron microscopy (TEM) of ND, ND-PG and ND-PG-TPP was conducted on a JEM-2200FS field emission microscope (JEOL). Thermogravimetric analysis (TGA) of ND-PG was performed on a Q-50 analyzer (TA Instruments) under N_2 in the temperature range of 50 to 1000 °C at a heating rate of 20 °C/min. The IR spectra were collected on an IR Prestige-21 (Shimadzu Co. Ltd.) in the range of 4000 to 500 cm^{-1} with a resolution of 4 cm^{-1} for 32 scans. ^1H NMR (500 MHz) was recorded on a ECX500 NMR spectrometer (JEOL) in D_2O. The elemental analysis of ND-PG-TPP was performed at Organic Elemental Microanalysis Center of Kyoto University. Dynamic light scattering (DLS) and zeta potential were measured on a Nanotrac UPA-UT151 (Microtrac, Inc., USA) and a ZetaSizer Nano Series (Malvern Instruments, UK), respectively. SDS-PAGE gel was scanned on a GT-X900 scanner (EPSON) with a resolution of 600 dpi. The absorbance of BCA and CCK-8 was recorded on a microtiter plate reader (MTD-310, Corona Electric Co., Japan) at 570 and 450 nm, respectively. The TEM observation of cell samples was carried out on a H-7650 TEM (Hitachi).

5-4-3 Synthesis of ND-PG-TPP

The ND-PG was prepared according to our previous methods [26]. The ND-PG-TPP was synthesized according to the reported procedure with slight modification [126]. The low (*l*) and high (*h*) densities of TPP in ND-PG-TPP were prepared by controlling the amount of TPP-COOH in these reactions. For ND-PG-TPP-*l*, a DMF solution (1.0 mL) of DCC (10 mg) and DMAP (10 mg) was

added dropwise to the DMF suspension (2.5 mL) of ND-PG (10 mg) with stirring. Then, the DMF solution (0.5 mL) of TPP-COOH (20 mg) was added to the mixture and stirred at room temperature overnight. The resulting suspension was dialyzed against Mill-Q H_2O (500 mL) for four times to fully remove the DMF solvent. The ND-PG-TPP-*l* was collected using a centrifugal filter (Millipore Amicon, Ultra-15, 100k) by repeated washing with ethanol/Milli-Q H_2O (1/1 v/v) and pure Milli-Q H_2O. In the preparation of ND-PG-TPP-*h,* 100 mg of TPP-COOH was used in the reaction.

5-4-4 Protein corona formation

The dispersions of ND-PG-TPP-*l*, ND-PG-TPP-*h* and ND-PG (300 μg) were incubated with 10% FBS or 55% HP in 10 mM PBS (1.0 mL) at 37 °C for 1 h. The aggregates from the freshly thawed protein solutions were removed by centrifugation at 23,000*g* for 20 min prior to the incubation. After incubation, the ND-protein complexes were collected by centrifugation at 116,000*g* for 20 min and the free unbound proteins were fully removed by redispersion/centrifugation washing cycles in Milli-Q water (1.0 mL) for three times. Then, the corona proteins were detached by 10% SDS (100 μL) and separated from NDs by another round of centrifugation at 116,000*g* for 20 min. The SDS solution containing the isolated corona proteins was defined as protein corona solution and used for further analyses.

5-4-5 Protein corona analysis

The protein corona was analyzed according to the procedures we reported previously [84, 92]. In the SDS-PAGE analysis, 5 μL of protein corona solution was mixed with 5 μL of protein loading buffer (2×) and boiled at 100 °C for 5 min. Subsequently, the denatured proteins were separated on a 5-20% precast polyacrylamide gel and visualized by a Pierce silver stain kit. The total protein amount was determined via a BCA kit according to the manufacturer's instruction.

5-4-6 Cell culture

HeLa and A549 cells were maintained in DMEM and F-12K culture media, respectively, supplemented with 10% FBS and 1% antibiotics penicillin/streptomycin. The cells were incubated at 37 °C in a humidified incubator (MCO-5ACUV-PJ, Panasonic Co., Japan) supplied with 5% CO_2. Cells were passaged once the confluent reached 70-80%.

5-4-7 Cytotoxicity assay of ND-PG-TPP with and without a protein corona

HeLa cells were seeded in a 96-well plate at a density of 8×10^3 cells per well. After 24 h incubation, the culture medium was replaced with fresh medium supplemented with or without 10% FBS. The dispersions of ND-PG, ND-PG-TPP-*l* and ND-PG-TPP-*h* with ND concentrations of 25, 50 and 100 μg/mL (material concentrations of 38, 76 and 152 μg/mL based on Figure 5-2) were added to the medium. After further incubation of 4, 12 and 24 h, the cell viability was assayed by a CCK-8 kit following the manufacturer's instruction. The cells without ND treatment at each time point were used as controls. Cell viability was calculated as the absorbance of ND-treated cells vs the ones of control

cells × 100%. In addition to the above assays, the cytotoxicity of ND-PG-TPP precoated with 10% FBS and 55% HP was assayed in HeLa and A549 cells in a serum-free culture medium with ND concentration of 50 μg/mL at 4, 12 and 24 h. ND-PG-TPP was precoated with 10% FBS and 55% HP in a procedure similar to that in the protein corona formation mentioned above. The experimental conditions are summarized in Table 5-3. The data were analyzed by two-tailed Student's t-test.

5-4-8 TEM observation of the mitochondrial targeting by ND-PG-TPP with and without a protein corona

HeLa and A549 cells were seeded into a ϕ 60 mm cell culture dish at a density of 6×10^5 cells per dish. After overnight incubation to allow cell adhesion, the suspensions of ND-PG-TPP-*l* and ND-PG-TPP-*h* with or without protein corona were applied to the fresh medium in a procedure similar to that of cell viability assay. The concentration of NDs in each dish was adjusted to be 50 μg/mL (material concentrations of 76 μg/mL based on Figure 5-2). Cells treated by PBS and ND-PG in medium of FBS (+) were also prepared. After 12 h incubation, cell pellets were collected and prefixed with 2% glutaraldehyde/4% paraformaldehyde in 100 mM PBS buffer (1 mL) overnight, followed by post-fixation with 1% osmium tetroxide for 2 h. Then, the cell pellets were dehydrated in ethanol series and passed through propylene oxide/epoxy resin (1/1 and 1/3) mixtures, embedded in epoxy resin and baked at 60 °C for 48 h. Finally, the frontal sections (60 − 80 nm) were cut by an ultramicrotome (EM UC6, Leica, Germany) and stained with uranyl acetate and lead citrate for observation.

Chapter 6: Conclusion

In this thesis, the author has quantitatively studied the protein corona formation and subsequent cellular uptake of NPs functionalized by PG and its derivatives.

By performing a comparison study on the protein corona formation and macrophage uptake of NP-PG and NP-PEG, the author demonstrated that PG resisted protein adsorption and macrophage uptake much more efficiently than did PEG. Particularly, dense PG grafting shielded NPs from protein corona formation and macrophage uptake almost completely. Based on corona-free PG interface, the author assessed the net interactions between charged functional groups and proteins quantitatively, and revealed that the charged functional groups exclusively interacted with proteins of opposite charge in a charge-density dependent manner. Then, the author probed the roles of charged functional groups in protein absorption and cellular uptake, and demonstrated that the cellular uptake efficacy and mechanisms of charged NPs were dictated by their affinity to proteins and distinct protein corona compositions formed on their surface, respectively. Lastly, the author investigated the effect of protein corona on the mitochondrial targeting ability of TPP functionalization. It was revealed that a thinner protein corona layer on the surface of TPP functionalized NP did not affect its targeting ability, whereas a thicker protein corona layer diminished its targeting specificity.

The findings presented in this thesis will contribute to understanding of protein corona formation and provide new strategies for 1) shielding NPs from protein corona formation to avoid non-specific uptake, 2) comparing the protein affinity of various NP surface coatings quantitatively, 3) controlling

cellular uptake of NPs by tuning the protein corona composition, and 4) designing NPs with active targeting moiety for more precise and safer delivery in subcellular level.

References

1. Jeevanandam, J., et al., *Review on nanoparticles and nanostructured materials: history, sources, toxicity and regulations.* Beilstein J. Nanotechnol., 2018. **9**: p. 1050-1074.

2. Ijaz, I., et al., *Detail review on chemical, physical and green synthesis, classification, characterizations and applications of nanoparticles.* Green Chem. Lett. Rev., 2020. **13**(3): p. 59-81.

3. Huang, C.H., et al., *Effect of structure: A new insight into nanoparticle assemblies from inanimate to animate.* Sci. Adv., 2020. **6**(20): p. eaba1321.

4. Liu, X.S., et al., *Surface tailoring of nanoparticles via mixed-charge monolayers and their biomedical applications.* Small, 2014. **10**(21): p. 4230-4242.

5. Lim, E.K., et al., *Nanomaterials for theranostics: Tecent advances and future challenges.* Chem. Rev., 2015. **115**(1): p. 327-394.

6. Greish, K., *Enhanced permeability and retention (EPR) effect for anticancer nanomedicine drug targeting.* Cancer Nanotechnol., 2010. **624**: p. 25-37.

7. Blanco, E., et al., *Principles of nanoparticle design for overcoming biological barriers to drug delivery.* Nat. Biotechnol., 2015. **33**(9): p. 941-951.

8. Mi, P., et al., *Ligand-installed nanocarriers toward precision therapy.* Adv. Mater., 2020. **32**(13): p. 1902604.

9. Yoshino, F., et al., *Preferential tumor accumulation of polyglycerol functionalized*

nanodiamond conjugated with cyanine dye leading to near-infrared fluorescence in vivo tumor imaging. Small, 2019. **15**(48): p.1901930.

10. Liu, G., et al., *Direct fabrication of the graphene-based composite for cancer phototherapy through graphite exfoliation with a photosensitizer.* ACS Appl. Mater. Interfaces, 2015. **7**(42): p. 23402-23406.

11. Caracciolo, G., et al., *Biological identity of nanoparticles in vivo: Clinical implications of the protein corona.* Trends Biotechnol., 2017. **35**(3): p. 257-264.

12. Monopoli, M.P., et al., *Biomolecular coronas provide the biological identity of nanosized materials.* Nat. Nanotechnol., 2012. **7**(12): p. 779-786.

13. Zanganeh, S., et al., *Protein corona: Opportunities and challenges.* Int. J. Biochem. Cell Biol., 2016. **75**: p. 143-147.

14. Gunawan, C., et al., *Nanoparticle-protein corona complexes govern the biological fates and functions of nanoparticles.* J. Mater. Chem. B., 2014. **2**(15): p. 2060-2083.

15. Poon, W., et al., *A framework for designing delivery systems.* Nat. Nanotechnol., 2020. **15**(10): p. 819-829.

16. Salvati, A., et al., *Transferrin-functionalized nanoparticles lose their targeting capabilities when a biomolecule corona adsorbs on the surface.* Nat. Nanotechnol., 2013. **8**(2): p. 137-143.

17. Lesniak, A., et al., *Nanoparticle adhesion to the cell membrane and itseffect on nanoparticle*

uptake efficiency. J. Am. Chem. Soc., 2013. **135**(4): p. 1438-1444.

18. Kreuter, J., et al., *Apolipoprotein-mediated transport of nanoparticle-bound drugs across the blood-brain barrier.* J. Drug Target., 2002. **10**(4): p. 317-325.

19. Schottler, S., et al., *Controlling the stealth effect of nanocarriers through understanding the protein corona.* Angew. Chem., Int. Ed., 2016. **55**(31): p. 8806-8815.

20. Amoozgar, Z. and Y. Yeo, *Recent advances in stealth coating of nanoparticle drug delivery systems.* WIRES Nanomed. Nanobi., 2012. **4**(2): p. 219-233.

21. Pelaz, B., et al., *Surface functionalization of nanoparticles with polyethylene glycol: Effects on protein adsorption and cellular uptake.* ACS Nano, 2015. **9**(7): p. 6996-7008.

22. Abu Lila, A.S., et al., *The accelerated blood clearance (ABC) phenomenon: Clinical challenge and approaches to manage.* J. Control. Release, 2013. **172**(1): p. 38-47.

23. Zhang, L., et al., *Zwitterionic hydrogels implanted in mice resist the foreign-body reaction.* Nat. Biotechnol., 2013. **31**(6): p. 553-556.

24. Garcia, K.P., et al., *Zwitterionic-coated "stealth" nanoparticles for biomedical applications: Recent advances in countering biomolecular corona formation and uptake by the mononuclear phagocyte system.* Small, 2014. **10**(13): p. 2516-2529.

25. Han, H.S., et al., *Spatial charge configuration regulates nanoparticle transport and binding behavior in vivo.* Angew Chem. Int. Ed., 2013. **52**(5): p. 1414-1419.

26. Zhao, L., et al., *Chromatographic separation of highly soluble diamond nanoparticles prepared by polyglycerol grafting.* Angew Chem. Int. Ed., 2011. **50**(6): p. 1388-1392.

27. Zhao, L., et al., *Hyperbranched polyglycerol-grafted superparamagnetic iron oxide nanoparticles: Synthesis, characterization, functionalization, size separation, magnetic properties, and biological applications.* Adv. Funct. Mater., 2012. **22**(24): p. 5107-5117.

28. Zhao, L., et al., *Polyglycerol-coated nanodiamond as a macrophage-evading platform for selective drug delivery in cancer cells.* Biomaterials, 2014. **35**(20): p. 5393-5406.

29. Lee, Y.K., et al., *Effect of the protein corona on nanoparticles for modulating cytotoxicity and immunotoxicity.* Int. J. Nanomedicine, 2015. **10**: p. 97-112.

30. Donahue, N.D., et al, *Concepts of nanoparticle cellular uptake, intracellular trafficking, and kinetics in nanomedicine.* Adv. Drug Deliv. Rev., 2019. **143**: p. 68-96.

31. Docter, D., et al., *The nanoparticle biomolecule corona: Lessons learned - challenge accepted?* Chem. Soc. Rev., 2015. **44**(17): p. 6094-6121.

32. Tonigold, M., et al., *Pre-adsorption of antibodies enables targeting of nanocarriers despite a biomolecular corona.* Nat. Nanotechnol., 2018. **13**(9): p. 862-829.

33. Lee, H., *Effects of nanoparticle electrostatics and protein-protein interactions on corona formation: Conformation and hydrodynamics.* Small, 2020. **16**(10): p. 1906598.

34. Walkey, C.D., et al., *Protein corona fingerprinting predicts the cellular interaction of gold and*

silver nanoparticles. ACS Nano, 2014. **8**(3): p. 2439-2455.

35. Kozma, G.T., et al., *Pseudo-anaphylaxis to polyethylene glycol (PEG)-coated liposomes: Roles of anti-PEG IgM and complement activation in a porcine model of human infusion reactions.* ACS Nano, 2019. **13**(8): p. 9315-9324.

36. Zahednezhad, F., et al., *Liposome and immune system interplay: Challenges and potentials.* J. Control. Release, 2019. **305**: p. 194-209.

37. Hadjidemetriou, M., et al., *The human in vivo biomolecule corona onto PEGylated liposomes: A proof-of-concept clinical study.* Adv. Mater., 2019. **31**(4): p. 1803335.

38. Cai, R. and C. Chen, *The crown and the scepter: Roles of the protein corona in nanomedicine.* Adv. Mater., 2019. **31**(45): p. 1805740.

39. Han, G.S. and D.W. Domaille, *Protein corona, with a twist.* ACS Cent. Sci., 2020. **6**(1): p. 14-15.

40. Schöttler, S., et al., *Protein adsorption is required for stealth effect of poly(ethylene glycol)- and poly(phosphoester)-coated nanocarriers.* Nat. Nanotechnol., 2016. **11**: p. 372-377.

41. Vroman, L., *Effect of adsorbed proteins on the wettability of hydrophilic and hydrophobic solids.* Nature, 1962. **196**(4853): p. 476-477.

42. Chen, S., et al., *Surface hydration: Principles and applications toward low-fouling/nonfouling biomaterials.* Polymer, 2010. **51**(23): p. 5283-5293.

43. Siegers, C., et al., *Self-assembled monolayers of dendritic polyglycerol derivatives on gold that resist the adsorption of proteins.* Chem. Eur. J., 2004. **10**(11): p. 2831-2838.

44. Wyszogrodzka, M. and R. Haag, *Study of single protein adsorption onto monoamino oligoglycerol derivatives: A structure−activity relationship.* Langmuir, 2009. **25**(10): p. 5703-5712.

45. Wyszogrodzka, M. and R. Haag, *Synthesis and characterization of glycerol dendrons, self-assembled monolayers on gold: A detailed study of their protein resistance.* Biomacromolecules, 2009. **10**(5): p. 1043-1054.

46. Li, X., et al., *Cationic polyarginine conjugated mesoporous bioactive glass nanoparticles with polyglycerol coating for efficient DNA delivery.* J. Biomed. Nanotechnol., 2017. **13**(3): p. 280-289.

47. Qin, H., et al., *Hyperbranched polyglycerol-grafted titanium oxide nanoparticles: Synthesis, derivatization, characterization, size separation, and toxicology.* Mater. Res. Express, 2016. **3**(10): p. 105049.

48. Mochalin, V.N. and Y. Gogotsi, *Wet chemistry route to hydrophobic blue fluorescent nanodiamond.* J. Am. Chem. Soc., 2009. **131**: p. 4594-4595.

49. Kusterle, M., et al., *Size of Pegylated protein conjugates studied by various methods.* Acta Chim. Slov., 2008. **55**: p. 594–601.

50. Perry, J.L., et al., *PEGylated PRINT nanoparticles: The impact of PEG density on protein binding, macrophage association, biodistribution, and pharmacokinetics.* Nano Lett., 2012. **12**(10): p. 5304-5310.

51. Bertrand, N., et al., *Mechanistic understanding of in vivo protein corona formation on polymeric nanoparticles and impact on pharmacokinetics.* Nat. Commun., 2017. **8**(1): p. 777.

52. Oh, J.Y., et al., *Cloaking nanoparticles with protein corona shield for targeted drug delivery.* Nat. Commun., 2018. **9**(1): p. 4548.

53. Larsen, M.T., et al., *Albumin-based drug delivery: Harnessing nature to cure disease.* Mol. Cell. Ther., 2016. **4**: p. 3.

54. Abu Lila, A.S., et al., *Use of polyglycerol (PG), instead of polyethylene glycol (PEG), prevents induction of the accelerated blood clearance phenomenon against long-circulating liposomes upon repeated administration.* Int. J. Pharm., 2013. **456**(1): p. 235-242.

55. Oh, N. and J.-H. Park, *Surface chemistry of gold nanoparticles mediates their exocytosis in macrophages.* ACS Nano, 2014. **8**(6): p. 6232-6241.

56. García, I., et al., *Glycans as biofunctional ligands for gold nanorods: stability and targeting in protein-rich media.* J. Am. Chem. Soc., 2015. **137**(10): p. 3686-3692.

57. Saha, K., et al., *Regulation of macrophage recognition through the interplay of nanoparticle surface functionality and protein corona.* ACS Nano, 2016. **10**(4): p. 4421-4430.

58. Rubio, N., et al., *Grafting from versus grafting to approaches for the functionalization of graphene nanoplatelets with poly(methyl methacrylate).* Macromolecules, 2017. **50**(18): p. 7070-7079.

59. Calderón, M., et al., *Dendritic polyglycerols for biomedical applications.* Adv. Mater., 2010. **22**: p. 190-218.

60. Pham, T.A., et al., *Covalent functionalization of graphene oxide with polyglycerol and their use as templates for anchoring magnetic nanoparticles.* Synth. Metals, 2010. **160**(17): p. 2028-2036.

61. Adeli, M., et al., *Carbon nanotubes-graft-polyglycerol: Biocompatible hybrid materials for nanomedicine.* Polymer, 2009. **50**(15): p. 3528-3536.

62. Zhao, L., et al., *Platinum on nanodiamond: A promising prodrug conjugated with stealth polyglycerol, targeting peptide and acid-responsive antitumor drug.* Adv. Funct. Mater., 2014. **24**(34): p. 5348-5357.

63. Yin, T., et al., *Superparamagnetic Fe3O4-PEG2K-FA@Ce6 nanoprobes for in vivo dual-mode imaging and targeted photodynamic therapy.* Sci. Rep., 2016. **6**: p. 36187.

64. Jing, X.N., et al., *Controlled synthesis of water-dispersible and superparamagnetic Fe3O4 nanomaterials by a microwave-assisted solvothermal method: From nanocrystals to nanoclusters.* Crystengcomm, 2017. **19**(34): p. 5089-5099.

65. Docter, D., et al., *Quantitative profiling of the protein coronas that form around nanoparticles.* Nat. Protoc., 2014. **9**(9): p. 2030-2044.

66. Yuan, Y., et al., *Biodistribution and fate of nanodiamonds in vivo.* Diamond Related Mater., 2009. **18**(1): p. 95-100.

67. Cedervall, T., et al., *Understanding the nanoparticle–protein corona using methods to quantify exchange rates and affinities of proteins for nanoparticles.* Proc. Natl. Acad. Sci., 2007. **104**(7): p. 2050-2055.

68. Lundqvist, M., et al., *Nanoparticle size and surface properties determine the protein corona with possible implications for biological impacts.* Proc. Natl. Acad. Sci., 2008. **105**(38): p. 14265-14270.

69. Mahmoudi, M., et al., *Emerging understanding of the protein corona at the nano-bio interfaces.* Nano Today, 2016. **11**(6): p. 817-832.

70. Calatayud, M.P., et al., *The effect of surface charge of functionalized Fe3O4 nanoparticles on protein adsorption and cell uptake.* Biomaterals, 2014. **35**(24): p. 6389-6399.

71. Shang, L. and G.U. Nienhaus, *In situ characterization of protein adsorption onto nanoparticles by fluorescence correlation spectroscopy.* Acc. Chem. Res., 2017. **50**(2): p. 387-395.

72. Aggarwal, P., et al., *Nanoparticle interaction with plasma proteins as it relates to particle biodistribution, biocompatibility and therapeutic efficacy.* Adv. Drug Deliv. Rev., 2009. **61**(6):

p. 428-437.

73. Shang, L., et al., *Nanoparticles interacting with proteins and cells: A systematic study of protein surface charge effects.* Adv. Mater. Interfaces, 2014. **1**(2): p. 1300079.

74. Zhang, X., et al., *Probing the binding affinity of plasma proteins adsorbed on Au nanoparticles.* Nanoscale, 2017. **9**(14): p. 4787-4792.

75. Hühn, D., et al., *Polymer-coated nanoparticles interacting with proteins and cells: Focusing on the sign of the net charge.* ACS Nano, 2013. **7**(4): p. 3253-3263.

76. Tenzer, S., et al., *Rapid formation of plasma protein corona critically affects nanoparticle pathophysiology.* Nat. Nanotechnol., 2013. **8**(10): p. 772.

77. Sakulkhu, U., et al., *Protein corona composition of superparamagnetic iron oxide nanoparticles with various physico-chemical properties and coatings.* Sci. Rep., 2014. **4**(1): p. 5020.

78. Sun, J., et al., *Protein binding on the surface of magnetic nanoparticles.* Part. Part. Syst. Charact., 2019. **36**(8): p. 1900072.

79. Huber, R. and S. Stoll, *Protein affinity for TiO2 and CeO2 manufactured nanoparticles. From ultra-pure water to biological media.* Colloids and Surf. A, 2018. **553**: p. 425-431.

80. Gessner, A., et al., *Functional groups on polystyrene model nanoparticles: Influence on protein adsorption.* J. Biomed. Mater. Res. A, 2003. **65A**(3): p. 319-326.

81. Garcia-Bennett, A.E., et al., *Influence of surface chemistry on the formation of a protein corona on nanodiamonds.* J. Mater. Chem. B, 2019. **7**(21): p. 3383-3389.

82. Kurtz-Chalot, A., et al., *Impact of silica nanoparticle surface chemistry on protein corona formation and consequential interactions with biological cells.* Mater. Sci. Eng. C, 2017. **75**: p. 16-24.

83. Hadjidemetriou, M. and K. Kostarelos, *Evolution of the nanoparticle corona.* Nat. Nanotechnol., 2017. **12**(4): p. 288-290.

84. Zou, Y., et al., *Polyglycerol grafting shields nanoparticles from protein corona formation to avoid macrophage uptake.* ACS Nano, 2020. **14**(6): p. 7216-7226.

85. Aramesh, M., et al., *Surface charge effects in protein adsorption on nanodiamonds.* Nanoscale, 2015. **7**(13): p. 5726-5736.

86. Carter, D.C. and Ho, J.X. *Structure of serum albumin.* Adv. Protein Chem., 1994. **45**: p. 153-203.

87. Behzadi, S., et al., *Cellular uptake of nanoparticles: Journey inside the cell.* Chem. Soc. Rev., 2017. **46**(14): p. 4218-4244.

88. Melby, E.S., et al., *Cascading effects of nanoparticle coatings: Surface functionalization dictates the assemblage of complexed proteins and subsequent interaction with model cell membranes.* ACS Nano, 2017. **11**(6): p. 5489-5499.

89. Kokkinopoulou, M., et al., *Visualization of the protein corona: towards a biomolecular understanding of nanoparticle-cell-interactions.* Nanoscale, 2017. **9**(25): p. 8858-8870.

90. Cai, R., et al., *Corona of thorns: The surface chemistry-mediated protein corona perturbs the recognition and immune response of macrophages.* ACS Appl. Mater. Interfaces, 2020. **12**(2): p. 1997-2008.

91. Rocker, C., et al., *A quantitative fluorescence study of protein monolayer formation on colloidal nanoparticles.* Nat. Nanotechnol., 2009. **4**(9): p. 577-580.

92. Zou, Y. and N. Komatsu, *Quantitative investigation of the interaction between proteins and charged functional groups on the polyglycerol-grafted nanodiamond surface.* Carbon, 2020. **163**: p. 395-401.

93. Turk, H., et al., *Dendritic polyglycerol sulfates as new heparin analogues and potent inhibitors of the complement system.* Bioconjug. Chem., 2004. **15**(1): p. 162-167.

94. O'Brien, J. and K.J. Shea, *Tuning the protein corona of hydrogel nanoparticles: The synthesis of abiotic protein and peptide affinity reagents.* Acc Chem. Res., 2016. **49**(6): p. 1200-1210.

95. Dernedde, J., et al., *Dendritic polyglycerol sulfates as multivalent inhibitors of inflammation.* Proc. Natl. Acad. Sci., 2010. **107**(46): p. 19679-19684.

96. Garcia-Alvarez, R., et al., *In vivo formation of protein corona on gold nanoparticles. The effect of their size and shape.* Nanoscale, 2018. **10**(3): p. 1256-1264.

97. Iruela-Arispe, M. L., *Regulation of thrombospondin1 by extracellular proteases.* Curr. Drug Targets, 2008. **9**(10): p. 863-868.

98. Tan, K., et al., *The structures of the thrombospondin-1 N-terminal domain and its complex with a synthetic pentameric heparin.* Structure, 2006. **14**(1): p. 33-42.

99. Rades, N., et al., *Dendritic polyglycerol sulfate for therapy and diagnostics.* Polymers, 2018. **10**(6): p. 595.

100. Simonsen, J.B. and R. Munter, *Pay attention to biological nanoparticles when studying the protein corona on nanomedicines.* Angew Chem. Int. Ed., 2020. **59**(31): p. 12584-12588.

101. Sanchez-Guzman, D., et al., *In situ analysis of weakly bound proteins reveals molecular basis of soft corona formation.* ACS Nano, 2020. **14**(7): p. 9073-9088.

102. Francia, V., et al., *Corona composition can affect the mechanisms cells use to internalize nanoparticles.* ACS Nano, 2019. **13**(10): p. 11107-11121.

103. Lesniak, A., et al., *Effects of the presence or absence of a protein corona on silica nanoparticle uptake and impact on cells.* ACS Nano, 2012. **6**(7): p. 5845-5857.

104. Adamiak, L., et al., *Peptide brush polymers and nanoparticles with enzyme-regulated structure and charge for inducing or evading macrophage cell uptake.* ACS Nano, 2017. **11**(10): p. 9877-9888.

105. Xin, H., et al., *The brain targeting mechanism of angiopep-conjugated poly(ethylene glycol)-*

co-poly(epsilon-caprolactone) nanoparticles. Biomaterials, 2012. **33**(5): p. 1673-81.

106. Tu, Z., et al., *Combination of surface charge and size controls the cellular uptake of functionalized graphene sheets.* Adv. Funct. Mater., 2017. **27**(33): p. 1701837.

107. Vogel S.M., et al., *Albumin uptake and transcytosis in endothelial cells in vivo induced by albumin-binding protein.* Am. J. Physiol. Lung Cell Mol. Physiol., 2001. **281**: p. 1512-1522.

108. Chen, D., et al., *Protein corona-enabled systemic delivery and targeting of nanoparticles.* AAPS J., 2020. **22**(4): p. 83.

109. Mirshafiee, V., et al., *Protein corona significantly reduces active targeting yield.* Chem. Commun., 2013. **49**(25): p. 2557-2559.

110. Su, G., et al., *Effects of protein corona on active and passive targeting of cyclic RGD peptide-functionalized PEGylation nanoparticles.* Mol. Pharmaceutics, 2018. **15**(11): p. 5019-5030.

111. Rosenblum, D., et al., *Progress and challenges towards targeted delivery of cancer therapeutics.* Nat. Commun., 2018. **9**(1): p. 1410.

112. Wang, J.Y., et al., *Triphenylphosphonium (TPP)-based antioxidants: A new perspective on antioxidant design.* ChemMedChem, 2020. **15**(5): p. 404-410.

113. Zielonka, J., et al., *Mitochondria-targeted triphenylphosphonium-based compounds: Syntheses, mechanisms of action, and therapeutic and diagnostic applications.* Chem. Rev., 2017. **117**(15): p. 10043-10120.

114. Battogtokh, G., et al., *Mitochondria-targeting drug conjugates for cytotoxic, anti-oxidizing and sensing purposes: Current strategies and future perspectives.* Acta Pharm. Sin. B., 2018. **8**(6): p. 862-880.

115. Reina, G., et al., *Chemical functionalization of nanodiamonds: Opportunities and challenges ahead.* Angew. Chem. Int. Ed., 2019. **58**(50): p. 17918-17929.

116. Jariwala, D.H., et al., *Surface functionalization of nanodiamonds for biomedical applications.* Mater. Sci. Eng. C, 2020. **113**: p. 110996.

117. Han, X., et al., *Triphenylphosphonium-modified mitochondria-targeted paclitaxel nanocrystals for overcoming multidrug resistance.* Asian J. Pharm. Sci., 2019. **14**(5): p. 569-580.

118. Liu, H.-N., et al., *Mitochondrial targeted doxorubicin-triphenylphosphonium delivered by hyaluronic acid modified and pH responsive nanocarriers to breast tumor: In vitro and in vivo studies.* Mol. Pharmaceutics, 2018. **15**(3): p. 882-891.

119. Biswas, S., et al., *Liposomes loaded with paclitaxel and modified with novel triphenylphosphonium-PEG-PE conjugate possess low toxicity, target mitochondria and demonstrate enhanced antitumor effects in vitro and in vivo.* J. Control. Release, 2012. **159**(3): p. 393-402.

120. Biswas, S., et al., *Surface conjugation of triphenylphosphonium to target poly(amidoamine) dendrimers to mitochondria.* Biomaterials, 2012. **33**(18): p. 4773-4782.

121. Wang, Z., et al., *Targeted delivery of geranylgeranylacetone to mitochondria by triphenylphosphonium modified nanoparticles: A promising strategy to prevent aminoglycoside-induced hearing loss.* Biomater. Sci., 2017. **5**(9): p. 1800-1809.

122. Bielski, E.R., et al., *Effect of the conjugation density of triphenylphosphonium cation on the mitochondrial targeting of poly(amidoamine) dendrimers.* Mol. Pharmaceutics, 2015. **12**(8): p. 3043-3053.

123. Boatman, E., et al., *Morphology, morphometry and electron microscopy of HeLa cells infected with bovine mycoplasma.* Cell Tissue Res., 1976. **170**(1): p. 1-16.

124. Chakraborty, A. and N.R. Jana, *Design and synthesis of triphenylphosphonium functionalized nanoparticle probe for mitochondria targeting and imaging.* J. Phys. Chem. C, 2015. **119**(5): p. 2888-2895.

125. Smith, S.A., et al., *The endosomal escape of nanoparticles: Toward more efficient cellular delivery.* Bioconjug. Chem., 2019. **30**(2): p. 263-272.

126. Marrache, S. and S. Dhar, *Engineering of blended nanoparticle platform for delivery of mitochondria-acting therapeutics.* Proc. Natl. Acad. Sci., 2012. **109**(40): p. 16288-16293.

Appendix I

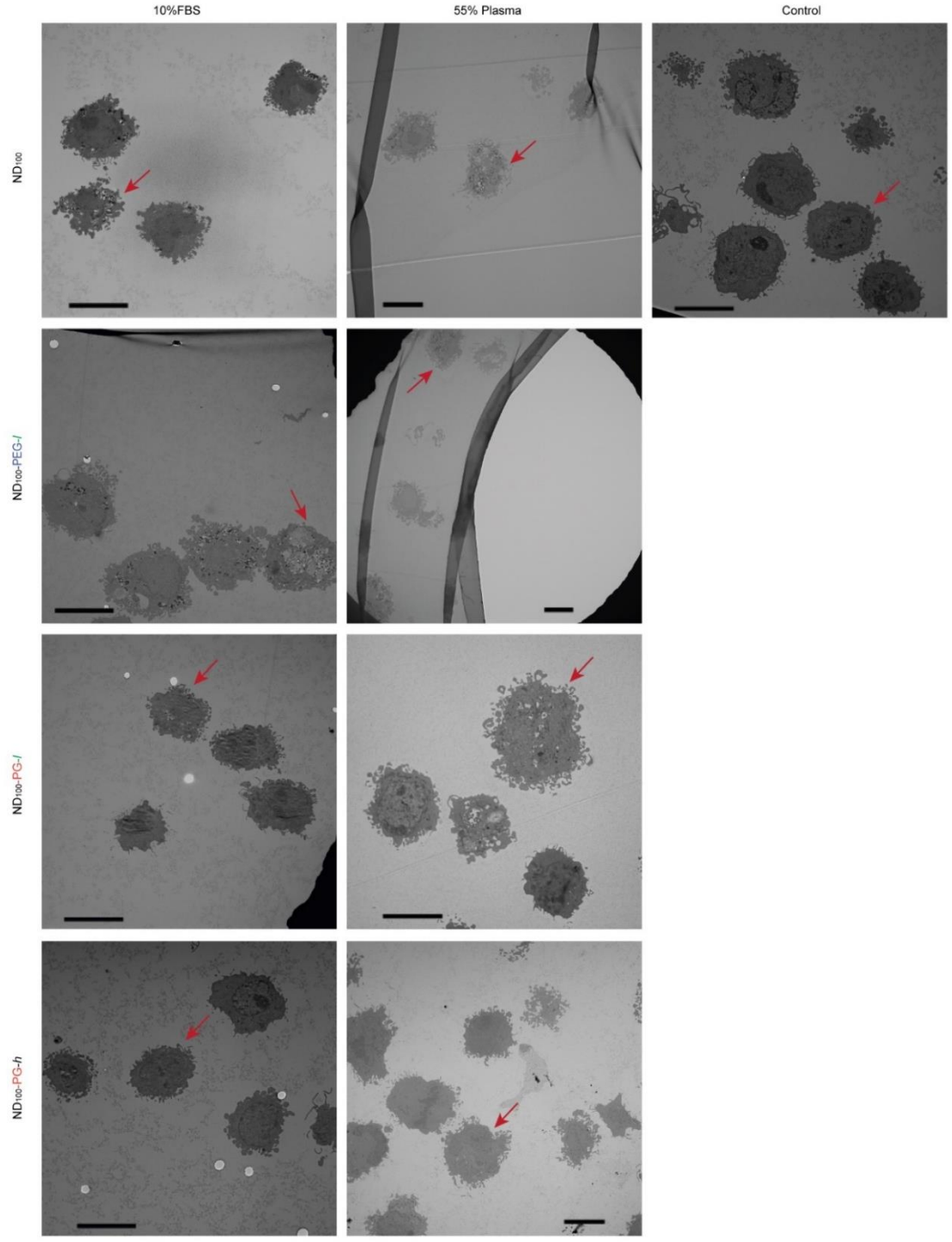

Appendix Figure 1-1. TEM images of NDs taken up by U937 macrophage at cell population magnification. The red arrow indicated the cells shown in Figure 2-8. These images indicated that not only the cells in Figure 2-8, but also other cells had a similar uptake behavior. Scale bar: 10 μm. Additional images are shown in Appendix Figure 1-2 and 1-3 for further verification.

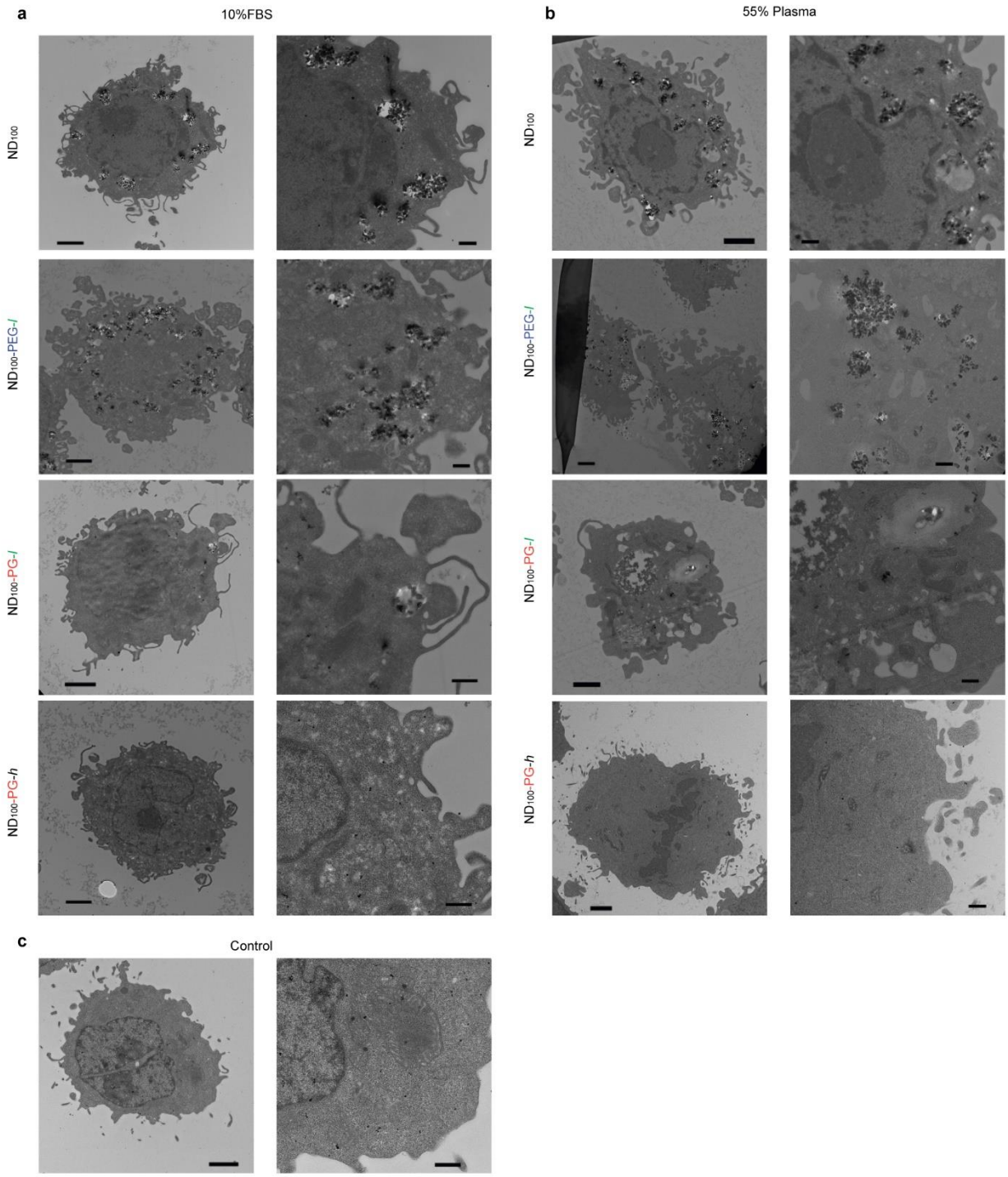

Appendix Figure 1-2. Additional TEM images evidencing the uptake behavior of PG and PEG coated NDs. Low and high magnification images are shown for each sample. Left images are low magnification images (scale bar: 2 μm) and right images are for high magnification images (scale bar: 500 nm).

a) 10% FBS

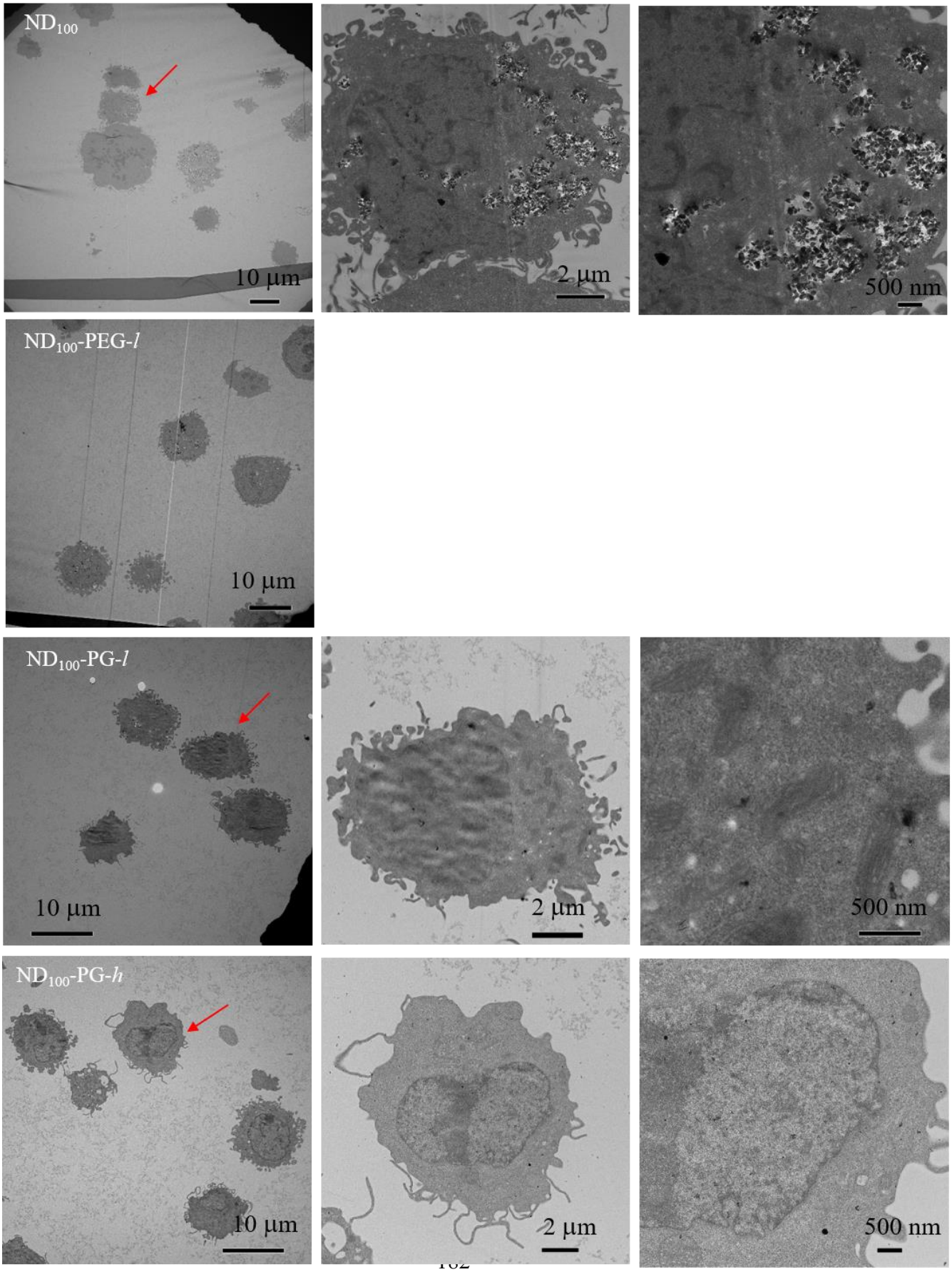
ND100
10 µm
2 µm
500 nm
ND100-PEG-l
10 µm
ND100-PG-l
10 µm
2 µm
500 nm
ND100-PG-h
10 µm
2 µm
500 nm

b) 55% Plasma

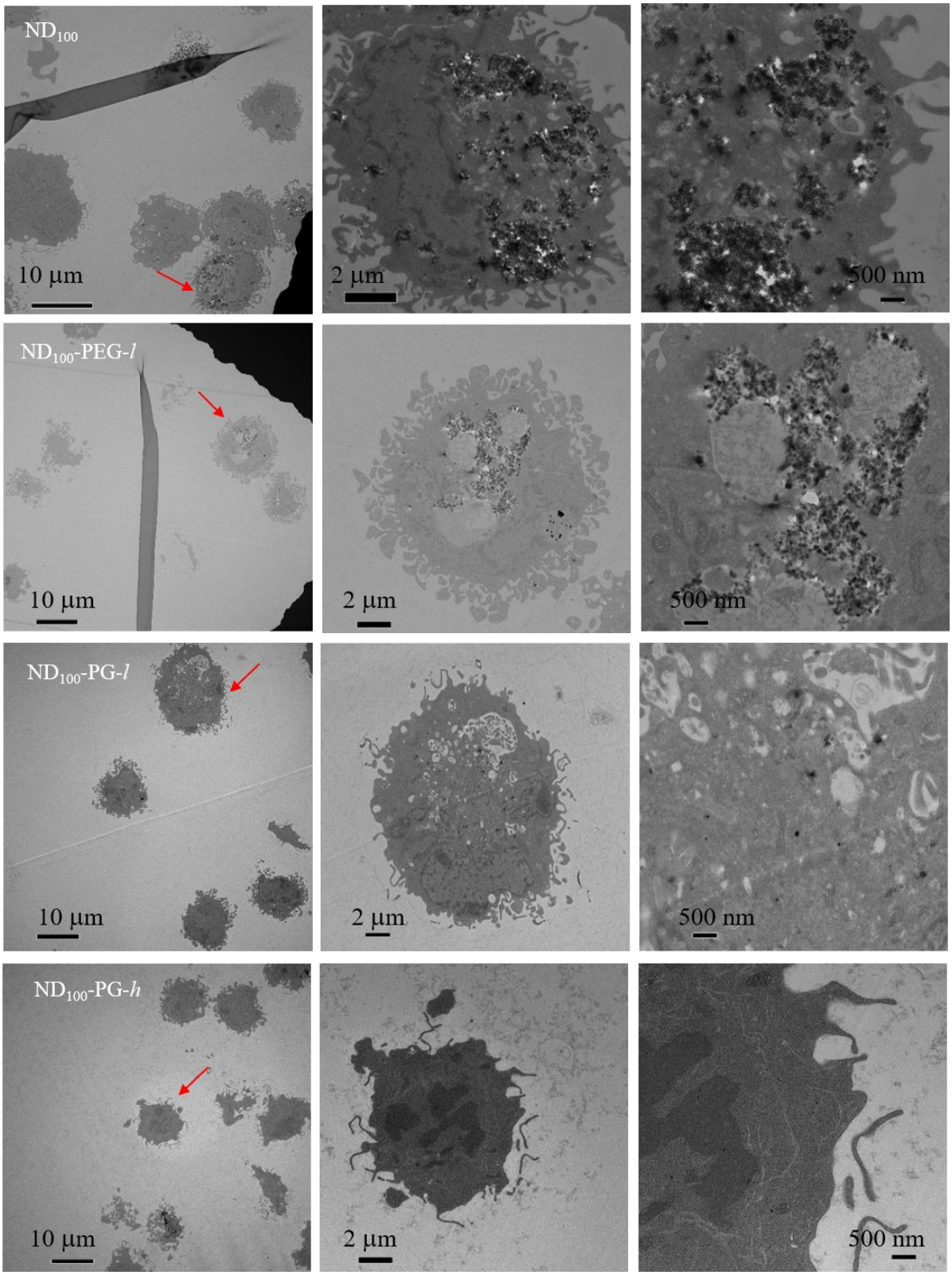
ND100
10 µm
2 µm
500 nm
ND100-PEG-l
10 µm
2 µm
500 nm
ND100-PG-l
10 µm
2 µm
500 nm
ND100-PG-h
10 µm
2 µm
500 nm

c) More images about ND_{100}-PEG-*l* and ND_{100}-PG-*l* in 55% Plasma

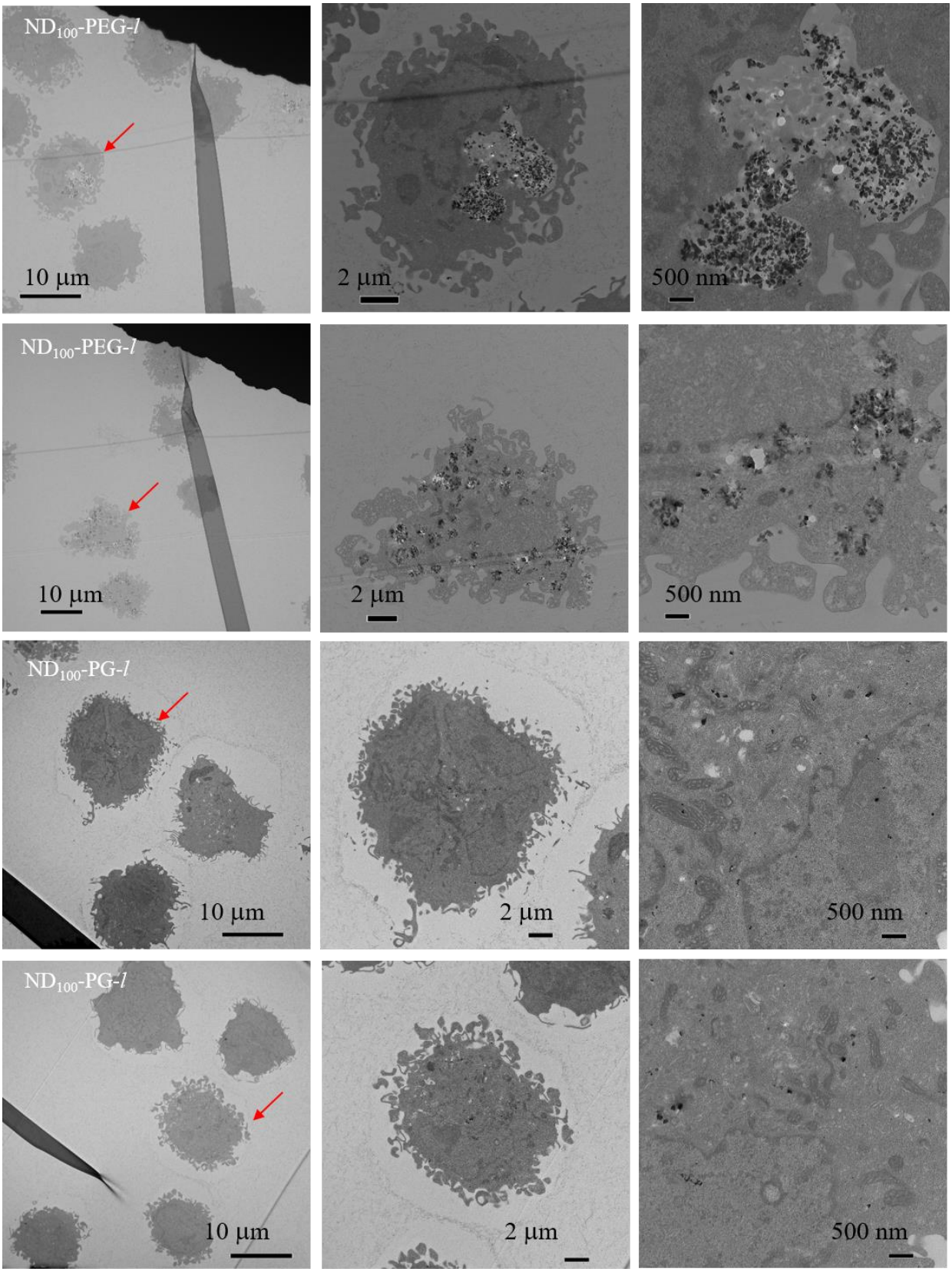

d) Control

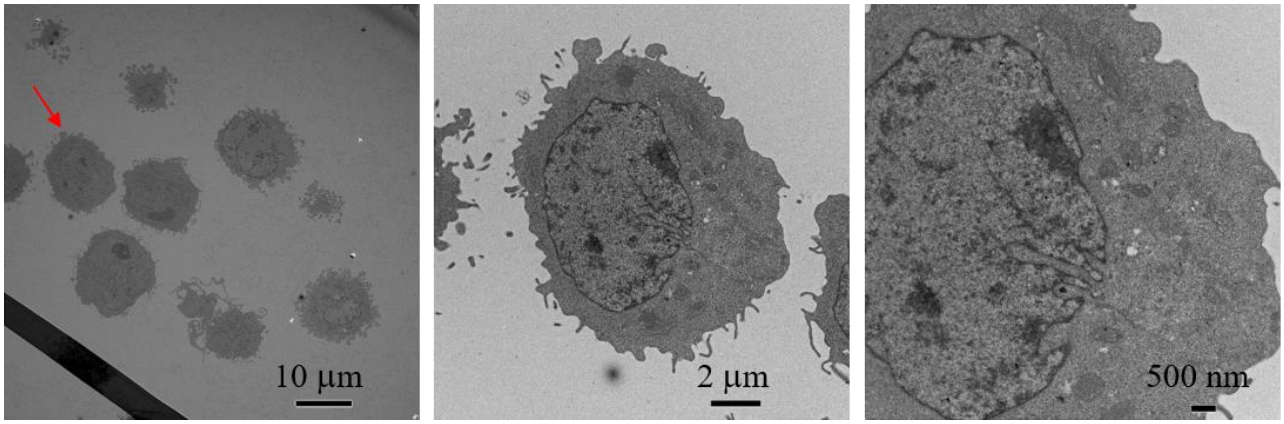

Appendix Figure 1-3. Additional TEM images of NDs uptake by U937 macrophages ranging from cell population to subcellular scale. a - b) 10% FBS (a) and 55% plasma (b) protein corona on ND_{100}, ND_{100}-PEG-*l*, ND_{100}-PG-*l*, ND_{100}-PG-*h* uptake; c) more images about 55% plasma protein corona on ND_{100}-PEG-*l* and ND_{100}-PG-*l* uptake (b); d) control U937 macrophage cells. In all the figures, the middle and right images are those with the higher magnification of the cell marked with red arrow in the left image.

Appendix II

a HeLa Control

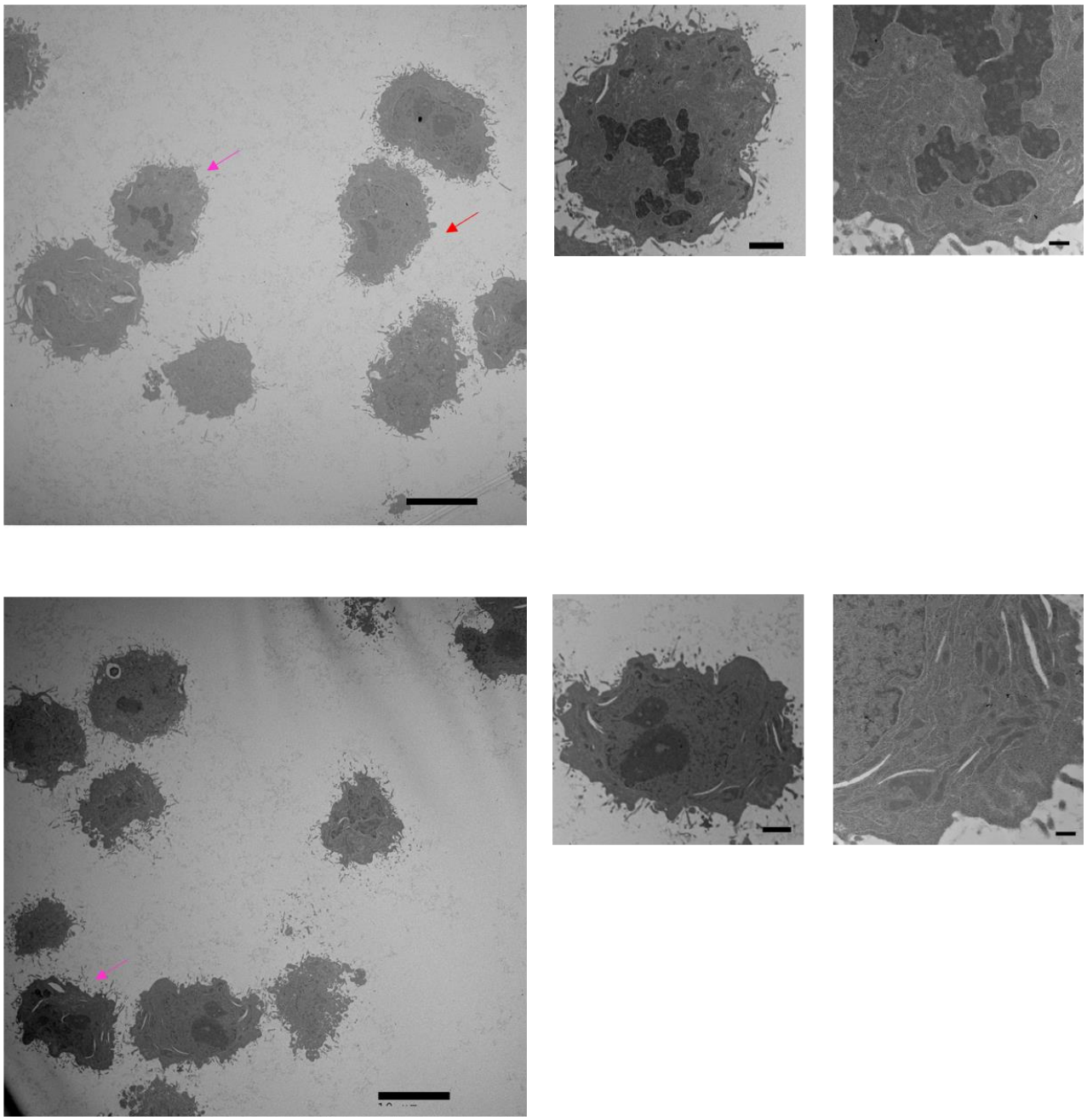

b HeLa + ND-PG

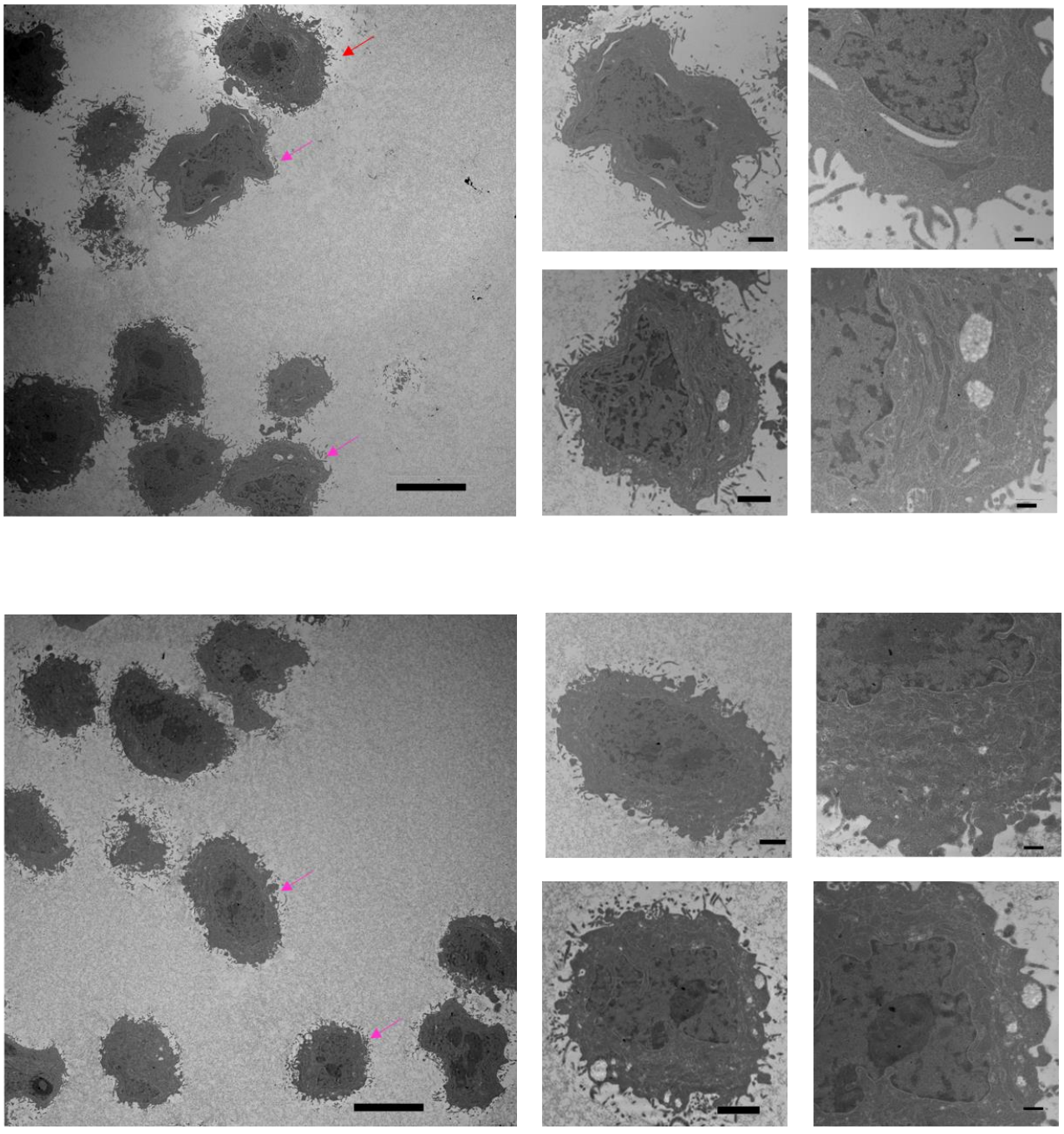

c HeLa + ND-PG-COO^--/ FBS (+)

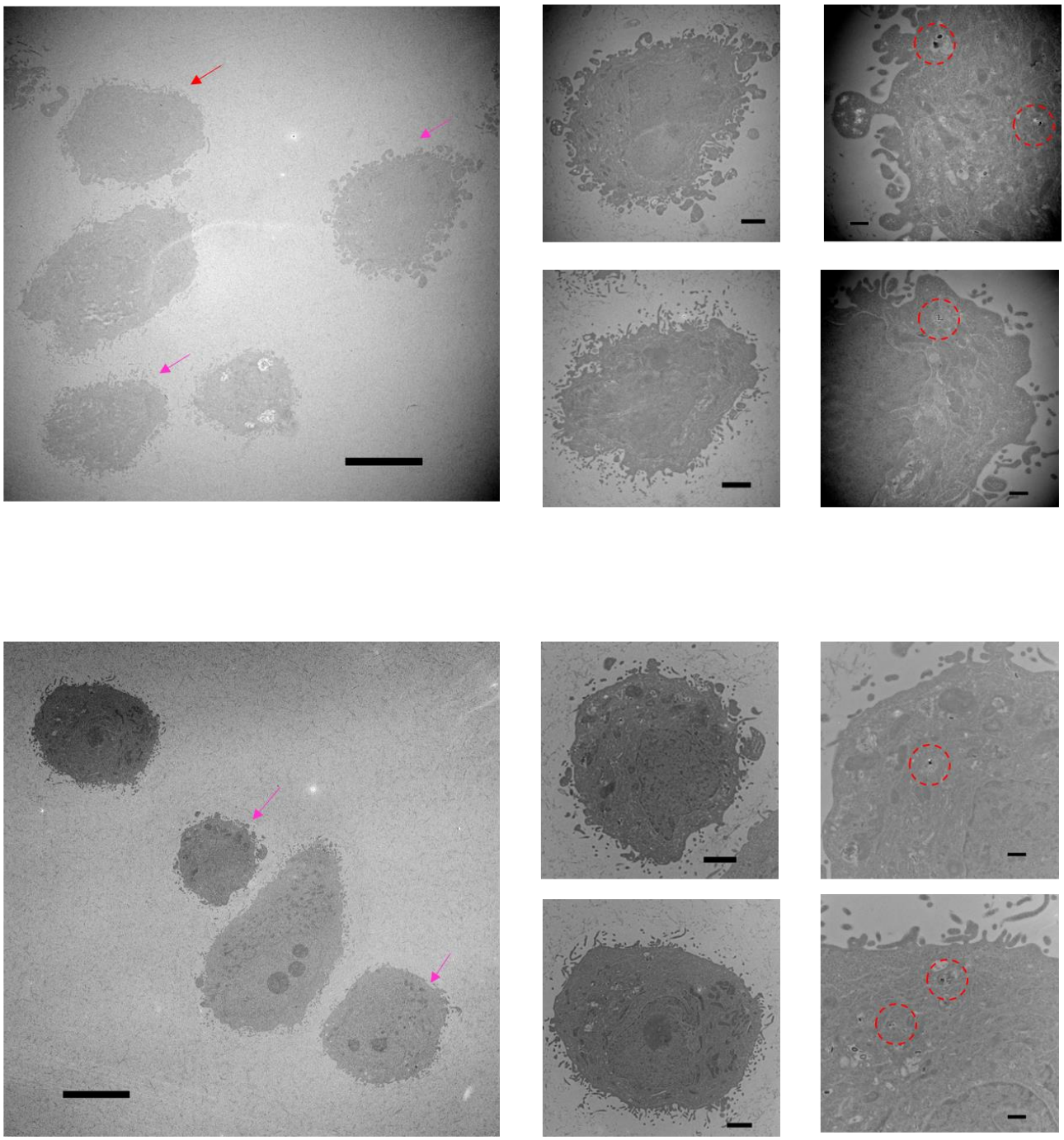

d HeLa + ND-PG-COO^{-}-*h* FBS (+)

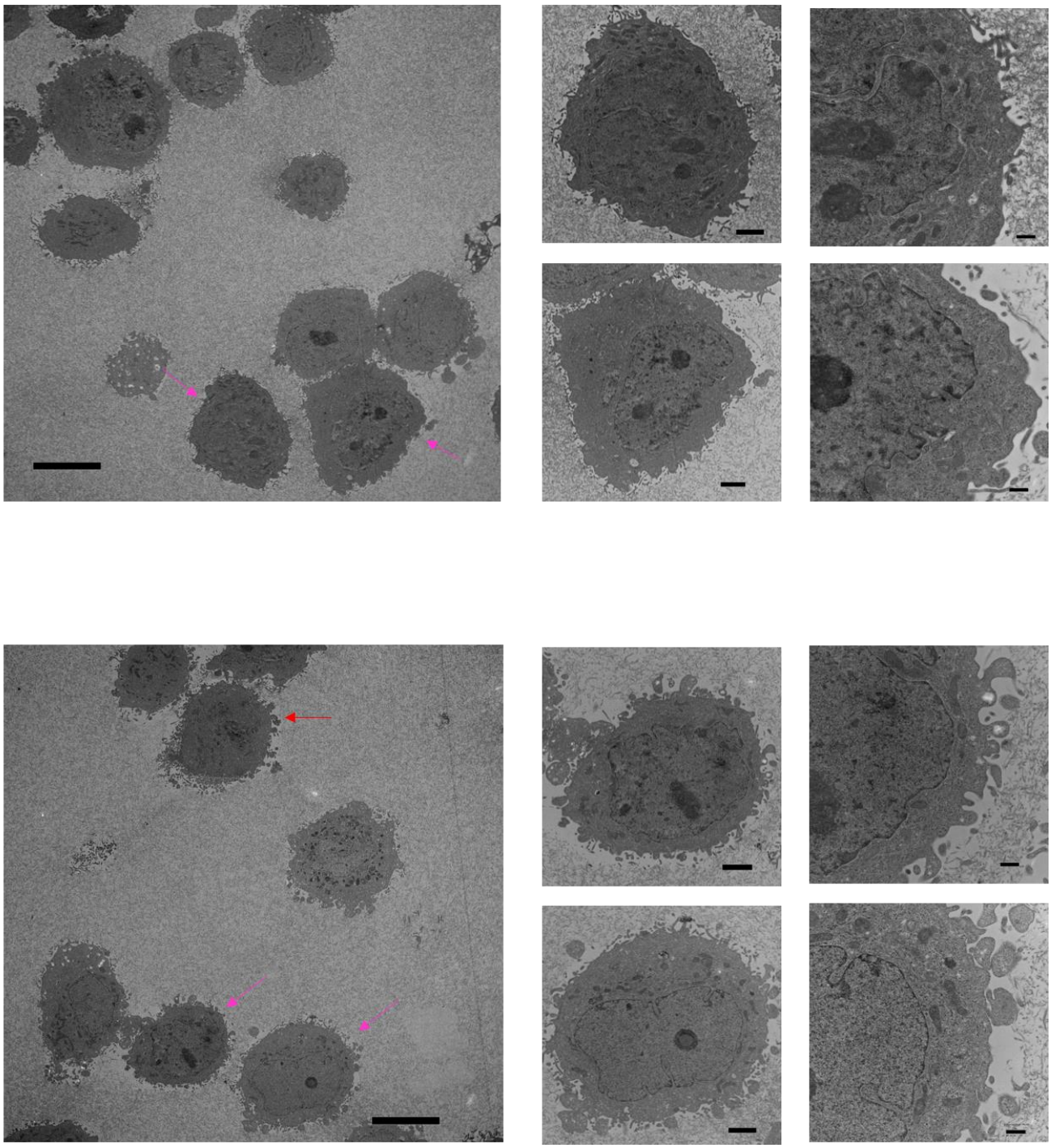

e HeLa + ND-PG-OSO_3^--/ FBS (+)

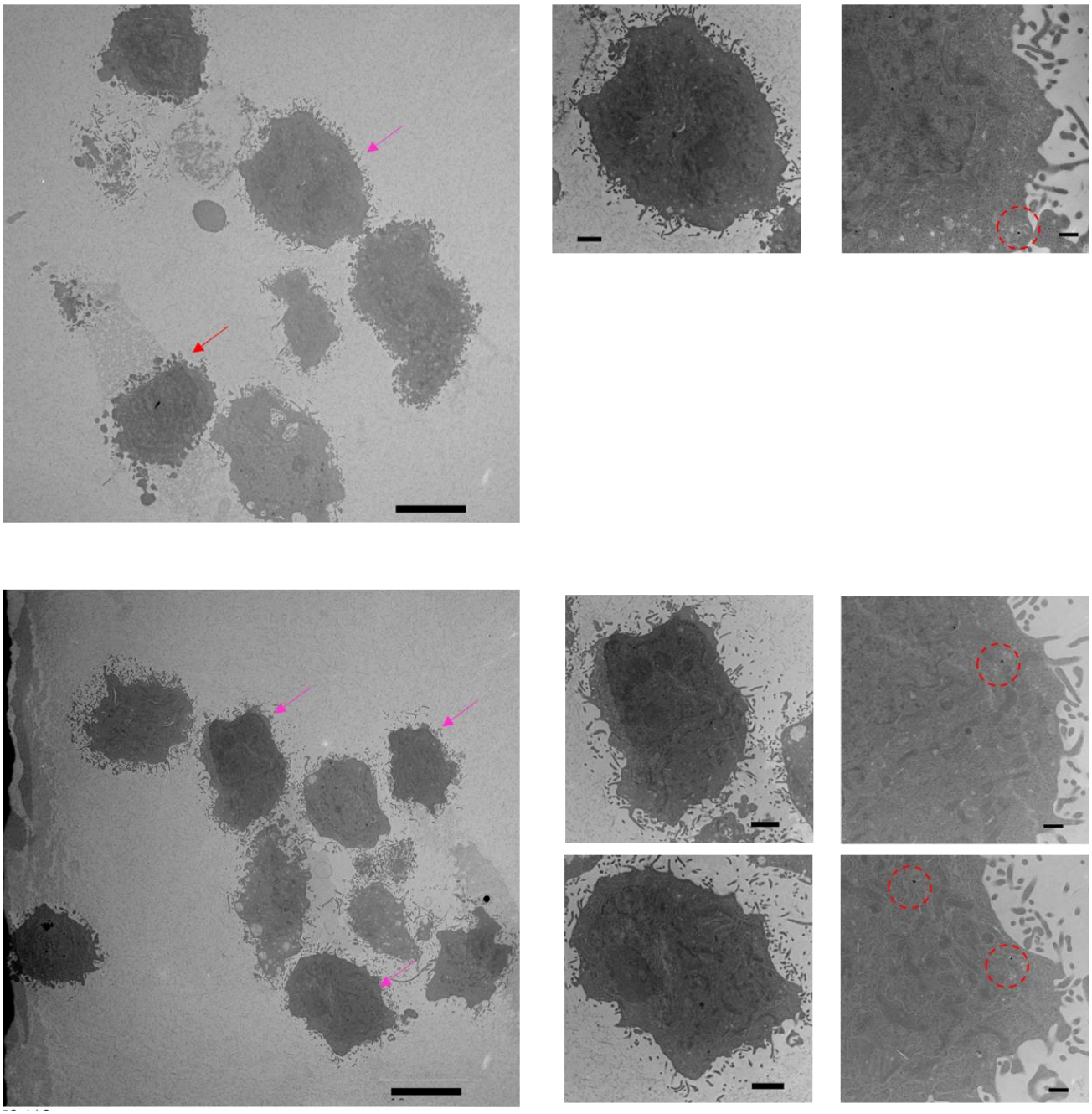

f HeLa + ND-PG-OSO_3^--*h* FBS (+)

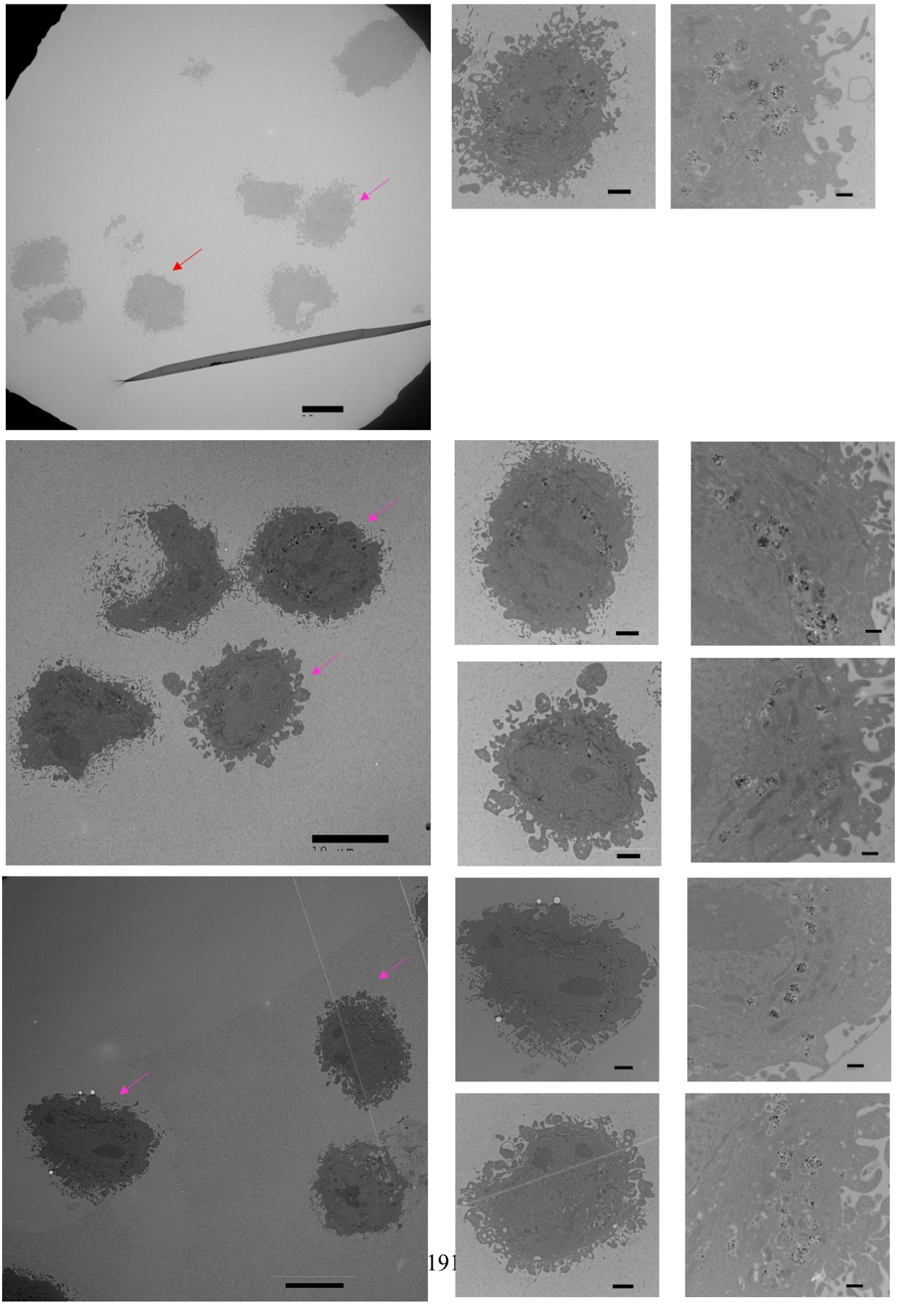

g HeLa + ND-PG-NH_3^+-/ FBS (+)

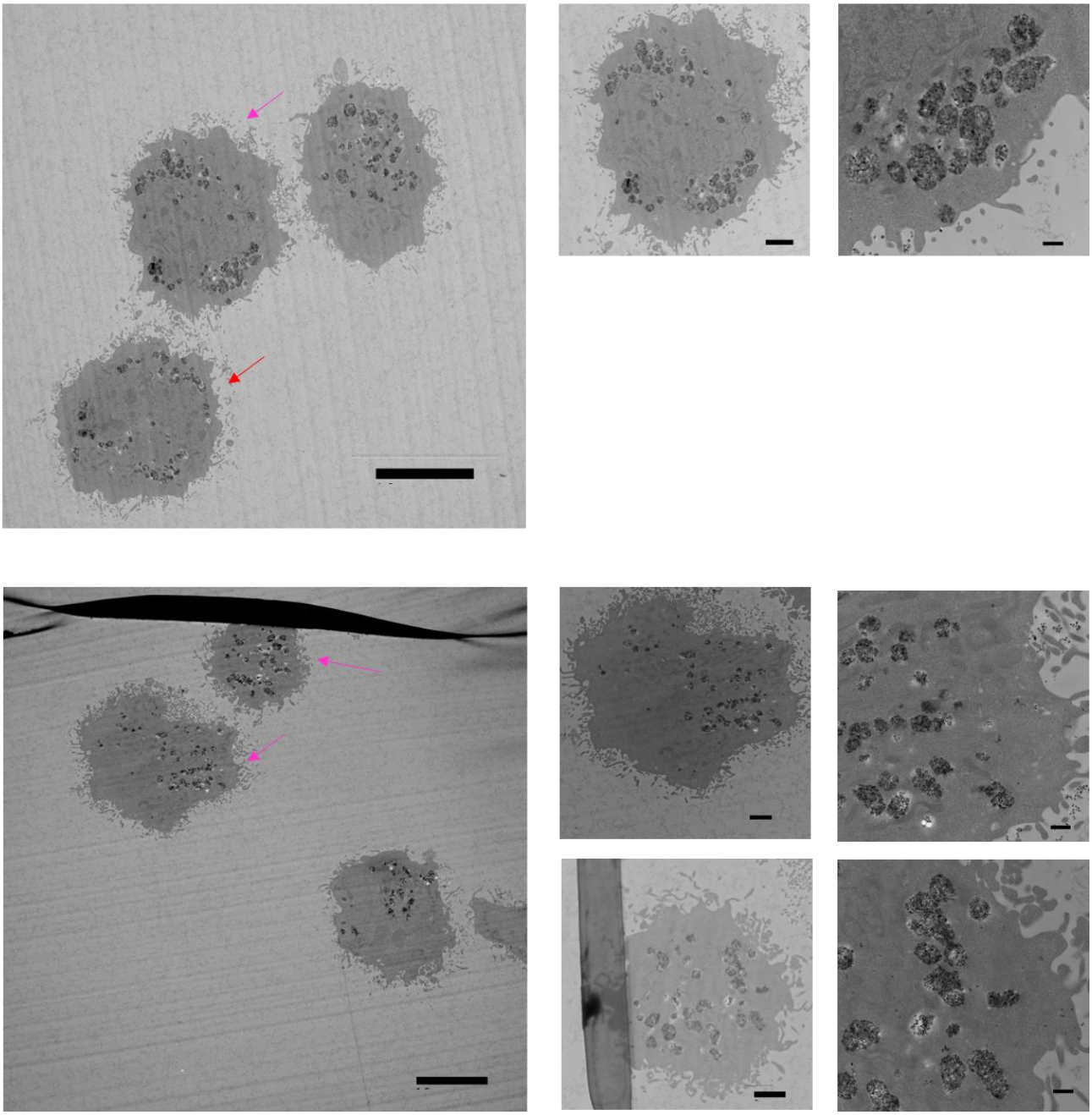

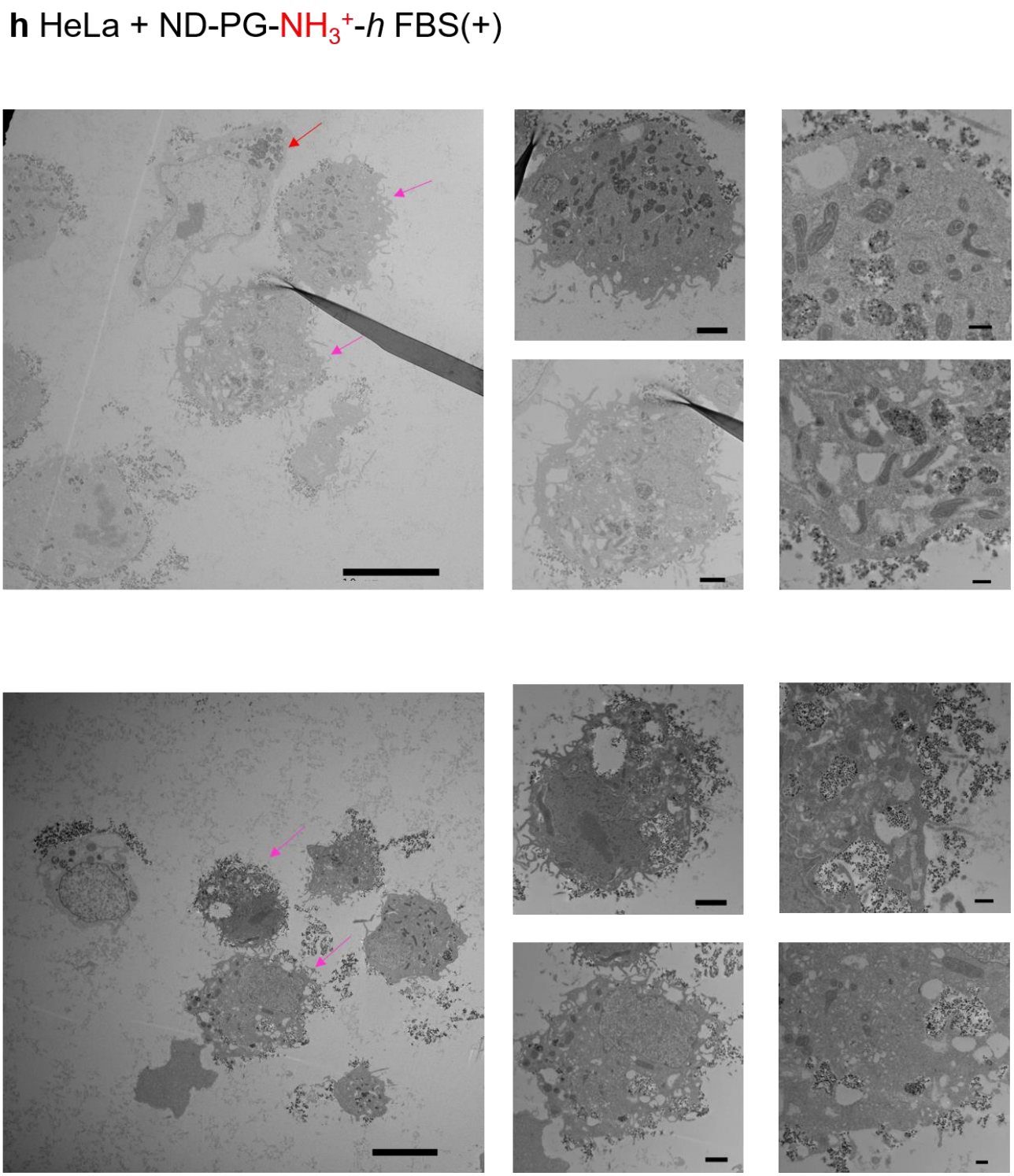

Appendix Figure 2-1. Additional TEM images of ND-PGs uptake by HeLa cells ranging from cell population to subcellular scale. The scale bar of images in left, middle, and right rows are 10 μm, 2μm, and 500 nm, respectively.

a A549 Control

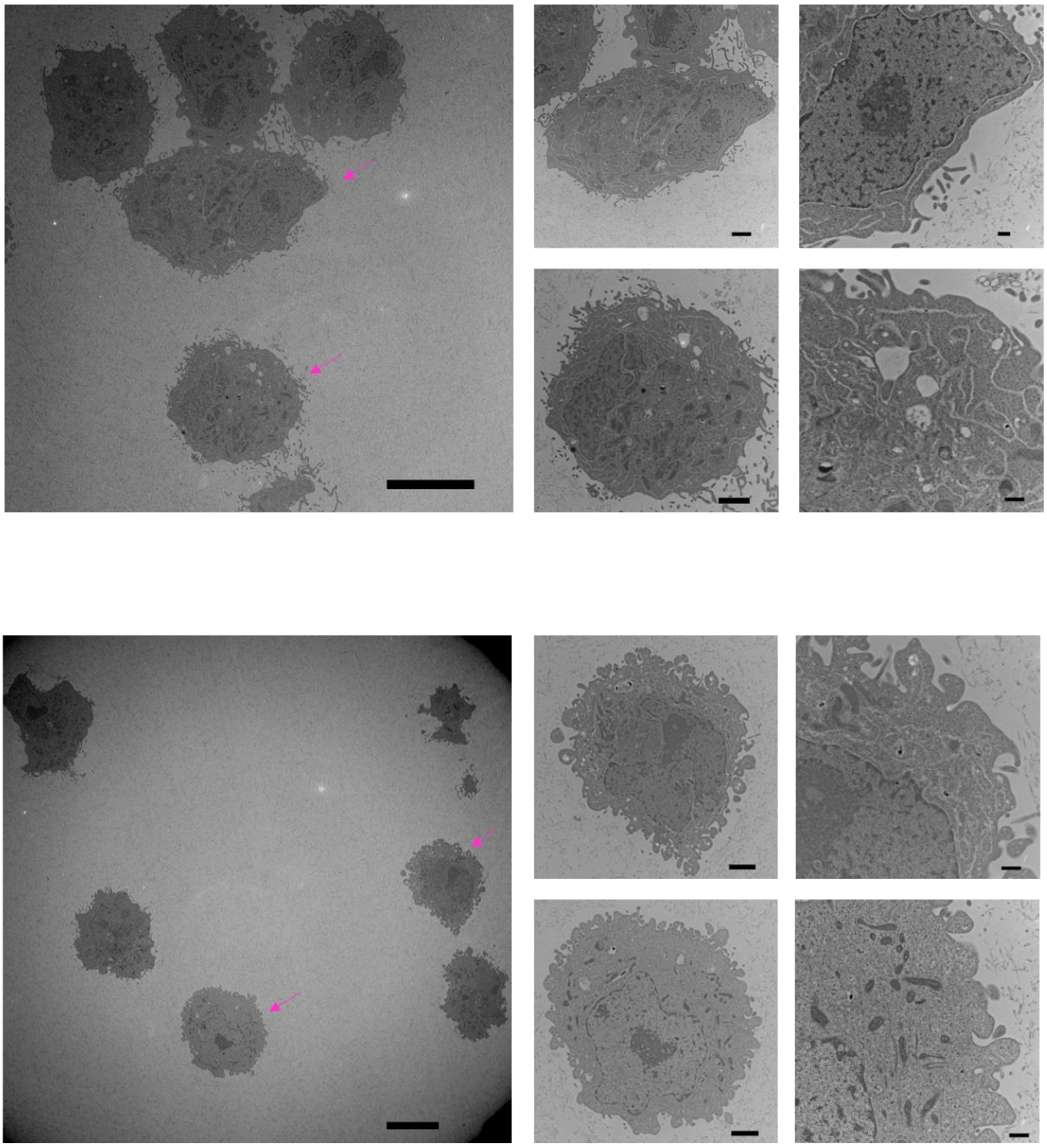

b A549 + ND-PG

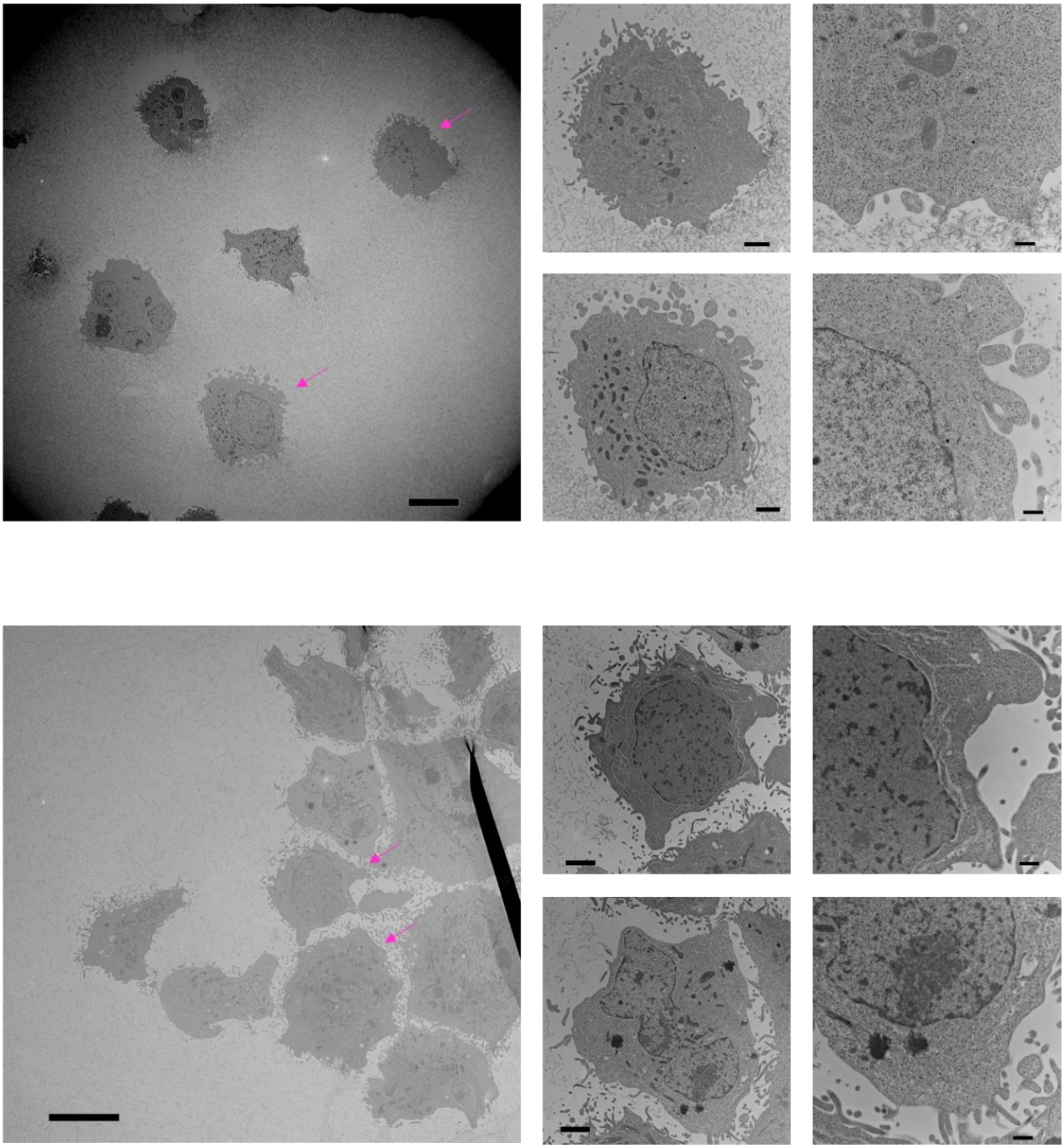

c A549 + ND-PG-COO^--/ FBS(+)

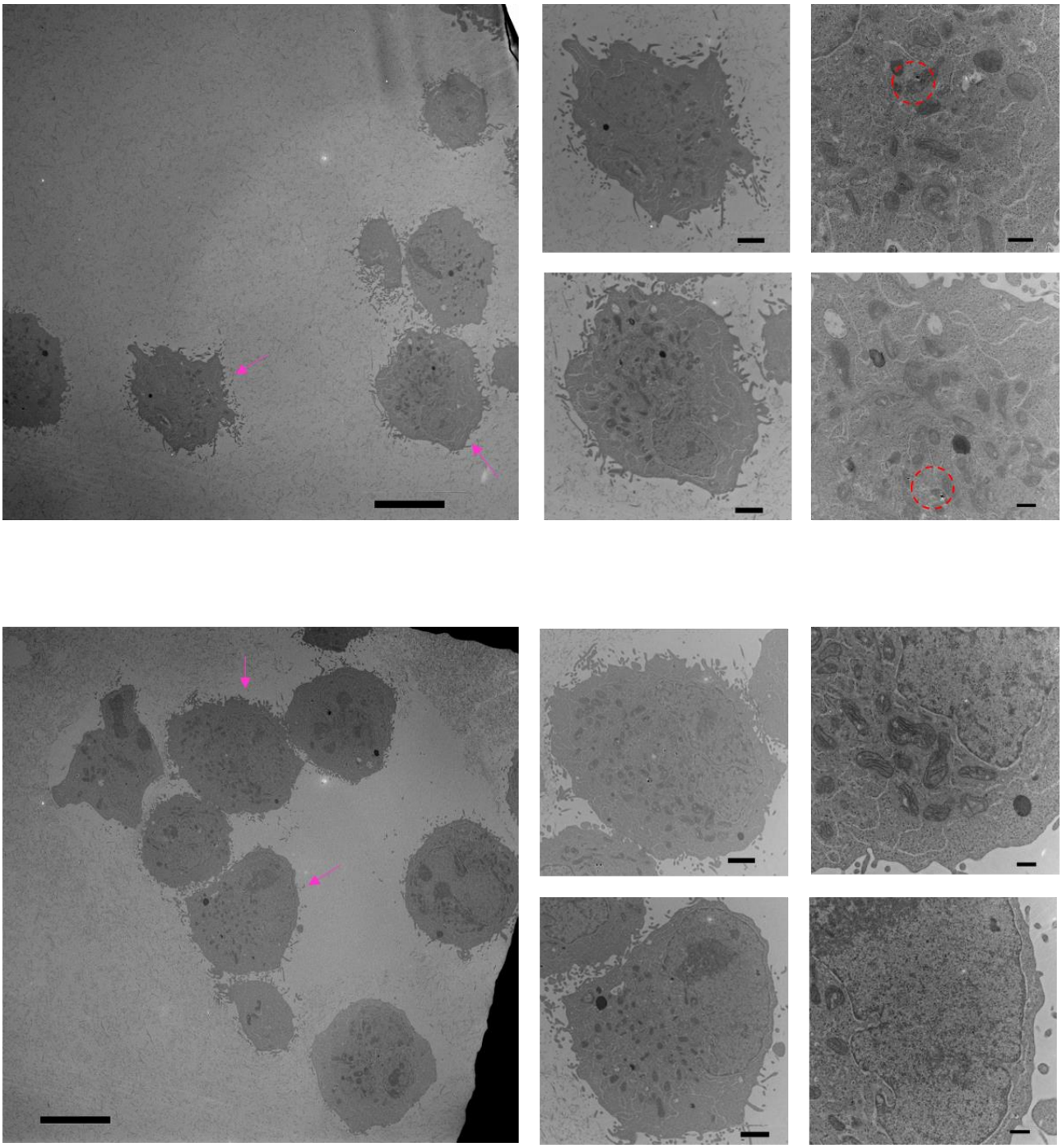

d A549 + ND-PG-COO⁻-*h* FBS(+)

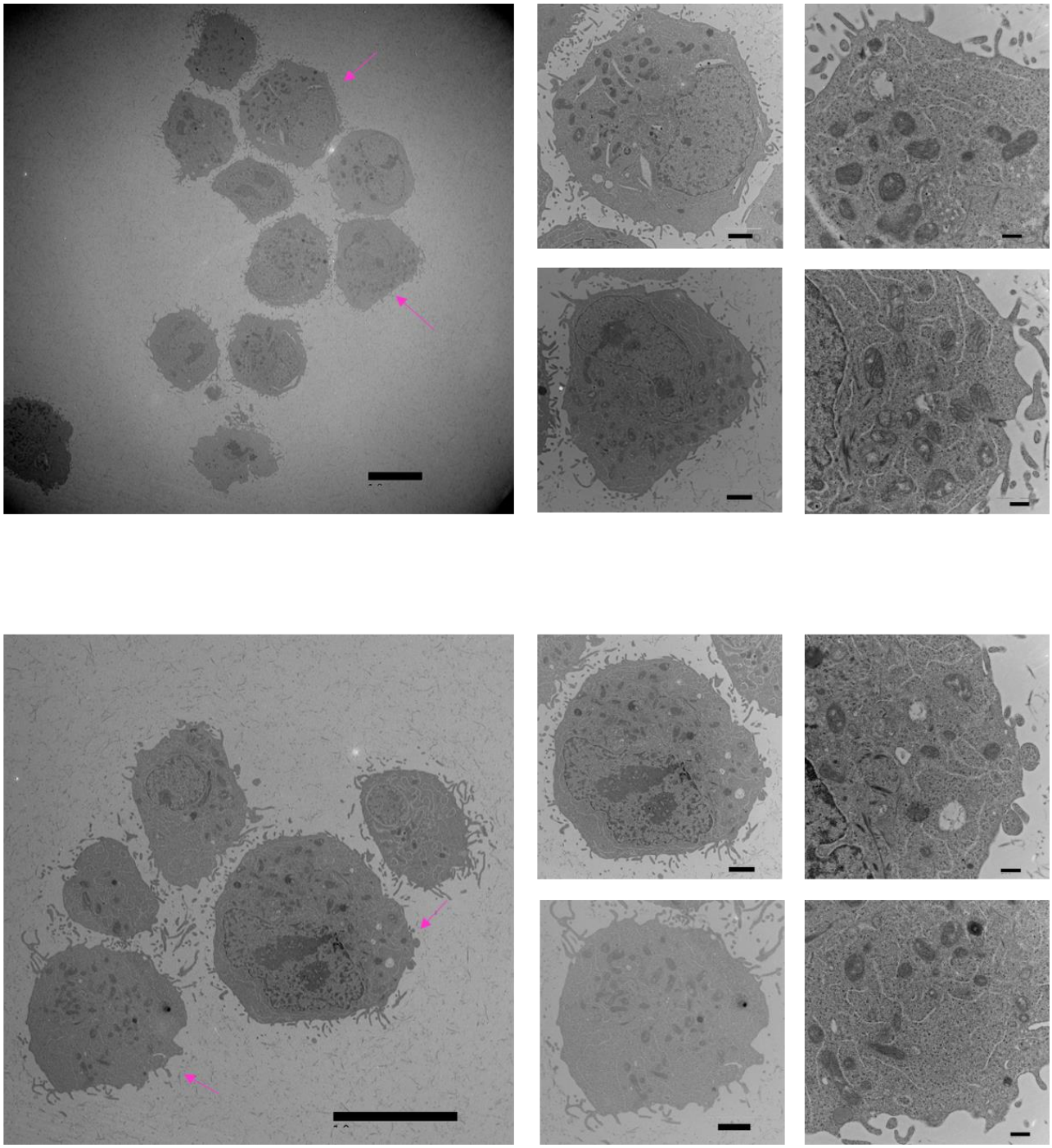

e A549 + ND-PG-OSO_3^--/ FBS(+)

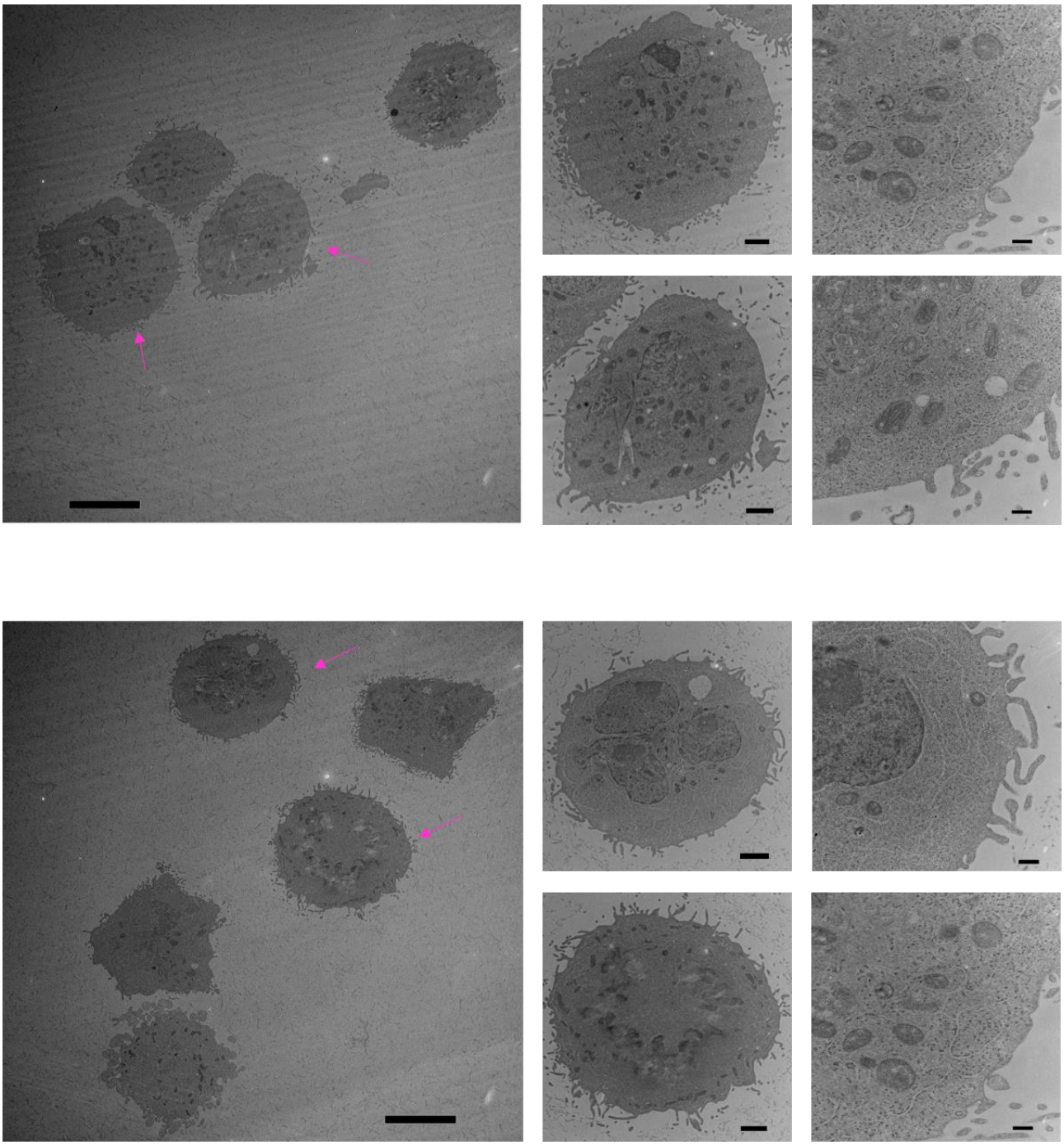

f A549 + ND-PG-OSO_3^--*h* FBS(+)

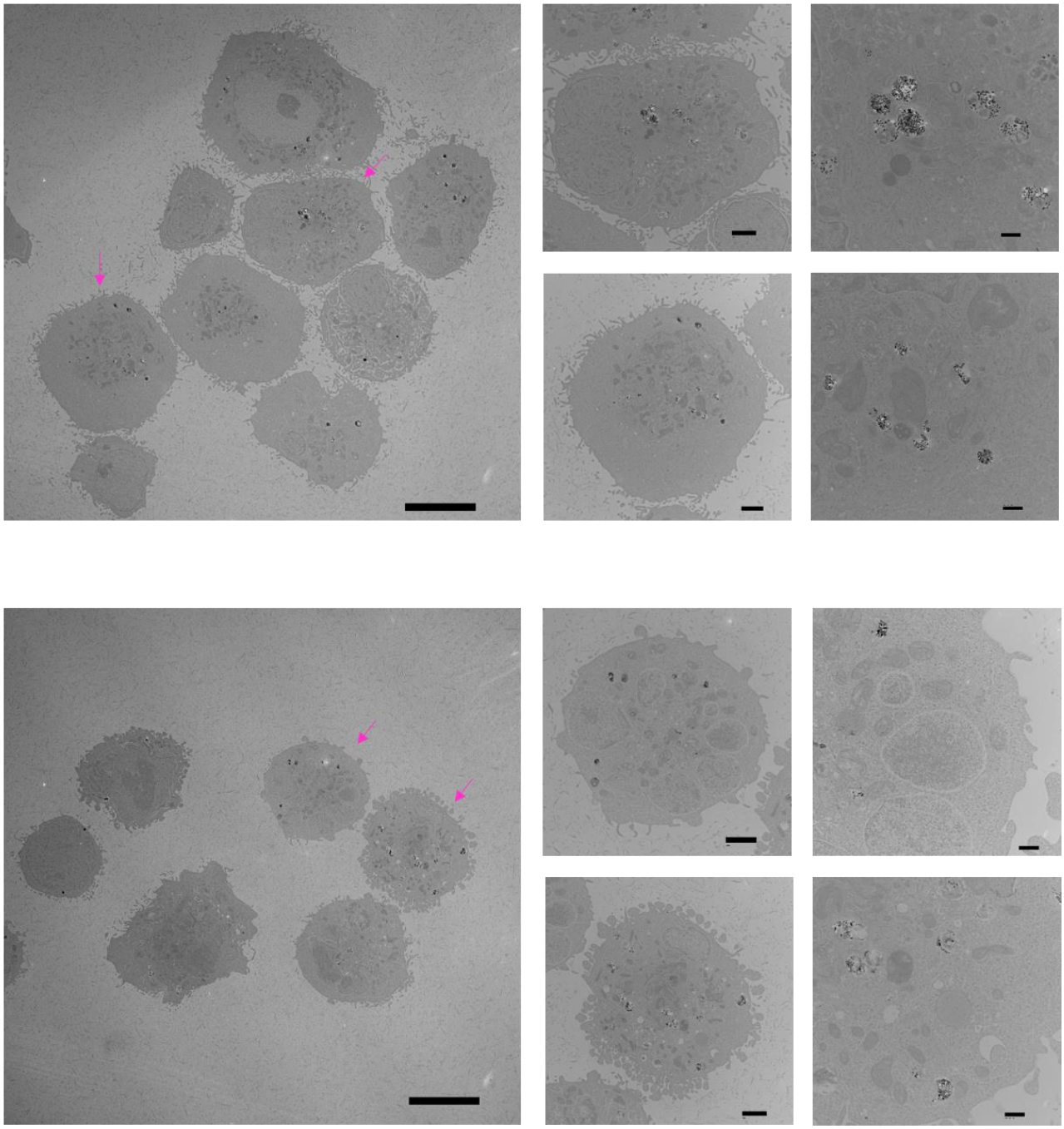

g A549 + ND-PG-NH_3^+-/ FBS(+)

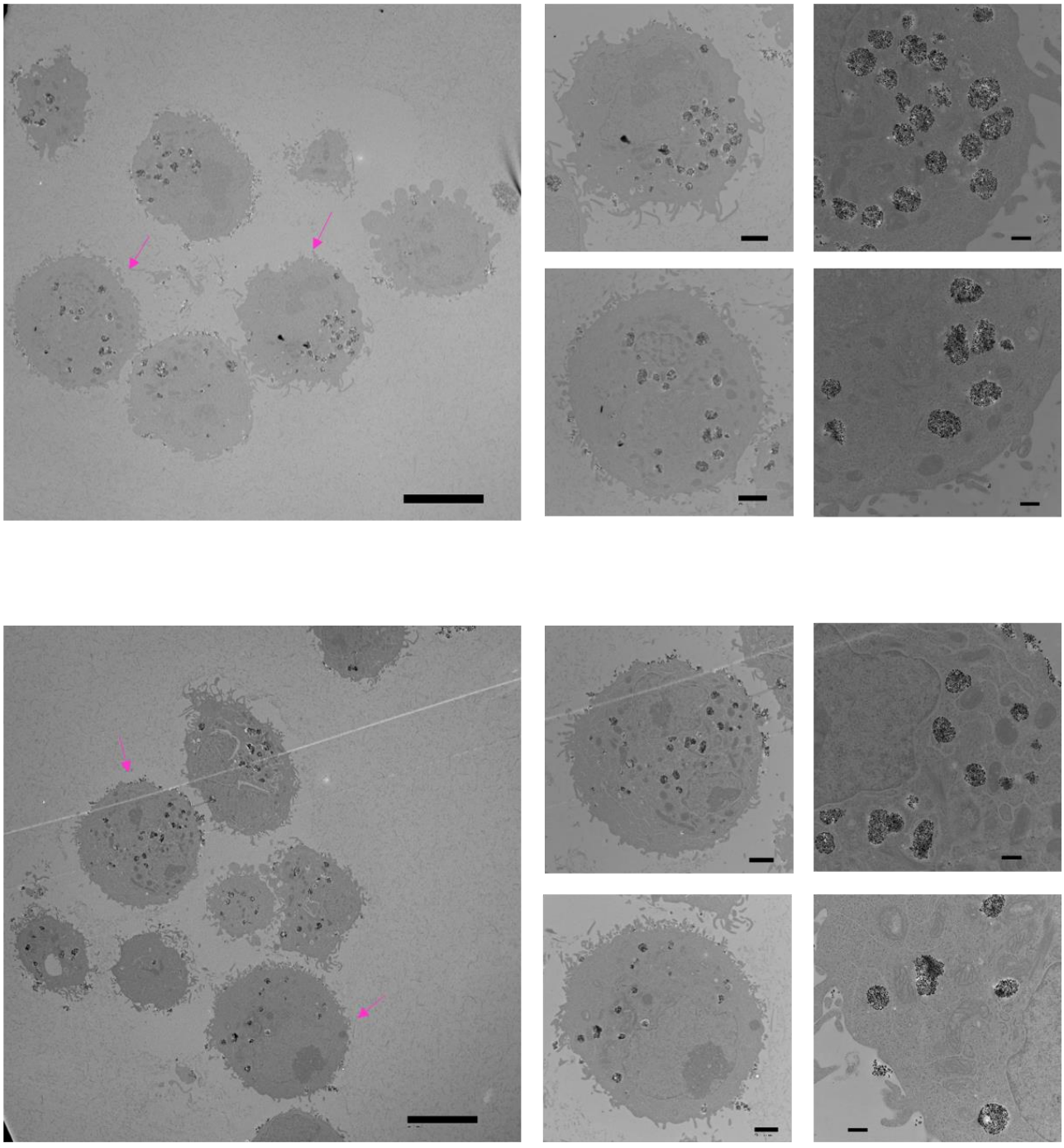

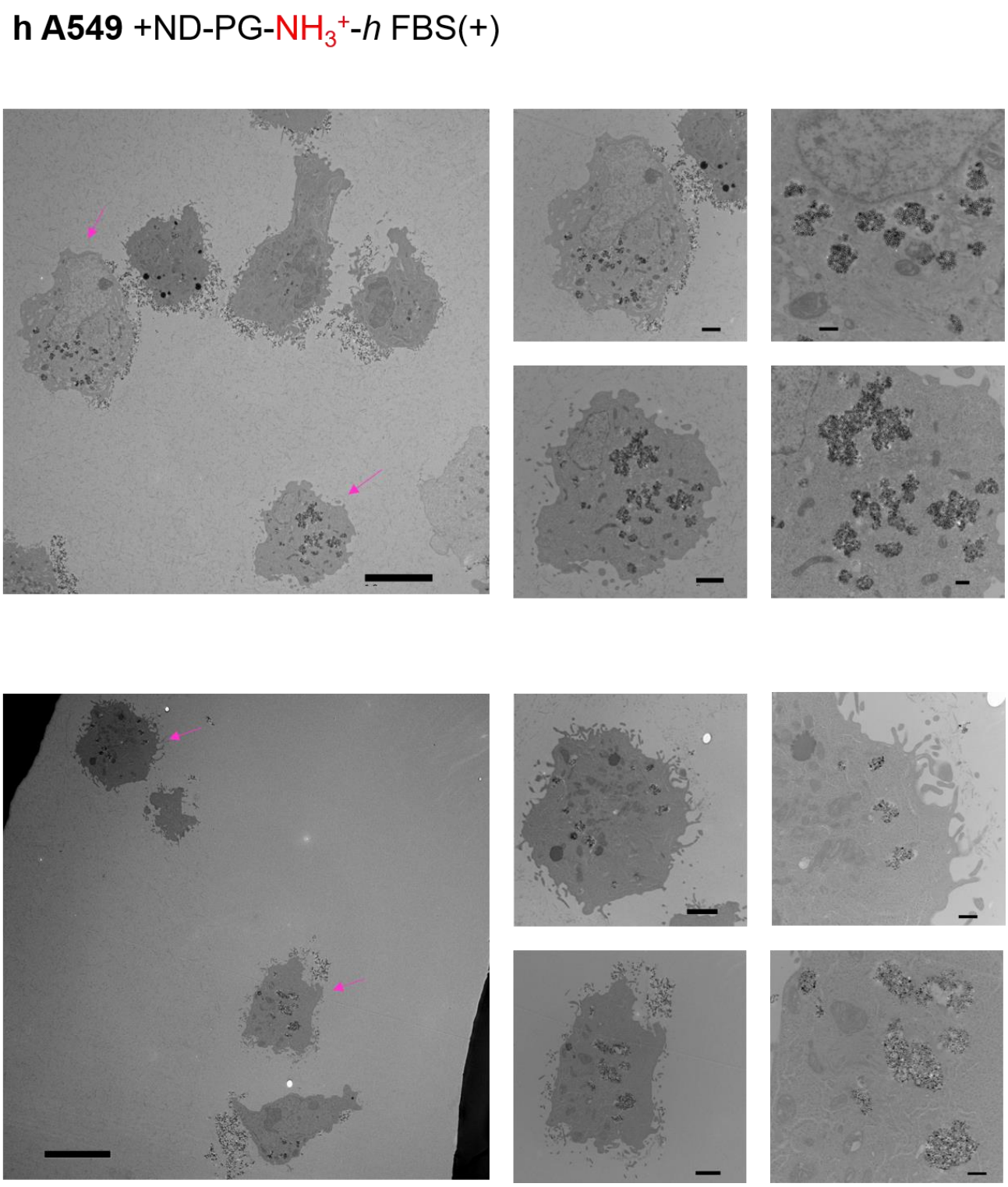

Appendix Figure 2-2. TEM images of ND-PGs uptake by A549 cells. The scale bar of images in left, middle, and right rows are 10 μm, 2μm, and 500 nm, respectively.

a HeLa + ND-PG-COO^--/ FBS (-)

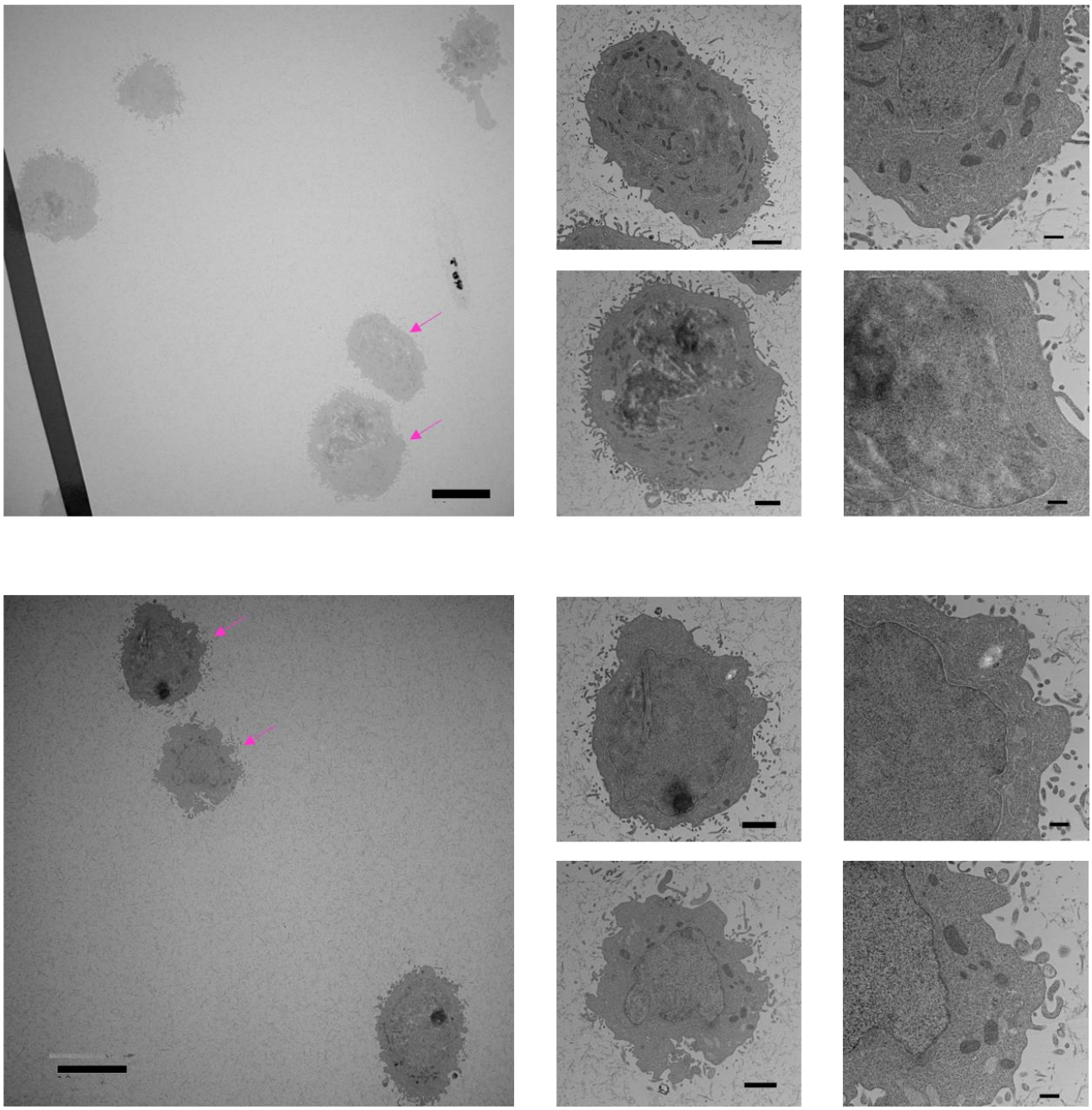

b HeLa + ND-PG-COO^--*h* FBS (-)

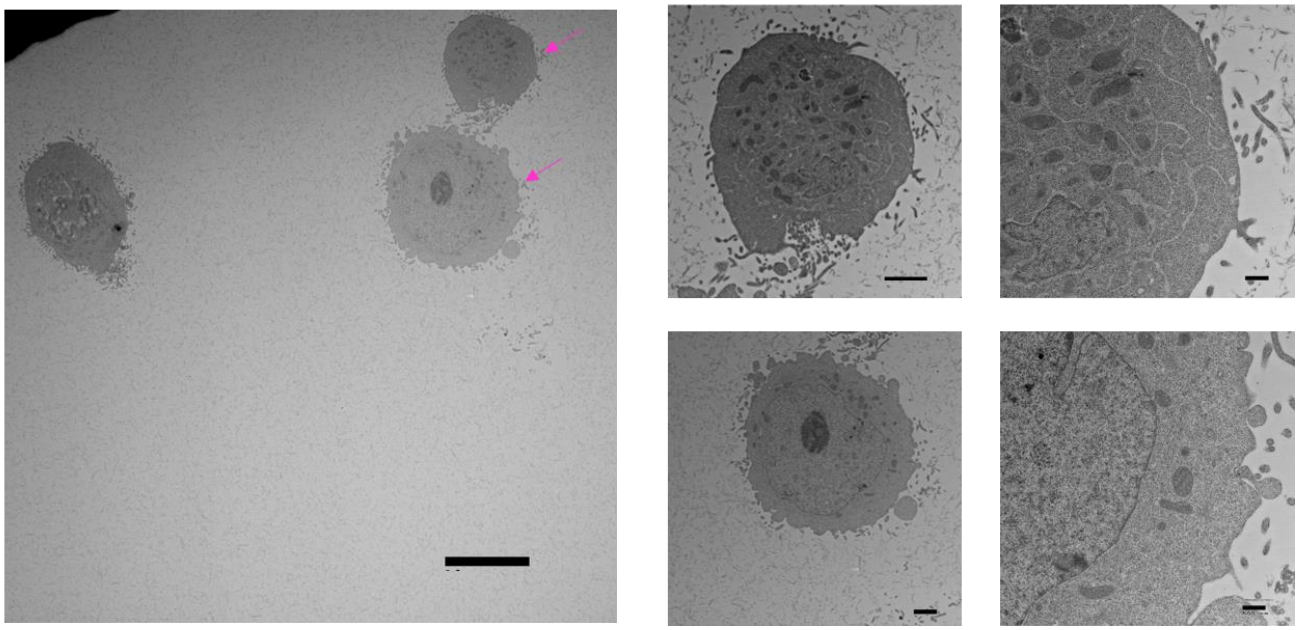

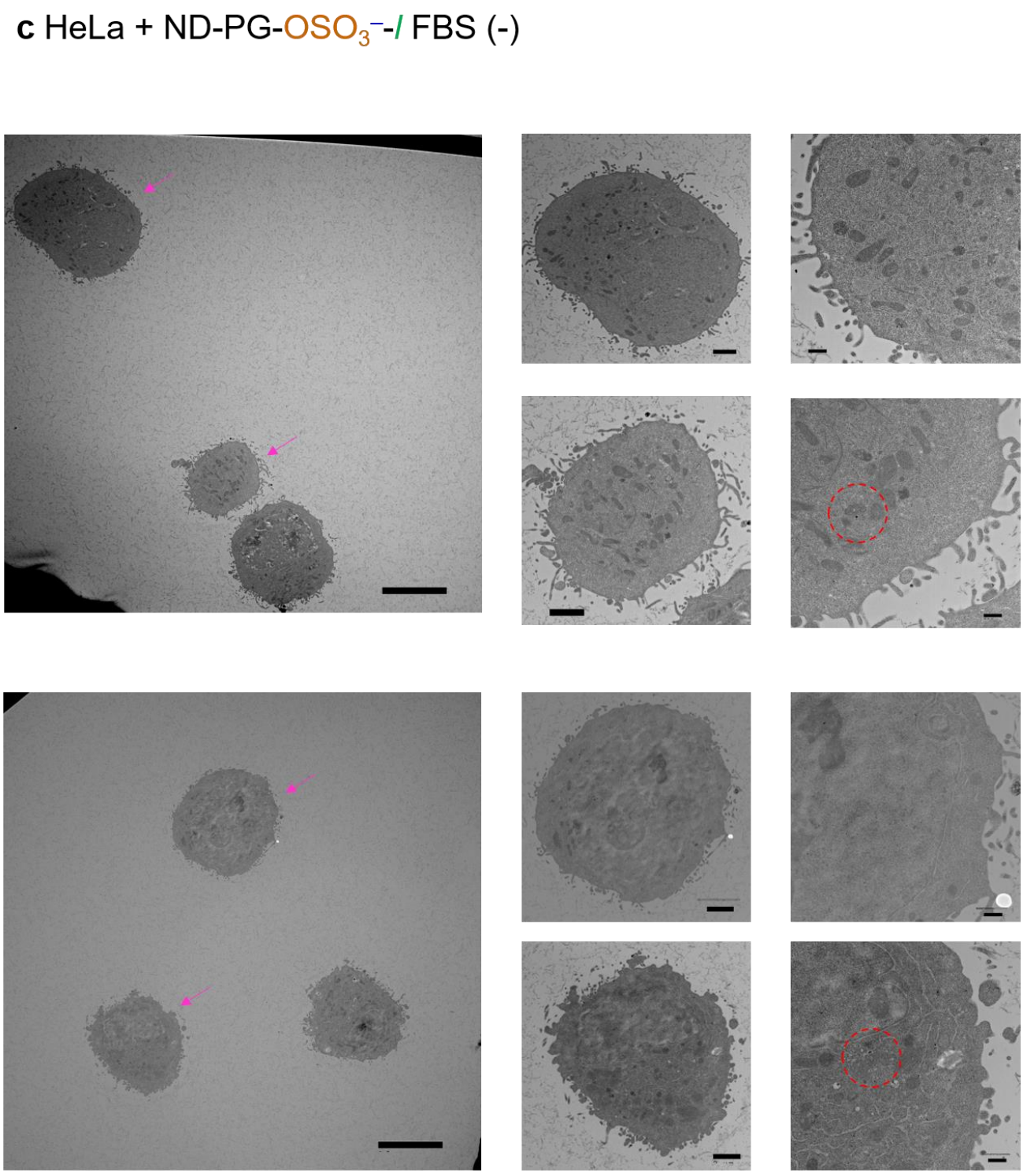

Appendix Figure 2-3. TEM images of ND-PG-COO^- and ND-PG-OSO_3^--*l* uptake by HeLa cells in the absence of FBS. The scale bar of images in left, middle, and right rows are 10 μm, 2μm, and 500 nm, respectively.

Appendix III

Raw abundance of proteins identified on the surface of ND-PG-OSO_3^--*h*, ND-PG-NH_3^+-*l*, ND-PG-NH_3^+-*h*, fND-PG-OSO_3^- and fND-PG-NH_3^+, as well as FBS proteins.

Proteins	Raw abundance					
	FBS	ND-PG-OSO_3^--*h*	ND-PG-NH_3^+-*l*	ND-PG-NH_3^+-*h*	fND-PG-OSO_3^-	fND-PG-NH_3^+
thrombospondin-1	325	2508	371	606	5750	765
keratin, type I cytoskeletal 17	44	144	160	1201	446	48
cartilage oligomeric matrix protein	17	11	167	277	30	244
thrombospondin-4	17	13	105	204	23	188
heat shock protein HSP 90-alpha	6	18	66	266	43	158
albumin	197467	22496	83061	133607	28419	71607
alpha-2-HS-glycoprotein	35327	2158	42436	98047	1399	53726
alpha-1-antiproteinase	17670	1516	10513	20198	1844	13679
alpha-2-macroglobulin	5032	1426	9654	16729	1512	15687
apolipoprotein A-I preproprotein	4872	3527	5520	13770	3808	11707
alpha-fetoprotein	4813	832	1526	2350	807	1385
vitamin D-binding protein	3868	127	1814	3687	282	3262
fetuin-B	3826	419	1230	2800	427	1426
serpin A3-7	2416	172	2767	6380	188	3489
serpin A3-2	2108	201	2717	5865	278	4001
inter-alpha-trypsin inhibitor heavy chain H4	1142	547	1330	2546	702	1709
alpha-1B-glycoprotein	1021	30	362	849	50	734
alpha-2-antiplasmin	921	376	1121	3001	473	1452
vitronectin	848	5912	1747	3547	10439	3132
keratin, type I cytoskeletal 14	797	2500	3306	27446	4607	1042

TPA: adiponectin D	730	285	4604	8527	380	8878
Prothrombin	600	1275	1397	2941	2358	2370
pregnancy zone protein isoform X1	352	166	964	1398	193	1385
complement C5a anaphylatoxin	260	658	380	776	790	1007
alpha-1-acid glycoprotein	240	52	252	538	89	548
fibulin-1	198	53	958	1891	87	1705
transthyretin	183	13	46	81	24	80
afamin	174	26	150	362	37	217
fibronectin	142	2214	895	1449	2227	1899
collagen alpha-1(VI) chain	140	226	208	287	435	275
apolipoprotein E	135	1592	402	1067	2901	877
thyroxine-binding globulin	129	12	131	334	13	164
actin, cytoplasmic 2	126	58	297	772	495	1351
lumican	123	103	367	921	169	592
coagulation factor V	116	1435	352	728	2899	413
myosin-9	92	320	155	289	508	234
gelsolin isoform a	92	4429	357	493	6391	479
collagen alpha-2(VI) chain	55	285	70	208	568	118
complement component C9	52	15	64	248	90	132
complement C1q tumor necrosis factor-related protein 3	52	215	79	174	335	166
collagen alpha-3(VI) chain isoform X1	52	260	124	233	346	181
hyaluronan-binding protein 2	51	504	74	164	825	94
Complement C4	35	59	188	662	86	385
tetranectin	28	207	25	30	1341	22
vitamin K-dependent protein S	27	13	141	253	7	314

galectin-3-binding protein	25	40	302	1368	123	594
C4b-binding protein alpha chain	12	315	121	208	159	244
osteomodulin	12	4	62	163	17	153
vitamin K-dependent protein C	9	18	51	140	20	106
thyroglobulin	8	0	107	356	3	215
carboxypeptidase N subunit 2	5	24	102	295	22	266
cation-independent mannose-6-phosphate receptor	4	10	60	160	13	183
coagulation factor XIII A chain	3	286	18	125	462	63
prolow-density lipoprotein receptor-related protein 1 isoform X1	1	3	71	122	11	104
radixin	1	139	0	0	333	0
serotransferrin precursor	20919	841	2135	4908	950	2541
inter-alpha-trypsin inhibitor heavy chain H2	3153	5160	25462	50438	6702	38603
factor XIIa inhibitor	1377	1485	3519	5890	1722	7060
Complement C3	1233	1061	3916	9032	1027	7302
complement C4	1043	5249	3368	12851	4410	4358
antithrombin-III	990	3467	786	1590	4492	1355
hemoglobin fetal subunit beta	979	532	714	1066	729	836
protein AMBP	887	1198	10551	23076	1853	17635
Angiotensinogen	794	116	195	372	177	292
heparin cofactor 2	548	1608	1131	2878	2072	1337
complement factor B	548	743	369	823	535	556
pigment epithelium-derived factor	427	2164	538	1648	3546	666
fibrinogen gamma-B	293	1108	160	338	213	179

chain						
complement factor H	164	1830	357	846	1394	686
kininogen-2 isoform I	78	34	132	350	39	244
complement component C7	44	112	67	181	103	91
skin-specific protein 32	10	49	76	1317	76	14
transforming growth factor-beta-induced protein ig-h3	9	74	68	157	92	132
lipopolysaccharide-binding protein	0	324	15	42	612	33
inter-alpha-trypsin inhibitor heavy chain H3	2194	897	7965	16027	1084	13792
inter-alpha-trypsin inhibitor heavy chain H1	1590	3501	5000	14275	4367	5453
keratin, type II cytoskeletal 59 kDa, component IV	1075	930	3416	14491	4640	870
keratin, type II cytoskeletal 75	735	554	3005	15977	2332	1293
hemopexin	665	55	195	380	68	299
keratin, type II cytoskeletal 5	419	286	1766	7225	1479	588
plasminogen	419	742	341	792	570	414
keratin, type II cytoskeletal 2 epidermal	255	664	1450	10994	1399	432
procollagen C-endopeptidase enhancer 1	61	875	253	608	1320	731
periostin	56	322	372	870	539	651
plasma kallikrein	53	282	49	95	542	90
complement factor I	44	1138	85	645	1622	176
complement component C8 beta chain	40	292	63	137	230	97
fibrinogen alpha chain	18	2374	57	80	219	94
Beta-2-glycoprotein 1	446	1361	191	415	1517	339
hemoglobin subunit alpha	361	516	511	626	272	497

cationic trypsin	312	769	526	464	1541	756
carboxypeptidase N catalytic chain	58	189	100	249	330	291
hepatocyte growth factor-like protein	22	83	10	25	182	11
fibrinogen beta chain	20	1089	47	128	139	110
glyceraldehyde-3-phosphate dehydrogenase	7	311	55	173	587	132
sulfhydryl oxidase 1	4	200	10	31	299	23
complement C1q subcomponent subunit C	1	306	8	29	819	27
plasma serine protease inhibitor	293	4316	294	1256	7179	378
collagen alpha-1(I) chain	166	601	143	265	1727	146
collagen alpha-1(II) chain isoform 1 preproprotein	67	472	45	106	1333	66
elongation factor 1-alpha 1	33	195	41	100	389	63
collagen alpha-2(I) chain	32	236	30	189	788	33
complement C1q subcomponent subunit A	0	240	2	13	614	24

List of abbreviations

ABC, accelerated blood clearance; A549 cells, human lung epithelial carcinoma cells; BCA, bicinchoninic acid; BSA, bovine serum albumin; CPZ, chlorpromazine hydrochloride; CytoD, cytochalasin D; DCC, *N,N′*-dicyclohexylcarbodiimide; DLS, dynamic light scattering; DMAP, 4-dimethylaminopyridine; DMF, *N,N*-dimethylformamide; EA, elemental analysis; EPR effect, enhanced permeability and retention effect; FACS, fluorescence-activated cell sorting; FBS, fetal bovine serum; FI, fluorescence intensity; fND, fluorescent nanodiamond; GEN, genistein; γ-GLO, γ-globulin; HeLa cells, human cervix epithelium cells; ^{1}H-NMR, proton nuclear magnetic resonance; HP, human plasma; ICP-MS, inductively coupled plasma-mass spectrometry; IR, infrared; LC-MS/MS, liquid chromatography-tandem mass spectrometry; LYS, lysozyme; MPS, mononuclear phagocyte system; MW, molecular weight; ND, nanodiamod; NPs, nanoparticles; PAGE, polyacrylamide gel electrophoresis; PB, polybetaines; PBS, phosphate buffer saline; PEG, polyethylene glycol; PG, polyglycerol; PMA, phorbol 12-myristate 13-acetate; p*I,* isolated point; SDS, sodium dodecyl sulfate; SPION, super paramagnetic iron oxide nanoparticle; STEM, scanning transmission electron microscopy; TEM, transmission electron microscopy; TGA, thermogravimetric analysis; THF, anhydrous tetrahydrofuran; TPP, triphenylphosphonium; U937 macrophage, human leukemic monocyte lymphoma cells; WSCD·HCl, water soluble carbodiimide hydrochloride; XRD, X-ray diffraction.

List of publications

- **Publications included in this thesis**

1) **Yajuan Zou**, Shinji Ito, Fumi Yoshino, Yuta Suzuki, Li Zhao, and Naoki Komatsu, [Polyglycerol grafting shields nanoparticles from protein corona formation to avoid macrophage uptake], ***ACS Nano***, 14, 7216-7226, 2020. (Chapter 2)

2) **Yajuan Zou**, Naoki Komatsu, [Quantitative investigation of the interaction between proteins and charged functional groups on the polyglycerol-grafted nanodiamond surface], ***Carbon***, 163, 395-401, 2020. (Chapter 3)

3) **Yajuan Zou**, Shinji Ito, Masazumi Fujiwara, and Naoki Komatsu, [Probing the role of charged functional groups on corona-free polyglycerol-functionalized nanoparticle in protein absorption and cellular uptake], Manuscript in preparation. (Chapter 4)

4) **Yajuan Zou,** Masahiro Nishikawa, Heon Gyu Kang, Guoqing Cheng, Wei Wang, Yuquan Wang, and Naoki Komatsu, [Effect of protein corona on mitochondrial targeting ability and cytotoxicity of triphenylphosphonium conjugated with polyglycerol-functionalized nanodiamond], ***Molecular Pharmaceutics***, 18, 2823-2832, 2021. (Chapter 5)

- **Publications not included in this thesis**

1) **Yajuan Zou**, Yizhao Wu, Yali Wang, Yinsheng Li, Chengyu Jin, [Physicochemical properties, *in vitro* cytotoxic and genotoxic effects of $PM_{1.0}$ and $PM_{2.5}$ from Shanghai, China], ***Environmental Science and Pollution Research***, 24, 19508-19516, 2017.

2) **Yajuan Zou**, Chengyu Jin, Yue Su, Jiaru Li, Bangshang Zhu, [Water soluble and insoluble components of urban $PM_{2.5}$ and their cytotoxic effects on epithelial cells (A549) *in vitro*], ***Environmental Pollution***, 212, 627-635, 2016.

3) Wei Wang, **Yajuan Zou**, Alejandro López-Moreno, Yujing Jiang, Feng Wen, Hong-Xing Wang, Naoki Komatsu, [Hydrophobic surface coating of nanodiamond by polyglycerol-based polymers with alkyl chains for dispersing in an organic solvent], ***ChemNanoMat***, 6(9), 1332-1336, 2020. [Highlighted at the front cover]

4) Dacheng Huang, **Yajuan Zou**, Anees Abbas, Bona Dai, [Nuclear magnetic resonance-based metabolomic investigation reveals metabolic perturbations in $PM_{2.5}$-treated A549 cells], ***Environmental Science and Pollution Research***, 25, 31656-31665, 2018.

5) Masahiro Nishikawa, Heon Gyu Kang, **Yajuan Zou**, Hidekazu Takeuchi, Naoyoshi Matsuno, Minoru Suzuki, Naoki Komatsu, [Conjugation of Phenylboronic Acid Moiety through Multistep Organic Transformations on Nanodiamond Surface for an Anticancer Nanodrug of Boron Neutron Capture Therapy], ***Bulletin of the Chemical Society of Japan***, accepted (DOI: 10.1246/bcsj.20210200).

6) Fumi Yoshino, Tsukuru Amano, **Yajuan Zou**, Jian Xu, Fuminori Kimura, Yoshio Furusho, Tokuhiro Chano, Takashi Murakami, Li Zhao, Naoki Komatsu, [Preferential tumor accumulation of polyglycerol functionalized nanodiamond conjugated with cyanine dye leading to near infrared fluorescence *in vivo* tumor imaging], ***Small***, 15(48), 1901930, 2019. [Highlighted at the back cover]

7) Gang Liu, Ping Zhao, Neng Liu, Fumi Yoshino, Hongmei Qin, **Yajuan Zou**, Shengwei Shi, Tsukuru Amano, Jose R Aguilar Cosme, Yasunobu Nagano, Hitoshi Tamiaki, Naoki Komatsu, [Photosensitizer and anticancer drug-loaded 2D nanosheet: Preparation, stability and anticancer property], ***2D Materials***, 6(4), 045035, 2019.

8) Anfeng Cui, Meng Xiang, Ming Xu, Peng Lu, Shun Wang, **Yajuan Zou**, Ke Qiao, Chengyu Jin, Yijun Li, Meng Lu, Alex. F. Chen, Sifeng Chen, [VCAM-1-mediated neutrophil infiltration exacerbates ambient fine particle-induced lung injury], ***Toxicology Letters***, 302 (1), 60-74, 2019

9) Lei Feng, Chenchen Chang, Dong Song, Chuang Jiang, Yang Song, Chaofan Wang, Wei Deng, **Yajuan Zou**, Haifeng Chen, Xiang Xiao, Fengping Wang, Xipeng Liu. (2018) [The trimeric Hef-associated nuclease HAN is a 3'→5' exonuclease and is probably involved in DNA repair], ***Nucleic Acids Research***, 46(17), 9027-9043, 2018.

10) Xiaoliang Guo, Qunli Rao, Lingling Li, **Yajuan Zou**, Chengchei Wu. (2016) [Characterization of the fluoridating process of hydroxyapatite], ***Journal of Ceramic Processing Research***, 17(8), 815-817, 2016.

11) Maoquan Chu, Qiang Wu, Hui Yang, Ruiqi Yuan, Shengke Hou, Yifeng Yang, **Yajuan Zou**, Shi Xu, Kaiyi Xu, Ailing Ji, Lingyi Sheng. (2010) [Transfer of quantum dots from pregnant mice to pups across the placental barrier], ***Small***, 5, 670-678, 2010.

List of presentations at international conference

1. ○**Y. Zou**, N. Komatsu, Polyglycerol grafted nanoparticles improve stealth effect by resisting protein corona formation: A comparison study to PEG. ***37th European Material Research Society 2019 Spring Meeting***, Symposium L(MXE7G), Nice, France, May 29, 2019, Oral

2. ○**Y. Zou**, N. Komatsu, Quantitative evaluation of polymer density and net charge effects on nanodiamond surface toward protein affinity. ***37th European Material Research Society Meeting 2019 Spring Meeting***, Symposium M (SGP4A), Nice, France, May 30, 2019, Oral

3. ○**Y. Zou**, N. Komatsu, The influence of nanodiamond size and surface functionality on protein corona formation and macrophage uptake. ***Japan-Russia Mini-workshop***, Kyoto, Japan, Sep. 28, 2018, Oral

4. ○**Y. Zou**, N. Komatsu, Polyglycerol grafted nanoparticles enhance stealth effect by shielding protein corona formation: A comparison study to PEG. ***International Workshop on Quantum Sensing and Biophotonics 2019***, Osaka, Japan, Sep. 30, 2019, Poster

5. ○**Y. Zou**, N. Komatsu, Evaluation of polymer content and net charge effects of nanodiamond toward protein affinity. ***International Workshop on Quantum Sensing and Biophotonics 2019***, Osaka, Japan, Sep. 30, 2019, Poster

6. ○**Y. Zou**, N. Komatsu, Polyglycerol grafted nanoparticles improve stealth effect by resisting protein corona formation: A comparison study to PEG. ***Kyoto Biomolecular Mass Spectrometry Society 2019 Symposium***, P22, Kyoto, Japan, Feb. 23, 2019, Poster

7. ○**Y. Zou**, M. Xu, L. Zhao, N. Komatsu, Fabrication of fluorescent nanodiamond-iron oxide nanocomposites for dual-modal cellular imaging. ***Asian symposium on nanoscience and nanotechnology 2018***, P48, Tokyo, Japan, May 12-14, 2018, Poster

List of presentations at domestic conference

1. ○**Y. Zou**, N. Komatsu, Polyglycerol Grafting Shields Nanoparticle from Protein Corona Formation to Avoid Macrophage Uptake. ***The 10th CSJ Chemistry Festa***, P2-071, Japan, Oct. 20, 2020, Oral

2. ○**Y. Zou**, N. Komatsu, The affinity of the charged functional groups on polyglycerol-grafted nanoparticles to proteins dedicates their cellular uptake. *第10回ナノカーボンバイオシンポジウム*, Japan, Sep.15, 2020, Oral

3. ○**Y. Zou**, N. Komatsu, Polyglycerol grafted nanoparticles improve stealth effect by resisting protein corona formation: A comparison study to PEG. *第九回ナノカーボンバイオシンポジウム*, Nagoya, Japan, Sep. 2, 2019, Oral

4. ○**Y. Zou**, N. Komatsu, The influence of nanodiamond size and surface functionality on protein corona formation and subsequent macrophage cellular uptake. ***28th Annual Meeting of The Materials Research Society of Japan*** (C1-O19-002), Kitakyushu, Japan, Dec. 19, 2018, Oral

5. ○**Y. Zou**, M. Xu, L. Zhao, N. Komatsu, Fabrication of fluorescent nanodiamond-iron oxide nano-composite for a multimodal bioimaging probe]. P21, *第八回京都若手ソフトマター研究会*, Kyoto, Japan, Mar. 7, 2018, Poster

Acknowledgements

Toward the end of this thesis, I have recalled that there are so many people who have walked along with me, guiding, helping, and supporting me throughout my PhD journey. Without them, I could not imagine how my PhD would have been possible.

First and foremost, I would like to express my sincere gratitude to my supervisor Prof. Naoki Komatsu, who definitely has been an inspiration for me. It is with gratitude for his wisdom and knowledge, his passion for teaching and his ability to inspire others, that made me possible to reach my full potential. I also appreciate very much that his door is always open for discussion, which efficiently promoted my research work.

Great appreciation is extended to Dr. Masazumi Fujiwara (Okayama University), Dr. Shinji Ito (Kyoto University), Dr. Fumi Yoshino (Shiga University of Medical Science), Dr. Yuta Suzuki (Kyoto University), and Dr. Li Zhao (Soochow University) for their kindly support. Without their help, my projects cannot proceed so smooth.

I am appreciative to Prof. Rubing Liang (Shanghai Jiao Tong University, SJTU), Dr. Toru Tsuchiya (Kyoto University) and Dr. Alberto Bianco (CNRS, France), whose helpful discussions make my PhD study easier. I am grateful for my former colleagues and friends from SJTU, Prof. Bangshang Zhu, Prof. Limin Sun, Prof. Xinyuan Zhu, Dr, Li Xu, Dr. Dali Wang, Dr. Qinghua Guan and Dr. Ting Yin, whose kind encouragement make me confidently to pursue this PhD study.

I am also deeply indebted to Mr. Haruyasu Kohda, Ms. Keiko Okamoto-Furuta and Mr. Tatsuya

Katsuno (Division of Electron Microscopic Study, Kyoto University) for their help with TEM sample preparation, Dr. Takahiro Fujiwara, Dr. Masahiko Tsujimoto and Dr. Takayuki Homma (iCeMS, Kyoto University) for their help in TEM, ICP, and FACS analysis as well as the usage of the shared cell culture room, Dr. Junko Satoh (Kyoto University) for her help with LC-MS/MS sample preparation, and Ms. Yukiko Koyama (Shiga University of Medical Science) for her help with ICP-MS analysis. I am also grateful to whole member of Tsue lab and Dr. Satoshi Shimono for always letting me get access to IR machine, and Mr. Yuki Maeda (Kageyama lab in Institute for Frontier Life and Medical Sciences, Kyoto University) for kindly guiding me for the use of FACS machine.

I would like to thank Prof. Tatsuya Hayashi and Dr. Tatsuro Egawa (Kyoto University) for their valuable suggestions in my manuscript preparation.

I am grateful to the previous and present members of Komatsu lab for having wonderful moment in these years. Special thanks to Ms. Yujing Jiang and Mr. Yuquan Wang, for their great help in my life.

Finally, all after this, deepest gratitude to my beloved husband Dacheng, our two prestigious daughters Hanzhang and Yongtang, and all my family members. I am grateful for their kind understanding on these years of absence and their loving support. It is all their love make me possible to finish this PhD thesis.

Polyglycerol grafting shields nanoparticles from protein corona formation to avoid macrophage uptake. ACS Nano 14 Issue6 7216-7226 (2020)
(DOI:10.1021/acsnano.0c02289)

Quantitative investigation of the interaction between proteins and charged functional groups on the polyglycerol-grafted nanodiamond surface. Carbon 163 395-401 (2020)
(DOI: 10.1016/j.carbon.2020.02.089)

Effect of Protein Corona on Mitochondrial Targeting Ability and Cytotoxicity of Triphenylphosphonium Conjugated with Polyglycerol-Functionalized Nanodiamond" Mol. Pharmaceutics, 18(7), 2823-2832 (2021)
(DOI:10.1021/acs.molpharmaceut.1c00188)